WA School of Mines: Minerals Energy and Chemical Engineering

Dopant Implications in a Lanthanide Perovskite for Symmetrical Solid Oxide Fuel Cell Electrodes

Paulo Sérgio Barros Julião

This thesis is presented for the Degree of

Doctor of Philosophy

Of

Curtin University

December 2019

(Page intentionally left blank)

Declaration

To the best of my knowledge and belief this thesis contains no material previously published by any other person except where due acknowledgment has been made.

This thesis contains no material which has been accepted for the award of any other degree or diploma in any university.

Signature: _____

Name (Student Id): Paulo Sérgio Barros Julião (18909917)

Date: ____ /05/2020

(Page intentionally left blank)

Abstract

Perovskites have been extensively pondered as electrode materials for Symmetrical Solid Oxide Fuel Cells (SSOFC). The present work approaches the consequences of the A site mismatch variation on the electrochemical properties of this cubic structure through the doping of Alkaline Earth Metals (Aem) in the chemical formula of $La_{0.7}Aem_{0.3}Ti_{0.5}Mn_{0.4}Ni_{0.1}O_3$. Barium and Calcium were the chosen Aem materials of this systematic analysis where X-ray diffraction (XRD) structural analysis, conductivity, impedance and performance variables were studied under both reducing and oxidizing atmospheres. Further implications were observed combining these with both Scanning Transmission Electron Microscopy (STEM) and Scanning Electron Microscopy (SEM) data. Regardless of the surrounding atmosphere, Calcium perovskite always revealed a higher degree of impurities as well as a much larger tendency to segregate Nickel and a consequent superior instability under reducing conditions. A high catalytic activity enhancement from the superior Nickel segregation is believed to be the major reason behind the (essentially anodic) performance improvement of Calcium over the Barium material. Regardless of the chosen dopant, the conductivity under reducing conditions revealed the existence of 2 thermal regimes. Assuming that the intrinsic conductivity would have a linear implication in the respective Peak Power Density (PPD), it was found that this simple hypothesis surprisingly estimates the intrinsic performances of each material with errors of 5.3 and 6%.

(Page intentionally left blank)

Research output and other collaborations

The contents of chapters III, IV and V were compiled into a manuscript entitled “A-site cation influences on performance, structure and conductivity of a lanthanide-based perovskite electrode for symmetrical solid oxide fuel cells” and later published (in February 2020) in a suitable scientific journal as a research paper:

Julião, P. S. B. (2020). A-site cation influences on performance, structure and conductivity of a lanthanide-based perovskite electrode for symmetrical solid oxide fuel cells. *Journal of Power Sources*, 450, 227723. https://doi.org/10.1016/j.jpowsour.2020.227723

During my academic path, I have engaged in other activities aside of my own research topic. Even though these works are not related to this thesis, such collaborations helped me to become a better scientist. I was also fortunate to have been granted the amazing experience of supervising the graduated student, Patrick Akang (17099189) during the end of 2018 (on the behalf of Professor Zongping Shao).

(Page intentionally left blank)

Acknowledgements

In my previous academic steps, I have always stated that physically and psychologically people are indeed made of other people. This work, though developed mostly by me, had the help of group members such as Xu Xiaomin (in the STEM analysis), Zhong Yijun (in the SEM session) and Wang Wei and Su Chao (both with initial laboratory guidance). It was a pleasure to collaborate with both visiting scholars Yong Jiao and Wenting Ann who have severely increased my contact with the publication side of the research field. Occasionally, I have also received further support from Curtin University Technical officers such as Ann Carroll, Ross Hayes and Roshanak Doroushi.

During my academic path, I have engaged in other activities aside of research such as mentoring and teaching. I was fortunate to have been granted the amazing experience of supervising the graduated student, Patrick Akang (17099189) during the end of 2018 (on the behalf of Professor Zongping Shao). Much more important than co-authorship collaborations, this experience made me understand my limitations. Either supervising undergraduate students is something I really like to do or at least I can say I was fortunate to have had a very positive experience with Patrick, leaving me very receptive to similar future experiences.

Not all help within this work resulted through collaborations or official Curtin staff members professionally doing their job. I have met people who went the extra mile with no real reason aside of kindness. Matthew Rowles (who sat with me through an XRD refinement process and latter had pointed me the Australian standards to determine the relative density) or Jason Wright (who simply solved a technical issue by picking up a call on the weekend during his family leisure time) are examples of that. Years of expertise in the SOFC field together with a pleasant personality resulted in remarkable insights from Ryan O'Hayre.

The Student Assist Officer Yiu Onki was of great initial help to me before I was put in touch with the Sessional Academic Andrew Cameron. Andrew was

an amazing source of advice and course of action for me to deal with faced obstacles inside Curtin University. Despite experiencing these issues, I am extremely grateful to have been granted a Curtin International Postgraduate Research Scholarship (CIPRS) together with an Office of Research and Development (ORD) Scholarship, which without those, this work would never exist. I can only hope my complete devotion to the project during these three years is truly recognized beyond my closer working colleagues.

Beyond scientific, technical and moral support, we are all made of every experience we go through as well as every important person we interact with. These people, whether friends, family or both, made me who I am and I will always carry them around wherever I go:

Filipe José Mariano dos Santos and Manuel José Barbosa Oliveira,

Pedro Miguel Fernandes da Silva, Sara Moreto Mafra

Jorge Fernando Soares Gonçalves and Nuno Gonçalo Ferreira Cordeiro,

Francisco José Almeida Loureiro and Tao Yang.

Liliana Isabel de Barros Julião, João Paulo Julião and Maria Julia Barros Ribeiro

Asti Wulan Korining Sukanti

Table of contents

(Page intentionally left blank)

List of figures

List of tables

List of equations

(Page intentionally left blank)

Chapter I - Introduction

1. Background

Several energetic alternatives have been studied extensively in the last decades in order to reduce the non-renewable sources dependency. Among the current technologies, fuel cells are known for their potential high efficiency of fuel conversion into to electricity. Many challenges still need to be surpassed in order to improve their durability, reliability and life time at a larger scale implementation scenario. Fuel cells can be broken down into their 3 main components of 2 electrodes (a cathode and an anode) and an electrolyte which together with the fuel choice classifies these devices into distinct groups (Figure I 1). Each of these categories has its typical efficiency, costs and typical/optimum temperature conditions of operation [1].

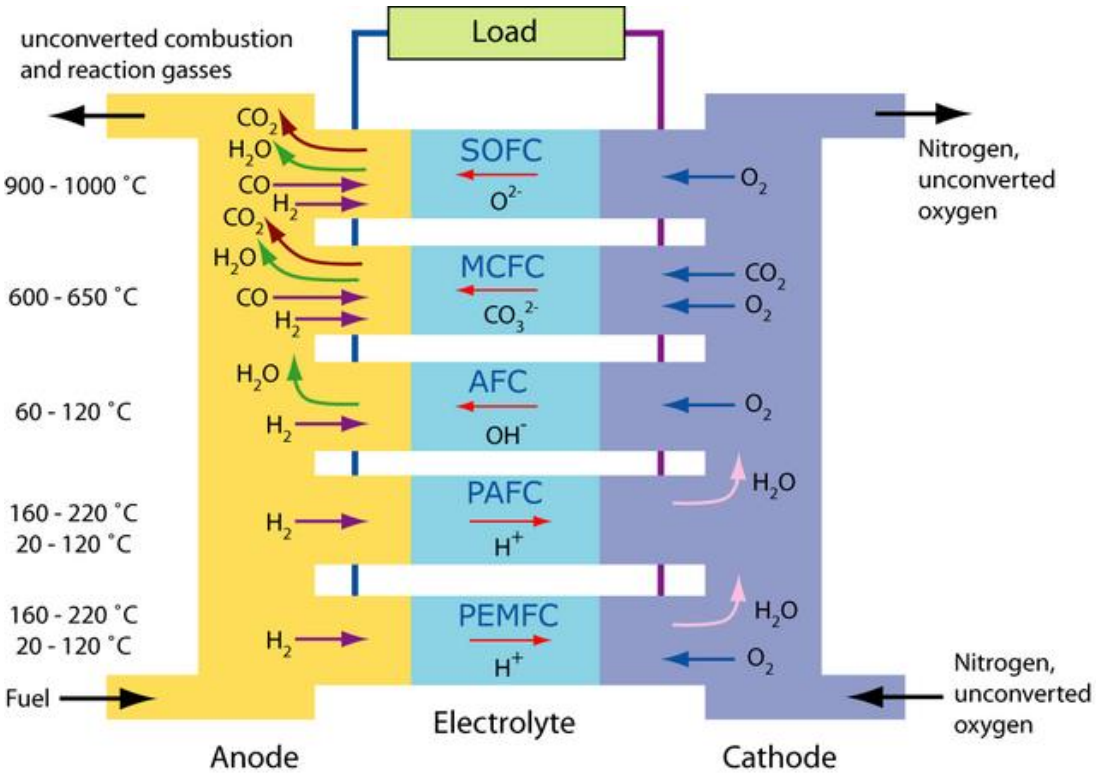

Figure I 1 - Fuel cell types [2]

The present thesis is solely focused in the development of electrodes for Solid Oxide Fuel Cells (SOFCs). Fuel versatility from the higher temperature conditions, high energy conversion efficiencies, easy assembly and minor leakage problems due to having all cell components in a solid state are some of the major advantages of these cells. Some of the barriers this technology still faces today are the fabrication and maintenance high costs [3] and the anode carbon deposition issue [4] - [7] which results from operating the cell on hydrocarbon fuels.

The stated fuel versatility advantage obviously results in different oxidation reactions to be considered in the anode. Since they can run on hydrogen or a hydrocarbon fuel, certainly this choice results in either the formation of solely water vapour or an additional CO_2 emission (respectively) as well as the release of electrons that can be conducted and used as electricity. On the cathode side, the electrochemical reduction of the air oxygen creates oxygen anions (O^{2-}), which, traveling through the electrolyte ion conductor, will oxidize the fuel on the anode side (Figure I 2). The electrolyte ion conduction property allows the charge transfer from the cathode to the anode side to occur without running into a short circuit scenario due to the typical low electronic conductivity of the electrolytes.

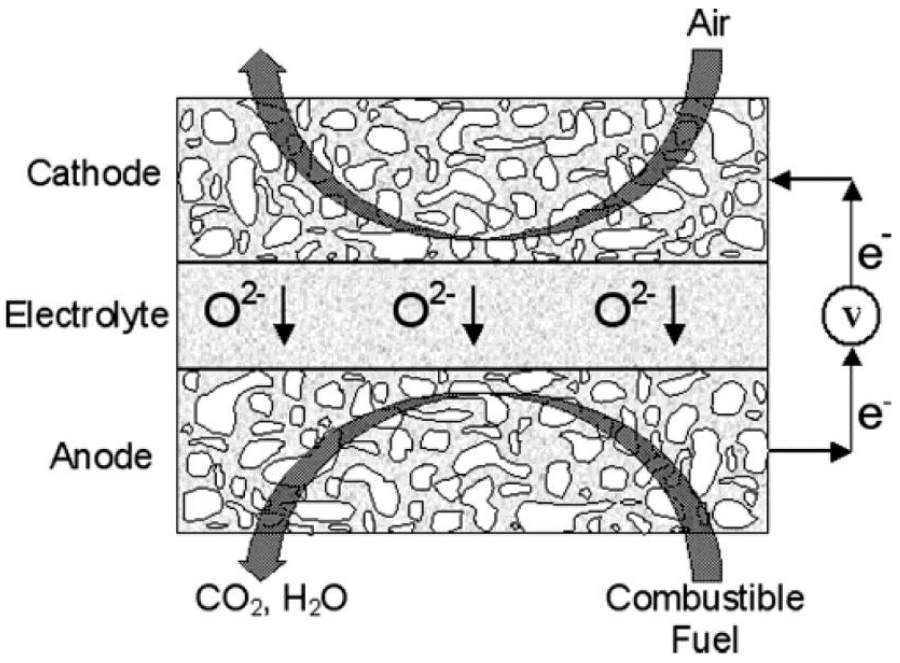

Figure I 2 - Brief squeme of an SOFC operation [8]

1.1 Symmetrical Solid Oxide Fuel Cell (SOFC) electrode requirements

SOFC cathodes must have sufficient porosity, chemical compatibility, a minimal miss match of thermal expansion coefficient (TEC) with the electrolyte as well as high electronic and ionic conductivities. Anodes require good electronic conductivity together with high catalytic activity for fuel oxidation so that the reaction losses can be minimized. Both electrodes obviously demand chemical and mechanical stabilities with the addiction of good porosity so that both the concentration of triple phase boundary (TPB) regions in the cathode side and the fuel diffusion process in the anode side are improved.

The Symmetrical Solid Oxide Fuel Cells (SSOFCs) provide significant advantages to surpass the main issues of the regular SOFC technology. This symmetrical approach consists in having both electrodes made of the same material. Obviously this results in further benefits regarding fabrication costs (since both electrodes can be sintered in one single step), thermal compatibility and gas flow reversibility to prevent carbon coking, however it also imposes further electrode criteria from the fact that the chosen material has to perform both (cathode and anode) roles. Furthermore, demanding both cathode and anode typical requirements is not enough as a decent SSOFC electrode also needs reasonable electronic conductivity and minimum thermal expansion coefficients (under both oxidizing and reducing conditions) [9] - [13]. In conclusion, SSOFCs are not necessarily better or worse than regular SOFCs, they are rather a change of perspective of this technology's current challenges where significant advantages are acquired at the cost of further electrode restrictions.

1.2 Perovskite structure

Perovskite materials have been extensively studied due to their physical and electrochemical properties to provide the required SSOFC electrode demands. The single perovskite cubic structure has the chemical formula of ABO_3 and contains the coordination numbers of 12 and 6 in the respective A and B sites (Figure I 3). The A site is always composed of a larger ion and the B site of a smaller one. In the SSOFC electrodes' ambit, popular choices for A and B site ions are alkaline earth metals and transitional metals respectively.

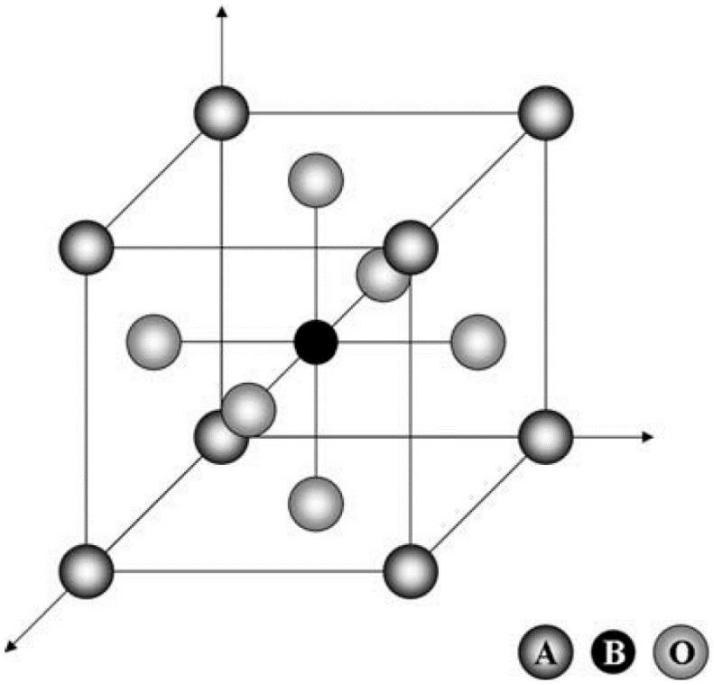

Figure I 3 - Perovskite ion disposition representation [14]

The stability and distortion of the desired crystal can be estimated theoretically using a dimensionless indicator resultant from the relevant ionic radius that is the Goldschmidt's tolerance factor (Equation I 1). Typically perovskites are likely to be formed and remain stable for a tolerance factor "t" value gap between 0.77 and 1 [14].

$$t = \frac{r_A + r_o}{\sqrt{2}(r_B + r_o)}$$

Equation I 1 - Goldschmidt's tolerance factor "t" (where "r_o", "r_A" and "r_B" are the radii of oxygen ion, the A-site and B-site ions respectively) [15]

2. Motivations

2.1 World's energy demand

The rising tendency of the word's energy consumption (Figure I 4) and its current dependency in fossil fuels exhibits today's necessity of alternative energy sources. Consequentially, efforts have been made and the latest reports already

display the renewables sector leading the global energy demand in electricity generation as well as the growth percentage in the global energy mix projection [16] - [19]. Due to being heavily dependent on weather conditions, most of these are generated under intermittent operation regimes, making it so that though the renewable energy is part of the solution to the fossil fuel dependency, the generated electricity still has to be stored. Fuel cell usage has been pondered for electricity storage (much like common batteries) in the form of chemical energy.

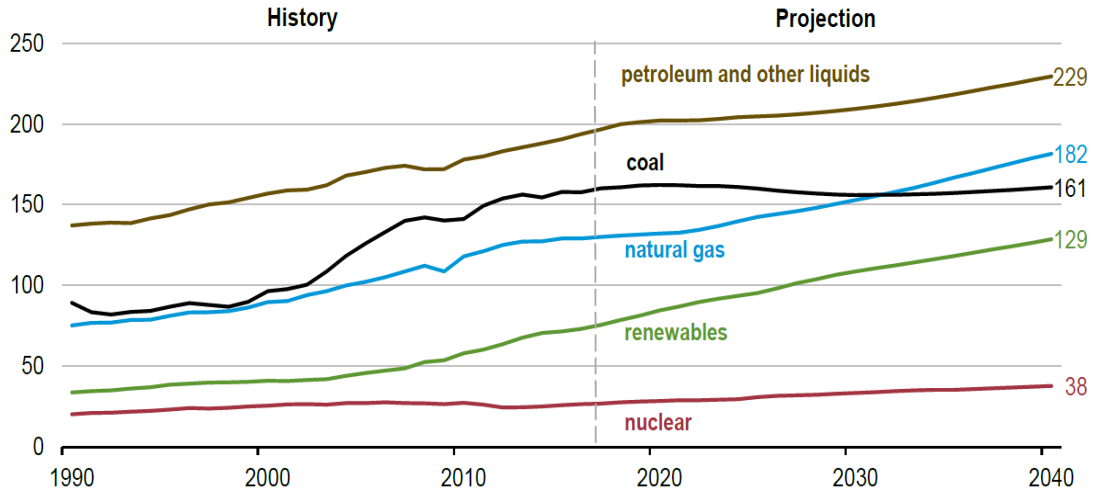

Figure I 4 - World's energy consumption history and projections in quadrillion Btu from the International Energy Outlook 2018 (IEO2018) [16]

2.2 Symmetrical SOFC advantages

The project consists in the development of an SOFC electrode, which means it does share the same basic motivation all SOFC projects do: to provide a clean and more efficient way to convert fuel into energy. Since it is a symmetrical design, not only it contains all the SOFC technology potential advantages, as it also tries to address some of its current challenges which are the fabrication and maintenance high costs, the short life time operation and carbon deposition problems.

2.3 Material advantages

The selected dopants are relatively abundant which, within a breakthrough, it assures the supply of raw materials. Since the prices of the electrode selected

chemicals are also relatively low, the present project attempts to start from an advantageous position regarding the issues of the SOFC commercialization barriers [3].

3. Objectives

The present work aimed to synthesize a novel SSOFC electrode material and define variable tendency relationships between the dopant size cation A site differences and the variables of electrochemical performance and impedance, structural purity estimation, conductivity and activation energy. Based on the acquired parameter trends and similar literature results, other optimization attempts (such as the B site dopant substitution) were also implemented together with the establishment of plausible hypothesis to interpret the obtained results which can be further tested.

4. Contributions

Asite and Bsite dopant effects in Perovskites regarding Performance, Impedance and Conductivity might generate valuable trends in the understanding of how these variables work together along with the temperature under oxidizing and reducing conditions. Gathering information regarding different chemical compositions in a consistent set of variables while still standing within a comparable range of conditions facing the literature results provides a strong set of data contributions to be consulted. Furthermore, if the phenomena influencing the improvement of the electrodes are understood then these relationships can be further explored in order to promote external improvements from adjusting those parameters into other systems. The findings of this thesis outputted 4 main plausible hypothesis to interpret the results obtained in each of the following experimental chapters:

Chapter 3 concludes that if the A site dopant-host difference minimization really improves the performance, then it only seems to do so by improving the anode side of the fuel cell, since both tested perovskites revealed comparable peak power density (PPD) results when assembled solely as cathodes.

Chapter 4 formulates the hypothesis of the presence of double sesquioxide impurities under reducing conditions (in the perovskite with the lowest dopant-host A site size difference) from the fact that this assumption significantly improved the respective agreement parameters of the Rietveld refinement analysis.

This perovskite unexpectedly revealed lower purity estimations and higher sensitivity towards reducing conditions, suggesting that further analysis needs to take place in order to fully understand possible interactions between the perovskite and sesquioxide impurity phases. The calcination temperature optimization as function of the estimated structural purity (which can potentially suggest starting conditions to new synthesis attempts in future projects with similar materials) is a valuable contribution that can also be found in this chapter.

Chapter 5 suggests that the performance improvement has higher influence under reducing conditions due to the existence of an intrinsic regime of conductivity. This hypothesis is supported by the respective average differences of conductivity and performance in which the influence of the intrinsic regime seems to be displayed.

Chapter 6's B site optimization attempt recognizes that the electronic conductivity also plays a role in the performance improvement, however if the dopant-host minimization affects the resulting cell PPD, then the relevant theoretical scenario to be considered regarding the Titanium oxidation state must be 4+. Further analysis can take place in order to further support or fully disprove this hypothesis.

Chapter 7 establishes a relationship to estimate the performance obtained under reducing conditions (in Chapter III section 3.5.1) solely within the temperature range of the intrinsic regime through the measured conductivity values in hydrogen (of Chapter V section 3.2). The obtained values of this model provided results with relative errors from 5.3 to 6%.

5. Thesis overview

This section is meant to explain the research path of this thesis as well as to guide the reader through the major highlights of each chapter. The course of this thesis along with its formulated hypotheses are represented in the following thesis diagram (Figure I 5) where the chapter areas and most relevant subsections are properly identified by the blue dashed lines and the blue numbers nearby the diagram boxes or nodes respectively.

Chapter I provides the relevant background information, motivations, objectives, contributions and this thesis overview.

Chapter II mainly divides the up to date performance results of SSOFCs graphical dispositions along with the 2 main measured parameters of resistive factors (such as the electrolyte thickness and polarization resistance) and other variables (like activation energy and conductivity).

Chapter III focuses on the perovskite A site dopant comparison in terms of PPD, polarization resistance and resultant total activation energy. These variables were measured and estimated in different cell configurations so that the obtained performance difference in an SSOFC could be established to be the consequence of an anodic performance difference.

Chapter IV, as the title suggests, is organized into two main subjects. The XRD analysis approaches the chemical compatibility between the electrode and electrolyte and the phase purity estimations. These topics were investigated after both treatments of reducing and oxidizing conditions. Since no additional phases in the mixture powders were identified and the relevant consideration of a double space group impurity strongly improved the refinement agreement parameters to acceptable standards, this chapter concludes that not only the cell components are chemically stable as well as the phase impurities can also be benefitting the anodic behaviour. The STEM analyses not only suggest that the performance difference might be coming from the superior Nickel segregation tendency as well as that this superior segregation tendency seems to provide a less stable perovskite structure.

Chapter V approaches the conductivity measurements under both oxidizing and reducing atmospheres, relating the average differences between both perovskite materials under the latest conditions with the respective average anodic performance differences observed in Chapter III. The acquired results revealed that these performance differences display the same double regime tendencies as the respective conductivity differences along with the temperature. The observation of this phenomenon gave birth to the hypothesis that the intrinsic conductivity regime seems to have a greater influence in the performance than the activation energy, structural purity or even the magnitude of the conductivity differences.

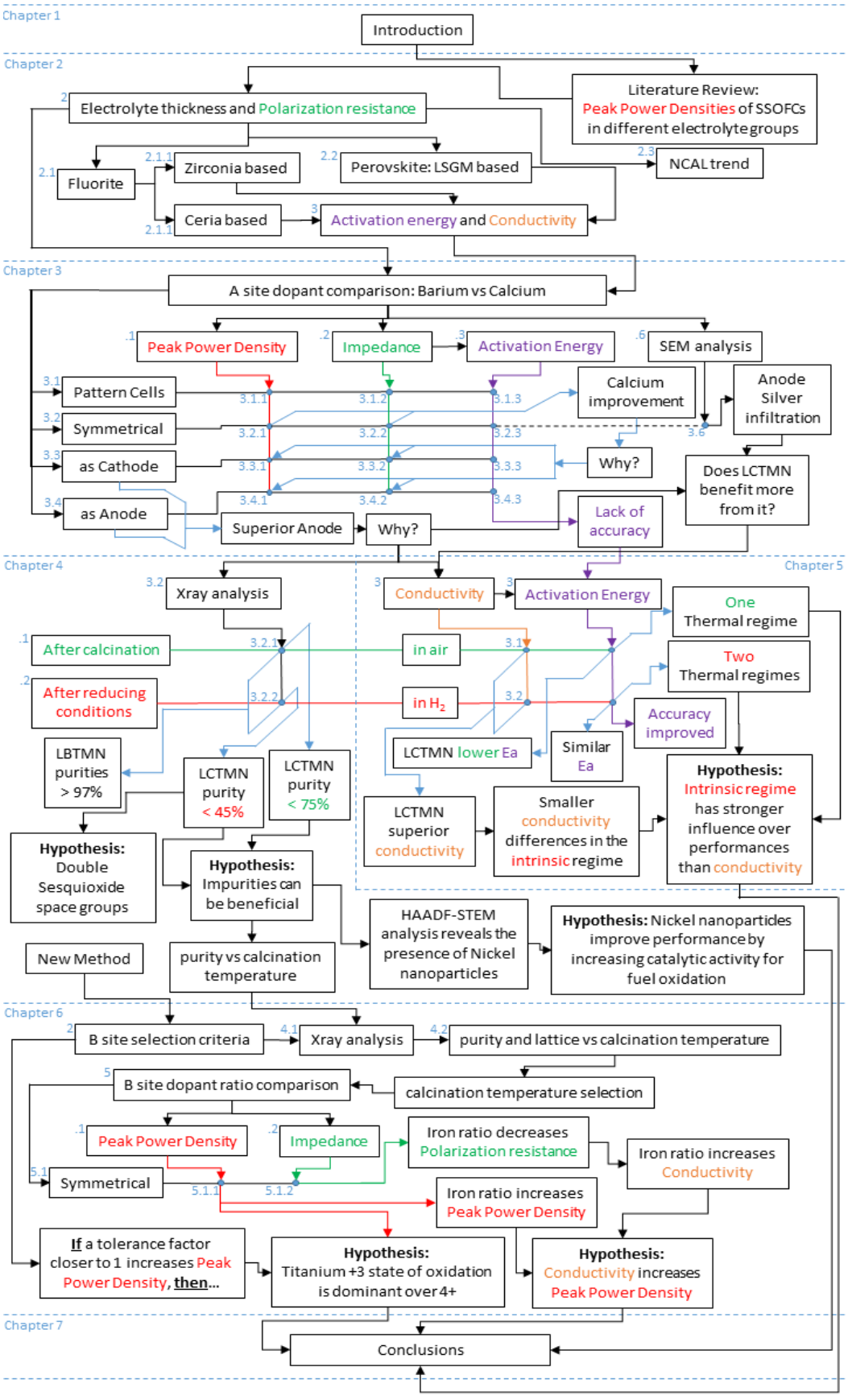

Figure I 5 - Thesis diagram

Chapter VI alters the perovskite composition in order to attempt to further improve the obtained results. Once the purity estimations defined the optimum calcination conditions, not only the results stand in line with expected beneficial conductivity influences, as they further lead to believe that if a tolerance factor closer to 1 increases the performance, then the Titanium 3+ state of oxidation is very likely to be dominant over the remaining valency states.

Chapter VII compiles the major findings of this thesis, while correlating the addressed parameters of each chapter and further proposing a humble model to explain the obtained results while enabling further test of its applicability in future synthesized materials.

Chapter II - Literature Review

1. Introduction

This chapter compiles some SSOFC performance results obtained in the last decade and attempts to spot pertinent tendencies every time comparable results are identified from reference to reference. To find these particular circumstances, section 2 dives into the Peak Power Density (PPD) point dispositions (measured at 800 ^{o}C) along with the respective supported electrolyte thickness and polarization resistance in each of the main electrolyte types (of Zirconia, Ceria and LSGM based compositions). Still within this section and considering the same variables, the recent promising research trend of the NCAL ($Ni_{0.8}Co_{0.15}Al_{0.05}LiO_{2-\delta}$) electrode was lightly approached (separately in section 2.3) given the fact that the operation temperatures are much lower. Since not all publications in the field consistently display activation energy and conductivity measurements, together with the fact that these parameters depend on the electrode properties only, each of these two variables was addressed in section 3, covering both reducing and oxidizing testing conditions whenever reported.

2. Influences of the main resistive factors

The following data results are organized by electrolyte species, given the fact that this cell component presents the least diversity in terms of material selection among literature results of symmetrical solid oxide fuel cells (SSOFC). This section briefly approaches performance results of symmetrical cells supported by Zirconia and Ceria based compounds (in section 2.1) as well as by the more popular LSGM perovskite electrolyte (in section 2.2). Since fair terms of comparison such as the same operation temperature have to be established among these results, a separated section 2.3 had to be defined exclusively to address the NCAL ($Ni_{0.8}Co_{0.15}Al_{0.05}Li$ oxide) electrode, since these cells operate at a much lower temperature gap from 550 to 600 ^{o}C.

2.1 Fluorite structured electrolytes: Zirconia and Ceria based compounds

Among the PPD results of SSOFC, the electrolytes based of Zirconia (ZrO_2), such as Scandia (Sc_2O_3) and Yttria (Y_2O_3) doped, respectively named of Scandia-stabilized Zirconia (ScSZ or SSZ) and Yttria-stabilized Zirconia (YSZ) are the most abundant in this category. In these composite oxides the common 8% ratio serves both purposes of stabilizing the fluorite cubic structure and increase the ionic conductivity (Figure II 1) through improving the concentration of oxygen vacancies. Zirconia based electrolytes provide decent ionic conductivity, as well as stability under both relevant atmospheres while being compatible with most electrode materials together with strong mechanical properties. The high operating temperature requirement is the main disadvantage of these electrolytes [83] from the fact that consequent high operating costs and leakage problems become more likely to occur (increasing sealant requirements to higher standards) [84] - [85].

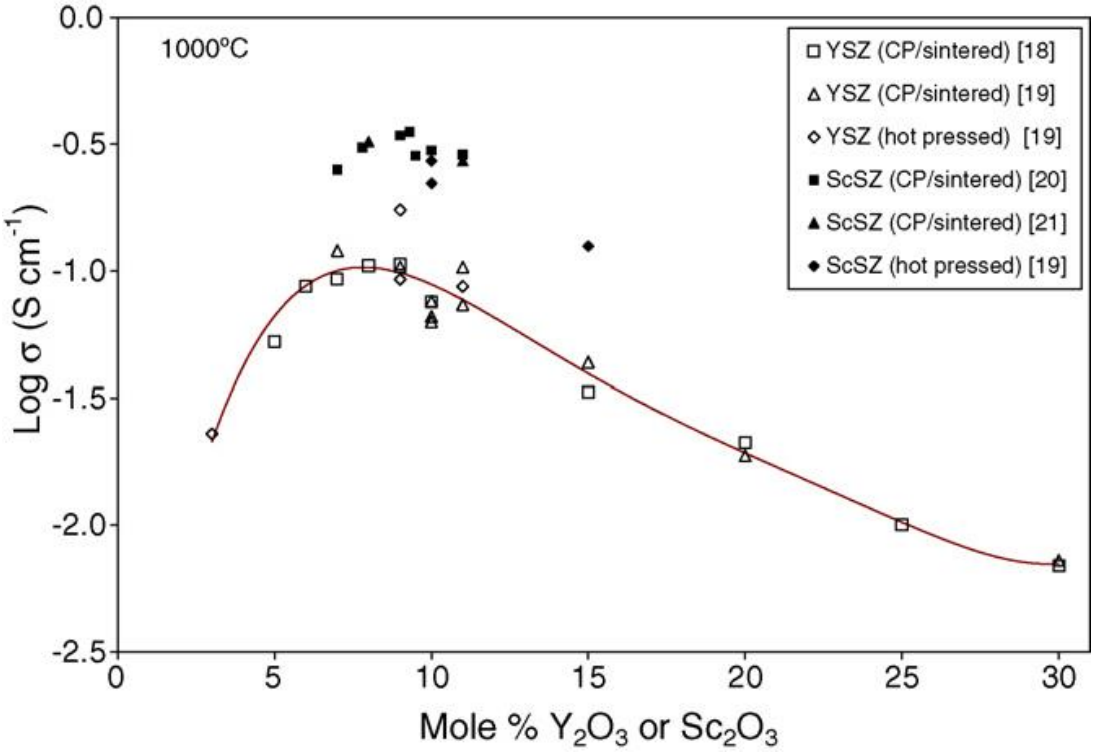

Figure II 1 - Yttria and Scandia mol percentage implications on ionic conductivities of the respective YSZ and SSZ electrolytes [82]

Much like the Zirconia based electrolytes, Ceria (CeO_2) fluorite structure can also be stabilized with sesquioxides such as Gadolinia (Gd_2O_3) and Samaria (Sm_2O_3), respectively forming this way the materials of GDC (Gadolinia-doped Ceria) and SDC (Samaria-doped Ceria). Just like Zirconia based electrolytes, ceria composites can also be used as additive performance enhancers for the electrode compounds through offering other advantages, such as higher ionic conductivity [86] - [87], while keeping reasonable chemical and thermal expansion coefficient compatibilities along with high performance cathode materials. Together with their benefits, ceria based electrolytes are also known to contain some drawbacks which are mainly experienced under reducing conditions, such as the reduction of the Cerium cation from Ce4+ to Ce3+ leading to the consequent lower open circuit voltage (OCV) and the increasing likelihood of short circuiting. Among the collected data of SSOFC OCV values at 800 ^oC, these ceria based electrolytes indeed tendentiously reflect a much lower average of 0.78859 V (Table II A3), while under the same operation conditions, this value is easily surpassed by the corresponding calculated average of 1.04778 V (Table II A1) that is found within Zirconia based electrolyte supported cell measurements.

2.1.1 PPD results with Zirconia based electrolytes (SSZ and YSZ)

The thickness of the electrolyte is well known to have its influence in the performance results, being the reason why it is widely mentioned in the experimental section of every publication. Gathering literature sources of symmetrical cell PPDs (measured at 800 ^oC) along with the respective electrolyte thicknesses (Table II A1 and Table II A2), the influence of this variable is not evident given the fact that a wide variety of electrodes is present (Figure II 2A). On the other hand, the sources located at a thickness of 0.4 mm allow some electrode material composition conclusions to be drawn. Sources seem to indicate that a B site with Iron (LSF) instead of Manganese (LSM) provides superior performance results (of 316 $mW.cm^{-2}$ [28] vs 67.45 $mW.cm^{-2}$ [22]) within the same A site perovskite ratios of Lanthanum (0.8) and Strontium (0.2). This improvement is further supported by both the respective differences in the total electrode polarization resistances (Figure II 2B) as well as the activation energy (Ea) values of 0.19 and 0.96 eV of LSF comparatively to the 1.68 and 1.35eV displayed by the LSM (in air and hydrogen respectively).

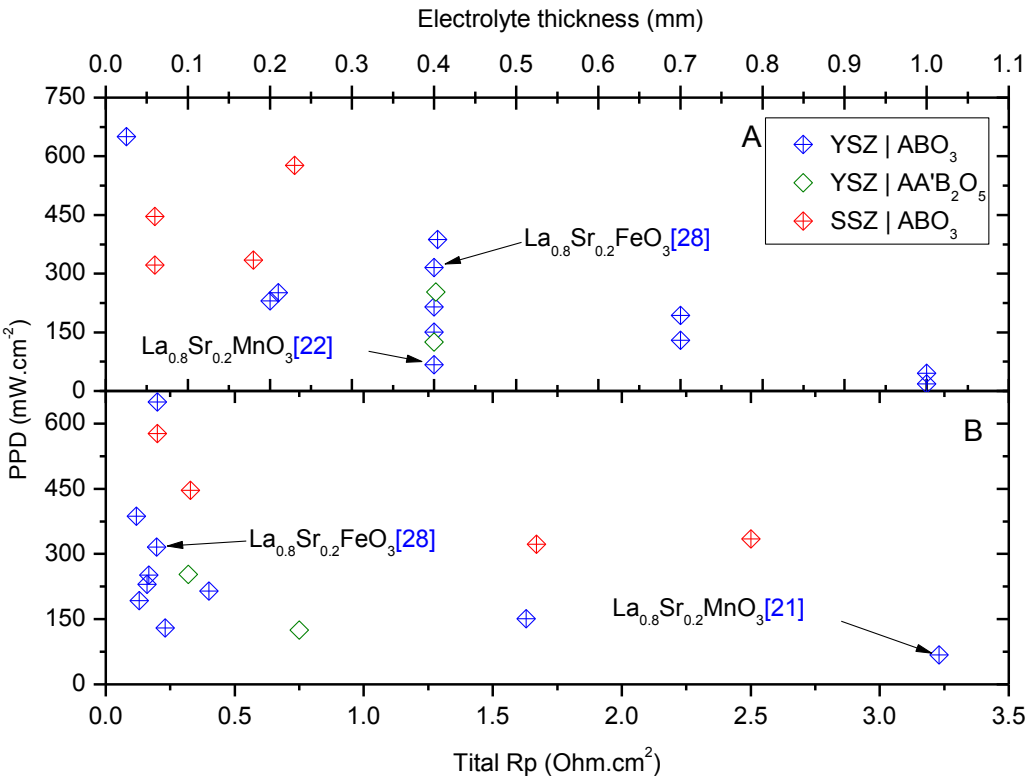

Figure II 2 – Graphical disposition of Zirconia based electrolyte thicknesses (A) and total polarization resistance (B) of electrodes vs literature performance results measured at 800 ºC [21] - [28], [30], [32] - [34]

The total polarization resistance can be estimated from an Electrochemical Impedance Spectroscopy (EIS) test of the operating cell in both atmospheres, where usually the resistive factor of the electrolyte can be extracted from the profile. Much like in the previous variable of the electrolyte thickness, it was still not possible to spot a clear tendency at 800 ºC, however the higher concentration of literature results in lower values of polarization resistances (Figure II 2B) is undeniable.

2.1.2 PPD results with Ceria based electrolytes (GDC and SDC)

At 800ºC and supported on a GDC pellet of 0.3 mm thick, the perovskite $Ba_{0.5}Sr_{0.5}Fe_{0.9}Cu_{0.1}O_3$ was reported by Yang G. and his co-workers in 2015 [36] to yield a PPD of 400 $mW.cm^{-2}$. The same publication reveals a further improvement to 480 $mW.cm^{-2}$ through doping a small ratio of Titanium while adjusting the amount of Iron (to form $Ba_{0.5}Sr_{0.5}Fe_{0.8}Cu_{0.1}Ti_{0.1}O_3$). Two years later, Ding X. et al. [42] reported the superiority of the infiltration technique versus the physical mixing in lanthanide

perovskites using a constant ratio of 30% in both scenarios and an SDC pellet support as thick as 0.28 mm. The physical mixing performance (of 140 $mW.cm^{-2}$) is surpassed by more than twice as much (with a value of 303 $mW.cm^{-2}$). Relating this result with an older publication of Yang G. from 2014 [38], it is found that this material performance can be further increased to 507 $mW.cm^{-2}$ by increasing the infiltration ratio from 30 to 70% (Figure II 3A). This is considered a plausible deduction from the fact that not only the operation temperature remains at a constant 800 ^{o}C, the electrolyte thickness parameter has negligible variation and the diminishing of the respective polarization resistances (Figure II 3B) also provides further agreement to the PPD improvement in these similar chemical compositions.

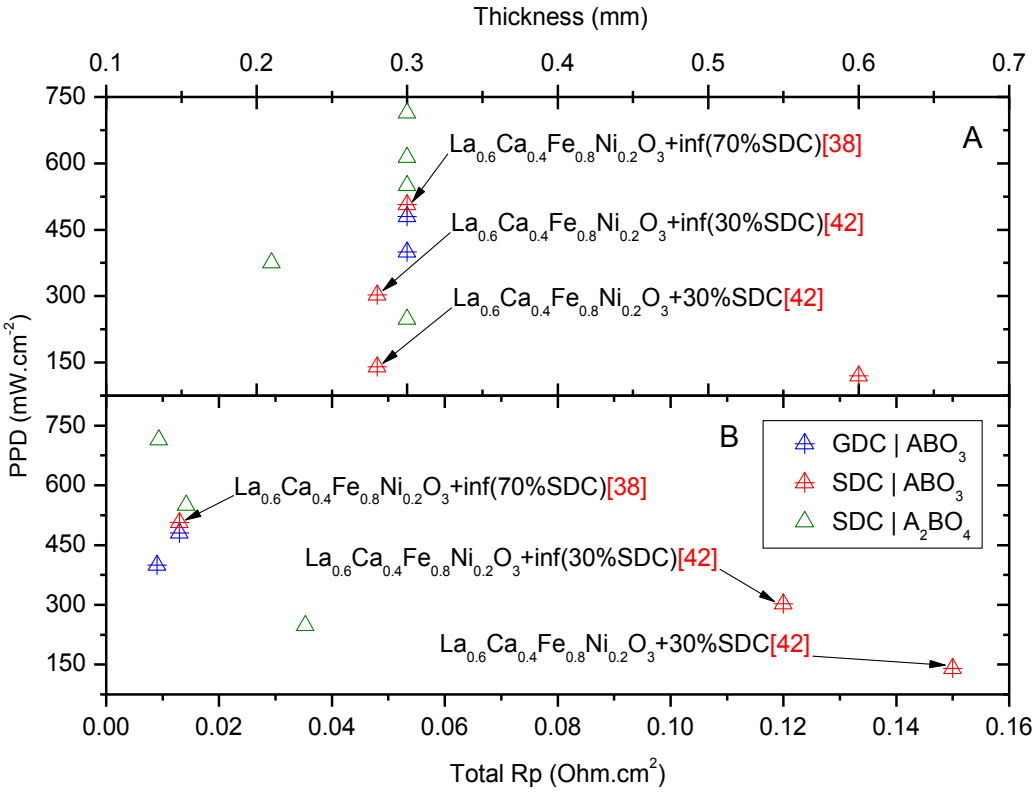

Figure II 3 – Graphical disposition of Ceria based electrolyte thicknesses (A) and total polarization resistance (B) of electrodes vs literature performance results measured at 800 ^{o}C [12], [36], [38], [41] - [42], [46] - [48]

Recently in 2016 and 2017, Shen J. and his collaborators [47] - [48] used both physical mixing and infiltration techniques in a combination of Nickel oxide, SDC and a lanthanide oxide. From both works, it can be deducted that the impregnation of the

layer-structured material provides superior performances (of 714 $mW.cm^{-2}$) comparatively to the instead impregnation of the SDC electrolyte material (which yield 614 $mW.cm^{-2}$). The respective polarization resistances of these results obtained on Ceria based electrolytes along with the performances (Figure II 3B) reveal another valid aspect to note from the point disposition. Most literature sources seem to be once more, located in the lower polarization resistance region, though comparatively to the zirconia based electrolytes, even more data would be required to validate the assumption that a similar point disposition would occur. All the gathered literature results used in this section 2.1.2 are also organized in the appendix Table II A3 and Table II A4.

2.2 Perovskite structured electrolyte: LSGM based compounds

Strontium, Magnesium doped Lanthanum Gallate (LSGM) is another popular electrolyte material, which has been reported with slight ratio variations in each measurement. Ignoring other factors such as buffer layers with other materials, the three most popular compositions of this perovskite are $La_{0.8}Sr_{0.2}Ga_{0.83}Mg_{0.17}O_3$, $La_{0.9}Sr_{0.1}Ga_{0.8}Mg_{0.2}O_3$ and $La_{0.8}Sr_{0.2}Ga_{0.8}Mg_{0.2}O_3$. Much like Ceria based electrolytes, comparatively to zirconia based materials, LSGM also processes higher ionic conductivity [88], good compatibility with mixed ionic-electronic conductors (MIEC), but it is not stable with large doping ratios of Nickel under reducing conditions and it pales in mechanical stability [89].

In 2012, the Journal of Materials Chemistry [49] has revealed three double-perovskites (varying ratios of Cobalt and Molybdenum) displaying decent performances ranging from 390 to 460 $mW.cm^{-2}$ .The ratio optimization of this variable seems to lie somewhere close to the specific chemical composition of $Sr_2Co_{1.15}Mo_{0.85}O_{6-\delta}$. Within the same electrolyte thickness of 0.3 mm, 4 years later Rath M. K. and Lee K. [57] showed a double perovskite symmetrical performance of 247 $mW.cm^{-2}$ using iron instead of cobalt (with the composition of $Sr_2FeMoO_{6-\delta}$). A lower value that was shown to be severely improved to 1066 $mW.cm^{-2}$ through impregnating Cobalt Nickel and Molybdenum in the molar ratios of 0.1:5:1 (Figure II 4A). Other Strontium based double perovskite symmetrical cell performance results were published in 2010 (500 $mW.cm^{-2}$) and 2018 (313 and 444 $mW.cm^{-2}$) by Liu Q. [54] and Niu B. [60] whose chemical compositions introduced Gallium ($Sr_2Fe_{1.5}Ga_{0.5}O_{6-\delta}$) and Titanium ($Sr_2TiFe_{(0.8;\ 0.9)}Mo_{(0.2;\ 0.1)}O_{6-\delta}$) respectively. These results seem to be comparable with the Cobalt-doped electrodes, however, they were

obtained in thinner electrolyte supported pellets of 0.265 and 0.2 mm respectively. These double perovskite performances at 800 ºC seem to point out that the Cobalt and Nickel influences undeniably lead to higher catalytic activities consequentially outputting higher PPD results. Apparently, not even performing measurements under advantageous inferior electrolyte thicknesses is enough to obtain higher power densities in Cobalt or Nickel free electrode materials.

Similar conclusions regarding the Nickel influence are present in the Lanthanum Calcium Chromium perovskites. In 2011, both works of Zhang Y. revealed firstly modest performances of 220 and 205 $mW.cm^{-2}$ [52] by mixing 20 and 40% weighting ratios of SDC ($Ce_{0.8}Gd_{0.2}O_{1.9}$) respectively which were later improved on a second publication [53] through the usage of the impregnation technique (obtaining this way a PPD of 400 $mW.cm^{-2}$). Superior performance results can be later found published in 2015 where Rath M. K. and Lee K. [68] displayed similar performances of 220 and 254 $mW.cm^{-2}$ with similar electrode compositions doped with a 0.2 B site ratio of Manganese ($La_{0.7}Ca_{0.3}Cr_{0.8}Mn_{0.2}O_3$) and Nickel ($La_{0.7}Ca_{0.3}Cr_{0.8}Ni_{0.2}O_3$) respectively. Since all of these measurements are reported to take place at the same temperature of 800 ºC, these results are considered an improvement, mostly because no electrolyte physical mixing or impregnation technique was used (to enhance the effective surface area and consequent triple phase boundaries) and most of all, because they were obtained on a 0.4 mm thick electrolyte instead of a 0.3mm thick supporting pellet.

Within the Lanthanum Strontium Ferrite (LSF) perovskite group of electrodes, the best of the gathered results seems to have been reported recently in 2018 in the Journal of Power Sources by Bian L. and his co-workers [59] displaying a notable performance of 820 $mW.cm^{-2}$ using the single perovskite $La_{0.5}Sr_{0.5}Fe_{0.9}Nb_{0.1}O_3$ supported on a 0.3 mm thick electrolyte. This promising result is further supported by one of the lowest polarization resistance values (0.185 $\Omega.cm^2$) among similar chemical compositions (Figure II 4B). Comparatively with the remaining literature sources, the main differences in the chemical composition were the usage of the same ratios of Lanthanum and Strontium (where usually Lanthanum always displays a larger ratio) and the small doping of Niobium in the B site. Other literature sources have chosen either different elements such as Scandium [51], Copper [62] or even Gallium [13] or two elements (instead of just one) to fill in this smaller ratio such as the material selected by Yang Z. [50], where both Copper and Niobium elements represent a total 30% of the B site occupancy. The most phenomenal aspect

regarding Bian's result is the fact that no electrolyte mixing/impregnation or even a buffer layer was used, whereas other sources obtained lower performances (of 536.36 mW.cm^{-2} [51]) even with the advantages of using both the infiltration technique (with $La_{0.9}Sr_{0.1}Ga_{0.8}Mg_{0.2}O_3$) as well as performing the measurements with a thinner pellet (of 0.2 mm instead of 0.3 mm).

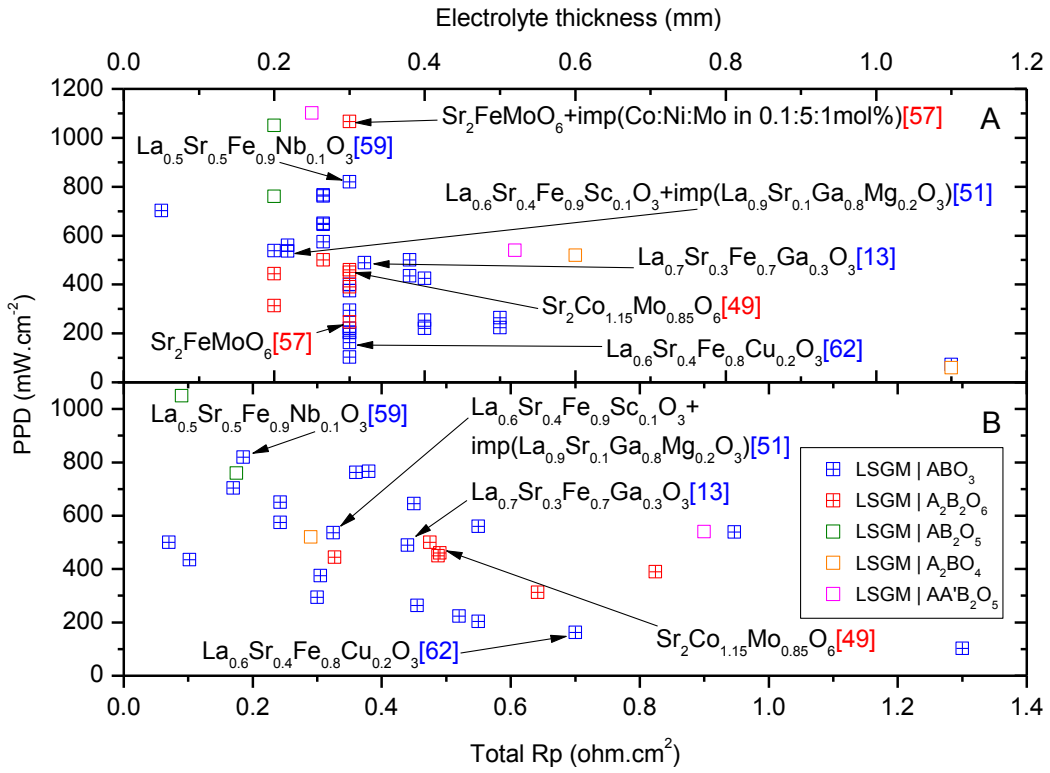

Figure II 4 - Graphical disposition of LSGM based electrolyte thicknesses (A) and total polarization resistance (B) of electrodes vs literature performance results measured at 800 ºC [40], [49] - [54], [56] - [62], [64] - [65], [67] - [73], [75] - [76]

Lanthanide perovskites are indeed the most popular group of oxides regarding the single perovskite materials to be applied as SSOFC electrodes (enabling this way the extensive collection of literature results organized in the appendix Table II A5 and Table II A6), however there are some works in the field replacing this element with Praseodynium. In 2014 Zang P. and his co-workers displayed an amazing symmetrical cell performance result of 766 mW.cm^{-2} with the A site perovskite excess electrode of $(Pr_{0.4})_{1.05}Sr_{0.6}Co_{0.2}Fe_{0.7}Nb_{0.1}O_{3-\delta}$ [58]. Later in that year [71], the author displayed a systematic approach to optimize this element ratio to a specific A site excess (where x=0.42) in the compound of $Pr_xSr_{0.8}Co_{0.2}Fe_{0.7}Nb_{0.1}O_{3-\delta}$. Supported on

the same 0.256 mm thick pellet, the optimal composition revealed a similar peak power density of 762 mW.cm^{-2}. Comparing these results with a more recent study (from 2017) by Lu X. [65] published in Electrochimica Acta, Nickel once more reveals itself as a viable option to replace Niobium in its small B site ratio to further improve the results. The larger Praseodynium stoichiometric content in $Pr_{0.6}Sr_{0.4}Co_{0.2}Fe_{0.8}Ni_{0.2}O_{3-\delta}$ and $Pr_{0.6}Sr_{0.4}Co_{0.2}Fe_{0.8}Ni_{0.1}Mo_{0.1}O_{3-\delta}$ revealed lower performances of 500 and 435 mW.cm^{-2}, however these results were obtained in a supporting electrolyte as thick as 0.4 mm.

It is expected that the SSOFC higher performances tend to belong to the lower total polarization records among literature, however the point disposition (in Figure II 4B) further suggests the existence of a higher power density variance among these less resistive electrodes. This not only disproves previous expectations of point dispositions whenever more data is available in a particular type of electrolyte, as this can also mean that once the polarization resistances are minimized, the influence of other factors become more visible.

2.3 NCAL ($Ni_{0.8}Co_{0.15}Al_{0.05}LiO_{2-\delta}$) electrode

In recent years a popular trend in symmetrical cell electrodes has emerged with the compound NCAL ($Ni_{0.8}Co_{0.15}Al_{0.05}LiO_{2-\delta}$) whose cells not only have been displaying fantastic performance values (Table II A7) but also operate as lower temperatures from 550 to 600 ^{o}C. In 2016 Zhang W. shared an outstanding performance of 1072 mW.cm^{-2} in the International Journal of Hydrogen Energy [29]. Not only was this performance value incredibly high as it was measured on a 1 mm thick electrolyte. This finding resulted from the systematic study of the electrode ratio mix into the electrolyte, in the form of x%(Na_2CO_3 + SDC) + y%($Ni_{0.8}Co_{0.15}Al_{0.05}LiO_{2-\delta}$), where the optimum values were found to be x=60% and y=40% (Figure II 5A). The second best ratio (where x=80% and y=20%) still displayed a strong PPD of 733 mW.cm^{-2} and still in the same electrolyte thickness conditions, no other measurements seem to display close values. Recently, last year, Qiao Z. [79] revealed in Journal of Power Sources a similar systematic approach to optimize the amounts of La/Pr co-doped CeO2 and ZnO where the optimum results were found in the respective ratios of 70% and 30% respectively. Also operating at 550 ^{o}C, the optimal this ratio exhibited a strong cell performance of 1055 mW.cm^{-2}, though it was supported in a 0.709 mm thick electrolyte.

Another systematic study of proportion optimization was published in 2017 by Xia C. [78] where both ratios of hematite/$LaCePrO_x$ and the perovskite $La_{0.6}Sr_{0.4}Co_{0.2}Fe_{0.8}O_{3-\delta}$ (LSCF) were found to output the highest performance of 662 $mW.cm^{-2}$ in the relative amounts of 70 and 30% respectively. The respective polarization resistances of these results (Figure II 5B) seem to display the expected descending tendency along with the performance. These measured peak power densities of the 4 experimented compositions are less promising comparatively to previous highlights from the fact that they occurred using a comparatively thinner electrolyte (0.4 mm) and under a higher temperature condition (600 °C).

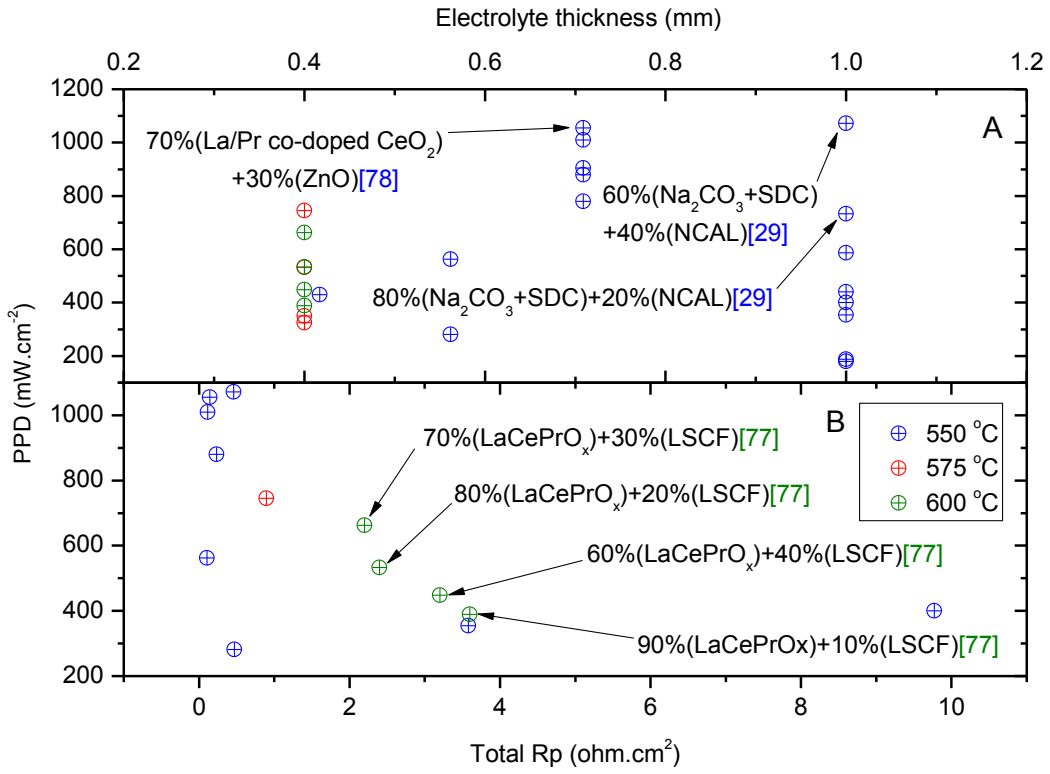

Figure II 5 – Graphical disposition of NCAL ($Ni_{0.8}Co_{0.15}Al_{0.05}LiO_{2-\delta}$ + Ni foam paste) electrode references on different electrolyte supports along with (A) the respective electrolyte thickness and (B) the total polarization resistance of the electrodes at 550, 575 and 600 °C [45], [77] - [81]

3. Influences of total activation energies and conductivity

The high material diversity regarding electrodes together with the fact that plenty of SSOFC performance measurements do not estimate respective activation energy and conductivity results under both relevant environments generates a

considerable lack of comparable results within these variables. Nevertheless, all the gathered information from literature sources used in this section regarding these variables is once more organized in the appendix Table II A8 and Table II A9.

In 2016, Acta Materialia released a study by Zurlo F. [62] where slightly higher performances (of 162 over 103 $mW.cm^{-2}$) where displayed in the ratios of $La_{0.6}$ and $Sr_{0.4}$ relatively to $La_{0.8}$ and $Sr_{0.2}$ (respectively) in a stoichiometric single perovskite composition of $La_{1-x}Sr_xFe_{0.8}Cu_{0.2}O_{3-\delta}$. These performance values are further supported by a corresponding minor improvement in the activation energies in air (displaying values of 1.48 and 1.52 eV). Within the same operation conditions of 800 ^oC and LSGM supporting pellet thickness of 0.3 mm, Bian L. in 2018 [59] shown a massive improvement of performance revealing a consequent much lower activation energy in air of 0.35 eV and a resulting power density of 820 $mW.cm^{-2}$ (Figure II 6A). Beyond similar experimental conditions, the A site ratios as well as the Iron content are close enough to suggest that Niobium might improve the overall performance through lowering the activation energy in air. Nevertheless, it should be mentioned that this assumption is overlooking the fact that this most recent higher performance value also revealed an extremely low anode activation energy (Figure II 6B), while the older results from 2016 seem to not have measured this specific parameter, disabling this way, a possible stronger comparison between both sources.

In the previous section 2.2, the performance result of $La_{0.7}Ca_{0.3}Cr_{0.8}Ni_{0.2}O_3$ was already mentioned to be slightly superior comparatively to $La_{0.7}Ca_{0.3}Cr_{0.8}Mn_{0.2}O_3$ from the work of Rath M. K. in 2015 [68], however the respective anode activation energies (of 0.48 and 0.44eV) measured in humidified hydrogen reveal a lower value in the Manganese perovskite electrode. This result also suggests that the higher performances of the Nickel doped perovskite might be justified through a greater difference in another parameter (such as the conductivity, as shown in Figure II 7A) since these activation energy values can still be considered similar. From both variables, the results could suggest the higher conductivity of the nickel perovskite seems to be compensating the higher activation energy of this material, however this conclusion is still faulty from the fact that each measured variable was estimated in different atmospheres.

It is however possible to find performance improvements in the already mentioned works of Luo X. [22] and Tian D. [28] whose conductivities under oxidizing and reducing conditions support this difference (Figure II 7B). The YSZ electrolyte supported cell performances of these sources seem to display a larger conductivity

difference under oxidizing conditions suggesting that the B site Iron doping could be providing a superior cathodic behaviour comparatively to Manganese. A larger conductivity influence under reducing conditions is also possible to be found, as displayed in the 0.3 mm thick LSGM electrolyte supported cells of Wei T. [49]. The obtained double perovskite performances (of 390, 450 and 460 $mW.cm^{-2}$) seem to rise softly when plotted along with the respective conductivities in H_2. Together with remaining literature results, this is an exception to the evident pattern of higher conductivity values under oxidizing conditions comparatively to reducing atmospheres. This leads to the further overall assumption that most semiconductor materials applied in SSOFC tests possess P-type conductivity from the fact that oxidizing conditions greatly increase this variable.

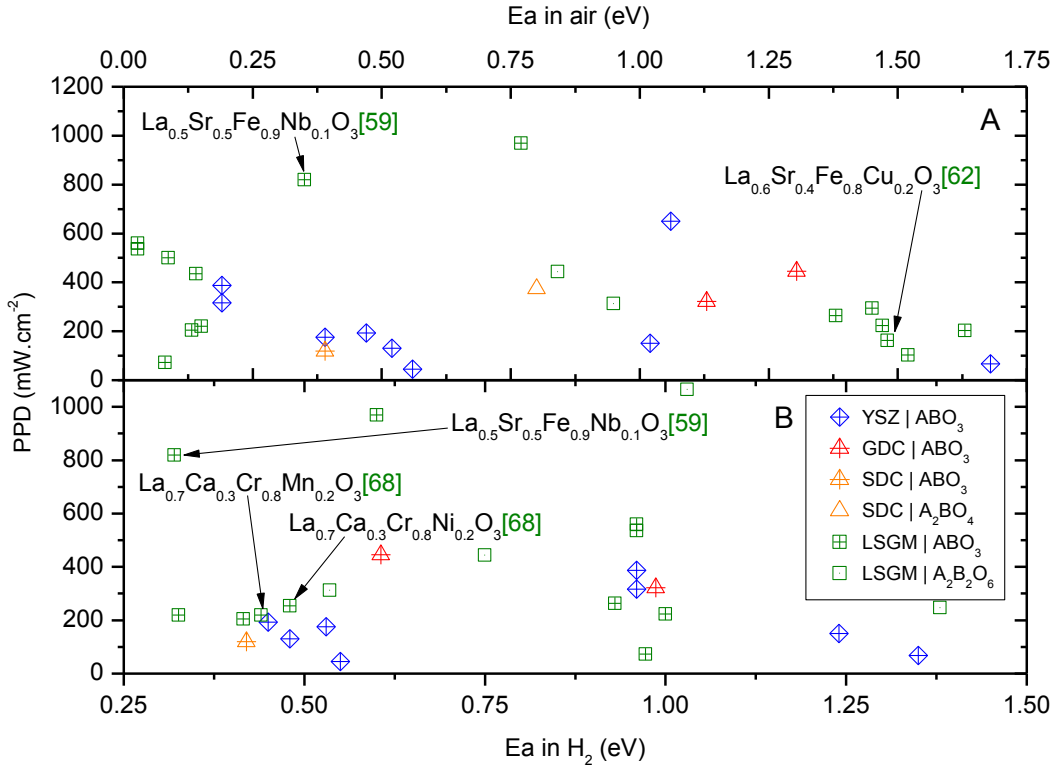

Figure II 6 - Graphical disposition of Activation Energy literature results (A) in air and (B) in hydrogen along with the respective cell performances (at 800ºC) in each electrolyte type [21] - [22], [24], [27] - [28], [34], [41], [46], [51] - [52], [56] - [57], [59] - [62], [65], [67] - [68]

The previously mentioned single perovskite from 2018 of $La_{0.5}Sr_{0.5}Fe_{0.9}Nb_{0.1}O_3$ [59] revealed conductivities of 82 and 0.47 $S.cm^{-1}$ in air and hydrogen respectively. Comparatively with a similar material (with the chemical

composition of $La_{0.7}Sr_{0.3}Fe_{0.7}Ga_{0.3}O_3$) from Yang Z. [13], the respective conductivities in air and hydrogen where 47.45 and 0.422 $S.cm^{-1}$. The resulting PPD differences from both sources are enormous. As already stated, Bian L. [59] and his co-workers achieved a performance of 820 $mW.cm^{-2}$, however, despite having a similar LSGM electrolyte thickness, the cell performance of the precedent work from 2014 had only achieved 489 $mW.cm^{-2}$. The similar conductivities under reducing conditions could suggest that the improvement is mainly cathodic, however, the polarization resistances already support this performance difference with values of 0.185 and 0.44 $\Omega.cm^2$ (for the Niobium doped and Gallium doped perovskites respectively).

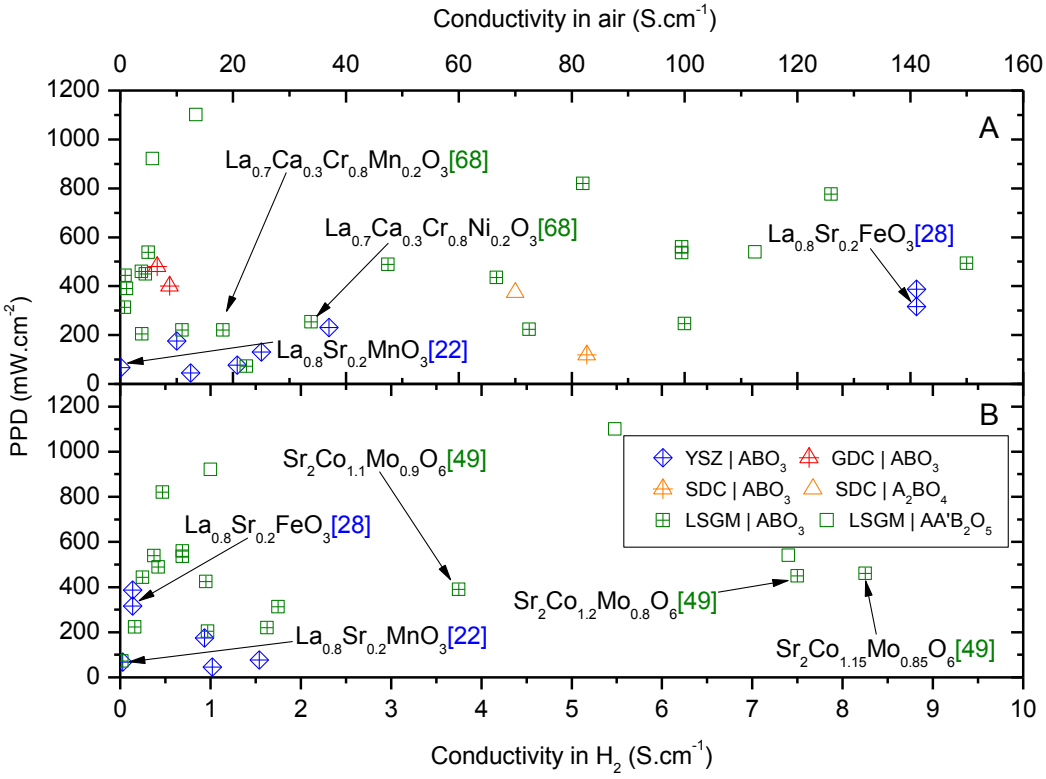

Figure II 7 - Graphical disposition of Conductivity literature results (A) in air and (B) in hydrogen along with the respective cell performances (at 800ºC) in each electrolyte type [13], [22], [24] - [25], [27] - [28], [31], [36], [41], [46], [49], [51] - [52], [57] - [61], [63] - [65], [67] - [68], [70], [74] - [77]

4. Literature trend barriers and considerations

The gathered literature results inevitably reveal that some electrolyte materials (such as LSGM) can be chosen more often than others. Their popularity definitely plays a role in the possible available trends to relate the important variables

which affect the electrode performances. Data scarcity is however not the only barrier that should be acknowledged. The main issue in generating valuable conclusions out of literature results is mainly the creation of an equivalent plane of conditions where both measurements can be fairly compared. A meaningful performance comparison not only requires the same electrolyte support (or a close chemical composition) as it also demands its thicknesses to be close enough. Following this required consistency, the present literature review already mainly addresses performance measurements at 800 ^{o}C together with minimal electrode composition variations.

The difficulties of generating valuable or even plausible conclusions among the literature sources strongly support the demand for more systematic studies so that the field of the SOFC electrodes can evolve to a more viable technology. The following experimental chapters provide useful characterizations regarding the dopant-host implications in the variables of cell performance, electrode structure, calcination temperature requirements, impedance, conductivity and Activation energies under reducing and oxidizing conditions. This information together with the existent and future chemical compositions, attempts to increase the possibility for new research directions to emerge as well as to provide a different perspective on how these parameters can influence the SSOFC performance.

5. Summary

The first aspect to notice about the performance results in the SSOFC field is the higher diversity of electrode compositions versus the evident much less variation of material selections regarding electrolytes. This fact dictated the overall structure of this brief literature review and defined the current data organization that was implemented. The collected results which allowed this brief analysis can be found organized in several tables located in the Appendix section. PPD and impedance results obtained on Zirconia, Ceria and LSGM based electrolyte types are respectively revealed from Table II A1 to Table II A6. The performance and impedance results of the most recent NCAL research direction can be found in Table II A7. Variables such as of the electrode materials are frequently not measured, therefore the lack of information regarding these parameters disables many attempts of finding further explanations to support the observed power density trends. Nevertheless, all the gathered information under both oxidising and reducing conditions regarding activation energy and conductivity parameters can be found in Table II A8 and Table II A9 respectively.

The fact that a general consideration of multiple results does not reveal even the most expected tendencies supports the existence of more variables to be considered such as distinct fabrication methods. Within the goal of searching for literature trends, a constant operation temperature of 800 ^{o}C among similar electrolytes was considered, however the demand for more data in the field becomes necessary in order to enable stronger or even decent data correlations. Further systematic and experimental results are needed in order to find innovative chemical compositions. This way, consequent measurements of electrochemical variables can define plausible directions to be explored so that field improvements can be conquered.

This brief review spotted some performance improvement tendencies through tunning the specific electrode chemical composition by ratio modification or cation replacement. Some highlights of these activities can be found in mentioned Iron B side performance superiority [28] over Manganese [22] (within the Zirconia based electrolytes group) as well as the small ratio of Niobium [59] comparatively to Copper [62] (in the respective LSGM supported cells). Some general conclusions are also established, such as the dominance of the Cobalt and Nickel elements among the highest performance results as well as the dominant P-type conductivity presence in most of the literature reported electrodes and even the acknowledgement of the NCAL promising research trend [29], [45], [77] - [81] which not only reveals higher performance results as also operates at significantly lower temperature conditions.

(Page intentionally left blank)

Chapter III - Peak Power Density (PPD) and Impedance

1. Introduction

In this chapter the performance and impedance of two perovskites with the same dopant ratio are compared. Pattern cells were firstly assembled in order to verify the experimental procedure and matched with the literature so that a second pattern (of electrolyte supported cells) could be established and enable individual electrode contributions through comparison. In order to further understand the implications of changing an element in the A site of the perovskite structure, the relevant cells were assembled in 3 distinct setups. Both variable tendencies along with the temperature were analysed in each cell setup so that the source of improvement could be attributed to the anodic behaviour difference. Observations of both electrode cross sections of the tested symmetrical cells later revealed the presence of a common phenomenon of silver infiltration solely in the anode sides.

1.1 Methodology

In order to fairly compare both dopants, several types of electrolyte supported cells (pattern, symmetric, cathode and anode test) were assembled (Table III 1). All 4 types of cells are supported on a Samarium doped Ceria (SDC) electrolyte ($Sm_{0.2}Ce_{0.8}0_{2-x}$) so that proper comparisons of electrode performances can roughly discard electrolyte effects since both the material and the handmade process is identical. Barium and Calcium were selected to be doped in a ratio of 0.3 and since both are alkaline earth metals (Aem), the generic formula of the tested materials is defined as $La_{0.7}Aem_{0.3}Ti_{0.5}Mn_{0.4}Ni_{0.1}O_3$ (LAemTMN). Through this comparison, analogously with the considered benchmarks of BSCF ($Ba_{0.5}Sr_{0.5}Co_{0.8}Fe_{0.2}O_3$) cathode and Nickel oxide anode mixed with 40% of electrolyte powder (NiO + SDC), both Barium and Calcium perovskites will eventually also be addressed as LBTMN ($La_{0.7}Ba_{0.3}Ti_{0.5}Mn_{0.4}Ni_{0.1}O_3$) and LCTMN ($La_{0.7}Ca_{0.3}Ti_{0.5}Mn_{0.4}Ni_{0.1}O_3$).

Table III 1 – Strategy for Calcium and Barium doping comparison

<table>
<tr><th>Cell Type</th><th>Cathode</th><th>Anode</th><th>Sample</th></tr>
<tr><td rowspan="2">Pattern</td><td rowspan="2">BSCF</td><td rowspan="2">NiO + SDC</td><td>A</td></tr>
<tr><td>B</td></tr>
<tr><td rowspan="4">Symmetrical</td><td colspan="2" rowspan="2">LBTMN</td><td>A</td></tr>
<tr><td>B</td></tr>
<tr><td colspan="2" rowspan="2">LCTMN</td><td>A</td></tr>
<tr><td>B</td></tr>
<tr><td rowspan="4">Cathode</td><td rowspan="2">LBTMN</td><td rowspan="4">NiO + SDC</td><td>A</td></tr>
<tr><td>B</td></tr>
<tr><td rowspan="2">LCTMN</td><td>A</td></tr>
<tr><td>B</td></tr>
<tr><td rowspan="4">Anode</td><td rowspan="4">BSCF</td><td rowspan="2">LBTMN</td><td>A</td></tr>
<tr><td>B</td></tr>
<tr><td rowspan="2">LCTMN</td><td>A</td></tr>
<tr><td>B</td></tr>
</table>

From this point on, it is easy to understand that both materials LBTMN and LCTMN were tested in these three combinations displayed previously in Table III 1. Each cell combination was tested twice through a second sample (for consistency purposes) to acquire the respective IP-IV curves and Impedances of the 6 temperatures from 550ºC to 800ºC (with an increment of 50ºC).

1.2 Driving forces behind Barium and Calcium selections

1.2.1 Cation radius structural match

The very first motivational argument supporting the selections of Calcium and Barium dopants has to do with their oxidation state. Gathering all the ionic radius with a coordination number (CN) of 12, it is found that Strontium is indeed a very good match and this is supposedly accepted to be the common sense reason to justify its outstanding performance in a Lanthanum host matrix. However, there are also other elements such as Cadmium and Calcium which provide even smaller cation differences within the same valency state of +2 (Table III 2).

Table III 2 - Ionic Radius differences (in CN=12) between Lanthanum and other possible perovskite A site dopants [90]

Ion	**Electrons of the element**	**Charge**	**Ionic Radius in CN12 (Å)**	**Ionic radius difference with La in CN12 (Å)**
Ba	56	2	1.61	0.25
Ca	20	2	1.34	0.02
Cd	48	2	1.31	0.05
Ce	58	3	1.34	0.02
		4	1.14	0.22
Cs	55	1	1.88	0.52
K	19	1	1.64	0.28
La	**57**	**3**	**1.36**	**0**
Na	11	1	1.39	0.03
Nd	60	3	1.27	0.09
Pb	82	2	1.49	0.13
Ra	88	2	1.7	0.34
Rb	37	1	1.72	0.36
Sm	62	3	1.24	0.12
Sr	38	2	1.44	0.08
Th	90	4	1.21	0.15
Tl	81	1	1.7	0.34
U	92	4	1.17	0.19

This work attempts to understand the implications of replacing an A site cation in a lanthanide perovskite. This comparison attempts to correlate performance, resistive/conductive and structural proprieties along with the temperature in order to understand the implications of the cation substitution. Calcium was selected because it has the closest ionic radius comparatively to the Lanthanum host. Still, within the same coordination number and valency state, Barium was selected exactly from the opposite reason of Calcium. It has the second biggest ionic radius considering the presented restrictions (where Radium, can be seen as the largest cation).

Strontium superiority as a dopant within a lanthanum host is inevitably recognized, which explains the popularity of the Lanthanum Strontium based perovskites [91] - [103] despite the fact that atomic radius differences are slightly bigger comparatively to Calcium. From the significance point of view, it is more valuable to contribute with information of less documented systems while also providing a different B site (with Titanium and Nickel) as well as increasing the size difference between dopants by choosing Calcium over Strontium. This decision is likely to provide more accurate conclusions regarding the influence of the cation size variable in the eminence of its influence to be proportionally weaker the smaller it is. These different cation sizes were selected in order to mitigate the element intrinsic properties that can possibly overshadow the size difference variable.

1.2.2 Price and abundancy in the earth's crust

The secondary reasons why a Calcium and Barium study gains relevance merely have to do with its price and abundancy. The rock-forming element of calcium is not only more abundant in the earth's crust than strontium (Figure III 1) which is still the state of the art dopant, but it is also cheaper despite having many applications such as the widely used Portland cement [104] - [105]. Here, this argument is considered to be secondary from the fact that it does not directly support a potential existence of a better performance prior to experimental procedures. However, it should still count as an extremely important benefit, since one of the major commercialization barriers of the SOFC today is simply the cost of the fuel cell itself. This cost can be roughly defined by 3 components: materials, labour and capital costs [3]. Since mass production can only reduce labour and capital costs, it becomes important to invest time and resources studying materials with potential economic viability advantages right from the start.

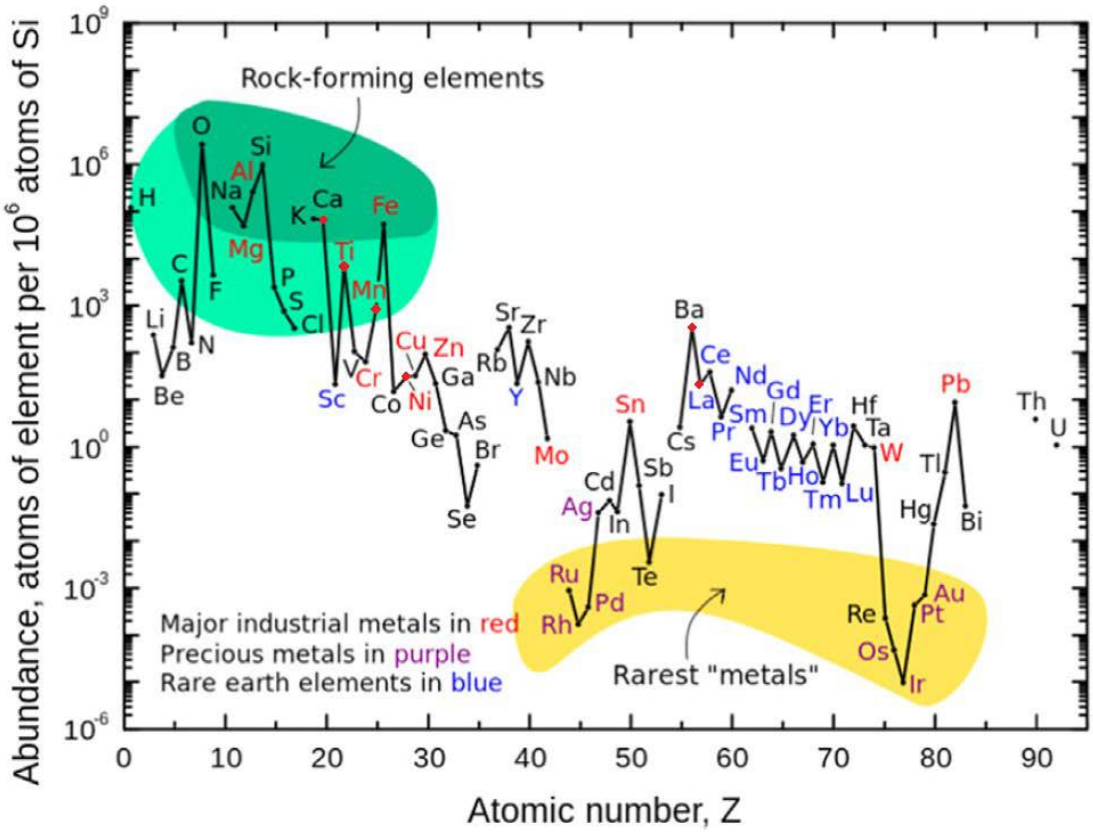

Figure III 1 - Relative element abundance in the earth's crust [106]

2. Experimental procedures

2.1 Electrode powders preparation

Two methods were used to obtain the required electrodes of the tested cells. The perovskites doped with an alkaline earth metal in the A site (LAemTMN) and the Nickel Oxide + SDC anode were synthesized through solid state reaction. As for the BSCF perovskite, the Sol-gel procedure was used.

2.1.1 Solid state reactions of LAemTMN

The oxides of the composing perovskite elements were properly weighted in the right proportions to be diluted in a pure ethanol solution that was further ball milled for 1 and a half hour at 400 rotations per minute (rpm). The grinded solutions were then dried at 75 ºC and then calcined firstly at 1000 ºC during 5 hours. Since the first XRD analysis (after calcination) did not demonstrate sufficient peak definition, the

second calcination conditions of 1100 ^{o}C for 10h were applied and these improved profiles (of the studied powders) will be later discussed (in Chapter IV). To compare these two dopants, only the specific A site ratio (of $La_{0.7}Aem_{0.3}$) was used in the upcoming perovskite performance analysis.

As for the anode powder of the pattern and cathode cells, the nickel (II) oxide and the SDC powders were respectively added together with Polyvinyl Butyral (Butvar B-98) in the weighting ratios of 56.075:37.383:6.542, respectively. All these components were diluted in an absolute ethanol solution which was ball milled at 400 rpm for 15 minutes. The obtained solution was then dried in a hot plate at 75 ^{o}C with a magnetic spinner at 150 rpm and latter hand grinded in a mortar.

2.1.2 Sol-gel powder synthesis of BSCF ($Ba_{0.5}Sr_{0.5}Co_{0.8}Fe_{0.2}O_3$)

The sol-gel method is widely reported in literature and is commonly used to synthesize electrodes for SOFC [107] - [116]. It starts with the proper mixing of ethylene diamine tetra acetic acid (EDTA) and citric acid (CA) diluted into deionized water. In parallel, the proper nitrates of the perovskite are also diluted in deionized water with a spinner at 300 rpm to promote homogeneity. Whenever the EDTA and CA solutions are evenly mixed, the proper amount of ammonia is added. Once a uniform solution is again obtained, this new solution of EDTA, CA and ammonia is added to the nitrates container and steered at 300 rpm in a hot plate at 150 ^{o}C where a proportion of 1:1:2 is used (for BSCF:EDTA:CA respectively).

The solution was tested with colour scale paper and revealed a ph of 7. Next, both the temperature as well as the spinning rotation parameters were respectively increased to 200 ^{o}C and 320 rpm. Once the precursor solution is formed, it was submitted to the first temperature profile of 250 ^{0}C for 5h and after this first thermic treatment, the calcination of this product takes place from applying a different profile of 1000 ^{o}C also during 5 hours. The calcined powder was hand grinded in a mortar, analysed through x-ray diffraction to confirm the perovskite structure formation and stored in a sample holder to later be used in its respective slurry synthesis.

2.2 Pellet synthesis

SDC and NiO+SDC (60:40) powders were individually dry pressed so that both electrolyte and anode supported cell types could be produced. The purchased

SDC powder was hand grinded with a mortar and a pestle for several minutes before it was weighted in portions of 0.3 g to be pressed at 2 MPa during 35 seconds. The resultant pellets were then sintered at 1400 ^{o}C for 5 hours. Once this furnace temperature profile was over, typically more than 70% of the pellets consistently did not display any cracks. These pellets which survive the sintering conditions move on to the next preparation stage which consists of polishing both of their sides to decrease the thickness (roughly up to 0.4 mm) and smoothen the surfaces.

The bi-layered pellets of the anode supported cells were obtained through dual dry pressing method. The NiO+SDC and the SDC powders (in amounts of 0.35 and 0.02 g respectively) were co-pressed, firstly during 60 seconds at 2 MPa and then at 4 MPa after the SDC powder layer addiction. These pellets were also calcined at 1400 ^{o}C for 5h, though obviously they were not polished on the electrolyte side, from the fact that the SDC layer is already very thin.

2.3 Slurry synthesis and cell assembly

All the slurries were sintered through simply adding 1 gram of each of the previously prepared powders with 1, 2 and 10 mL of glycerol, ethylene glycol and isopropyl alcohol respectively. These distinct mixtures were ball milled for one and a half hour at 400 rpm and then properly saved in glass containers to be spray painted into the electrolyte pellets according with the cell configurations expressed in Table III 1 of section 1.1.

In order to obtain the circular shape in the spray painted electrode areas, high temperature resistant tape was pierced with an office hole puncher, forming circular sections of 0.23758 cm^2 that were concentrically placed in the electrolyte pellet surfaces of 0.95033 cm^2. The taped pellets were positioned in a hot plate and properly spray painted in the desired configurations, carefully considering the fact that the NiO+SDC anode is sintered at the higher temperature of 1400 ^{o}C for 5 hours, nevertheless the remaining electrodes are sintered at 1000 ^{o}C. Therefore, all the electrolyte supported cells containing the NiO + SDC electrode in its composition (such as the pattern and cathode test cells) had its anode side separately sintered before the cathode is spray painted on the opposite surface. It is still relevant to mention that all electrodes were fairly spray painted seven times in order to attempt to obtain a comparable thickness between all cells.

Once all the cell components are completely synthesised, the final steps of assembly before testing begin with brush painting 4 layers of current collector in both cell sintered electrode areas. This current collector solution was simply prepared through diluting 0.2 grams of polyvinyl butyral (PVB) and 1 gram of silver paste into 10mL of pure ethanol. Just like during the spray paint procedures, the brush painting activities also took place in a hot plate so that each of the applied layers dries faster. Two silver wires were sealed with silver paste in each of the electrode sides of every cell and placed in an oven at 180 ^{o}C for 30 minutes for each side. Past this point, the cells are ready to be sealed into the sample holder alumina tube through applying the previous thermic treatment in each of the sealing silver paste layers. Containing the sealed cell, the alumina tube is then assembled into a sample holder and the silver wires of the electrode sides are carefully connected with the sample holder ones. To avoid short circuits derived from the temperature silver wire softening, a small piece of super wool insulator was used to prevent any of the cathode wires from establishing contact with the sealing silver paste surrounding the cell (that is in contact with the anode side through its respective wires). The sample holder is then carefully inserted in to the tubular furnace that is properly isolated with the same super wool in the edges (to promote thermal stability during measurements) and the proper wire and gas connections are established. The polarization curves were obtained with a Keithley 2440 5A SourceMeter instrument in conjunction with the LabVIEW software. The impedance data profiles were collected using the Solartron instruments SI 1260 (Impedance/Gain-Phase Analyser) and SI 1287 (Electrochemical/Interface) together with the ZPlot impedance software.

2.4 SEM preparation and equipment

After testing, the symmetrical cells were removed from the holder and broken so that the observation of the cross-sections could take place through Scanning Electron Microscope (SEM). The equipment used for this analysis was a Neon Dual-BEAM FESEM.

3. Experimental results

3.1 Anode supported pattern cells: BSCF/SDC/NiO+SDC

Before executing the explained strategy in section 1.1, anode supported cells were tested in order to verify the experimental techniques involved in this part through the relative proximity with already reported results. Literature information regarding cell layouts with the components of BSCF, SDC and NiO+SDC (assigned as cathode, electrolyte and anode respectively) are much more abundant with the anode supported design comparatively to the electrolyte supported one. This fact is likely a consequence of the experimental results improvement which is essentially derived from a much thinner electrolyte layer that leads to inferior resistive effects, resulting in superior cell performances. Peak Power Densities (PPD) as well as relative impedance profiles (at 650 ^{o}C) while operating on hydrogen were obtained (Figure III 2). The Area of Specific Resistance (ASR) was determined using humble linear interpolations between the positive and negative points in both Z"(a) axis interceptions.

A decent variable agreement between both samples was established, nevertheless, these results were found to be below the average of the reported performance results (Table III 3). The highest PPD obtained (of 758 mW.cm^{-2} in sample B) is 16% below the average (of 903 mW.cm^{-2}) among the literature sources summarized in Table III 3, however so it is its ASR value (of 0.0607 comparatively to 0.09636 Ω cm^{2}). It is known that a decrease in either polarization or ohmic resistance benefits the cell performance, however, the discrepancies between literature results indicate that other factors are playing major roles in these results. Variables such as powder synthesis technique and milling time/method, pressing conditions, calcination temperatures or even the anode ratios (which vary between 60 to 66 wt% of NiO content) are only some of the evident spotted differences among these literature references which are worth to mention. Moreover, a much thinner electrolyte also means that consequent relative thickness variations (resultant from the artisanal experimental procedures) also become more significative comparatively to the respective electrolyte supported cells.

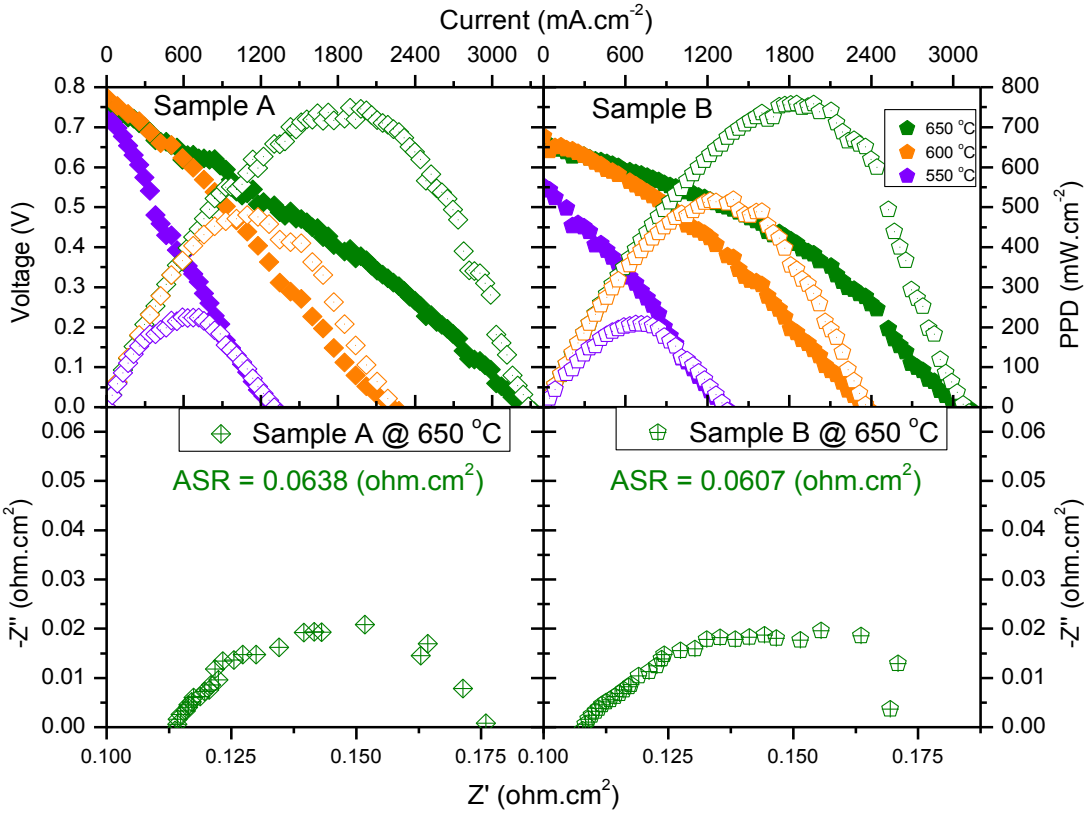

Figure III 2 - Anode supported pattern cells I-P I-V curves (at 650, 600 and 550 ºC) and impedance profile at 650 ºC

The open circuit voltage (OCV) of 0.75 V displayed in sample A (at 650 ºC) is not too far from the average found among the collected literature sources (0.8 V). There is however an evident lower result in Sample B (0.66 V), which is believed to be highly related with its respective resistance and reactance values found in the higher frequencies of its Nyquist plot. Attributing this impedance shape to the presence of mass transport losses phenomena (Figure III 3) explains both the loss of potential difference between both sides resulting in the consequent lower OCV and its stronger degradation along with the temperature.

Though these results could have been optimized by tweaking the experimental procedures to obtain a superior literature match, it is important to acknowledge that the anode supported cells have limited application in the symmetrical SOFC cell design approach. Nevertheless, this humble comparison serves the purpose of matching the pattern materials with literature results, since in the electrolyte supported design there are not enough literature sources to allow the existence of a relevant average value.

Table III 3 – Brief list of anode supported cell (BSCF/SDC/NiO+SDC) references of PPD and Impedances operating on hydrogen

Reference	**Year**	**PPD & OCV temperature**	**PPD**	**OCV**	**Rp temperature**	**Rp**
#		**(ºC)**	**(mW.cm^{-2})**	**(V)**	**(ºC)**	**(Ω.cm^2)**
[117]	2014	650	519	0.88	-	-
[118] and [119]	2006/8	650	1280	0.77	600	0.08
[120]	2008	600	500	0.82	600	0.14
[121]	2017	650	917	0.81	650	0.046
[122]	2012	650	730	0.81	600	0.1
[123]	2006	650	869	0.71	650	0.1
[124]	2016	700	966	0.75	-	-
[125]	2010	650	1250	0.75	650	0.02125
[126]	2007	650	825	0.85	600	0.067
[127]	2010	650	1054	0.85	550	0.2
[128]	2011	600	940	0.86	600	0.091
[129]	2012	650	1280	0.79	650	0.045
[130]	2008	600	880	0.86	600	0.15
[131]	2010	600	525	0.77	600	0.09
[132]	2007	650	1085	0.79	600	0.14
[133]	2008	600	930	0.81	-	-
[134]	2008	650	1026	0.8	600	0.05

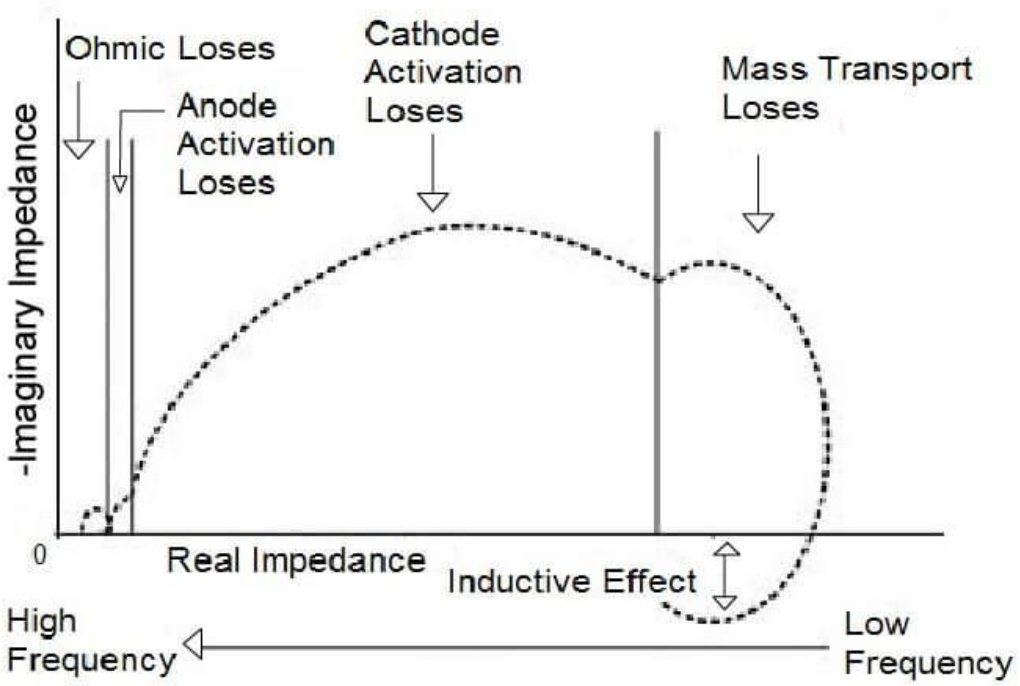

Figure III 3 - Typical loses of the Impedance spectra [137]

3.2 Electrolyte supported pattern cells: BSCF/SDC/NiO+SDC

3.2.1 Performance of pattern cells

The pattern cells IP-IV curves (Figure III 4) seem to be the most reliable results among all of the samples. Even though the two first samples provided a very solid agreement of performance results, a third sample was tested because these cells were supposedly the comparison model for each of the particular electrode position tests in each of the cathode and anode test cell configurations. This cell configuration was chosen as a standard reference from the fact that, at intermediate temperatures, BSCF and Ni+SDC have been reported to respectively have high catalytic activity for oxygen reduction reaction (ORR) and hydrogen oxidation reaction (HOR). An electrolyte supported cell with a maximum PPD of 105 $mW.cm^{-2}$ was reported in a no chamber assembly operated on ethanol flame (at 500-830 ^{o}C) [135]. Thought these results are not comparable, they can still be considered plausible from the fact that higher power densities are naturally expected from the superior testing conditions provided by the hydrogen atmosphere in the anodic chamber.

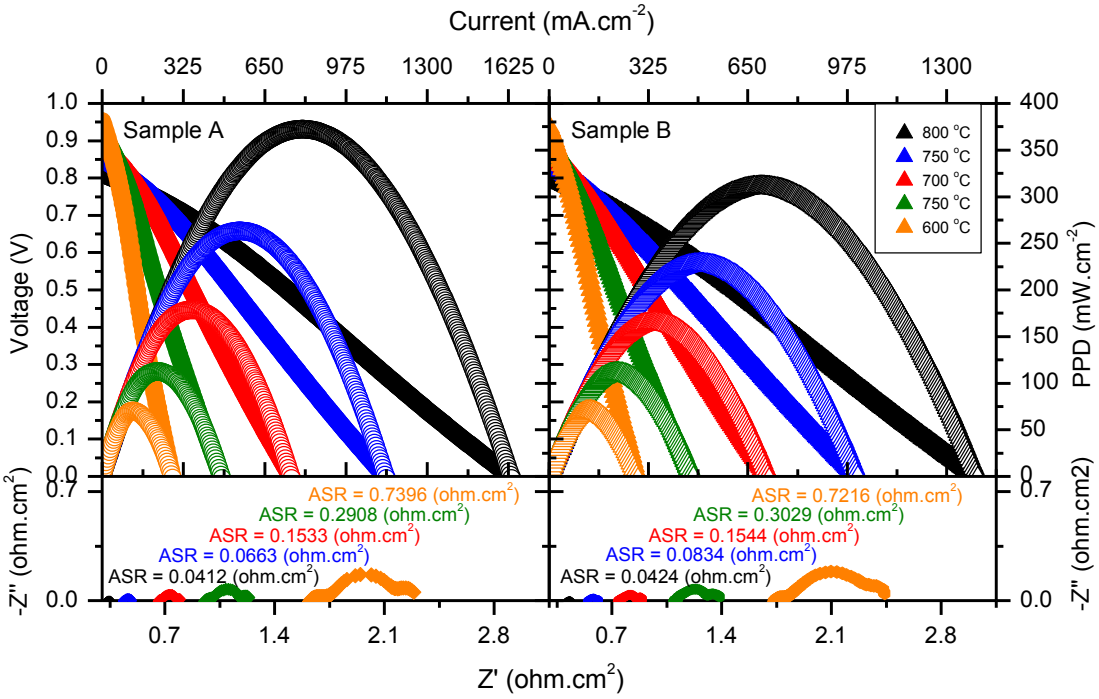

Figure III 4 - Electrolyte supported pattern cells I-P I-V and impedance curves of pattern cells ($Ba_{0.5}Br_{0.5}Co_{0.8}Fe_{0.2}O_3$ / SDC / NiO+SDC)

3.2.2 Impedance of pattern cells

The OCV and the maximum PPD values in all of the 3 samples provided indeed veracity to the results. In these samples, the coherence of having the total resistance being dominantly contributed by the ohmic part is evident. This resistive ohmic component is well known to be governed by the electrolyte parameters and if it becomes relevant, a cross section SEM analysis can easily demonstrate a possible thickness difference between the electrolyte pellets in each of the samples to further support this theory. As for the polarization resistances, all samples seem to modestly agree with each other. Ascending tendencies of the maximum points of resistance and reactance in each sample were observed as well as the overall inverse tendency of the respective frequencies of those values.

To conclude the impedance analysis of the pattern cells, it might be relevant to say that all cells seem to suffer some losses in the ambit of mass transport. Since relatively long time gaps are required for the reactants to penetrate into both catalyst and gas diffusion layers and since the time period is inversely proportional to the frequency, it makes sense for these phenomena to be typically observed at low frequencies [136]. At higher temperatures (such as 800 and 750 °C), these losses

even become completely imperceptible, however briefly comparing the shape of the second curves (visible in lower temperatures) analogously with the typical shape of this phenomena (Figure III 3) it is possible to identify the similarity which becomes stronger as the temperature decreases. The same thought process can also be applied regarding anode activation losses.

3.2.3 Activation energy of pattern cells

From the Arrhenius equation, the activation energy of each of the samples was calculated and a strong agreement between samples of the same type was once again found (Figure III 5). Not only the slopes and the intercepts seem to be really close, but also all of the samples revealed correlation coefficients superior to 0.99 as well as standard relative errors of less than 1. The polarization resistance differences from sample to sample become considerably stronger at the lowest temperature of 550 ºC and since sample A still holds the highest value (as well as the lowest one in the highest temperature of 800 ºC), it is expected for its relative slope to be slightly higher (14.523 K) comparatively to sample B (13.297 K).

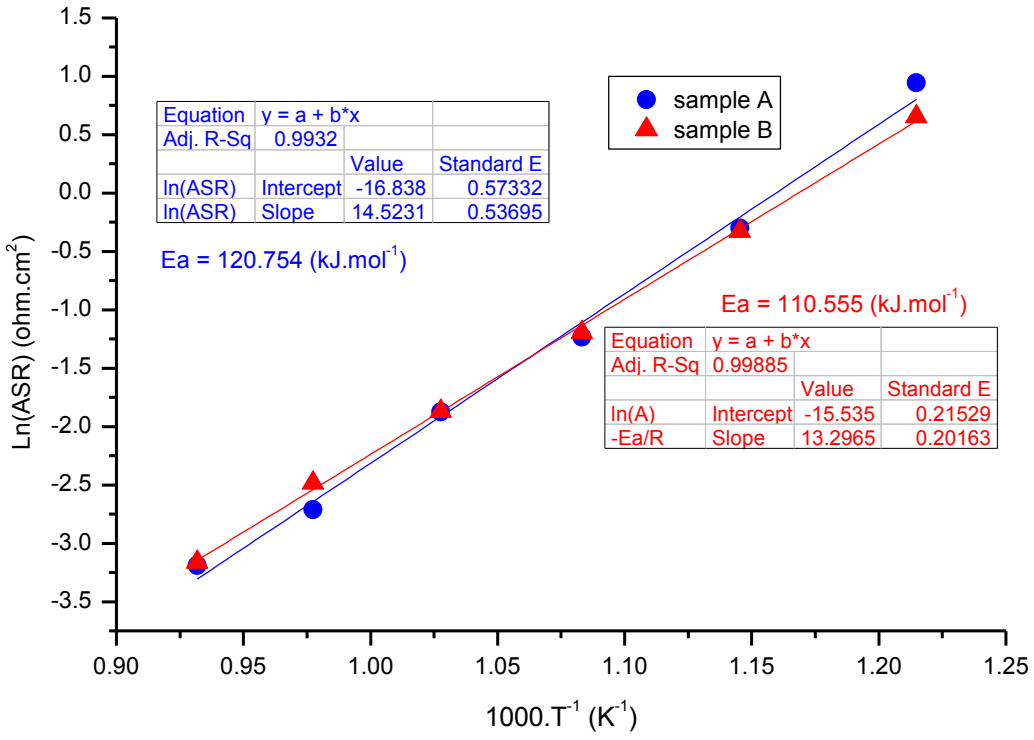

Figure III 5 - Activation energies of pattern cells ($Ba_{0.5}Br_{0.5}Co_{0.8}Fe_{0.2}O_3$ / SDC / NiO+SDC)

3.3 Electrolyte supported symmetrical cells: LAemTMN/SDC/LAemTMN

As it was previously explained in the section 1.1 of this chapter, the symmetric setup was tested with both dopants in the exact same perovskite A site molar ratio of 0.3. In this section, the Calcium doped cells performance is irrevocably superior. Not only much higher PPDs were exposed, but also slightly lower ohmic and polarization resistances (as well as the resultant calculated activation energies) were also observed. The activation energies of the two samples in each dopant seem to differ enough to support that the Calcium dopant also provides a total lower activation energy, however, the lack of data from the lowest temperature in the LBTMN symmetrical samples has to be acknowledged even if slightly higher correlation coefficients are displayed.

3.3.1 Performance of symmetrical cells

The symmetrical cells with Barium showed comparable results regarding IP-IV curves (Figure III 6). An unexpected feature found among this cells was the not fully OCV descendent behaviour along with the temperature. The OCV maximum values were always located at 750 ^{o}C, and counterintuitively, they decrease progressively moving from this point towards to respective lower temperatures.

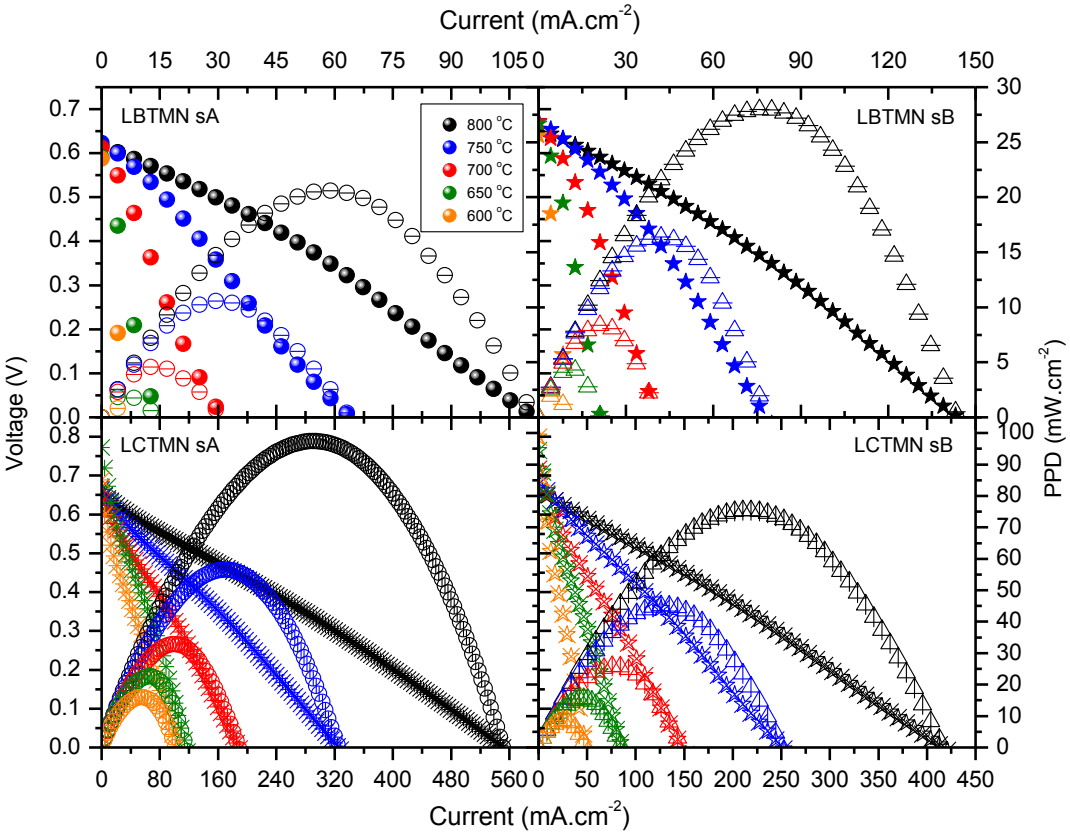

Figure III 6 – IP-IV curves of symmetrical cells ($La_{0.7}Aem_{0.3}Ti_{0.5}Mn_{0.4}Ni_{0.1}O_3$ / SDC / $La_{0.7}Aem_{0.3}Ti_{0.5}Mn_{0.4}Ni_{0.1}O_3$)

In this setup, both samples seem to deliver consistent results. Withal, the OCV values at each temperature seem to be more coherent between both samples, also possessing the expected decreasing behaviour along with the temperature. Comparatively to the Barium system, these LCTMN PPD values are roughly 3.5 times higher (Figure III 6), which validates the matching theory announced in the section 1.1 of this chapter (which suggests that Calcium is a superior dopant within a Lanthanum A site).

3.3.2 Impedance of symmetrical cells

The impedance profiles of the symmetrical cells with Barium displayed the most exotic shapes among all of the other Nyquist plots (Figure III 7). Following the typical loses of the impedance spectra represented in Figure III 3, it seems that mass transport losses are firmly present in both LBTMN samples. However, symmetrical SOFC literature sources have established the connection between the first and

second semi-circumferences of the impedance spectra and the cathode and anode components respectively [35]. Regardless of which electrode is the limiting factor, consistently with what was displayed in this section 3.3.2, the obtained increase of resistive effects as temperature diminishes is expected.

The impedance profiles of the symmetric cells display very distinct curve shapes for each perovskite and these differences become vigorous as temperature decreases (Figure III 7). Still, none of the symmetrical cell types seem to show an agreement in the maximum reactance values between samples. The maximum reactance displayed a descendant tendency as the temperature increases, nonetheless, its respective frequencies seem to contain the opposite trend. This phenomena was not clearly visible in Barium symmetrical cells.

There is an overall consistent agreement in regards to the polarization resistance of both samples and their respective power densities, however, the same cannot be said about the ohmic resistance despite containing considerable differences that become more evident as temperature decreases. At lower temperatures the mass transport losses in the LBTMN material seem to differ particularly at 650 ^{o}C. Further less consistency is found among the respective Calcium perovskite samples where sample B electrode activation losses seem to be particularly higher in the lower temperatures of 550 and 600 ^{o}C. In these conditions, no mass transfer losses were spotted in this sample, therefore, the resultant polarization resistance is solely attributed to electrode activation losses. Comparatively to the ohmic component, the polarization resistive effect seems to present a greater influence in the power densities once the sample pairs are compared with each other.

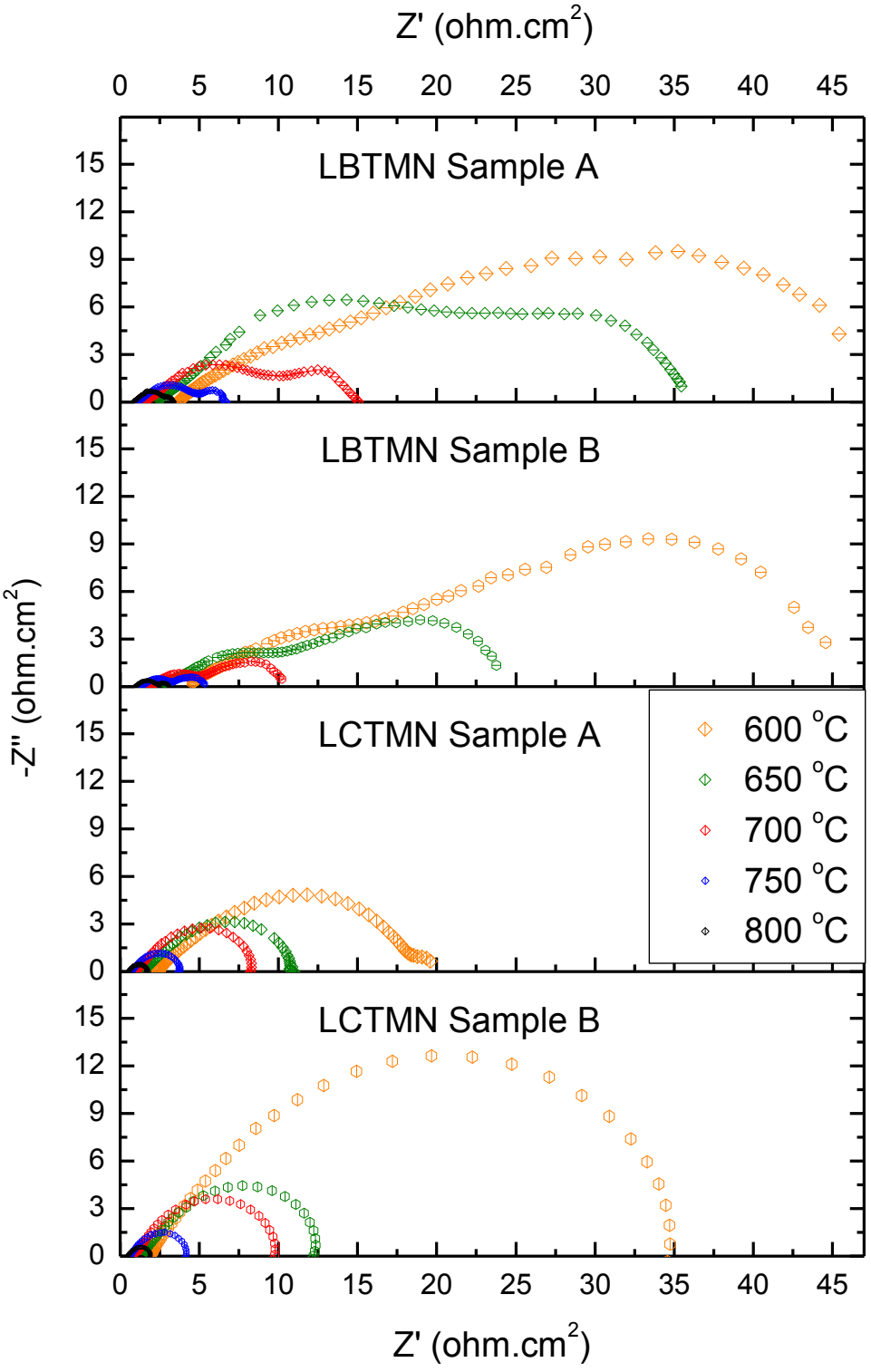

Figure III 7 - Impedances of symmetrical cells ($La_{0.7}Aem_{0.3}Ti_{0.5}Mn_{0.4}Ni_{0.1}O_3$ / SDC / $La_{0.7}Aem_{0.3}Ti_{0.5}Mn_{0.4}Ni_{0.1}O_3$)

3.3.3 Activation energy of symmetrical cells

It was expected that the higher electrode activation losses of Barium perovskite sample A would also result in an overall higher activation energy, notwithstanding, only the pre-exponential factor of the Arrhenius equation seems to be marginally affected by this (Figure III 8). Both polarization resistances at 650 and 700 ^{o}C consequently offered higher ASR values which one might expect to strongly increase the resultant slope of the linear regression, yet, the value observed at 600 ^{o}C seems to partially nullify this effect. It should be noted that the missing points at 550 ^{o}C could have countered this effect resulting in a stronger activation energy difference between both materials, however those values could not be obtained. At the lower temperature of 550 ^{o}C the final minimum frequency of 0.01 Hz was not enough to visualize any signs of a descendent tendency in the impedance curves in order to estimate the respective polarization resistance, therefore this data was discarded from the fact that the ohmic resistance values did not really add any useful information. The overall result (of Barium perovskite samples) consists in slightly higher activation energies with different correlation coefficients and standard relative errors increased by one order of magnitude (from sample B to sample A or the already met pattern cells).

The polarization resistances found in the impedance spectra of the Calcium dopant sample B consequently provided higher values of ASR. Since these differences in the resistive factors are stronger at lower temperatures, then logically the calculated slope from these samples would be lower, resulting in the respective lower activation energies. Though the calculated activation energy of sample B is greater than sample A, the correlation coefficients and standard errors of both of the linear regressions are not strong enough to comfortably differentiate the sample results from each other (Figure III 8).

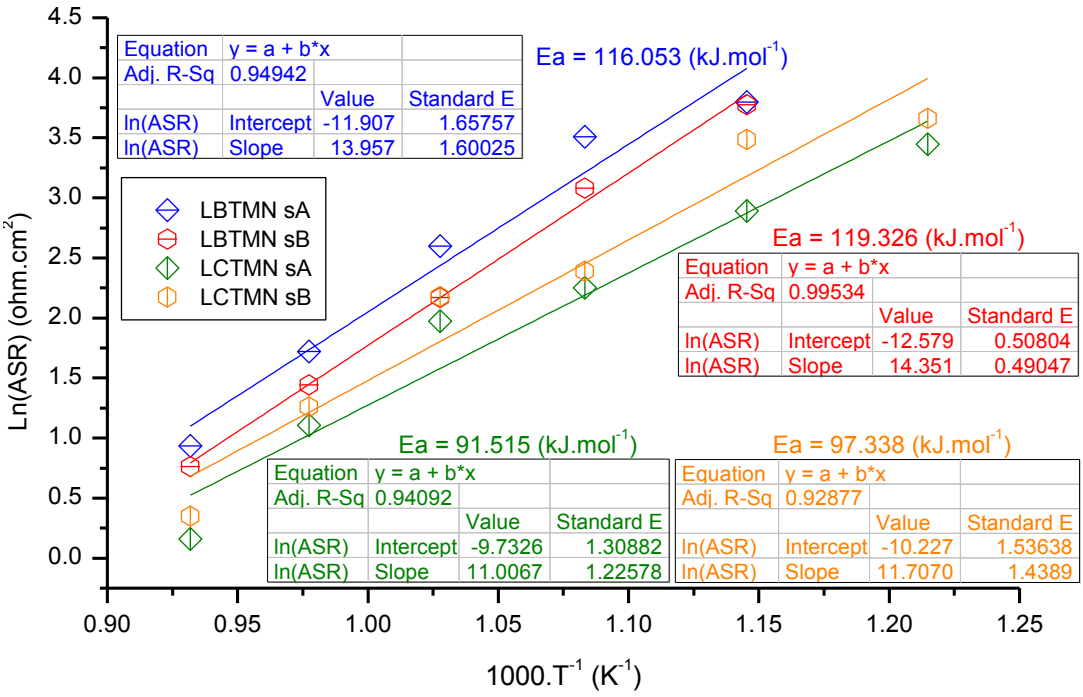

Figure III 8 - Activation energies of symmetrical cells ($La_{0.7}Aem_{0.3}Ti_{0.5}Mn_{0.4}Ni_{0.1}O_3$ / SDC / $La_{0.7}Aem_{0.3}Ti_{0.5}Mn_{0.4}Ni_{0.1}O_3$)

3.4 Electrolyte supported cathode cells: LAemTMN/SDC/NiO+SDC

From the superior performance of the Calcium doped symmetrical cells displayed in the previous section 3.3, asymmetrical cells were also assembled in order to test the same electrode materials now as cathodes. The SDC electrolyte and the NiO+SDC anode are constant among all cells within this section in order to evaluate whether or not the source of LCTMN better results as a symmetrical solid oxide fuel cell electrode lie within a superior cathodic performance.

3.4.1 Performance of cathode cells

The irregular OCV trend along with the temperature seems to not delineate a definitive sinking or rising behaviour, creating an exotic pattern that is not even congruent among both samples. The significant differences of OCV in each temperature are most likely inhibiting both A samples from displaying PPDs closer to their pairs, though they can still be considered comparable results (Figure III 9).

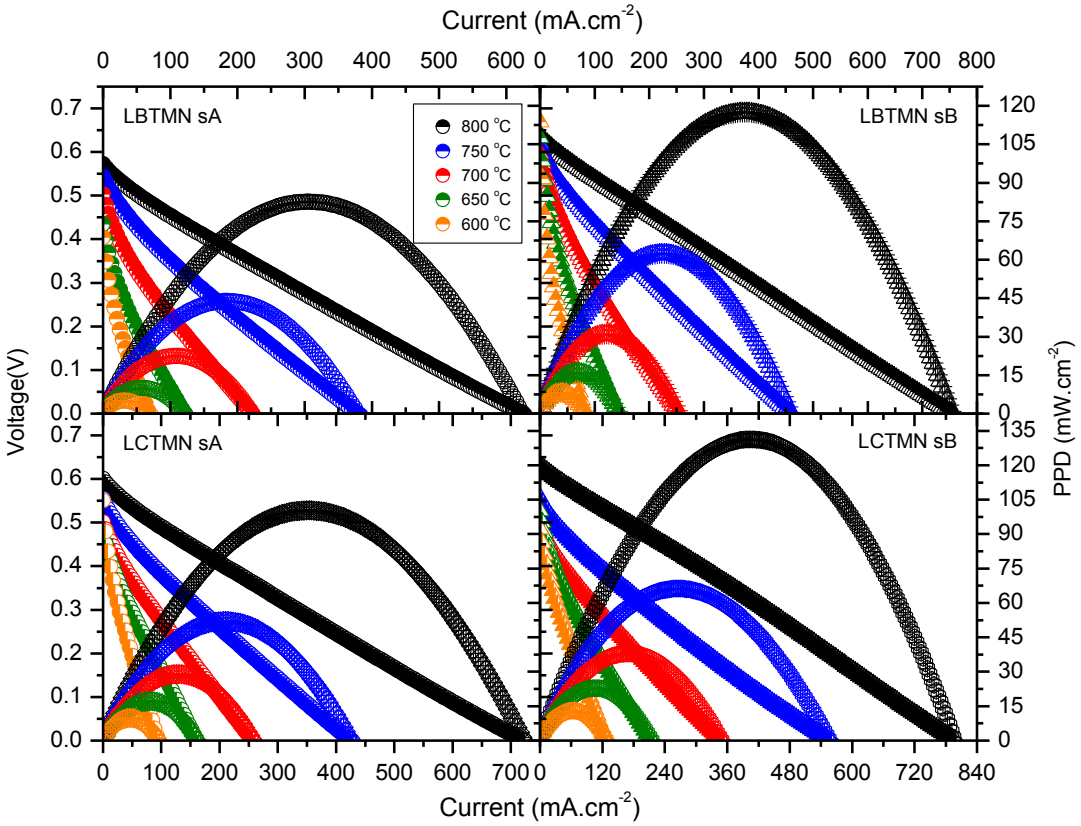

Figure III 9 - IP-IV curves of cathode cells ($La_{0.7}Aem_{0.3}Ti_{0.5}Mn_{0.4}Ni_{0.1}O_3$ / SDC / NiO+SDC)

The irregular OCV trend along with the temperature tends to display minimum values at different temperatures from 600 and 700 °C among both electrode materials, while keeping a solid agreement in regards to power density values between samples. The average PPDs of the Calcium doped samples seem to provide a minor improvement in comparison with Barium (Figure III 9), on the other hand this difference is still not substantial enough to advocate its better performance as an electrode of a symmetrical SOFC. Comparing both of these materials with the pattern cells, it is extremely safe to affirm the superiority of the BSCF cathode even though it was synthesized through a different method. BSCF displayed on average more than 3 times the peak power densities yielded in any of these alkaline earth metal doped perovskites assembled as cathodes in this section 3.4.

3.4.2 Impedance of cathode cells

The ohmic resistances seem to match closer in higher temperatures, and the same can also be said about the polarization resistances (Figure III 10). LBTMN

higher values of polarization resistances overall reside in its sample A and this prior disadvantage versus its pair might be enough to directly create the worst output of PPD results expressed in the previous section.

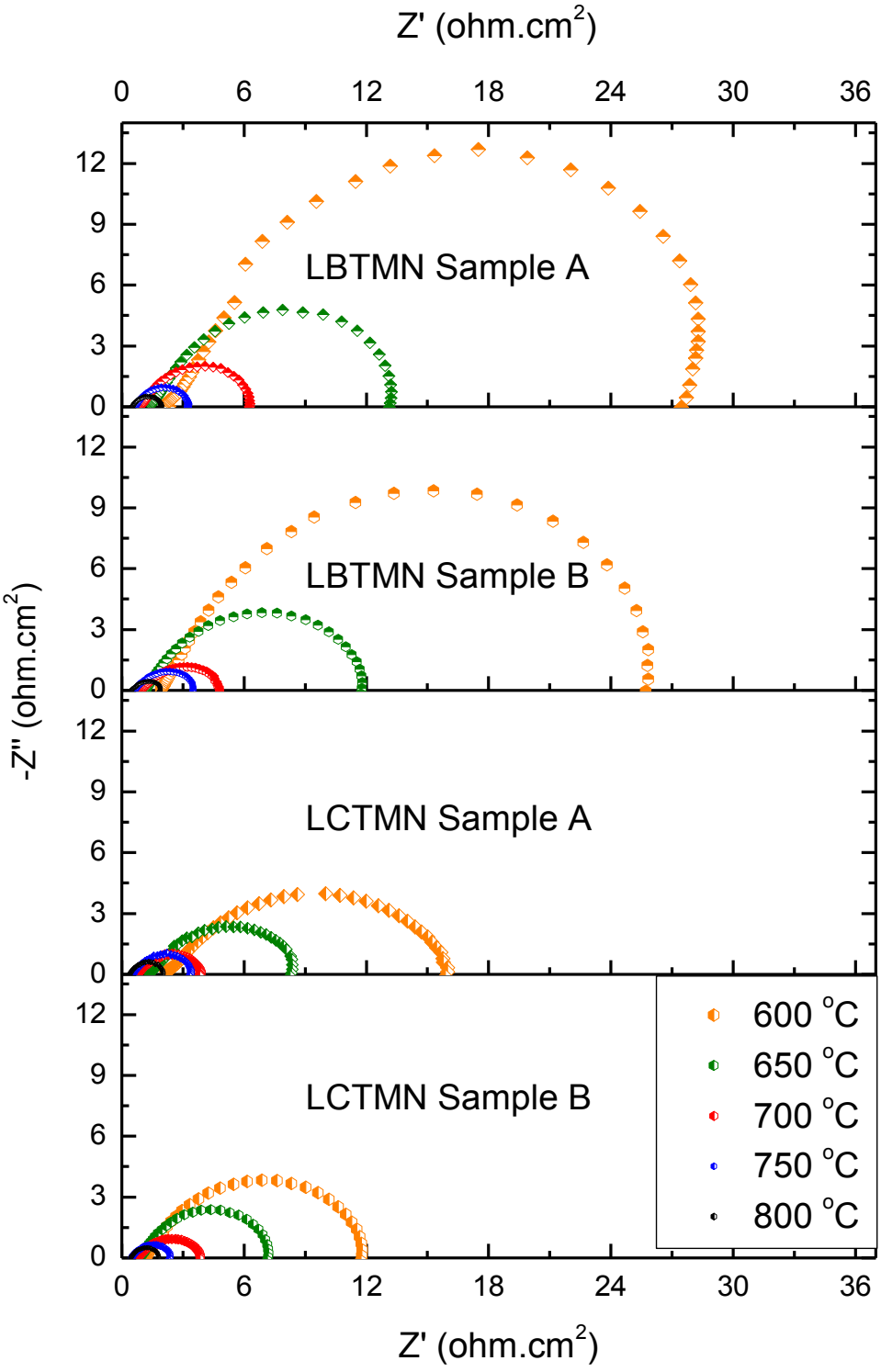

Figure III 10 - Impedances of cathode cells ($La_{0.7}Aem_{0.3}Ti_{0.5}Mn_{0.4}Ni_{0.1}O_3$ / SDC / NiO+SDC)

As for Calcium samples, the small gain of power densities visible in sample B is likely to also be influenced by its lower polarization resistances (Figure III 10). Just like in the previous impedance profiles, these polarization differences between samples become more evident as the temperature diminishes. Ohmic resistances shared this temperature influence, but, as expected, their values among both samples are more compatible since the electrode pellets have similar thickness.

3.4.3 Activation energy of cathode cells

The general stronger polarization resistance development of LBTMN electrode (as temperature diminishes) provides the consequent higher activation energy (Figure III 11). The considerable difference between the slopes of the linear regressions as well as their extremely reliable correlation coefficients could lead to believe that the activation energy cannot be considered the main factor of influence in these performance results. From the previous results this was not evident due to the existence of minor differences from sample to sample or weak regression parameters.

This section clearly exhibits a lower activation energy present in LCTMN sample A which also had lower power densities and similar ohmic resistances, evidencing this way, the low direct correlation between these two variables, however the linear regression correlation coefficients and standard errors seem to not yet be strong enough to fully support the following statement. Notwithstanding, as a hypothesis, it might be possible to have similar ASR values (especially in higher temperatures) while still having slightly different PPDs. This basically means that the sample with better performance will not necessarily always reveal the lowest activation energy value, either because at low temperatures the ASR variable increases exponentially (strongly influencing the resultant calculated slope) or because the small differences in both of these variables are still within the ambit of the experimental errors.

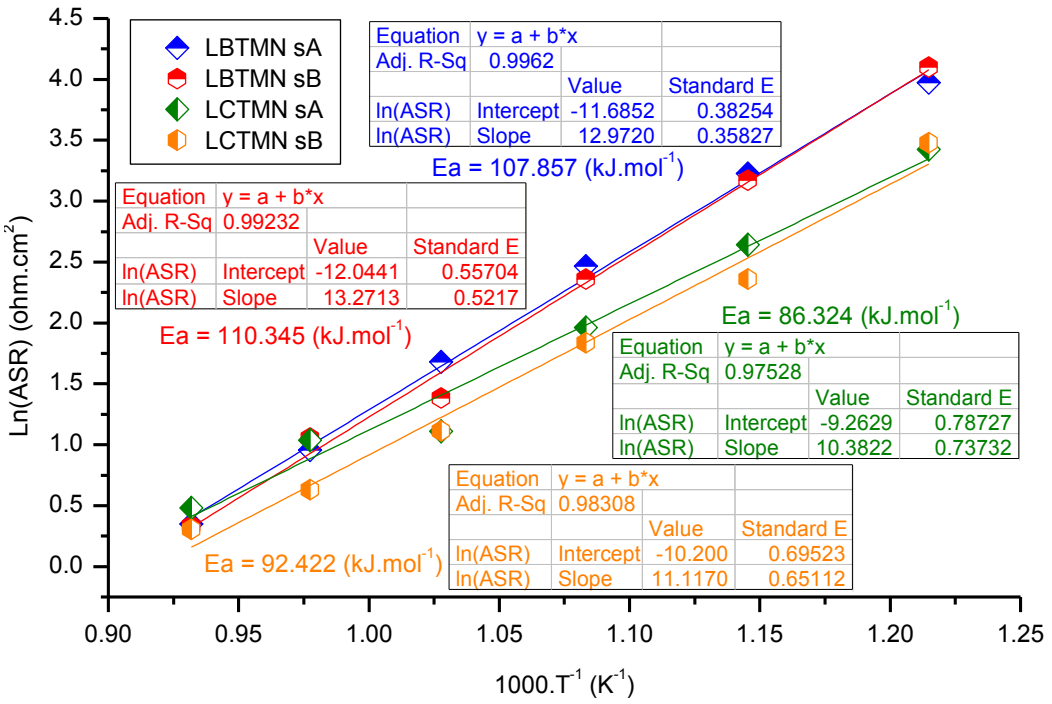

Figure III 11 - Activation energies of cathode cells ($La_{0.7}Aem_{0.3}Ti_{0.5}Mn_{0.4}Ni_{0.1}O_3$ / SDC / NiO+SDC)

3.5 Electrolyte supported anode cells: BSCF/SDC/LAemTMN

As seen in the previous section 3.4, the cathodic performance of both materials seems to not differ too much in order to justify the superior performance of the Calcium dopant obtained in the symmetrical cells. Therefore, in this section both materials were assembled as anodes of asymmetrical cells (with BSCF as cathode and the very same SDC electrolyte) so that some information about anode performances could be extracted through comparison.

3.5.1 Performance of anode cells

A regular increase of the OCV with the temperature was consistently witnessed in both LBTMN samples (Figure III 12). The anode obviously plays an important role in this phenomena, but experiencing the exact opposite tendency within the pattern cells suggests that the anode thermal proprieties are the main source defining this feature. Once more, the obtained power densities of both samples match closely, though it is important to mention that the OCV values of sample B in each temperature are always higher (exhibiting differences ranging from 0.041 to 0.085 V).

From this fact, it would be acceptable to think that sample A would have a noticeably higher performance (in comparison with B), if only its OCV values were closer.

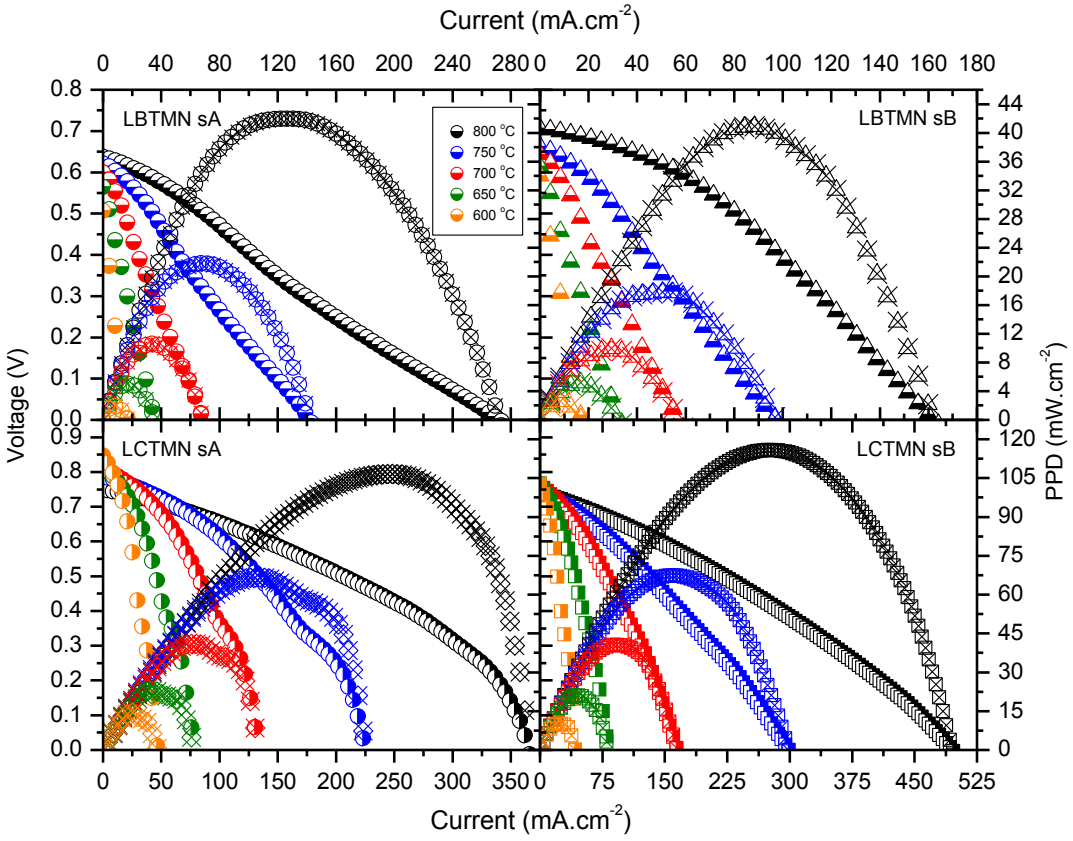

Figure III 12 - IP-IV curves of anode cells (BSCF / SDC / $La_{0.7}Aem_{0.3}Ti_{0.5}Mn_{0.4}Ni_{0.1}O_3$)

Since the symmetrical cells doped with calcium already displayed the same OCV (overall) decreasing trend along with the temperature, again it is witnessed that this behaviour is apparently strongly influenced by the anode thermo-electrical behaviour, because once this material is assembled only as a cathode the same phenomena is not seen. In comparison with the Barium doped material, Calcium seems to enhance the perovskite anodic performance as the higher peak power densities suggest. This greatly substantiates the structural cation theory presented in section 1.2.1. However, the same cannot be strongly affirmed regarding superior cathodic performances given the fact that the respective differences obtained in section 3.4 were not powerful enough to sturdily support the cation radius matching theory.

Indeed the peak power densities displayed from assembling $La_{0.7}Ca_{0.3}Ti_{0.5}Mn_{0.4}Ni_{0.1}O_3$ as an anode are yet no match comparatively with the much higher values exposed in the pattern cells profiles in section 3.2.1. However, to counter this fact, it must not be forgotten that both the barium and calcium systems are intended to have the versatility of also work as a cathodes (enabling the versatility advantage of being used in a symmetrical arrangement). Furthermore, the Nickel oxide anode is not entirely in the same level of comparison with both perovskites from the fact that it was mixed with the electrolyte powder, increasing the surface area between the anode and the electrolyte beyond the spray painted area of the pellet.

Comparing these results with the Symmetrical cells (in section 3.3), it seems that the perovskites $La_{0.7}Aem_{0.3}Ti_{0.5}Mn_{0.4}Ni_{0.1}O_3$ are not too far behind from the BSCF in terms of a cathode performance, however these differences are severely amplified if the anode NiO + SDC is used instead of this chosen perovskite. Therefore, in order to properly evaluate the lanthanide cathode performances vs BSCF, the pattern cells (from section 3.2) and the cathode cells (from section 3.4) are much more appropriate to spot the differences while mitigating inhibiting factors (in the other electrode). In other words, to compare the performances of any particular electrodes, the non-compared electrode should limit the performances as little as possible. This being said, matching the pattern cells (in section 3.2) with these anode test cells (of this section 3.5), the true performance superiority of the NiO + SDC is revealed.

3.5.2 Impedance of anode cells

The slightly higher PPD values of LBTMN sample A are supported by its modest improvements in its ohmic resistances identified in all temperatures. Aside of these minor differences, the polarization resistances seem to not favour the same sample consistently regarding all measurements. Instead, both samples seem to constantly permutate the higher value between each other (Figure III 13 and Figure III 14). The temperature attenuation of these polarization and ohmic resistances differences seems to be an overall constant behaviour in all cell types.

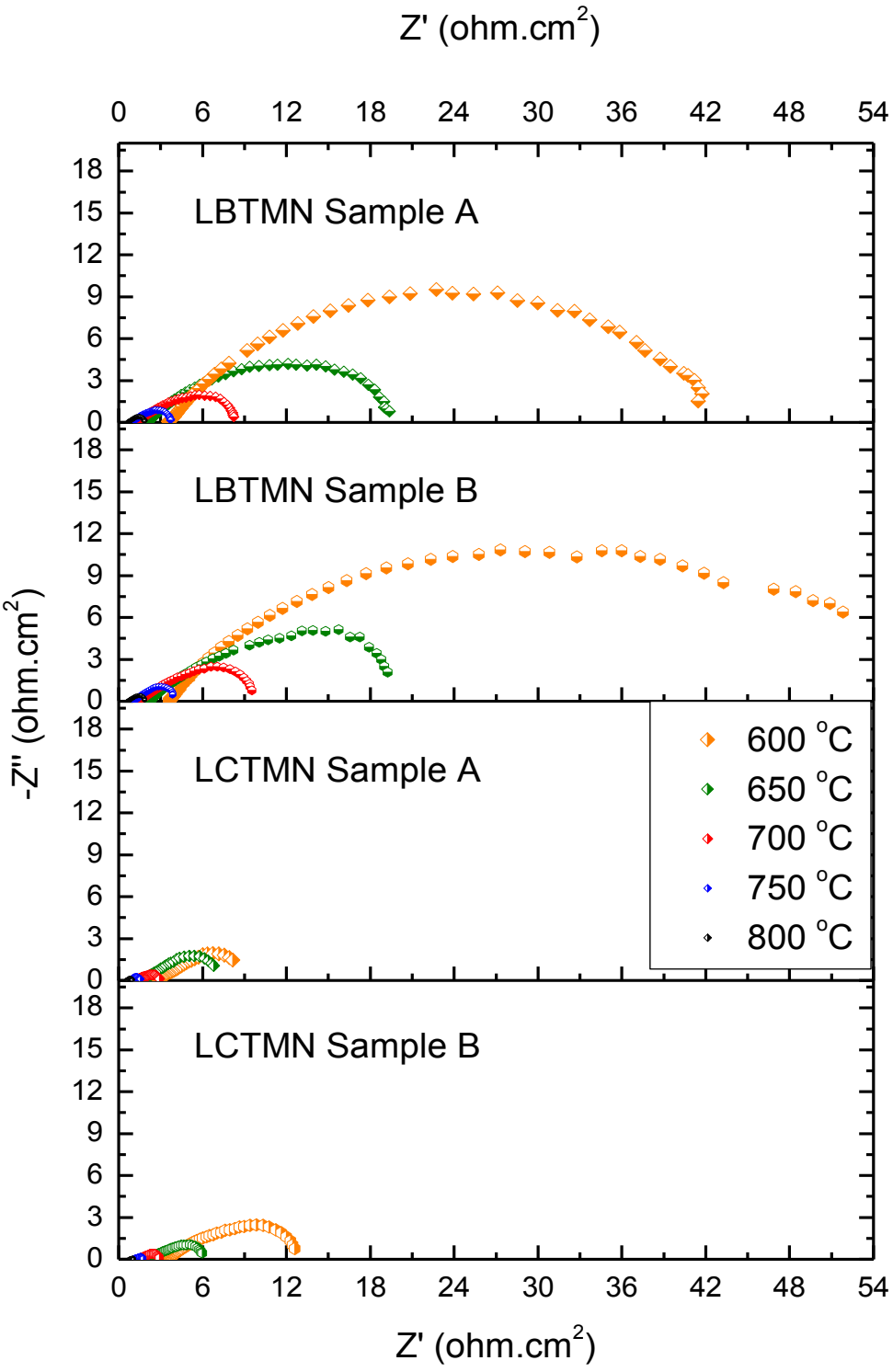

Figure III 13 - Impedances of anode cells (BSCF / SDC / $La_{0.7}Aem_{0.3}Ti_{0.5}Mn_{0.4}Ni_{0.1}O_3$)

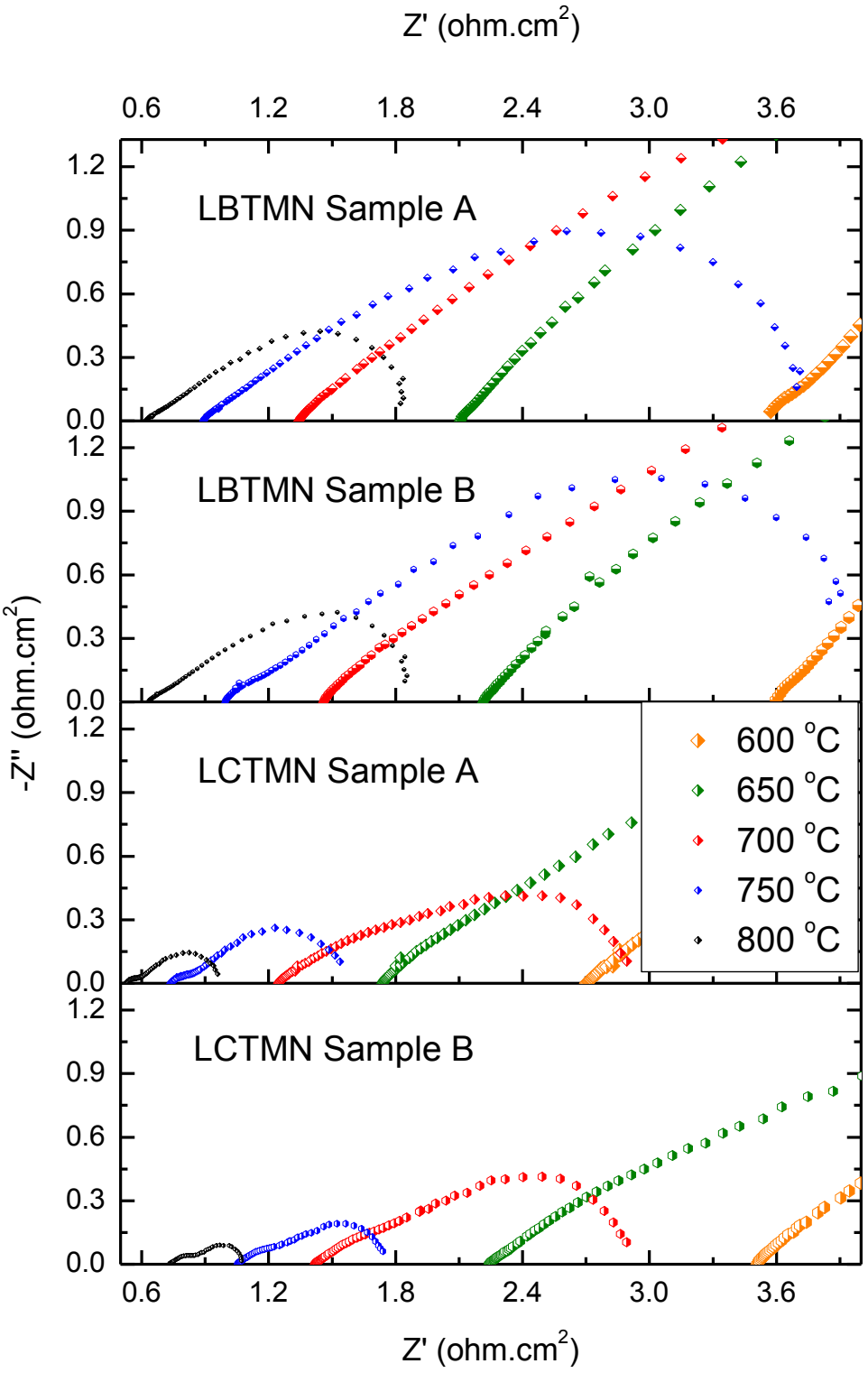

Figure III 14 - Impedances of anode cells (BSCF / SDC / $La_{0.7}Aem_{0.3}Ti_{0.5}Mn_{0.4}Ni_{0.1}O_3$) zoomed in the higher temperatures

As for the Calcium doped perovskite, regarding both ohmic and polarization resistances, a close agreement regarding the impedance profiles was found between

both samples. Withal, regardless of the power density performances or resistive effects experienced in each sample, the Nyquist plots seem to share the same shape (Figure III 13 and Figure III 14). Despite matching peak power densities and OCV values with sample B, LCTMN's sample A displayed a constant graphical shape anomaly located after the PPD points of each curve (Figure III 12). These curves do not completely expose the typical IP IV curves, since at higher current values, the corresponding measured voltage seems to plunge somewhat sharper and then lightly softer than usual. Since this abnormality is present past the PPD points, the cause of this effect is suspected to derive from higher concentration/mass transport losses (Figure III 15) [138]. Unfortunately, this theory cannot be endorsed by the respective sample A impedance profiles. Not only at higher temperatures the mass transport losses are much less evident (as already displayed in the pattern cells Figure III 4 in section 3.2.2), but also at low temperatures, the minimum frequencies seem to not be small enough to enable the acquisition of the respective higher/lower resistance/reactance points (in order to assertively reveal the polarization resistance value of each profile).

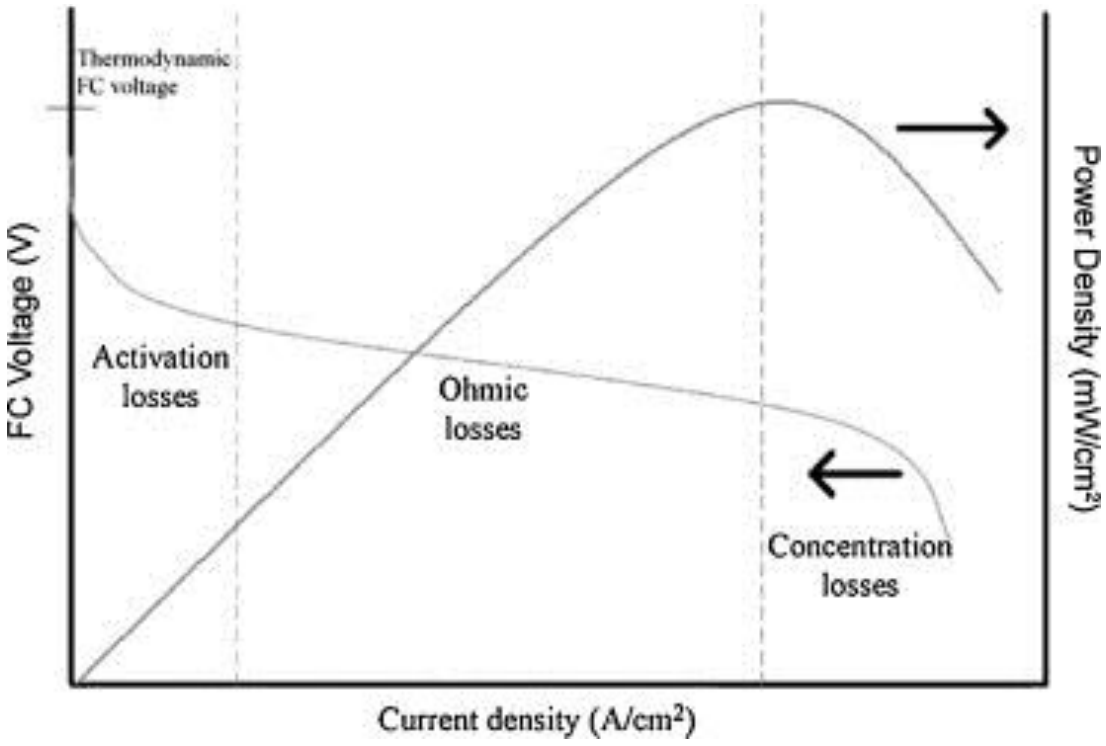

Figure III 15 - The three main reasons associated with irreversible Fuel cell losses [138]

As expected, comparatively with the Barium perovskite cells, obviously similar ohmic resistances are exhibited (since the electrolyte is exactly the same material roughly with the same thickness). As for the polarization resistances a serious improvement is observed between these two elements. Given the fact that both anode test cells are fabricated through the same procedure, the ASR differences can be attributed to their correspondent perovskite phases and this would justify the Calcium much superior anodic performances.

3.5.3 Activation energy of anode cells

Since the higher polarization resistance differences are observed in the lower temperatures, then it would be expected to obtain a respective higher activation energy in LBTMN sample B (Figure III 16). Even though the linear regressions confirm this logic with a significant difference of activation energies, the correlation coefficients and standard errors of these samples are not strong enough to fully ascertain this idea.

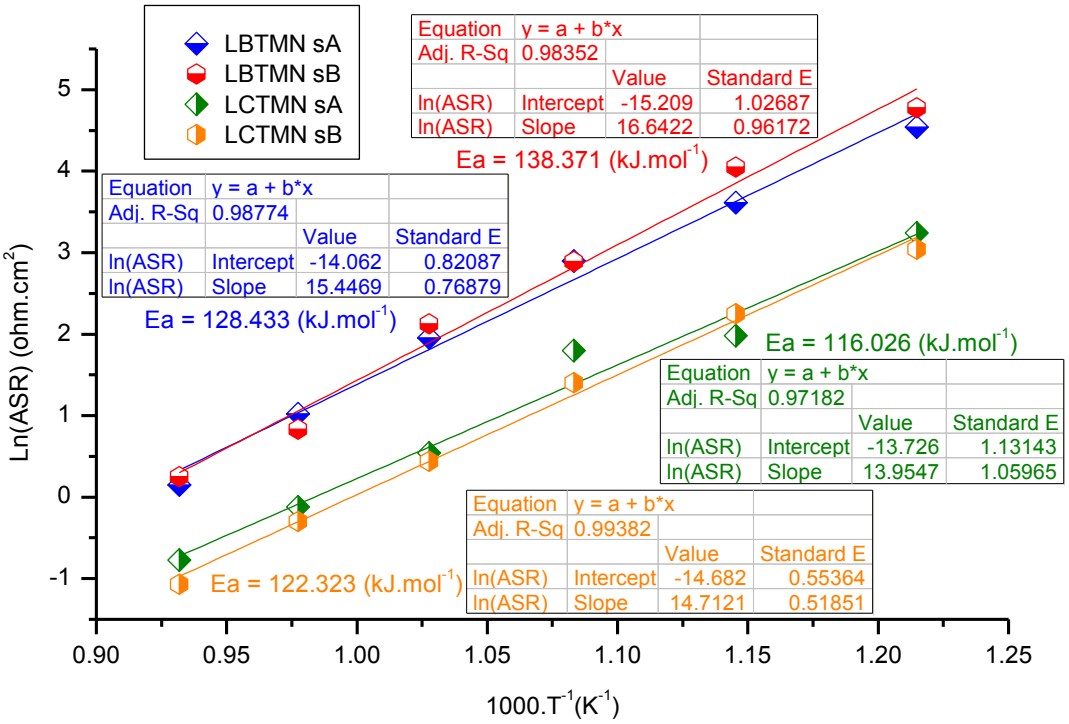

Figure III 16 - Activation energies of anode cells (BSCF / SDC / $La_{0.7}Aem_{0.3}Ti_{0.5}Mn_{0.4}Ni_{0.1}O_3$)

The most curious fact regarding the activation energies of the Calcium doped perovskite assembled exclusively as an anode is to retrieve even lower activation energies in the sample with overall higher polarization losses (Figure III 16) (with the exception of the temperature of 600 ^{o}C). A greater slope value is indeed expected, because (as it was said) as temperature decreases, the differences in the ASR and its Napierian logarithm also increase. The result of this ASR differences increment along with the temperature decline is expected to develop a greater output of activation energy from the relatively greater linear regression slope. LCTMN sample A unexpectedly yield a lower activation energy result, but also its regression correlation coefficient is less favourable. Regardless, LCTMN sample B activation energy seems to not be too far from sample A, providing a higher activation energy value supported by a stronger correlation coefficient.

Comparing with the Barium perovskite anodes, Calcium activation energies are slightly lower, still, since these polarization resistances range from 2 to 4.5 times lower in comparison to Barium, much noticeable activation energy differences were expected. Instead, the clear differences can only be seen if the resulting values of the samples are faultily averaged into one value for the Barium doped anode (133.591 J.mol^{-1}) and another for the Calcium one (119.175 J.mol^{-1}).

3.6 SEM brief analysis

The cross sections of both LAemTMN materials (Figure III 17) revealed a constant dense electrolyte as well as porous electrodes, however, it seems that on the anode side, reducing conditions have promoted some silver infiltration (Figure III 17 C and D) regardless of the dopant. The resultant electrode thickness seems to reveal a similar value of about 4 - 5 µm among all four scenarios. Since the silver infiltration is constant among both anodes it is legitimate to assume the hypothesis of having the same influence in both anode results.

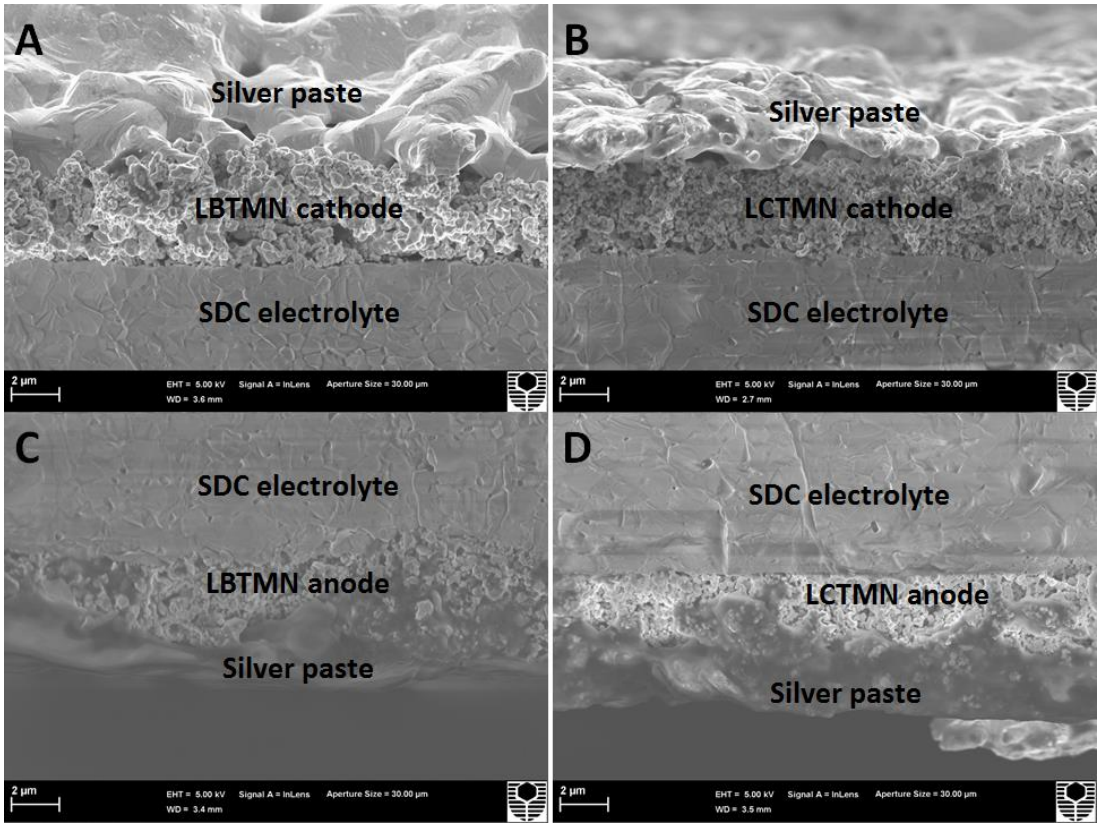

Figure III 17 - SEM images of Symmetrical cell cross-sections of LBTMN and LCTMN cathodes (A and B) and anodes (C and D)

4. Summary

Once the anode supported cell results were shown not to be too far from the literature average result (while overlooking some procedure differences), the present chapter analyses the electrolyte supported cell configurations. More detailed information regarding the acquired data is fully displayed in the Appendix section (in Table III A1, Table III A2, Table III A3 and Table III A4). In order to understand the implications of the cation change, all the configuration results had to be strongly verified by a second sample.

The electrolyte supported pattern cells are the only ones displaying a consistent increasing and decreasing tendencies along with the temperature in every sample regarding PPD and OCV respectively. In the setups where the LAemTMN materials are assembled as anodes, the Calcium system seems to display this OCV trend, however Barium cells do not follow this tendency at all and they even seem to reverse this behaviour. Assembling both materials in symmetrical and asymmetrical cells leads to believe their OCV tendencies (along with the temperature) seem to be

more influenced by the anode side than that of the cathode one. None of the selected materials comes even close to the PPD values obtained with the pattern system. Even though the BSCF cathode powders were synthesized through a different method, it is still remarkable the performance differences found between these pattern cells in section 3.2 and the cathode cells (LAemTMN/SDC/NiO+SDC) presented in section 3.4. This strong discrepancy suggests that even if the synthesis method was the same, the outstanding performance of the BSCF cathode would still persist.

Comparing any of the symmetrical cells (in section 3.3) either with the anode or cathode cells, it seems that the lanthanide perovskite materials performances are not too far behind. However, when the comparison becomes the pattern cells (in section 3.2) versus any of the specific electrode cells (either in section 3.4 or in section 3.3), not only the superiority of the pattern electrodes becomes evident, as the inhibiting performance factor emerges as the reason behind the lower performances of the LAemTMN perovskites comparatively to BSCF or NiO + SDC. That is to say, these materials are far behind in terms of electrode performances when compared with NiO + SDC or BSCF and the symmetric cells provide a much less accurate comparison with the other cell designs from the fact that their constant electrode will always limit more the potential cell performances comparatively to the usage of the benchmark electrode in any cell configuration.

As expected, the impedance profiles reveal increasing values of ohmic and polarization resistances along with the decreasing temperature in each sample. The bigger differences between comparable samples seem to belong to the lower temperatures where these values reveal higher resistances. Just like these resistive effects, reactance seems to also increase along with the temperature as expected, however, no coherent behaviour in the frequencies or resistances of these maximum values was identified. The pattern cells are the only samples where ohmic resistances are the dominant factor of the total resistivity, a variable that is attributed to the electrolyte limiting factors (which is obviously corroborated by the extremely superior performances of the anode supported design). In all of the remaining cell types where the lanthanide perovskites were used, the inhibiting characteristics now reside in the electrode parameters, since these polarization resistances are by far the main contribution (except in higher temperature values of the LCTMN anode cells). This suggests that this electrode can potentially be closer to NiO + SDC if it was also mixed with SDC. Since the polarization resistances are always more than 10 times higher (comparatively with the pattern cells), it would be expected that their sum obtained in

each electrode test would be roughly equal to the values observed in the corresponding symmetrical cells, however, this aspect is not perfectly evident amongst all the tested temperatures (though this approximation has been used in literature [26]). The resistive factor values obtained in each of the symmetrical cells are on average 20% larger than the sum of the same in each of the specific electrode cell types.

Most of the calculated activation energies seem to be roughly in agreement with each other from sample to sample. LCTMN perovskite seems to consistently display lower values comparatively to LBTMN, however this cannot really justify its superior performance as an anode from the fact that the pattern cells exhibited higher activation energies (with very strong correlation coefficients) while irrevocably displaying much superior performances. The correlation coefficients associated to the activation energy linear regression calculations are globally acceptable, but the differences in this variable between both dopant systems in all of the cell types are not yet strong enough to bring up a solid conclusion, therefore they will be analysed in further detail in Chapter IV.

The main point of this chapter was to study the implications of a cation replacement in the performance and impedance. Overall the results show the system containing Calcium performs better when compared with Barium. The higher PPD values of the Calcium system in a symmetric cell are concluded to be severally boosted by its superior anodic performance, suggesting that LCTMN provides superior electro catalytic activity for hydrogen oxidation comparatively to LBTMN. This is further supported by the differences in the symmetrical and anode test cells polarization resistances, where the values presented by Barium cells are roughly twice and four times larger than the ones presented by Calcium respectively. As a cathode, both systems seem to display similar performances (once more supported by similar polarization resistances), which suggests that if a closer size between both A site cations really improves the results, its influence is in the anodic performances.

Chapter IV - XRD and STEM analyses

1. Introduction

The present chapter firstly applies the Rietveld refinement technique to the well reported X-ray diffraction (XRD) patterns of BSCF and SDC (cathode and electrolyte materials respectively). Strongly matching the literature with good agreement and structural lattice parameters, this technique was considered successfully executed and ready to be applied in the previously selected perovskite materials of LBTMN and LCTMN under several conditions. The studied diffraction patterns observed the chemical compatibility with the electrolyte, while providing estimations of structural purities under oxidizing and reducing conditions in both mixture and single powder scenarios. The optimal calcination temperature gap to obtain the highest structural purity was also suggested. High-Angle Annular Dark-Field Scanning Transmission Electron Microscope (HAADF-STEM) data together with Energy Dispersive Spectroscopy (EDS) was used to identify the homogeneity of both specimen and, together with tolerance factor calculations an explanation for the different tendencies of segregation among the perovskites is pondered. Fast Fourier Transform (FFT) pattern phase reciprocal distances allowed the identification of the respective inter-planar distances so that a valid interpretation of the results could emerge which further supported the XRD refinement results.

2. XRD and HAADF-STEM analyses considerations

The relevant powders of the electrodes and electrolyte used in the previous chapter were submitted to an X-ray diffraction (XRD) analysis so that the upcoming Rietveld refinements could take place. All of the following electrode and electrolyte patterns have good or at least decent levels of agreement with the respective space group numbers 221 (P m -3 m), 225 (F m -3 m) and other impurities whose specific patterns were properly addressed were also considered. Within all refinement analysis, convergence was reached and the number of fit parameters widely varied from 14 to 45 depending on each sample requirements.

In every profile the peaks were defined through the second derivative method, assuming peak tip widths between 0.01 and 1 along with a base of 2 degrees (in 2θ). In order to reduce the probability to consider noise induced peaks, a statistical significance value of 1 was found to be an acceptable solution to balance time and results among such a considerable amount of samples. Each phase purity percentage was estimated using a similar equation already reported in literature (Equation IV 1) which ponders the relative peak intensities of the pondered space group and the remaining peak intensities which are not part of it. In the relevant results where impurity percentages are extremely significant (such as in Calcium samples), some efforts towards their identification took place. The upcoming estimations which attempt to quantify these non-perovskite phases, considered a matching tolerance of 5%, which means that only matching gaps inferior to 0.1 degrees in the 2θ scale where accepted within the relevant peak phase. This way a brief quantitative phase analysis [139] - [140] was achieved.

$$Phase\ Purity\ (\%) = \left(\frac{I_{Phase}}{I_{Phase} + \sum I_{non-Phase}}\right) \times 100$$

Equation IV 1 - Phase purity percentage formula where "I_{Phase}" and "$\sum I_{non-Phase}$" are the highest peak intensities of the relevant phase and the sum of the impurity peak intensities, respectively both in counts [141] - [143], [213] - [214]

The XRD data was obtained on a Bruker D8 Advance diffractometer (Cu $K\alpha_1$ radiation). The following Rietveld refinement analyses were carried out in MAUD [144] (Materials Analysis Using Diffraction) software developed by Luca Lutterotti [145] - [149] while also recurring to the academic project Crystallography Open Database (C.O.D.) [150], which is an open-access collection of crystal structures (created in the 5th of March of 2003) [150] - [167].

The electron microscope sample thin films were prepared using the minimum unit of the scales to weigh approximately 0.01 mg of each perovskite powder to be mixed with 20mL of pure ethanol. After submitting the products under ultrasonic treatment for 20 minutes, the sample holder copper grids received 8 depositions of 2.5 μL. The STEM data (obtained on a Titan G2 80-200) not only provided the elemental mapping together with the Energy Dispersive Spectroscopy (EDS) analysis as well as the direct observation of the particle size tendency between specimens. Using the Scherrer equation (Equation IV 2) on the highest intensity peaks of the main

phase, further agreement between the microscope and the x-ray data was found. The results of this equation are considered to be acceptable since the calculated average particle size values are still equal or inferior to 100 nm. The FFT reciprocal distances were matched assuming the same relevant lattice parameters obtained in the XRD Rietveld refinements while only accepting matching errors inferior to 5%.

$$\tau = \frac{K.\lambda}{\beta.\cos(\theta)}$$

Equation IV 2 - Scherrer equation where τ, K, λ, β and θ are the mean size particle size, the shape factor, the x-ray wavelength, the full width half-maximum intensity broadening and the Bragg angle, respectively in nm, dimentionless, nm, radian and radian

3. XRD analysis results

3.1 BSCF pattern cathode and SDC electrolyte analysis

Before applying the Rietveld refinement technique and the phase purity estimation calculations in the Barium and Calcium doped perovskites, these tools were firstly used in the well reported BSCF ($Ba_{0.5}Sr_{0.5}Co_{0.8}Fe_{0.2}O_3$) cathode and SDC ($Ce_{0.8}Ce_{0.2}O_{1.9}$) electrolyte materials. It was important to establish matching results with the current available literature to provide credibility and veracity to the obtained computed solutions in the not so well reported perovskites that where compared in the previous chapter. From all of the XRD refinements, the BSCF powder displayed by far the lowest weighted profile R-factor (R_{wp}) of 3.370 with a goodness of fit (GoF) of 1.082 (Figure IV 1). The calculated cubic lattice parameter is 3.983 Å, which very well matches the expectations from the relevant values currently available in literature [157] - [167]. The structural purity further supports this deeply reliable result displaying an average high percentage of 99.541% (Figure IV 1).

As it was mentioned, a powerful literature agreement is extremely important to be obtained given the fact that the upcoming electrode specimen refinements of the lanthanide unique perovskites doped with Calcium and Barium are not exactly reported in literature. A strong literature agreement in this (BSCF) reference cathode material is also important from the fact that obtaining good fitting parameters does not necessary mean that the refinement is a good representation of the structural reality or that all applied considerations retain relevance and physical meaning.

Therefore the SDC benchmark electrolyte material X-ray pattern was also refined to further stress the successfulness of the Rietveld refinement method application and also to allow further comparison with mixture powders in further analysis.

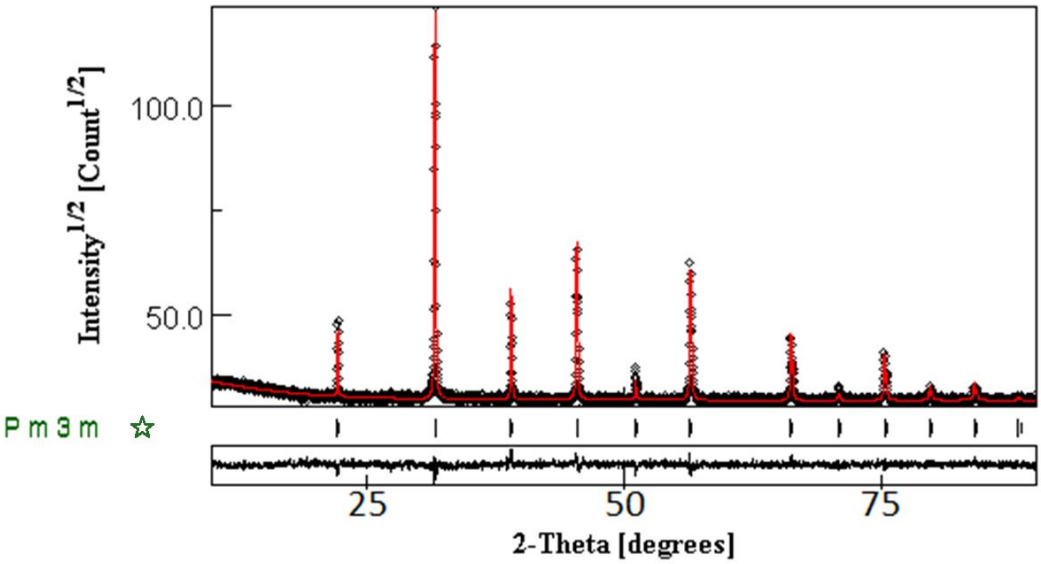

Figure IV 1 - Rietveld refinement of BSCF powder used as the reference cathode calcined at 1000 ^{o}C for 5 hours in air

The SDC pellets also revealed acceptable agreement parameters of GoF and R_{wp} of 1.478 and 9.134% respectively (Figure IV 2). The calculated lattice parameter was found to be 5.430 Å, a value that was used for comparison with further powder mixture analysis in order to evaluate the chemical compatibility between electrode and electrolyte. Not only this estimated SDC unit cell length is in line with the values presented in literature [168] - [177], but it also exhibits a high purity estimation (of 99.504% as expected from a commercialized product). This lattice parameter also dictating an average relative density of 97.134+/-0.508% (estimated using the Archimedes procedure to determine the bulk densities in a total of 9 pellets where the largest deviation was found to be 3.106%).

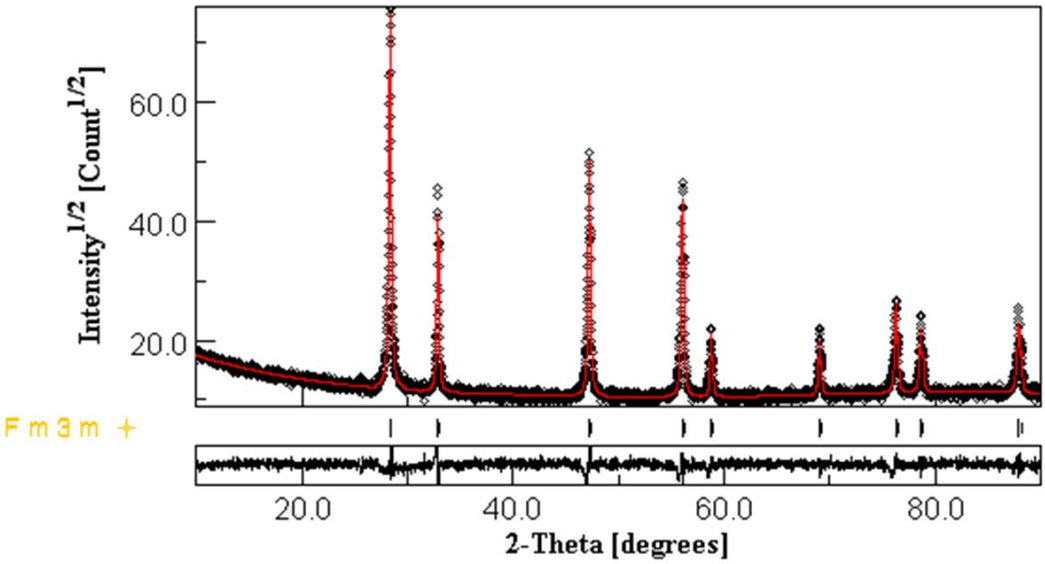

Figure IV 2 - Rietveld refinement of an SDC pellet used as the electrolyte calcined at 1400 ºC for 5 hours in in air

3.2 Electrode powders

In order to understand the superior anodic performance of the Calcium perovskite when compared to the Barium one, specimens of the relevant powders used in this comparison were also analysed by XRD technique at room temperature. Both perovskite powders were submitted to this analysis after calcination and after experiencing reducing conditions (in hydrogen during 2 hours at 800 ºC).

3.2.1 Electrode powders analysis after calcination

The Barium perovskite powder refinement easily reveals strong agreement elements of R_{wp} (7.503%) and GoF (1.364) (Figure IV 3). A lattice parameter of 3.911 Å and a strong P m -3 m phase purity of 97.021% were obtained. As expected, the calculated Calcium oxide lattice parameter exhibited a smaller value (of 3.889 Å), however, the fitting parameters are now significantly weakened. The 10.394% and 2.729 values of R_{wp} and GoF respectively, push this model slightly beyond the general limit of acceptance (Figure IV 4). The main discrepancies between the data points and the function are located between 28.8 and 31.8º. Literature sources [12], [20] - [21], [32], [38], [40], [49] - [53], [55] point out potential routes to be explored in regards

to the identification of the unknown phase/s within this specimen, which leads to another multiple phase refinement approach. Among a wide variety of possible space groups, the best fitting results achieved (seen in Figure IV 5) do display a significant amount of improvement over the previous single phase analysis. In this comparative scenario, having a GoF of 2.160 and an R_{wp} of 8.827%, the estimated cubic lattice parameter was still consistent (3.886 Å), however, comparatively to the high space group definition observed in the Barium specimen (of 97.021%), Calcium perovskite average cubic structure purity estimation was found to be significantly lower (74.595%).

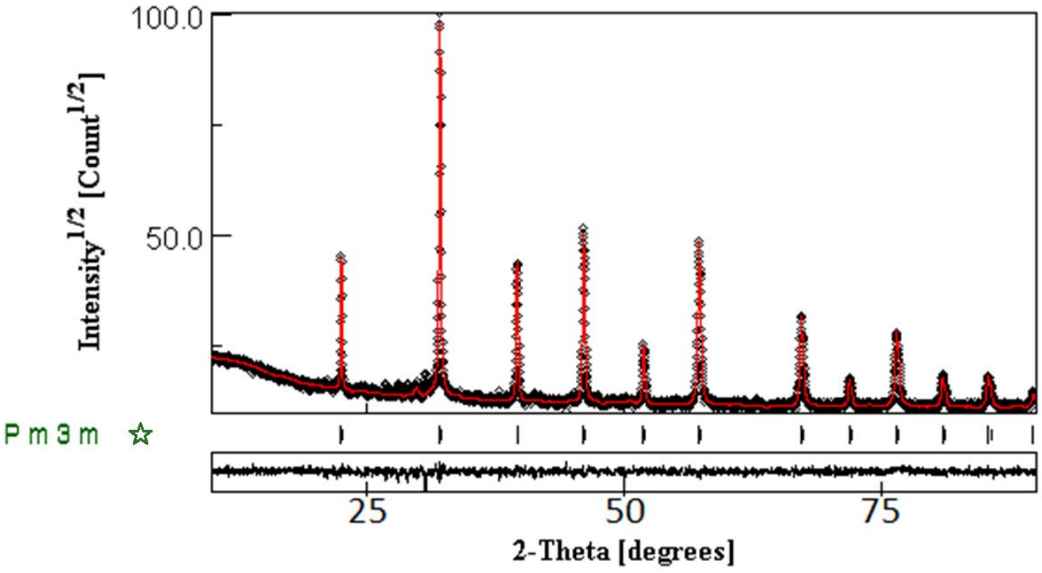

Figure IV 3 - Rietveld refinement of $La_{0.7}Ba_{0.3}Ti_{0.5}Mn_{0.4}Ni_{0.1}O_3$ after 10 hours at 1100 ^oC in air

The additional phases considered to attempt to match the unknown peaks in the Calcium specimen can very well be present has oxides formed with the relevant composition elements. Both the space groups of P 6_3/m m c (from the hexagonal crystal system) as well as the P 3 2 1 arrangement can be adapted by the Lanthanum (III) oxide. Therefore, these were considered as possible alternative phases within the LCTMN electrode powder. Typically this oxide is more frequently associated with the space group P 3 2 1 [182] - [185], however this chemical was also reported displaying the relative disposition of the space group number 194 [186] and [187]. This hypothesis is further supported by literature reports where the presence of impurities in the region between the first and second P m -3 m phase peaks have also been

related to the lanthanum oxide [189] - [200]. The figured “a” and “c” lattice distances from the P 6_3 /m m c phase were determined to be 16.877 and 6.930 Å. As for the trigonal symmetry, the unit cell corresponding “a” and “c” lengths were found to be 3.809 and 5.966 Å. Though the consideration of these two structures improved the overall refinement agreement, many peaks are yet to be matched. Even the ones that seem to belong to these new phases, their lack of intensity in the model assures that even if this hypothesis is true, this phase configuration is still incomplete (Figure IV 5).

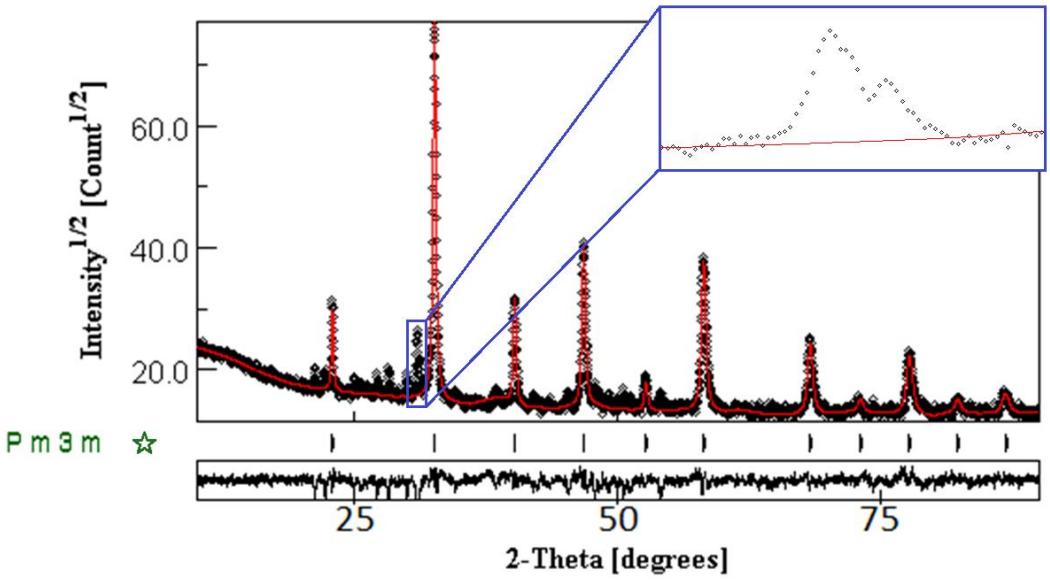

Figure IV 4 - Rietveld refinement of $La_{0.7}Ca_{0.3}Ti_{0.5}Mn_{0.4}Ni_{0.1}O_3$ after 10 hours at 1100 ºC in air

Multiple space groups regarding the same oxide could have also been considered, even if those phases were not identified in the source reagent itself, however It makes little to no sense to consider phases which can only be formed at high pressures (since the powders are sintered under atmospheric pressure). Titanium dioxide (for example) which can display multiple phases, such as Anatase (within the source powder), Rutile, and Brookite, consequently provides different space group patterns (of I41/a m d, P 42/m n m and P b c a respectively). However, in this case, both Anatase and Brookite phases will irreversibly convert to the Rutile structure at temperatures around 600 to 800 ºC [188], [201], which explains why no

improvement is really found if these space groups are also considered in the refinement.

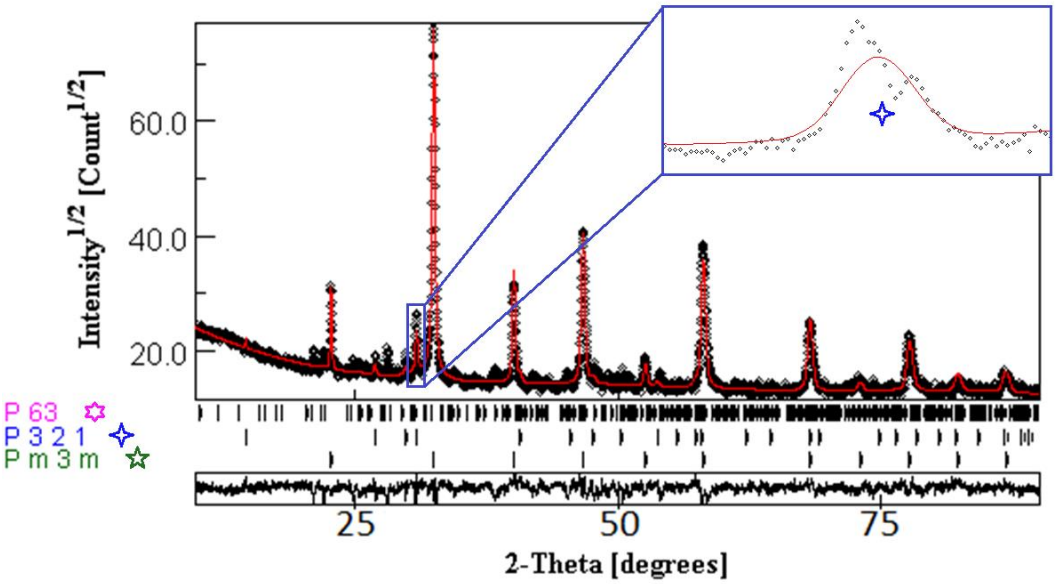

Figure IV 5 - Rietveld refinement of $La_{0.7}Ca_{0.3}Ti_{0.5}Mn_{0.4}Ni_{0.1}O_3$ after 10 hours at 1100 ºC in air considering 3 phases.

3.2.2 Electrode powders after reducing conditions of 2 hours at 800 ºC in H_2

The results in Chapter III (in section 3) reveal that the $La_{0.7}Ca_{0.3}Ti_{0.5}Mn_{0.4}Ni_{0.1}O_3$ electrode provides better performances comparatively to the $La_{0.7}Ba_{0.3}Ti_{0.5}Mn_{0.4}Ni_{0.1}O_3$ material essentially from its superiority as an anode (since the cathode effectiveness was considered to be similar). From the fact that this difference is attributed to the anodic behaviour, it becomes mandatory to obtain structural information of these compounds under reducing conditions. Under this atmosphere, both Xrd results showed evident pattern differences as well as apparent peak pattern definition tendencies along with the new surrounding environment.

Comparing with its previous analysis (after calcination), the Barium perovskite (now under reducing conditions) seems to reveal minor differences that are only perceptible between the first and second P m -3 m typical peaks (Figure IV 6). The agreement values of this refinement increased slightly exhibiting values of R_{wp} and GoF equal to 6.879% and 1.203 respectively. The determined lattice parameter also

increased now to 3.972 Å, which is expected to happen given the fact that fundamental knowledge states that a decreased average state of oxidation directly implies an increase of electron density which leads to an increase of the average size of the ionic radius [181]. The calculated purity was found to be 98.141% (which is not much of an improvement facing the value obtained after calcination), nevertheless, it shows that LBTMN is indeed a very structurally stable perovskite under both oxidizing and reducing conditions.

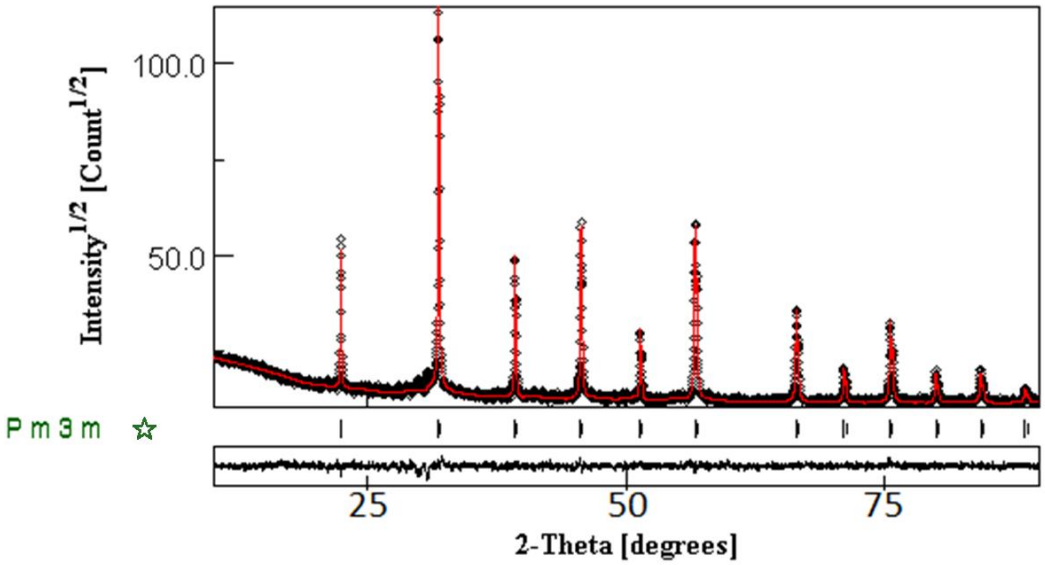

Figure IV 6 - Rietveld refinement of $La_{0.7}Ba_{0.3}Ti_{0.5}Mn_{0.4}Ni_{0.1}O_3$ after 2 hours at 800 ºC in H_2

Under reducing conditions the $La_{0.7}Ca_{0.3}Ti_{0.5}Mn_{0.4}Ni_{0.1}O_3$ perovskite reveals itself as much more sensitive to this atmosphere change comparatively to its rival. The hydrogen atmosphere drastically decreased this perovskite purity to an average value of 42.920%. Even considering a triple phase model (as previously), the refinement parameters are still quite on the edge of typical acceptance limits, where values of Rwp and GoF are equal to 9.788% and 2.509 correspondingly (Figure IV 7). Just like in the previous refinement (and still for the same reasons), the Calcium perovskite calculated cubic lattice parameter also increased (to 3.914 Å).

Further efforts took place in order to improve this particular refinement, since some unmatched peaks in the same problematic range (between 28.8 and 31.8º) could still be seen. Here, some lattice distortions are about to be considered in the P

3 2 1 phase so that its second peak in this area could support the lack of intensity of the P 6_3 peak on the left (Figure IV 7). This peak position release enables the existence of a parallel phase with inferior lattice parameters (possibly from higher average states of oxidation). This new refinement model with 4 phases provided a substantial improvement in regards to the agreement parameters displaying an R_{wp} and GoF values of 8.758% and 2.120 respectively (Figure IV 8).

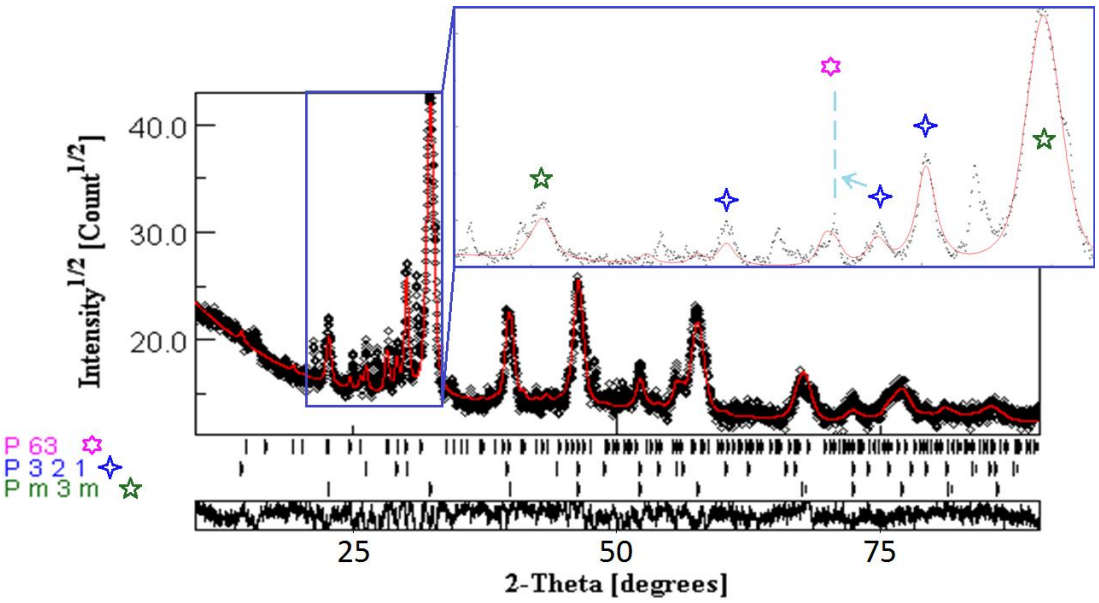

Figure IV 7 - Rietveld refinement of $La_{0.7}Ca_{0.3}Ti_{0.5}Mn_{0.4}Ni_{0.1}O_3$ after 2 hours at 800 ºC in H_2 considering 3 phases

Two sizes within the same (P 3 2 1) phase were considered not only from the fact that the agreement parameters improved, but also because the calculated lattice parameters kept their consistency comparatively with the previous approach. The first P 3 2 1 unit cell was slightly shaped to exhibit “a” and “c” lattice values of 3.893 and 6.308 Å, while its latest introduced coexistent version is estimated to have the smaller lengths of 3.774 and 6.118 Å respectively. The perovskite unit cell lattice variable also remained extremely close to its previous calculation (now being 3.918 Å), however, the initial considerations of distorting the P 3 2 1 unit cell also decreased some of the intensity present in the peak at 52.2º, which was being matched by the previous approach. The P 6_3 “a” and “c” lattice parameters were found to be very different comparatively with the previous section 3.2.1 (Figure IV 5) displaying now values of

10.028 and 7.480 Å respectively, which is unexpected since reducing conditions usually do not decrease the lattice parameters.

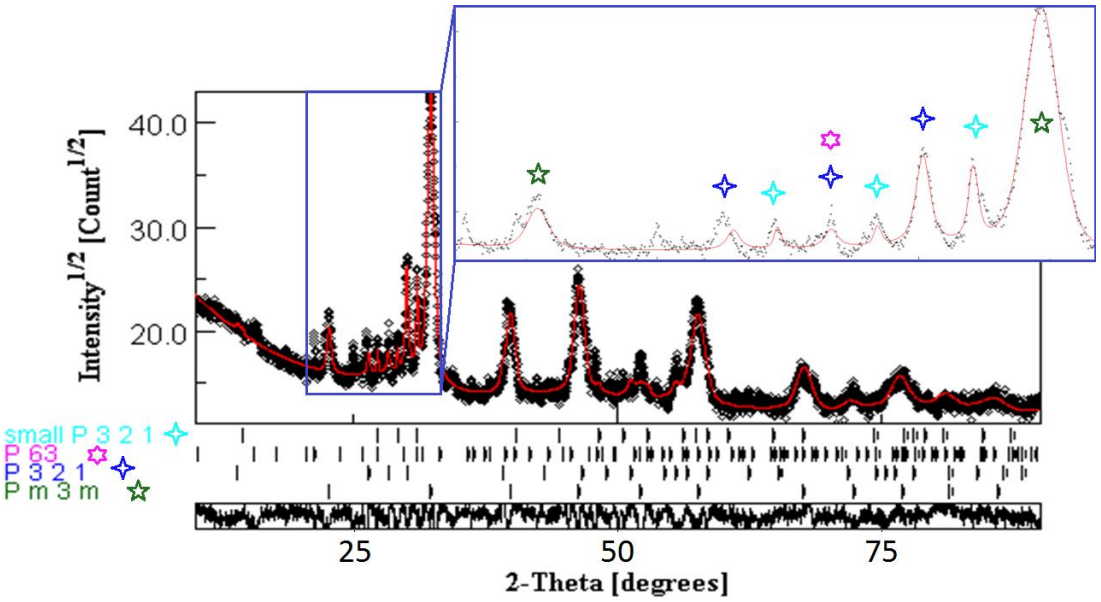

Figure IV 8 – Rietveld refinement of $La_{0.7}Ca_{0.3}Ti_{0.5}Mn_{0.4}Ni_{0.1}O_3$ after 2 hours at 800 ºC in H_2 considering 4 phases where the space group P 3 2 1 displays two different unite cell sizes.

The main issue with this assumption is that calcium monoxide cannot be assigned to justify the smaller P 3 2 1 unit cell, since its space group is the same as Nickel monoxide and SDC (that is F m -3 m) which does not fit the impurities pattern. This may suggest that Lanthanum oxide enormous stability does not come solely from its incredibly strong enthalpy variation (of roughly -1250 kJ.mol^{-1} [202]) which makes it hard to be reduced to inferior valency states. Instead, this may mean Lanthanum oxide (La_2O_3) can potentially adjust its bonding lengths to smaller sizes under reducing conditions, preserving this spatial cationic arrangement until temperature (and or pressure conditions) favour an alternative atomic disposition. Nevertheless, the limitations of this hypothesis must be accepted and the need for further structural analysis is acknowledged.

3.3 Chemical stability between electrode and electrolyte

3.3.1 After oxidizing conditions

In the previous chapter sections 3.3 and 3.4, where the calcium perovskite was under oxidizing conditions, slightly lower ohmic resistances were observed in comparison to the barium perovskite. The fact that under reducing conditions (section 3.5) this small difference was not seen, it could suggest the existence of a reaction between the electrode and the electrolyte favoured by oxidizing conditions. Each $La_{0.7}Ba_{0.3}Ti_{0.5}Mn_{0.4}Ni_{0.1}O_3$ and $La_{0.7}Ca_{0.3}Ti_{0.5}Mn_{0.4}Ni_{0.1}O_3$ powders (previously sintered at 1100 ^oC as described in Chapter IIIsection 3.2.1) was then mixed with the SDC electrolyte in a weight ratio of 1:1 and grinded in a mortar until colour homogeneity was obtained. These 2 samples were submitted at 1000 ^oC during 5 hours in air (simulating extreme cathodic conditions) before an XRD analysis at room temperature took place followed by the respective first Rietveld refinements (Figure IV 9, Figure IV 10 and Figure IV 11).

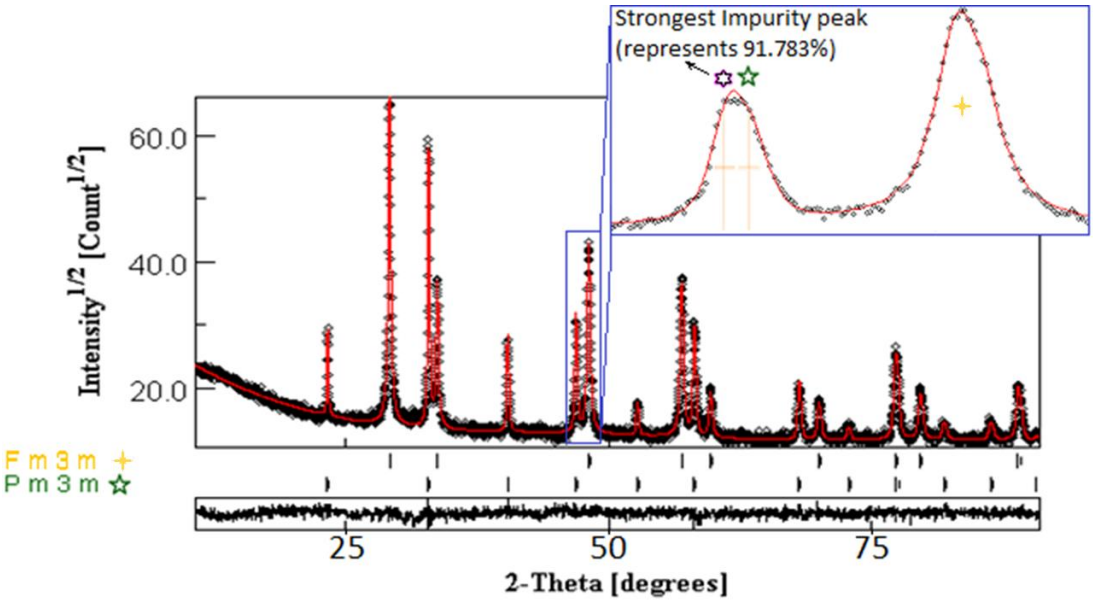

Figure IV 9 - Rietveld refinement of $La_{0.7}Ba_{0.3}Ti_{0.5}Mn_{0.4}Ni_{0.1}O_3$ + SDC after 5 hours at 1000 ^oC in air

The Barium perovskite mixture refinement (Figure IV 9) reveals a very solid co-existence of both relevant space groups of the SDC (F m -3 m) and the single perovskite (P m -3 m). The calculated lattice parameters for both the electrode and electrolyte structures were correspondingly 3.919 and 5.409 Å. Both the P m -3 m

and F m -3 m phase determined average purity ratios (of 40.654 and 50.256 respectively) are not far from the 1:1 known weighted ratio. The main reason behind the P m -3 m's weaker presence seems to be that more than 90% of the impurities are quantified in its broad peak around the 46º (Figure IV 9). Discarding this peak would result in calculated ratios of 44.779 and 54.770% (for the perovskite and the SDC powders respectively), however the peak criteria definition had to remain unaltered through the whole XRD analysis section for the purposes of consistency in order to provide reliable comparisons between samples. This means that even if crystal size and or microstrain variables are still not enough to quantify Full Width Half Maximum (FWHM) unexpected enlargements (of at least twice the expected 2θ gap), then indeed more than one peak has to be considered in order to preserve the constant criteria through the whole analysis. Nevertheless, these results were obtained under amazing refinement agreement parameters with an Rwp of 6.479% and a GoF of 1.076. With an average estimated mixture purity of 90.910% (while respecting the previously established criteria), a definitive proof of a cathode-electrolyte reaction is yet to be seen regarding this Barium perovskite oxide powder and if there really is any, still no new possible resultant phases were identified. The individual calculated percentages of these main phases might be pointing out that either the standalone purity of the individual powders really differs that much, or that a possible reaction between both powders would highly affect the perovskite phase while altering less the other reagent's crystal shifting the estimated ratios away from the 1:1 proportion.

Relatively to the Calcium perovskite cubic structure, the relevant refinement seems to claim it also co-exists very well along with the SDC's F m -3 m space group (Figure IV 10). Despite slightly decreasing the overall level of the agreement in the refinement, very good values of R_{wp} (6.946%) and GoF (1.310) were still obtained. The respective calculated lattice parameters of 3.869 and 5.421 Å are also reasonable from the fact that it is naturally expected of the Calcium perovskite lattice parameter to be slightly smaller comparatively with the Barium one from the dopant cation size difference. The constant compound (SDC) among both refinements is extremely coherent in regards to its phase lattice parameter independently of the perovskite that it was mixed together with, displaying an error of 0.22%. The proportional relation between the A site cation radius and the resultant unit cell dimensions is intuitive, and as expected, the correlation between experimental and calculated results is usually compatible with experimental results [180]. This unit cell shrinkage roughly results in a peak pattern dislocation to higher 2theta angles, which

in this case moves the very same perovskite 4th peak too close to the 3rd peak of the F m -3 m space group. Though there is still enough FWHM degrees gap between these two peaks, a simple observation of the point displacement easily leads to the conclusion that there is no possible negative second derivative within this gap (respecting the same gap and peak base widths as before) because the data is mostly concave upwards (Figure IV 10).

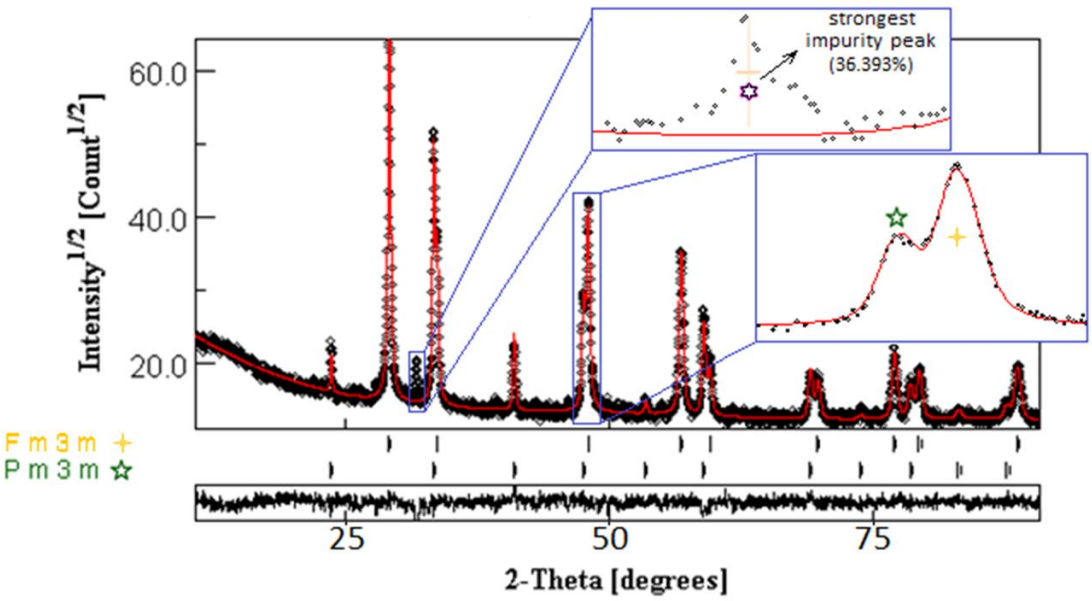

Figure IV 10 - Rietveld refinement of $La_{0.7}Ca_{0.3}Ti_{0.5}Mn_{0.4}Ni_{0.1}O_3$ + SDC after 5 hours at 1000 ºC in air

As observed previously in section 3.2.1, Calcium perovskite mixture still displays the same unmatched peak (located at 30.875º) which is right in the middle of each phase corresponding main peaks. Given the fact that this anomaly belongs to neither of the pattern phases, this assures the existence of (at least) a third phase within this specimen, suggesting that these impurities belong solely to the LCTMN powder. This unmatched peak strongly represents on average 36.393% of the total impurities, still, the overall purity of this mixture (having a value of 95.049%) remains higher than the previous one. These numbers do not mean that this/these unidentified phase/s is/are necessarily a product of reactions between the electrodes and the electrolyte exactly from the fact that the largest unmatched peak was already observed in the electrode powder (Figure IV 4 and Figure IV 5). Based on the previous attempt of quantifying the impurities (in section 3.2.1), the same phases were once more considered (Figure IV 11). As expected, this hypothesis improves the

agreement variables of GOF and R_{wp} values (specifically to 1.114 and 6.402% respectively), while outputting slightly higher lattice parameters of 3.895 and 5.459 Å in both main phases.

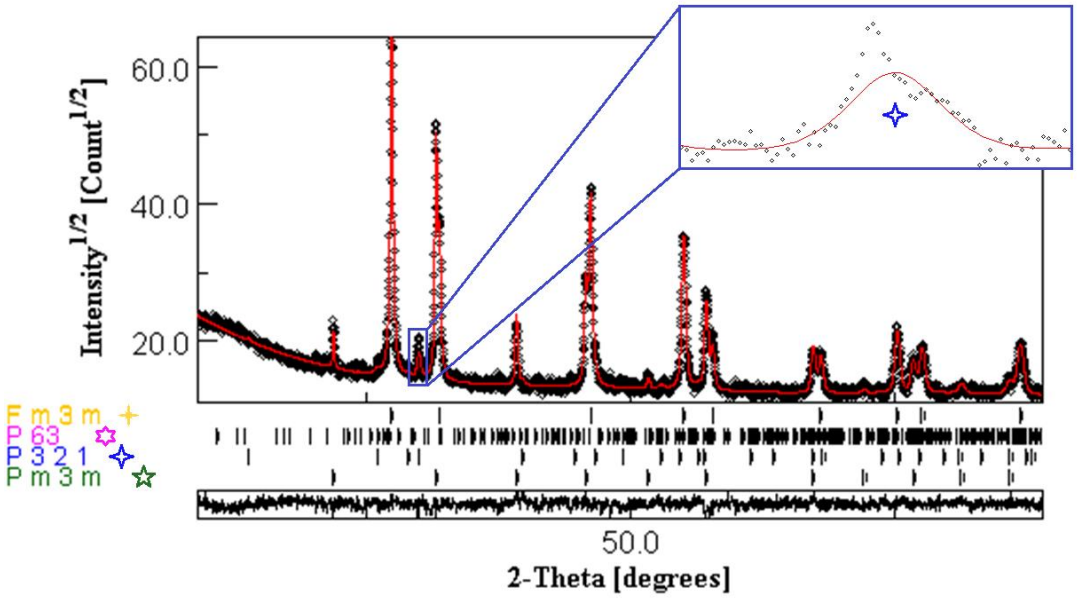

Figure IV 11 – Rietveld refinement of $La_{0.7}Ca_{0.3}Ti_{0.5}Mn_{0.4}Ni_{0.1}O_3$ + SDC after 5 hours at 1000 ºC in air considering 4 phases

Among the considered impurities, the "a" lattice cell parameter of the P 6_3/m m c space group (being 14.938 Å) shows the largest difference comparatively to the electrode powders after calcination (16.877 Å), while the "c" lattice parameter (value of 7.007 Å) remains much closer to the previous number (6.930 Å). This could suggest that either the SDC powder is interacting to distort this crystal system, or that the hypothesis of considering this space group as an impurity of LCTMN might not be the most appropriate. Regarding the trigonal space group, the lattice values of 3.822 and 5.974 Å seem to display a higher level of agreement in comparison to the previous ones displayed in section 3.2.1, which supports its consideration as an impurity of the LCTMN powder. However, its lack of intensity in its main peak to cover the pattern data assures that other space groups have to be considered in order to fully characterize all impurities.

The evident difference in the calculated weighted ratios of 36.311 and 58.127% (relatively to the P m -3 m and F m -3 m space groups) suggests the LCTMN

impurity phases are overlapping with the F m -3 m space group peak positions consequently causing its overestimation (through boosting its phase peak amplitudes). Clearly these values are further from the 1:1 ratio comparatively to Barium's perovskite mixture, which supports this theory from the fact that LBTMN displayed much higher estimated purities.

3.3.2 After reducing conditions

In the previous chapter (in section 3.5), the clear differences in performance between these two powders were attributed to anodic behaviour, therefore, it also becomes important to search for possible structural changes in the mixtures under reducing conditions even if the respective ohmic resistances under this atmosphere did not display significant discrepancies. Since a structural difference might hold the key to understand the Calcium perovskite superior performance over Barium as an anode, the reduced powder mixtures were submitted to a longer range of 2θ values from 10 to 130º (instead of the usual 10 to 90). Only the Barium perovskite displayed impurity peaks located in the larger 2θ angles (over 90º), however these four impurity peaks only represent 29% of the total estimated impurities of 11.561%. Once treated with hydrogen, LCTMN is undeniably the most affected in terms of impurities in comparison with any other and both mixture purities decreased regardless of the considered phases scenario.

Barium mixture displays improved phase purity ratios of 43.916 and 44.801% regarding the respective space groups of P m -3 m and F m -3 m (Figure IV 12). This overall mixture ratio improvement is not a product of lower impurity peak amplitudes, but rather a relativistic result that is highly dominated by the considerable peak definition enhancement in both known and unknown phases. The highest impurity peak intensity also increased (from 757 to 2187 counts) under reduced conditions which means that this atmosphere seems to also develop the presence of this/these particular phase/s even though the resultant calculated mixture ratio is now closer to 1:1. This very same impurity peak was found to be located around the same zone as in the equivalent profile under oxidizing conditions (Figure IV 9), whereas now it is located at the right side of the perovskite peak (Figure IV 12) instead of at the left. This suggests that, though both crystal systems seem to have grown under reducing conditions, the perovskite seems to possibly display a larger size difference in the hypothesis of this unknown peak to solely represent a constant impurity phase. Since the mixture purity only decreased by 2.193% (from 90.910 to 88.718%), it seems

more likely that these impurities benefit from neither one of the atmospheres, but rather belong to the Barium perovskite powder.

Reducing conditions do not seem to have much of an impact in the agreement parameters, displaying a GOF slightly higher (2.526), but an R_{wp} lightly diminished (6.068%). The consequent enlargement in the unit cells due to the average valency state decrease was highly expected. As it was already mentioned, the fundamental knowledge dictates cations increase their ionic radius when their valency state decreases simply because the electronic cloud grows by electronic repulsion [181]. The F m -3 m space group slightly enlarges its unit cell by 0.02 Å (to 5.429 Å) and Barium perovskite lattice parameter also increases to 3.967 (which is a little over 1% of its initial size).

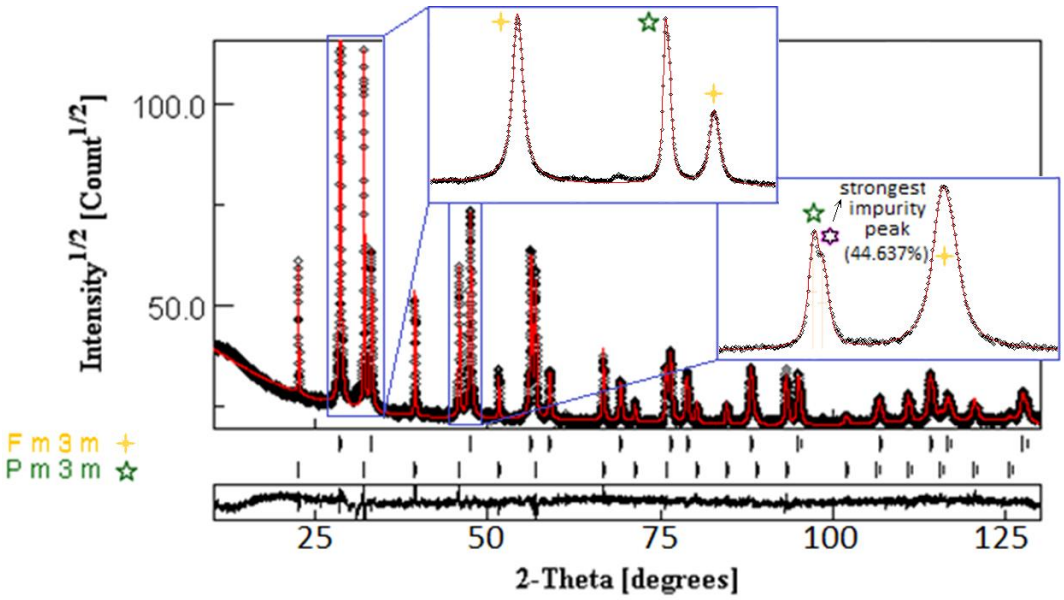

Figure IV 12 - Rietveld refinement of $La_{0.7}Ba_{0.3}Ti_{0.5}Mn_{0.4}Ni_{0.1}O_3$ + SDC after 2 hours 800 ^oC in H_2

As seen before in section 3.2.2 Calcium perovskite seems to be much more affected by these atmospheric conditions especially in the 2theta gap from 28º to 34º. Within this interval, the presence of the three strongest impurity peaks is evident (Figure IV 13), whereas in the Barium corresponding profile (Figure IV 12), a smooth point arrangement is observed in the angle gap between each of the higher intensity peak phases. These impurity peaks represent more than 60% of the estimated total mixture impurity of almost 11%, which is essentially twice as much as the value

observed under oxidizing conditions (5.364%). Not only the calculated impurities are now higher, but also the estimated mixture ratios are further from the 1:1 powder ratio, displaying percentages of 12.279 and 77.187% regarding the P m -3 m and F m -3 m space groups respectively. These results seem to fully counter the hypothesis of a reaction between cathode and electrolyte powders under any atmosphere to create a beneficial phase (to justify the small ohmic resistance differences in chapter III), again from the fact that these peaks were already observed in section 3.2.2 also after reducing conditions. Not only it is very likely that these impurity peaks come solely from the LCTMN powder itself, but also they seem to be under estimated from overlapping with the SDC phase peaks (over estimating the F m -3 m phase), justifying this way the calculated ratio discrepancy (of 12.929 and 77.187%) from the 1:1 proportion.

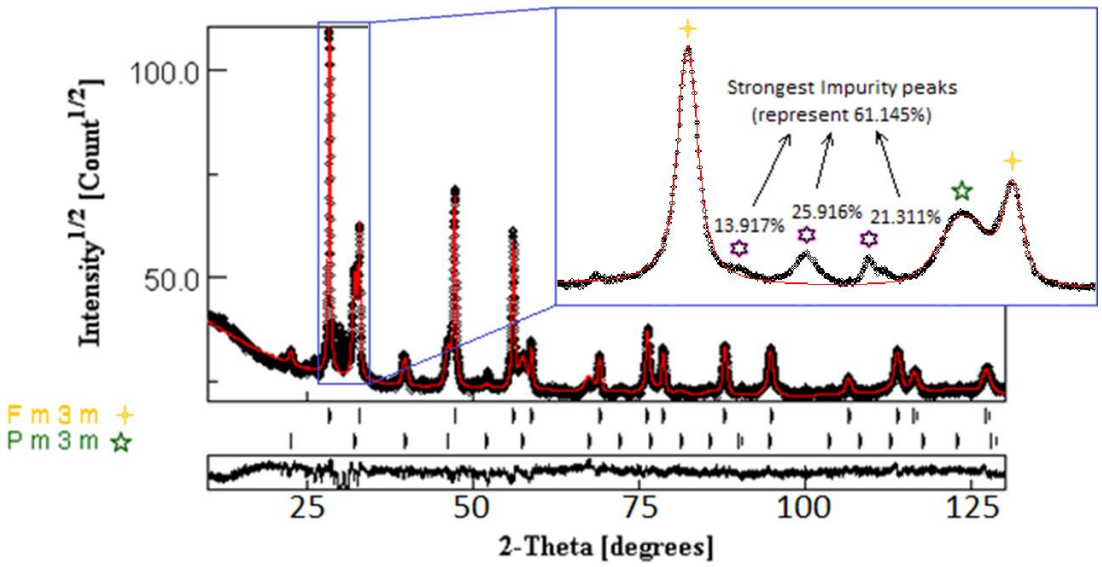

Figure IV 13 - Rietveld refinement of $La_{0.7}Ca_{0.3}Ti_{0.5}Mn_{0.4}Ni_{0.1}O_3$ + SDC after 2 hours 800 ^oC in H_2

The GOF of 3.678 and the R_{wp} of 7.123% show a small decrease in the overall refinement level of agreement. After the hydrogen treatment, the Calcium perovskite lattice parameter expanded 1.525% of its initial length (of 3.869 Å), which is a slightly stronger enlargement comparatively to LBTMN. It should be mentioned that the SDC powder always displayed larger unit cell volumes in this Calcium mixture. Both SDC lattice differences under oxidizing and reducing conditions of 0.012 and 0.014 can potentially be boosting the ionic conduction of the electrolyte and consequently justify

the existence of slightly lower ohmic resistances comparatively to Barium samples (in sections 3.3 and 3.4 from Chapter III). Though this theory may help to explain the small ohmic resistance difference under oxidizing conditions, it does so not by implying the existence of a less conductive layer resultant from a reaction between SDC and LBTMN. Instead, it softly suggests that the LCTMN electrode layer would slightly increase the SDC unit cell and consequently improve its ionic conductivity in the contact vicinity of the two compounds. Since the anode performances (and polarization resistances) were the clear differences found between both materials, the slightly larger SDC unit cell expansions under reducing conditions could work in favour of this premise, however the ohmic resistances found under reducing conditions were negligible. Therefore, even if this hypothesis of a synergetic third layer is somehow plausible (from the fact that differences in the ohmic resistance could come from consequent small SDC unit cell different expansions), it surely becomes invalid in the presence of hydrogen atmosphere. Even attempting another approach of now considering the SDC lattice expansions from the atmosphere change, the electrolyte powder in the Calcium mixture displayed a lightly larger unit cell expansion of 0.419% while the respective value found for LBTMN was lower (0.375%), but still too similar. It looks like independently of how the lattice parameter differences are approached, the observed differences do not really seem helpful enough to solve the mystery behind Calcium superior anodic performance.

The previously considered hexagonal and trigonal crystal systems (in section 3.2.2) once more improved the refinement agreement with GOF and R_{wp} values of 2.044 and 5.307% while displaying similar values in the lattice parameters of the P m -3 m (3.928 Å) and F m -3 m (5.447 Å) cubic main phases (Figure IV 14). Comparatively to the single LCTMN powder sample, all considered impurity “a” lattice lengths are larger, however the “b” lattices are smaller. Since the biggest differences in these parameters not only belong to the same P 6_3/m m c phase, but also are well over 1 Å, this suggests that this hexagonal system is less likely to be part of the LCTMN impurity phases comparatively to the P 3 2 1. The trigonal system displayed differences of less than 0.04 and 0.17 respectively in the “a” and “c” lattice parameters and these variations are much closer to the ones observed in the cubic crystal systems.

Comparatively with oxidizing conditions, it would be expected that all the lattice parameters would increase, however, some exceptions were found. The “c” parameter of the hexagonal crystal system was estimated to be more than 0.6 Å

shorter and this phenomenon is also observed comparing single powder samples though in the “a” variable. Such inconsistencies in this phase suggest that its matching peaks might belong to multiple phases instead. The F m -3 m space group also displayed some lattice parameter inconsistencies from one atmosphere to another, though these differences are one order of magnitude below the smallest observed in the hexagonal considered system.

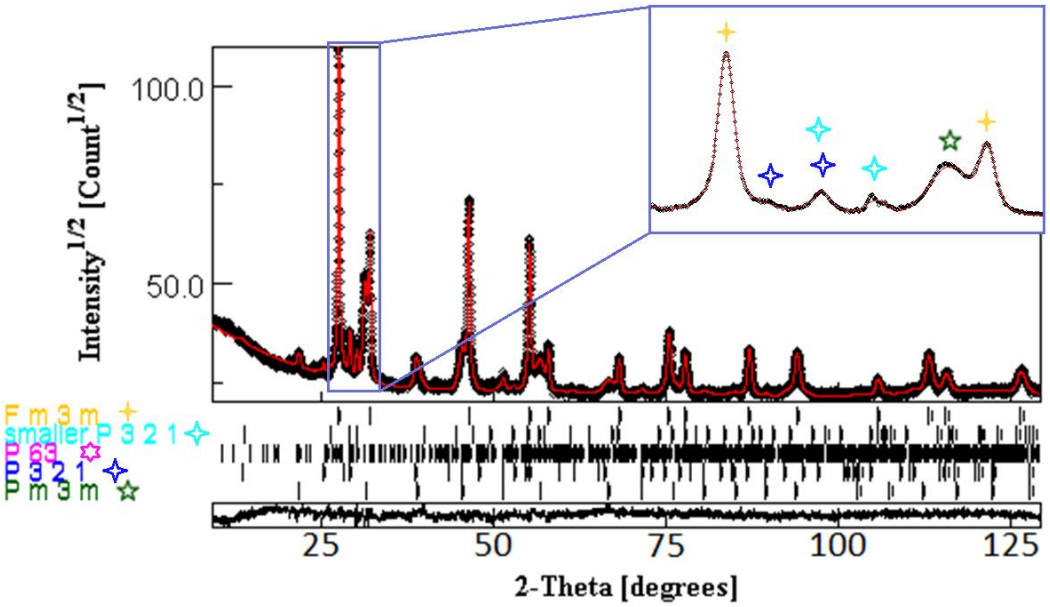

Figure IV 14 - Rietveld refinement of $La_{0.7}Ca_{0.3}Ti_{0.5}Mn_{0.4}Ni_{0.1}O_3$ + SDC after 2 hours 800 ºC in H_2 considering 5 phases

3.4 Brief analysis of the calcination temperature influence

3.4.1 Optimum calcination temperature of LCTMN

Attempting to decrease the impurities in the LCTMN powder, several XRD analysis were obtained after different calcination temperatures followed by their relative Rietveld refinements. This brief analysis attempts to show whether or not it is possible to push the LCTMN purity estimation closer to the LBTMN much higher values so that both perovskites are more comparable. Furthermore, obtaining a significant purity estimation difference might stimulate a new performance comparison between both LCTMN powders so that the (beneficial/jeopardizing) influence of these impurities can be quantified and better understood in the future. Overall the calcination temperature increase seems to not only improve the cubic

structure definition, but it also increases the intensity of other peaks in the typical problematic segment between the first and second P m -3 m phase peaks.

The refinement parameters provided overall satisfying results, notwithstanding, at 1150 and 1250 ^{o}C the weighted profile R-factors (of 10.380 % and 10.516 %) are commonly understood to indicate a slightly lower level of agreement even in the presence of generally acceptable GoFs (of 2.929 and 2.709) [139], [140], [203]. Though these specimens seem to show considerable inferior agreement results, their best insights lie within their evident superior intensities just like the sample calcined at 1200 ^{o}C (Figure IV 15). This particular sample seems to benefit from a good intensity scale, while keeping a slightly lower R factor. At first sight, this suggests that among all of the 5 calcination conditions, 1200 ^{o}C seems to provide the highest P m -3 m structural definition. Estimating the perovskite purities from the computed data, the highest average value is indeed found in this particular calcination temperature (Figure IV 16) when a matching tolerance of 5% is considered (as explained in section 2). This theoretical highest degree of perovskite purity is outputting a balance between the largest possible intensity scale (governed by the P m -3 m space group strongest peak) while displaying the lowest number of counts in the secondary impurity peak phases. The purity calculations indeed display the highest value of 83.813 %, though the calculated lattice unit cell in these conditions is slightly smaller (3.867 Å). Nevertheless, an estimated improvement a little over 9% might be enough to understand the nature of the LCTMN impurities. The calculated edge values do not seem to display any particular regular tendency, but the purity improvement might be enough of an argument to reassemble LCTMN electrode cells so that a comparison with the previous samples (calcined at 1100 ^{o}C) can occur.

The smallest cubic lattice length belongs to the highest purity specimen, however, the size differences of the closest values from the average (of 3.877 Å) always represent less than 0.3 %. The strongest differences do exist within these particular calcination temperatures (of 1150 and 1200 ^{o}C), nevertheless they are in the “c” lattice parameter of the considered P 6_3/m m c phase where percentages of shrinkage and enlargement above 10% can be spotted. Both “a” and “c” impurity lattice parameters of the phase P 3 2 1 seem to overall display considerable lower shrinkage or expansion ratios relatively to the average. Obviously, the same cannot be said about the P 6_3/m m c space group lattices where the average of these absolute differences for the “a” and “c” lattice parameters is found to be 3.097 and 8.124 % correspondingly. These length parameters displayed no clear tendency at

all, still, the respective unit cell volumes were calculated to see if both “a” and “c” parameters would somehow balance each other resulting in a definitive cell volume expansion or shrinkage tendency.

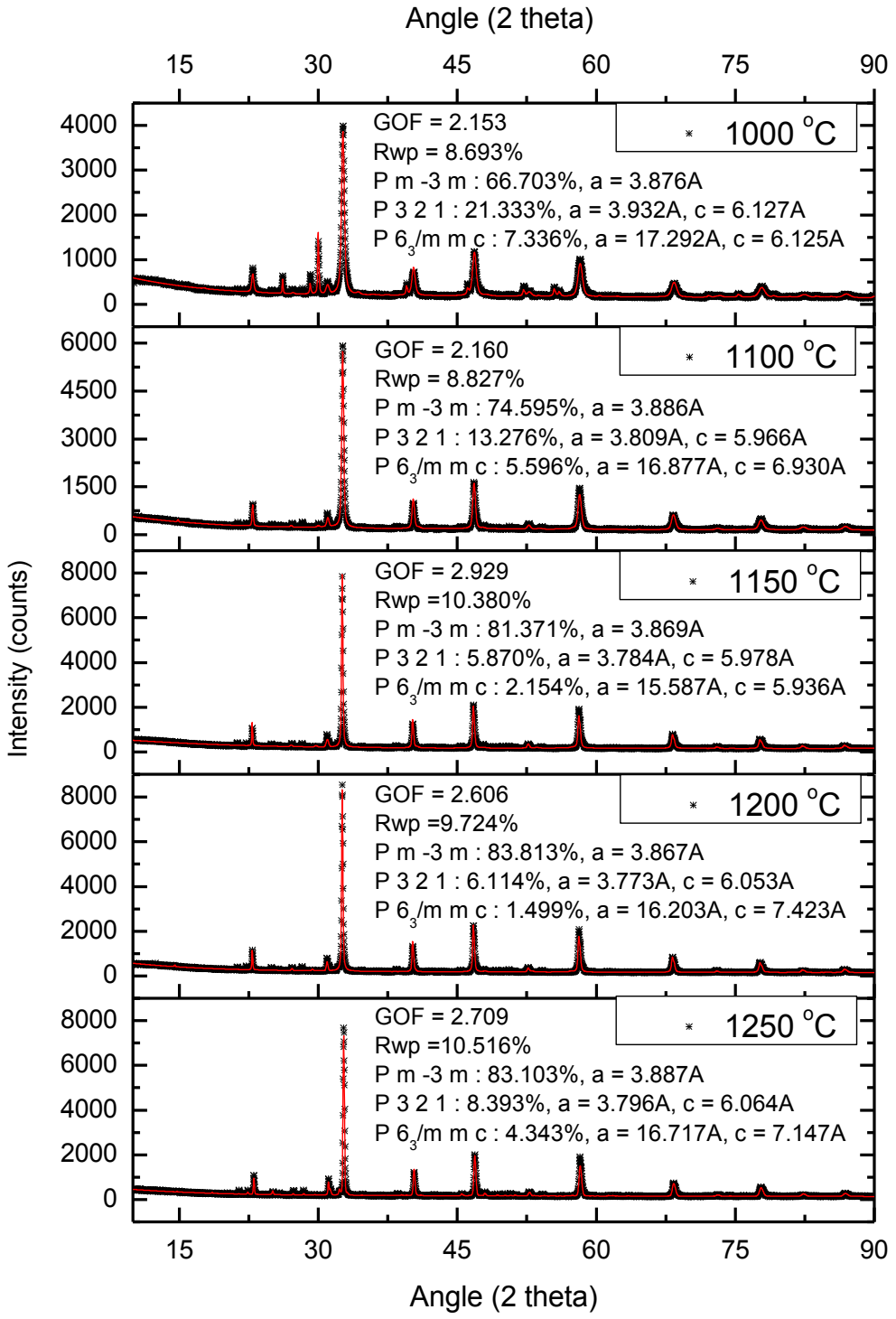

Figure IV 15 - Rietveld refinements of $La_{0.7}Ca_{0.3}Ti_{0.5}Mn_{0.4}Ni_{0.1}O_3$ calcined at 1000 °C during 5 hours, at 1100, 1150, 1200 and 1250 °C during 10 hours in air (from the bottom to the top respectively) together with estimated 5% tolerance purities

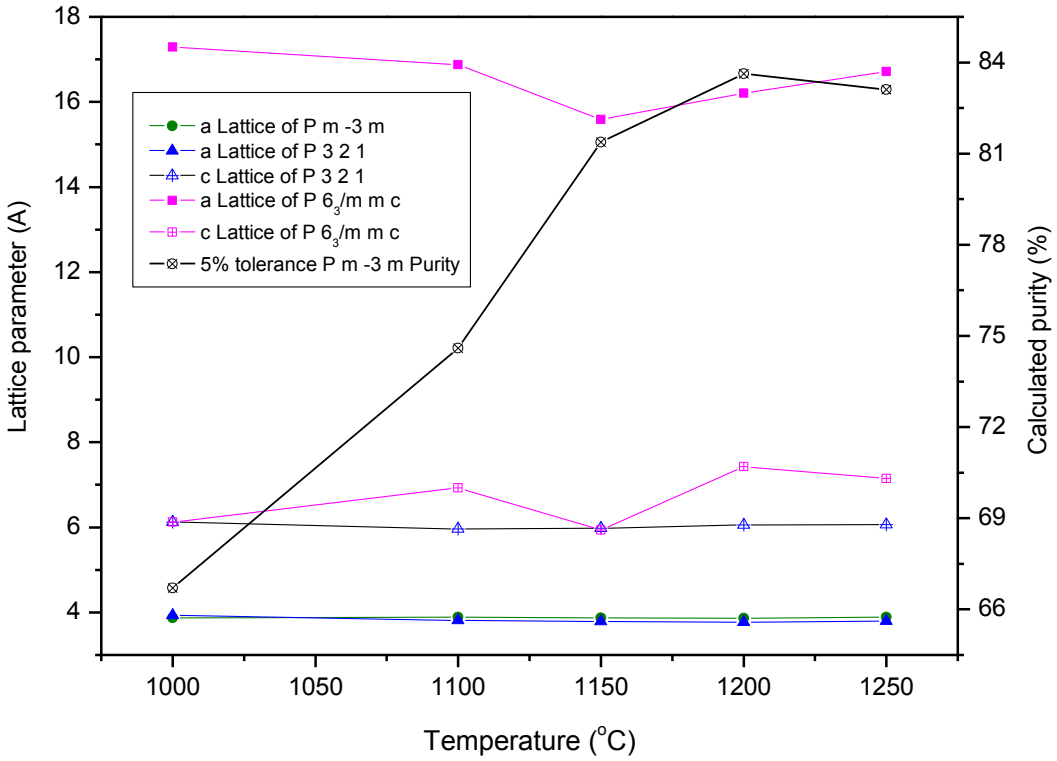

Figure IV 16 – Perovskite calculated purity with 5 % of peak matching tolerance and estimated P m -3 m lattice parameter of $La_{0.7}Ca_{0.3}Ti_{0.5}Mn_{0.4}Ni_{0.1}O_3$ powder along with the calcination temperature

The P 3 2 1 space group displays no volume absolute differences higher than 7.540%, but the P 6_3/m m c cell seems to be highly affected in the sample calcined 1150 ºC (Figure IV 17). The resultant unit cell volume of the considered P 3 2 1 phase roughly follows the P m -3 m's constant behaviour around its average (of 88.086 Å^3), however P 6_3/m m c's reveals the abnormal value in the middle calcination temperature (which corresponds to a strong shrinkage of more than 20 %). Obviously, this high shrinkage ratio was somehow expected from the fact that this sample contains both the lowest values in each of the lattices, however, this phenomenon seems to not be correlated with any other variable, since the closer candidates are the minimum and maximum estimated ratios of the P 3 2 1 and amorphous phases respectively at these calcination conditions (Figure IV 17). These impurity minimum and maximum values cannot be assertively correlated with the P 6_3/m m c volume shrinkage since they correspond to small differences from the average of 5.127 and

3.705 % respectively. Still in these conditions, the P 3 2 1 unit cell volume also reaches its minimum value (of 135,215 Å^3), but the shrinkage ratio from the average (of 2.893 %) is still too small to be considered a reason outputting the P 6_3/m m c volume shrinkage of more than ¼ of its average (751.019 Å^3) showing a value of 549.185 Å (Figure IV 17).

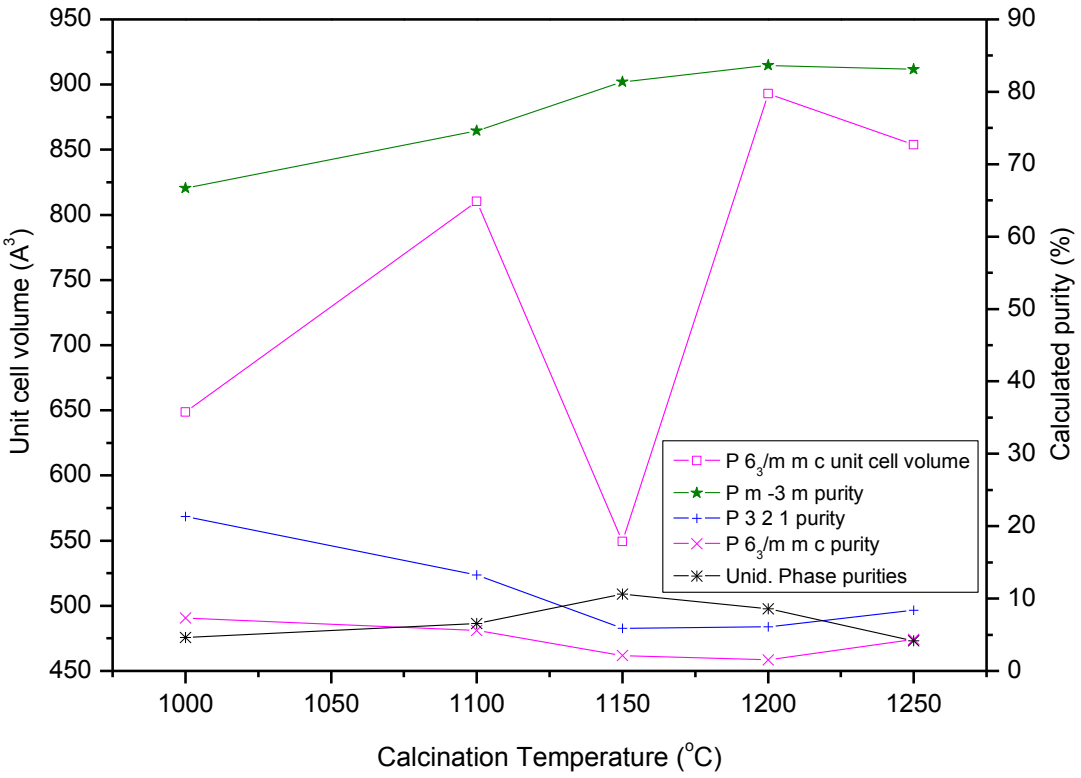

Figure IV 17 - P 6₃/m m c's unit cell volume (in Å³) and average phase ratios considering 5% of matching tolerance along with the calcination temperature (in ºC)

The refinement parameters provided overall acceptable results, notwithstanding, it should be acknowledged that in order to obtain a more precise answer regarding the best calcination conditions, a smaller gap of temperatures which leads to a higher number of XRD refinements can always take place in order to produce a more accurate analysis of the structural implications that this variable carries. Still, for further understanding the nature of the impurities, the given analysis serves its purpose and points the direction of possible further improvements. The highest attempted temperature (of 1250 ºC) seems to establish that (with the

presented strategy) the best achievable purity is not located at any higher temperatures. The way the main perovskite phase peak intensity evolves along with the temperature (with 7577, 8123 and 7174 counts at 1150, 1200 and 1250 ^{o}C respectively) could mislead that slightly better purity results are achieved somewhere in first gap of calcination temperatures (between 1150 and 1200 ^{o}C). Notwithstanding, the perovskite average purity tendency (of 81.371, 83.813 and 83.103 % at 1150, 1200 and 1250 ^{o}C respectively) once more shows that a higher intensity scale in the perovskite main peak does not necessarily mean this phase presence is stronger within the sample. Even though this theoretical highest degree of perovskite purity is more precise, it should not be forgotten that it is simply outputting a balance between the largest possible intensity scale (governed by the P m -3 m space group strongest peak) while displaying the lowest number of counts in the secondary impurity peak phases.

3.4.2 Optimum calcination temperature of LBTMN

Regarding the LBTMN powder, all the temperatures of 1000, 1100 and 1250^{o}C consistently revealed strong agreement results of R_{wp} (such as 8.776, 7.503 and 8.401) as well as GoF (equal to 1.706, 1.364 and 1.405 respectively presented in Figure IV 18). Perhaps a flawed naked eye observation already suggests the higher calcination temperature seems to provide higher structural purity results because it seems that the problematic zone between the first and the second perovskite peaks is more confined to follow the red line of the model, which results in a flatter residual graphic.

The calculated impurity percentages (of 76.443, 97.021 and 99.147%) in each of these 3 temperatures (of 1000, 1100 and 1250 ^{o}C respectively) reveal an obvious increasing tendency (Figure IV 19). However, the superiority of the agreement parameters in the calcination temperature of the middle sample as well as the fact that its intensity count scale reaches a higher value, might mislead to a flawed conclusion to nominate this specimen as the purest (Figure IV 18). As it was previously mentioned, a superior number of counts in the highest pattern peak defines the intensity scale, which is in fact proportional to the weight fraction of that phase [139] - [140], nevertheless, the highest impurity peak is also stronger, decreasing the overall estimated purity of this specimen comparatively to the powder calcined at 1250 ^{o}C. The middle specimen calcined at 1100 ^{o}C provides the best refinement

agreement parameters, but it does not reveal itself as the one with the strongest cubic phase presence. Instead, the powder calcined at highest temperature is in fact the one holding the highest P m -3 m space group estimated purity value (Figure IV 19).

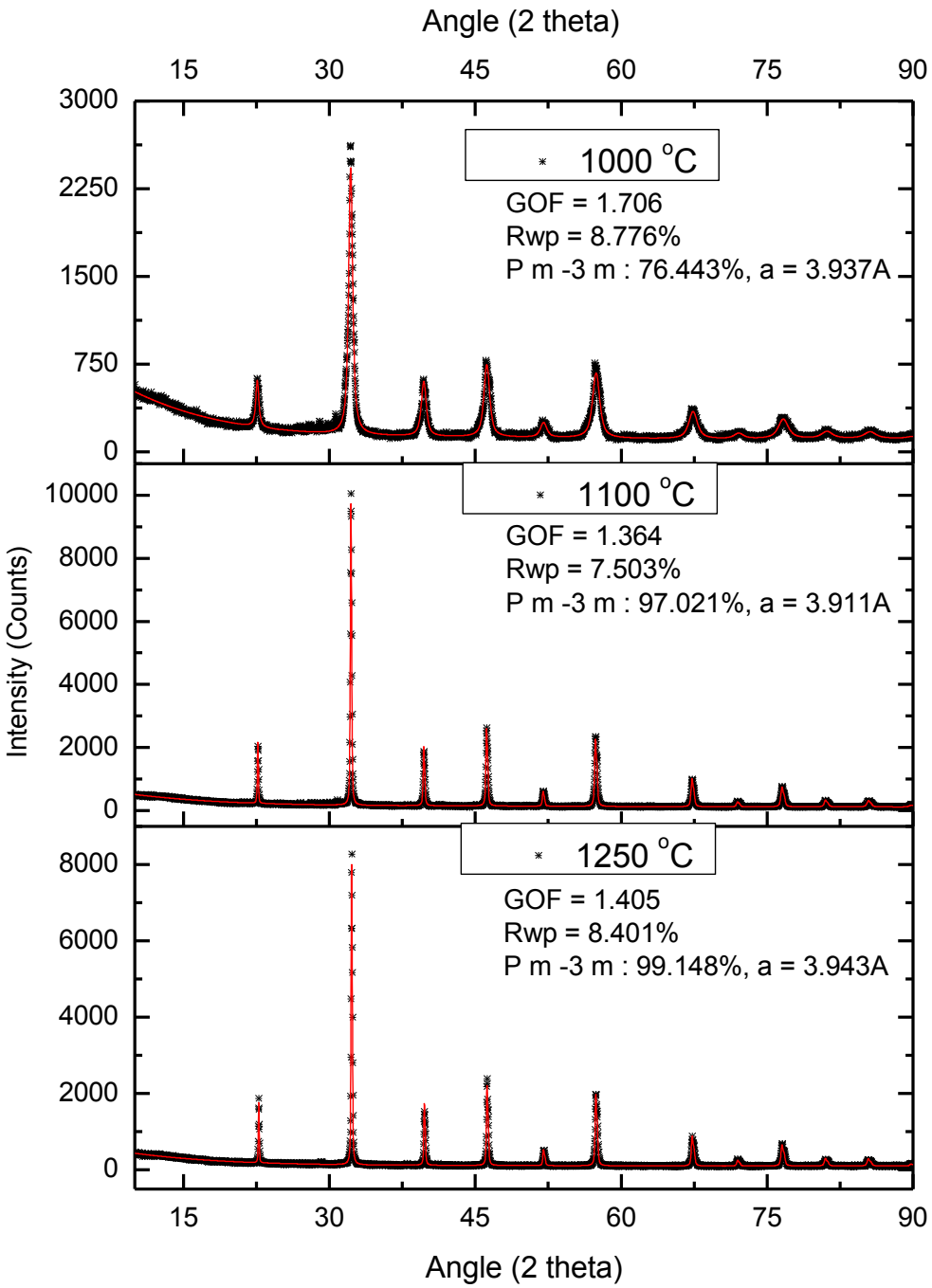

Figure IV 18 - Rietveld refinements of $La_{0.7}Ba_{0.3}Ti_{0.5}Mn_{0.4}Ni_{0.1}O_3$ calcined at 1000 ºC during 5 hours (A), 1100 ºC during 10 hours (B) and 1250 ºC during 10 hours (C) in air together with estimated 5% tolerance purities

Though the calculated average purity levels of LBTMN are much higher than the samples doped with Calcium, the cell lattice parameter shows much higher standard deviations. A slightly shorter edge of 3.911 in the calcination temperature of 1100 ºC represents a shrinkage of 0.478% from the average value of 3.930 Å (Figure IV 19). Among the literature, the unit cell volume with high calcination temperatures in oxides can display both ascendant and descendent tendencies [204] - [209] and the same can also be stated while confining the considered oxides to perovskites only [210] - [216]. It was even possible to find a report where a perovskite oxide with the same elements of Barium and Titanium seems to have no lattice variation at all along with the calcination temperature [217]. Considering the similar calcination temperatures of 1000, 1100 and 1200ºC found in this publication, the roughly constant tendency is observed. It should be noted that these lattice parameter values do not vary as much as the synthesized perovskites of LBTMN or LCTMN, however, this trend type seems to have been consistently reported among literature allowing therefore the acceptance of the minor length deviations of less than 0.5% in either Barium or Calcium doped perovskites.

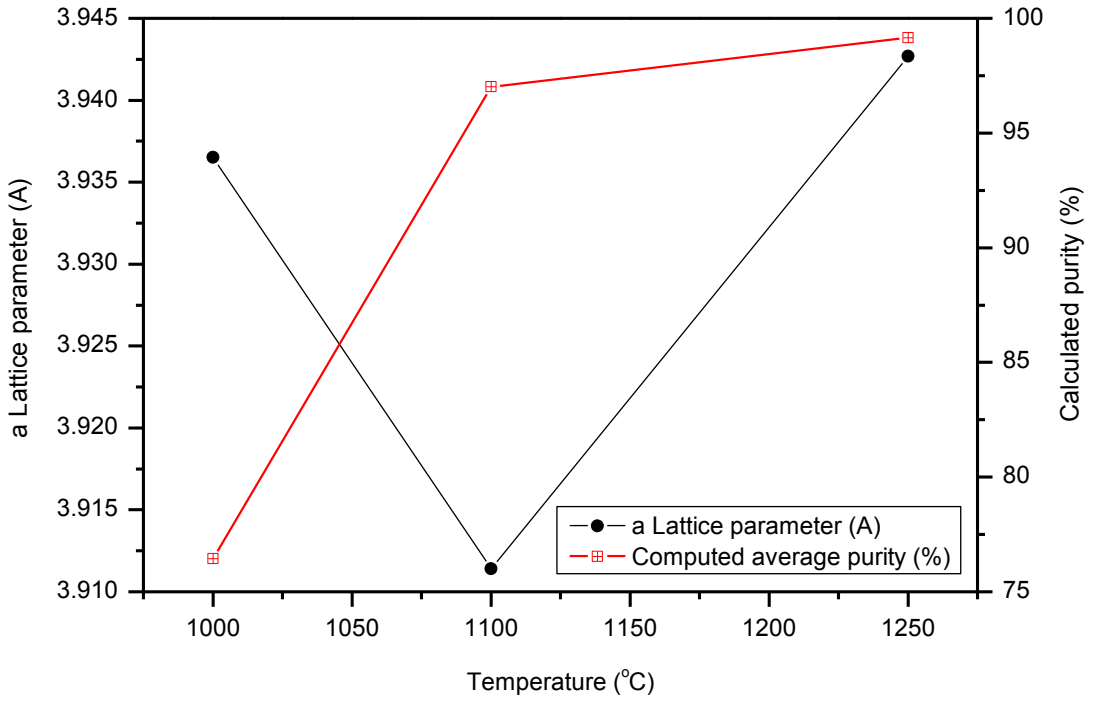

Figure IV 19 - Perovskite computed average purities and estimated P m -3 m lattice parameter of $La_{0.7}Ba_{0.3}Ti_{0.5}Mn_{0.4}Ni_{0.1}O_3$ powder along with the calcination temperature in (ºC)

Just like in LCTMN, further calcination temperatures could also take place in order to establish the optimum conditions to form this perovskite structure, however, the calculated purity level is already much higher than LCTMN and the cathodic performances observed in the previous chapter are incredibly similar. For this reason, no further time was invested into the optimization of this perovskite, instead, understanding the Calcium impurity properties became much more relevant as a scientific contribution.

The highest estimated purity of LBTMN was found at a calcination temperature of 1250 ^{o}C, nevertheless the perovskite intensity peaks are already decreasing in comparison with the profile obtained in the previous calcination temperature of 1100 ^{o}C. From this fact, the best purity value for the LBTMN is expected to be found somewhere between these two calcination temperatures, where the optimum balance between a low intensity of impurity phases and a high perovskite intensity peak can be found.

4. HAADF-STEM analysis

4.1 Element mapping and EDS results

The STEM analysis provided a deeper understanding regarding the different segregation tendencies observed among both specimens. Comparatively to LCTMN, the scanned Barium perovskite particles (Figure IV 20) displayed an overall higher element homogeneity as well as less Nickel segregation tendency, however some nanoparticles can still be found. Considering the applied reducing treatment conditions (of 800 ^{o}C during 10 hours), following Nickel Gibbs energy variation (of $|\Delta G_{red}|$=288.565 kJ.mol^{-1}), Manganese contains the closest value regardless of the considered states of oxidation in comparison with any other perovskite element. This might be the reason behind having the Manganese elemental mapping to be the second less homogeneous among the remaining 5.

Further EDS characterization took place in two different areas of the same LBTMN particle E (Figure IV 21). This allowed the evident observation of the spectre differences between the respective segregated Nickel nanoparticle and the remaining equally dispersed element distribution. Not only the obtained spectres reveal the evident Nickel peak difference as well as they seem to agree with the previously stated principle of the Manganese to be the closest element to be reduced

(considering the Gibbs energy variation) from the fact that the second highest peak in the segregation area spectrum is around the energy value of 5.88 eV.

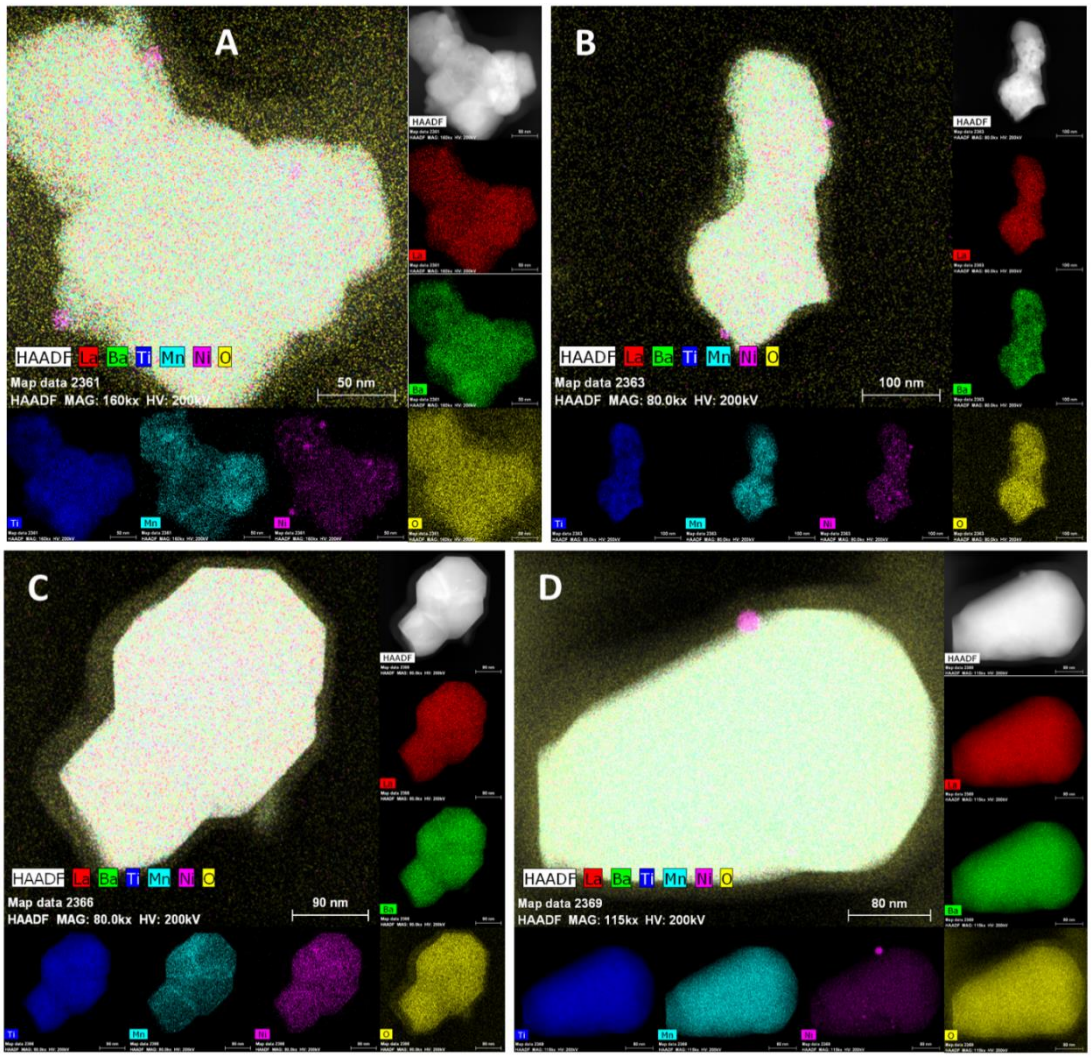

Figure IV 20 - Element mapping of $La_{0.7}Ba_{0.3}Ti_{0.5}Mn_{0.4}Ni_{0.1}O_3$ particles A, B C and D

Analogously, the respective elemental mappings of LCTMN particles were also obtained (Figure IV 22). Most Calcium perovskite particles reveal lack of homogeneity even in elements where the segregation is not intended. This agrees with the previous purity estimations from the X-ray analysis (in section 3.2.2) where the LCTMN structure revealed itself as being much more sensitive once submitted to reducing conditions. On the other hand, lesser agreement with the X-ray results is also found through the mean particle size estimations from the Scherrer formula

(Equation IV 2). Despite providing the expected lower value in the Calcium perovskite, the averages of 82 and 17 nm (for LBTMN and LCTMN respectively) are found to be underestimating the observed dimensions of the 5 particles in each specimen.

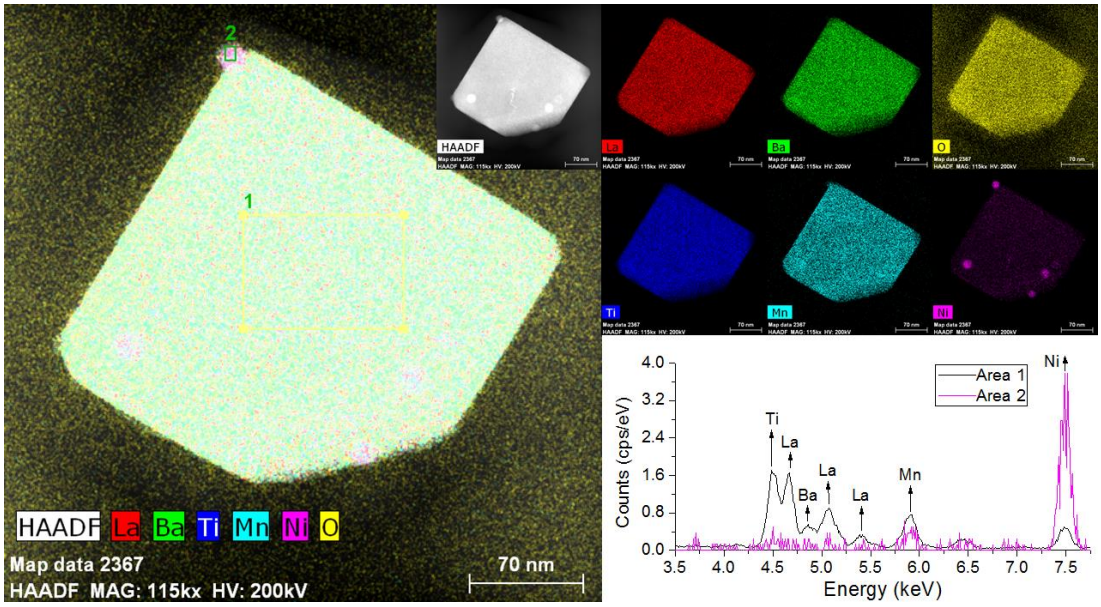

Figure IV 21 - Element mapping of $La_{0.7}Ba_{0.3}Ti_{0.5}Mn_{0.4}Ni_{0.1}O_3$ particle E and EDS spectrums

After a careful observation, there seems to be a tendency for the larger and smaller cations of each perovskite site to share a similar dispersion image (respectively Calcium mapping being similar to Manganese's and the same similarity between Lanthanum and Titanium). This fact (which is particularly evident among the scanned LCTMN particles C and D) seems to also be slightly present among some of the Barium perovskite particles (A and B), however, in this case, Barium is now the A site larger cation sharing its mapping resemblance with Titanium. At this point, the LCTMN's stronger tendency for Nickel segregation is evident and even though this instability might be considered unexpected, it is very likely to be increasing the catalytic activity for fuel oxidation, improving this way the anodic performance.

An EDS spectrum was also obtained in an LCTMN particle (Figure IV 23) where the Nickel peak (around 7.5 eV) is clearly seen. In the selected area 2 (where Nickel is exsolved), the Manganese respective peak intensity seems to be similar as seen with the previous LBTMN specimen, however the different A site cation seems to display a slightly higher peak in comparison with the respective Barium one. This Calcium presence among the Nickel segregation spectrum area could suggest that

this A site element partially segregates under reducing conditions originating structural instabilities that consequentially facilitate the intended Nickel segregation. Calcium's slightly larger electronegativity (of 1) comparatively with Barium (with is 0.89) also supports this possibility to explain this alternative order of events. On the other hand, since the Gibbs energy for Calcium reduction is larger than the one required for Barium or even Lanthanum, then it is also possible that the formation of Nickel nanoparticles would consequently promote some Calcium segregation due to it not being large enough to hold the A site of the perovskite structure together with Lanthanum in a B site deficient scenario. With this in mind, the LBTMN perovskite might also be able to better hold its structure not simply because of its lower Nickel segregation tendency, but also due to the fact that Barium larger ionic radius can probably compensate the lack of B site content (while also being a lesser electronegative perovskite element). That being said, the higher tendency for Nickel ex-solution in LCTMN material can either be the cause of the weaker perovskite structure under reducing conditions or its consequence. In-situ analysis can potentially clarify the order of events so that the mechanisms involved in these materials are further understood.

Another idea supporting the superior LCTMN segregation tendency is found through Goldschmidt (Equation I 1) tolerance factor values for both perovskites with and without Nickel. The average value of the LBTMN factor (0.98899) is closer to 1 comparatively to the LCTMN (0.96073). In a simple approach to consider a complete ex-solution, which means the resultant perovskites would become B site deficient (LAemTM), the resultant average factors of 1.03375 and 1.00421 (for LBTM and LCTM respectively) reveals that both values move closer to 1. Since previous sections of this chapter successfully matched both perovskites with a cubic structure (with the P m -3 m space group), then if a factor of 1 is assumed to be the optimum value of stability, the relative distance from this (assumed to be) point of optimum stability should indicate how stable the perovskite is. Calculating the difference between the distances to 1 in both scenarios with and without Nickel (Equation IV 3), a humble reasoning rises up. The idea behind this rough concept is to understand which one of the tolerance factor scenarios (of with and without Nickel) contains the smallest distance to 1 so that the favourability of the segregation event can be presumed as favourable ($S>0$) or not ($S<0$). Barium and Calcium perovskite reveal the values of -0.023 and 0.035 respectively, which according to this modest vision, it would exactly fit the obtained results where the segregation tendency is clearly higher in LCTMN. Yildiz B. et all [218] studied the segregation tendencies of A site dopants

of Barium and Calcium in similar perovskites (of $La_{0.8}Ba_{0.2}MnO_3$ and $La_{0.8}Ca_{0.2}MnO_3$) and this systematic work also experienced the lowest extent of segregation in Calcium element, which had the smallest mismatching size. Introducing 50% of Titanium, enlarges the average B site radius, making it so that the Barium perovskite has a superior matching size between both sites as the tolerance factor already suggests.

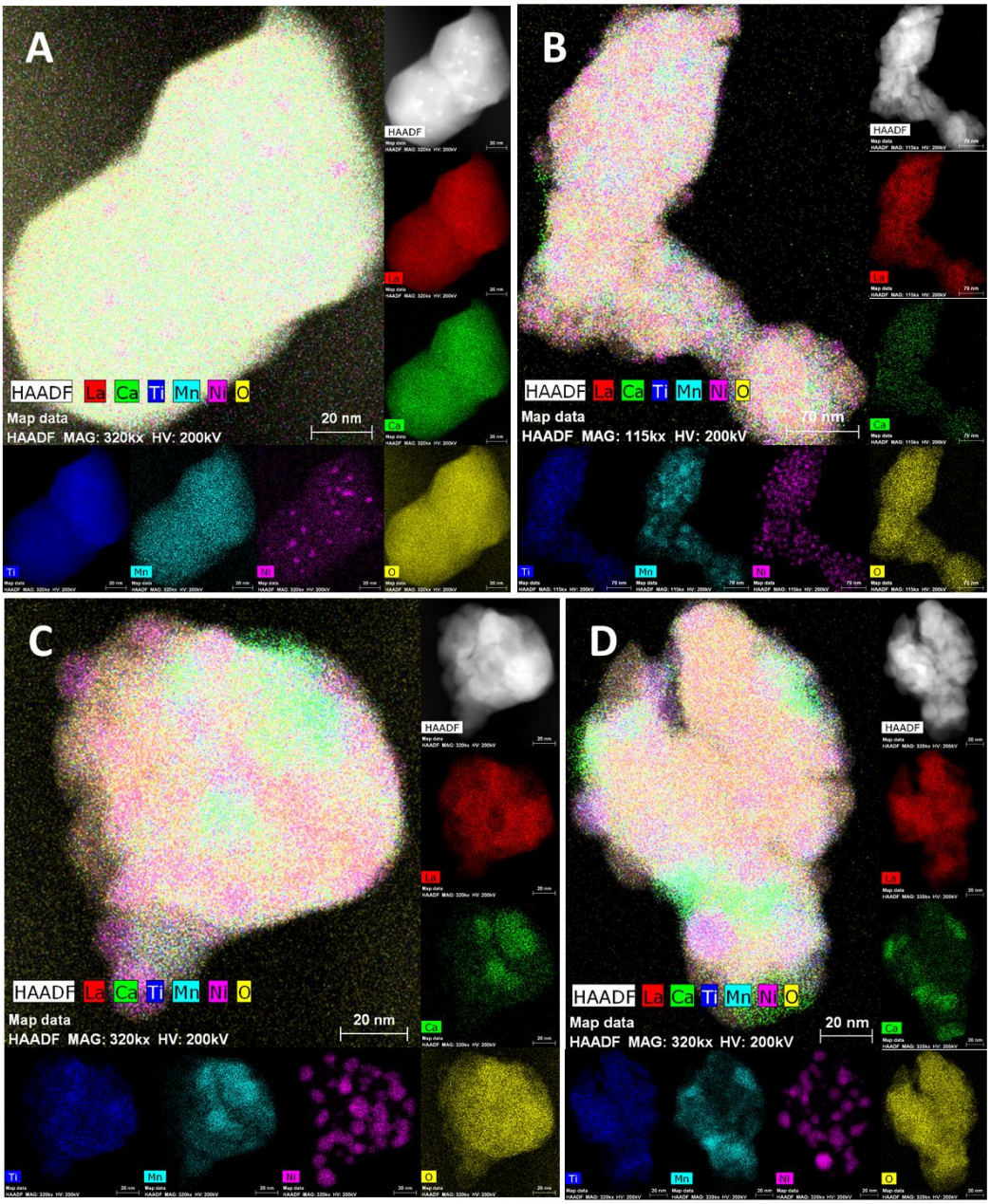

Figure IV 22 - Element mapping of $La_{0.7}Ca_{0.3}Ti_{0.5}Mn_{0.4}Ni_{0.1}O_3$ particles A, B C and D

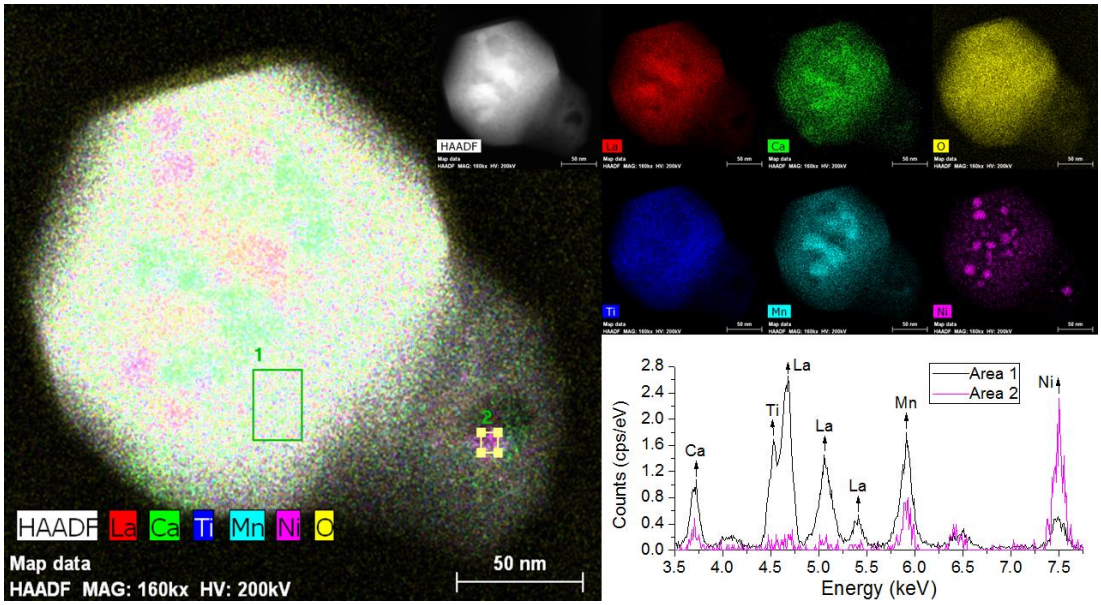

Figure IV 23 - Element mapping of $La_{0.7}Ca_{0.3}Ti_{0.5}Mn_{0.4}Ni_{0.1}O_3$ particle E and EDS spectrums

It should be mentioned that the Goldschmidt tolerance factor has been reported to accurately predict the perovskite formation with a success rate of 83% for oxides in the form of ABO_3 [219]. Understanding the limitations of this approach, Bartel C. J. et al. [219] recently has contributed with a new tolerance factor formula where now the A site state of oxidation is also factored in. The proposed new formula (Equation IV 4) was reported to improve the prediction accuracy to 92% for oxides, indicating a perovskite formation for values of $\tau_{new}<4.18$, however further experimental agreement (of 100% from 152 compounds) is obtained if the τ_{new} gap is decreased to values within $\tau_{new}<3.31$ (and $\tau_{new}>12.08$). Further agreement with the LAemTMN materials (where the calculated τ_{new} average values of 2.41 and 2.52) as well as their corresponding total segregation scenarios LAemTM with values of 2.65 and 2.67 always verify this condition. According to the source, the probability of being a perovskite decreases as τ_{new} increases, which means that both perovskites are predicted to become less stable under reducing conditions. Since this variation is not linear, the same analysis used previously to attempt to comparatively quantify the amount of stability loss is automatically discarded. In another words, the fact that the new tolerance factor differences "$\Delta\tau_{new}$" are larger in the Barium perovskite (τ_{LBTM}-$\tau_{LBTMN}<\tau_{LCTM}$-τ_{LCTMN}), does not mean the stability loss is grater comparatively to the Calcium one.

$$S = |1 - t_{LAemTMN}| - |1 - t_{LAemTM}|$$

Equation IV 3 - Segregation tendency "S" where "$t_{LAemTMN}$" and "t_{LAemTM}" are the tolerance factors for the perovskites with and without Nickel respectively with dimensionless units

$$\tau_{new} = \frac{r_X}{r_B} - \left(n_A - \frac{{}^{r_A}/_{r_B}}{ln\left({}^{r_A}/_{r_B}\right)} \right)$$

Equation IV 4 - New tolerance factor "t_{new}" where r_X, r_A, r_B and n_A are respectively the anion, A site and B site cation radius and the A site oxidation state [219]

4.2 FFT reciprocal space pattern phase matching

Further agreement was found with the XRD cubic phase through matching the FFT pattern of the LBTMN particle D in 2 distinct areas (Figure IV 24). The perovskite pattern remains perfectly identifiable in both areas, however some of the remaining points can be matched with both Nickel and Nickel oxide cubic structure planes of diffraction. One particular inter-planar distance in the nanoparticle pattern solely matches the d spacing 2.02 Å of the known family of [1 1 1] hkl planes in the cubic diffraction peak of the F m -3 m cubic space group (number 225). This fact suggests that the most reasonable interpretation to be considered might be that both cubic phases co-exist, meaning that the Nickel nanoparticle would be surrounded by an oxide layer. Both Nickel and Nickel oxide considered lattices (of 3.52 and 4.18 Å respectively) are well established among literature results [220] - [231], therefore both scenarios are presented.

Regarding the Calcium perovskite it was not possible to find a clear perovskite lattice match in an area of Nickel segregation. This fact supports the previous cause effect explanation, not entirely supporting the order of events (where the segregation occurs first followed by the consequent structure partial collapse), but providing agreement to the statement that both events are very likely to be entwined. Obviously the fact that a segregation zone together with a well-defined perovskite lattice was not found within the same FFT pattern among the scanned particles does not mean that such observation might be impossible, however this reality sadly seems to counter argue the previous concept of segregation tendency (Equation IV 3) explained in the previous section 4.1. Following this hypothesis, the segregation event

can simply be explained through the fact that Nickel is the element that is easier to be reduced (with lower $|\Delta G_{red}|$ value). Regardless, an FFT pattern in a Nickel nanoparticle area was successfully matched with the Nickel structure (Figure IV 25), however this time no other phases were identified.

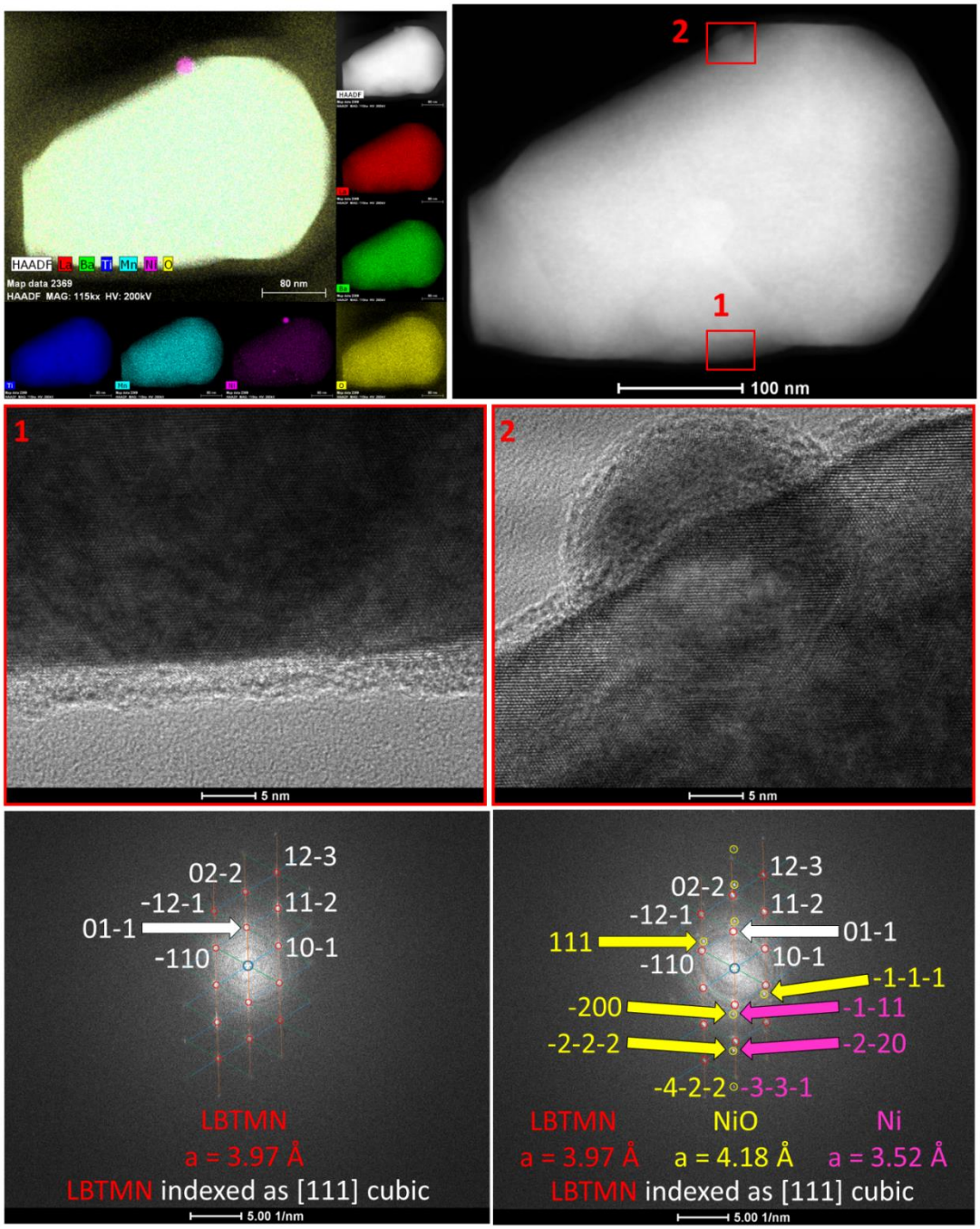

Figure IV 24 - FFT patterns of LBTMN particle D in an area (1) without Nickel segregation and (2) with Nickel segregation

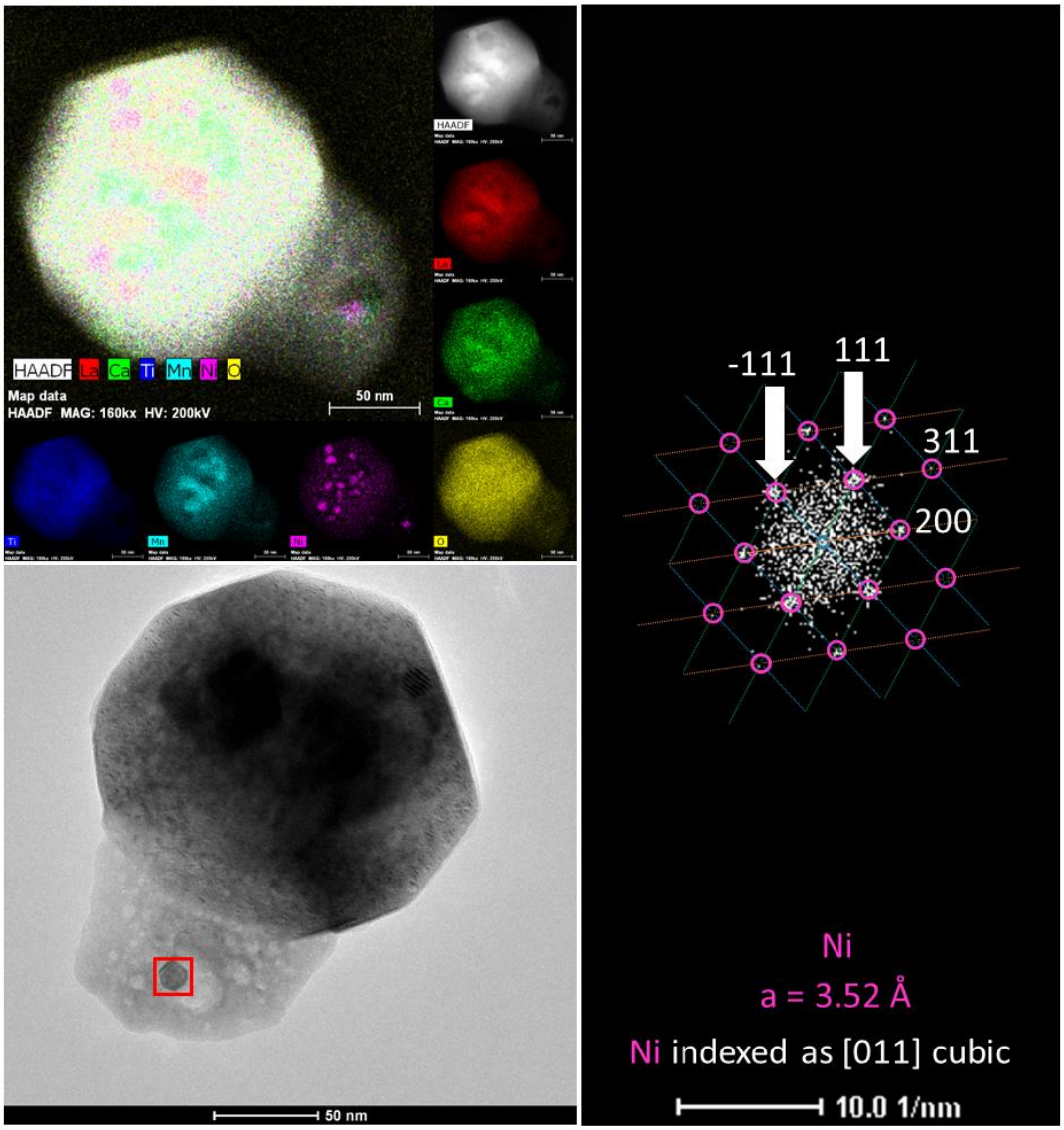

Figure IV 25 – FFT pattern of LCTMN particle E in an area with Nickel segregation

5. Summary

The Rietveld refinement method was successfully implemented. The lattice parameter values obtained from the data profiles of the benchmark materials of BSCF cathode (3.983 Å) and SDC electrolyte (5.430 Å) match the literature results ([157] - [167] and [168] - [177] respectively). To compile this chapter's results, all the relevant information regarding both electrode chemical stabilities as well as the brief calcination temperature optimization in function of the estimated purities can be found in the Table IV A1 and Table IV A2 in the Appendix.

The chemical stability of both lanthanide perovskites was studied in both oxidizing and reducing atmospheres and also varying the presence of the electrolyte material. From these refinements there seems to be no reactions between any of the electrodes and the electrolyte regardless of the surrounding atmospheric conditions. However it was found that not all the lanthanide oxides seem to be stable under both atmospheres. LBTMN provided a much superior structural stability under both environments always displaying purities above 97%. LCTMN however, not only its purity was estimated to be much lower (74.595%) after calcination (at 1100 ^{o}C) as it further decreases (to 42.92%) after submitted in hydrogen for 2 hours at 800 ^{o}C. These results are totally unexpected from the fact that in the previous chapter LCTMN cells provided superior performances comparatively to LBTMN and this difference was concluded to come from the anode performance. Since the perovskite structure decreases its purity under reducing conditions but its performance is superior than LBTMN, than the structural impurities can be benefitting the anodic behaviour.

Based on the purity estimation tendencies along with the calcination temperatures of the refined profiles, the highest perovskite purities of LBTMN and LCTMN are expected to be located in the intervals from 1100 to 1250 and 1200 to 1250 respectively. Given the fact that Barium perovskite purity is already much higher comparatively to LCTMN and its improvement is capped at less than 3% at best, it becomes less relevant to decrease the optimum calcination temperature gap. From the fact that LCTMN displayed better performances comparatively to LBTMN while displaying much lower purities in both environments, it becomes more valuable to understand the natures of these impurities and how their electrochemical proprieties are affecting this electrode performance. Within this topic, an improvement of 9% in the LCTMN purity level might be enough to understand the performance implications in future studies between the different calcination temperatures of 1100 and 1200^{o}C.

The HAADF-STEM analysis clearly shows higher homogeneity of element dispersion as well as the existence of a perovskite phase in both zones with and without Nickel segregation in the Barium perovskite which agrees well with the previous X-ray results (displayed in this chapter's section 3). The LCTMN compound on the other hand, seems to have a larger tendency to segregate the Nickel element out of the structure which can possibly explain the performance gain (through catalytic activity increase for fuel oxidation). The concept of segregation tendency was explored through simply observing the tolerance factor distances to 1 in both materials together with both scenario considerations of having no Nickel and no

segregation. This aspect, together with the theoretical larger Gibbs energy required to reduce Calcium followed by Barium's larger cation radius (to better hold the perovskite in a B site deficiency occurrence) constitute plausible arguments to support that the superior segregation of Nickel is the driving force of LCTMN structure degradation. However, the fact that it was not possible to find an FFT perovskite pattern together with a zone of Nickel segregation, may also mean that the segregation event does not occur to stabilize the structure of the perovskite, but rather to stabilize the elements into different structural arrangements which might also be more stable under the reducing conditions.

Further attempts to find reasoning behind the LCTMN higher segregation tendency over LBTMN took place through X-ray photoelectron spectroscopy (XPS) analysis (Figure IV A1 and Figure IV A2). These results proved to be inconclusive from the fact that the nickel lower states of oxidation binding energies of 852.6 and 856.6 eV overlap with the lanthanum typical peaks of $3d_{3/2}$ (Figure IV A1 – A and E and Figure IV A2 – B and E). In order to avoid this overlap, the intensity of the binding energy gap (roughly from 75 to 65 eV) was also captured, however the signal is too noisy (Figure IV A2 – C and F) in order to allow the proper Nickel 3p peak identification (which is expected to be located nearby 67.6 eV).

Chapter V - Conductivity

1. Introduction

To investigate a possible source regarding the performances of the materials observed in chapter III, this chapter provides the fundamental knowledge to understand the upcoming conductivity analysis under both reducing and oxidizing atmospheres. The four probe method followed by the activation energy (Ea) estimation from the conductivity measurements was firstly applied to the BSCF ($Ba_{0.5}Sr_{0.5}Co_{0.8}Fe_{0.2}O_3$) cathode material, where good literature agreement results were obtained. The strategy was then analogously implemented in the $La_{0.7}Aem_{0.3}Ti_{0.5}Mn_{0.4}Ni_{0.1}O_3$ (LAemTMN) perovskite materials (where Aem = Ba or Ca) using both ln(σ) and ln(σT) approaches to attempt to bring up the possible reason regarding their the anodic performance discrepancy (found in Chapter III).

1.1 Fundamental theory

In chapter III, considerable differences in the polarization resistances of the presented perovskite electrodes were spotted. Since conductivity is an important propriety influencing the performance, it became extremely relevant to understand if this propriety is limiting the performance of the LBTMN ($La_{0.7}Ba_{0.3}Ti_{0.5}Mn_{0.4}Ni_{0.1}O_3$) and LCTMN ($La_{0.7}Ca_{0.3}Ti_{0.5}Mn_{0.4}Ni_{0.1}O_3$) materials comparatively to the pattern electrodes of BSCF cathode and NiO+SDC anode.

Conductivity is the parameter that quantifies how easy it is to transmit charge carriers through a certain material, however, there are different mechanisms to describe the thermal behaviour of this variable [178]. According to the band theory ohmic conduction, it can be described as a relation between the drift current density and the electric field ($\sigma=J/E$). The drift current density can be written as a function of the electric field, the mobility and the charge carriers' concentration/density ($J=q¢\mu E$). Combining these 2 equations it is possible to obtain a relationship between the conductivity and both the charge carriers density and mobility (Equation V 1). Conductivity can also be seen as the reciprocal of resistivity "ρ", which as the name suggests, quantifies the ability to resist to the flow of an electric field ($\sigma=1/\rho$).

$$\begin{pmatrix} \sigma = \frac{J}{E} \\ J = q.₵.\mu.E \end{pmatrix} \Rightarrow \sigma = q.₵.\mu$$

Equation V 1 – Conductivity relationships where "σ", "J", "E", "q", "₵" and "μ" are the conductivity, the current density, the magnitude of the electric field, the carrier/elementary charge constant, the carrier concentration and the mobility (respectively in $S.m^{-1}$, $A.m^{-2}$, $V.m^{-1}$, C, m^{-3} and $m^2.V^{-1}.s^{-1}$)

From Einstein's law of diffusion (Equation V 2) it is easy to understand that increasing the temperature will decrease the mobility, simply because all the remaining parameters are constant. In order to better explain this thermal tendency, mobility can be presented in function of the average time between two carrier collisions (also called as the relaxation time) and the effective mass (Equation V 3). Since the temperature increases the frequency of carrier collisions, then the average time between each collision ("τ") decreases. This relaxation time decreasing tendency along with the temperature is commonly taken as the main contribution to lower the mobility since in most practical cases the effective mass is considered to be constant [232].

$$D = \frac{k_B.T}{q}\mu$$

Equation V 2 – Einstein law of diffusion where "D", "k_B" "T", "q" and "μ" are the diffusion coefficient, Boltzmann constant, temperature, carrier/elementary charge constant and the mobility (usually respectively in $m^2.s^{-1}$, $J.K^{-1}$, K, C and $m^2.V^{-1}.s^{-1}$)

$$\mu = \frac{q}{m^*}\tau$$

Equation V 3 – Mobility relation with the relaxation time where "μ", "q" "m^*" and "τ" are the mobility, the carrier/elementary charge constant, the effective charge carrier mass, and the relaxation time (usually respectively in $m^2.V^{-1}.s^{-1}$, C, kg and s)

From the band theory, the energy gap (E_{gap}) between valence and conduction bands is what defines if a material is designated as Insulator (E_{gap} > 4 eV), Semiconductor (E_{gap} < 1.1 eV) and Conductor (where both bands are partially

overlapped). This aspect has consequences in both the conductivity magnitude values (Figure V 1) and thermal tendencies. The existence of an energy band gap generates a negative resistivity temperatures coefficient. Band theory dictates mobility decreases along with the temperature, however as Equation V 1 shows, it is not the only variable affecting the conductivity. The charge carrier concentration ascending behaviour along with the temperature enables a semi-conductor to increase its conductivity along with the temperature despite the decreasing influence of mobility. As Einstein's law of diffusion (Equation V 2) shows, mobility is inversely proportional to temperature, however, the charge carrier concentration variable (in semi-conductors) varies exponentially with the temperature [232]. In a metallic conductor, since there is no energy gap (between valency and conduction bands), the temperature is much less beneficial to the charge carrier concentration improvement because the carriers are already in contact with the conduction band. Therefore, increasing the temperature will decrease the mobility also decreasing the resultant conductivity. The proportional relationship between the mobility and the conductivity/resistivity together with the low charge carrier increase is the reason why metallic conductivities/resistivities can roughly be estimated with linear models (using a temperature coefficient "α" (in K^{-1}).

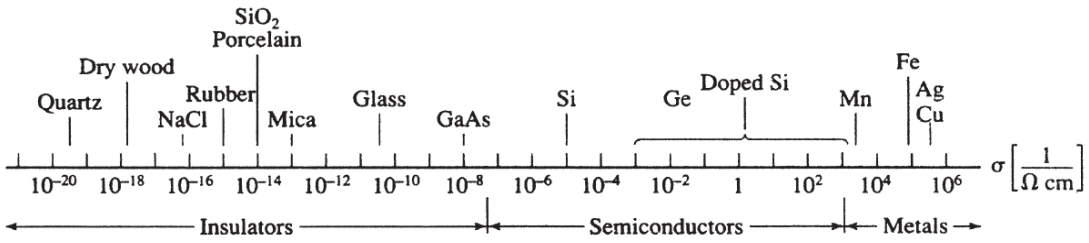

Figure V 1 – Conductivities at room temperature and consequent classifications as Insulators, Semiconductors and Metals [240]

Semiconductors possess two types of electrical conductivity, which are defined by their relative charge carrier species that are transferred through electron excess and electron deficiency mechanisms, accordingly. Since the charge of an electron (by convention) is considered to be negative, if the majority of charge carriers are free electrons, the resultant conductivity mechanism is called n-type (in which "n" simply stands for "negative"). P-type (or Positive-type) conductivity works through the opposite mechanism, in which the majority of the charge carriers are structural

vacancies where electrons can be. These vacancies are called electron holes and are essentially taken as positively charged particles which also propagate themselves in the opposite direction of the electrons (Figure V 2). Usually one of the charge carrier species is dominant over the other, defining this way the type of conductivity, nevertheless, both species coexist. In short, depending on the conductivity type-n/p, the structural atoms consequently release more often free electrons/holes and become positively/negatively charged being defined as donor/acceptor, respectively.

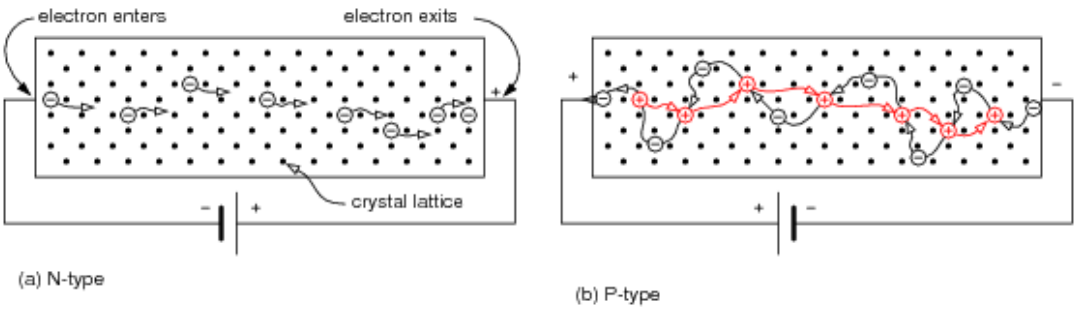

Figure V 2 – Charge transfer scheme of N and P-type electrical conductivities (respectively at the left and right side) [239]

The Seebeck coefficient quantifies the thermoelectric voltage difference within a small temperature gradient (Equation V 4) and can be used to estimate which one of the conductivity types is dominant over the other. A positive coefficient result indicates that p-type conductivity is dominant over the n-type and vice versa. In semiconductors the Oxygen partial pressure variation can also indicate the type of conductivity of a material. If the conductivity benefits from the increase of this variable, typically it dictates that the dominant conductivity type is p and vice versa.

$$Q = -\frac{\Delta V}{\Delta T} = -\frac{V_h - V_c}{T_h - T_c}$$

Equation V 4 – Seebeck coefficient definition where "Q", "ΔV" and "ΔT" are the Seebeck coefficient, the voltage difference between the hot "V_h" and cold "V_c" ends and the temperature difference also between the hot "Th" and cold "Vc" ends (respectively in $V.K^{-1}$, V and K^{-1})

In semi-conductors, the conductivity is usually divided in two or three regions in regards to its thermal tendency [232] - [238]. At lower temperatures, in the

extrinsic/ionization region (where not all structure atoms are ionized), the conductivity increases with the temperature through the increase of charge carriers concentration in the conduction band (Figure V 3). The intrinsic region also displays an ascendant behaviour along with the temperature, though at much higher temperature values, the exponential influence of the charge carriers completely hides the mobility descendent trend and basically rules the conductivity graphical aspect. The main difference between these two regions is the fact that at high temperatures, not only the thermal energy has already excited most of the available charge carriers across the band gap, but it also produces intrinsic charge carriers [238]. Between these thermal regimes, there is a zone of transition (occasionally mentioned as freeze out) where (like in the intrinsic one) most of the structure atoms are already ionized. In this intermediate region, charge carriers can hop to the conduction band, but the thermal energy is still not yet high enough to generate further intrinsic charge carriers. Since most of the structural ions are already ionized, the charge carrier concentration can only increase through generating intrinsic charge careers. In this zone, the mobility decreasing trend along with the temperature can be spotted until thermal energy allows the generation of intrinsic charge carriers.

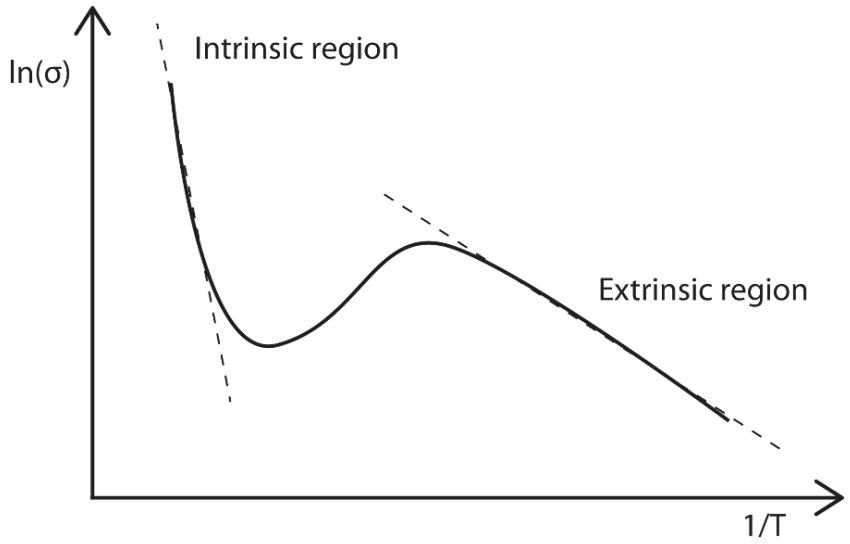

Figure V 3 - Semiconductor conductivity temperature regions [233]

The direct movement of electrons is not the only way to transfer charge from one point to another. Ionic conductivity also provides a charge flow, notwithstanding, as the name suggests, through the motion of ions. Electrons are still traveling through

the structure, however they are aggregated to an ion particle. In the specific case of SOFC, oxide ion (O^{-2}) conductivity is beneficial to electrodes and electrolyte performances. Since the oxide ion carries two electrons, then the elementary charge constant 'q' has to be multiplied by the modulus of this valency state (|-2|). The resultant charge flow and consequent conductivity expressions can this way be adjusted (Equation V 5) to analogously describe the ionic behaviour.

$$\sigma_{ion} = |Z|.F.₵_{ion}.\mu_{ion}$$

Equation V 5 – Ionic conductivity expressions where "σ_{ion}", "|Z|", "F", "$₵_{ion}$" and "μ_{ion}", are the ionic conductivity, the ionic species valence number, the Faraday's constant, the ionic carrier concentration and the ionic mobility, the electric field and the ionic conductivity (respectively in $S.m^{-1}$, dimensionless units, $C.mol^{-1}$, m^{-3} and $m^2.V^{-1}.s^{-1}$)

Since both ionic and electronic conductivities play important roles in the performance of the selected electrodes, it becomes important to acquire information regarding both contributions in order to attempt to understand the reason behind the LCTMN superior anodic performance comparatively to LBTMN. The four probe method allows the estimation of the total conductivity of a specimen with known dimensions. The combination of both Ohm's and Pouillet's laws (I=V/R and $R=\rho l/A$, respectively) dictates the voltage output according to the conductivity of the specimen and the direct current that is applied (Equation V 6). Obtaining the total conductivity values in each temperature enables the calculation of the activation energy and possibly the identification of thermal regimes (such as intrinsic and extrinsic) depending on the relevant consideration. The ohmic conduction mechanism implies that the activation energy value is constant along with the temperature (Equation V 7).

$$\begin{pmatrix} I = \dfrac{V}{R} \\ R = \rho \dfrac{l}{A} \end{pmatrix} \Rightarrow I\left(\frac{l}{A}\right) = V.\sigma$$

Equation V 6 – Ohm's and Pouillet's laws and the resultant linear regression equation for electrical conductivity calculation where "I", "V", "R", "ρ", "l", "A" and "σ" are the current, the voltage, the resistance, the resistivity, the length, the cross-sectional area and the electrical conductivity (respectively in A, V, Ω, $\Omega.m^{-1}$, cm, cm^2 and $S.m^{-1}$)

$$\sigma = q.\mu.¢.e^{\left(\frac{-\Delta G_{act}}{R.T}\right)}$$

Equation V 7 - Ohmic conductivity for activation Energy determination through linear regression, where "σ", "q", "μ", "¢", "ΔG_{act}", "R" and "T" are the ohmic conductivity, the elementary charge constant, the mobility, charge carrier concentration, the activation energy, the ideal gas constant and the temperature, (respectively in $S.m^{-1}$, C, $m^2.V^{-1}.s^{-1}$, m^{-3}, $J.mol^{-1}$, $J.K^{-1}.mol^{-1}$, K)

Despite having the ionic conductivity being known for typically displaying much lower magnitude values (comparatively the ohmic process essentially from the fact that the larger size of the charge carrier turns this mechanism into a slower process), under reducing conditions, the upcoming conductivity results can also be interpreted as a result of a small pollaron hopping conduction mechanism. Considering both scenarios of transport mechanisms, linear regressions of ln(σ) and ln(σT) where then calculated and the consequent activation energies estimated. The non-constant activation energy through the whole range of measurements under reducing conditions demanded the definition of 2 distinct thermal regimes of conductivity. The main difference among the extrinsic and intrinsic conductivity regimes is considered to be the respective constant (Equation V 8) and increasing (Equation V 9) behaviour of the charge carrier concentration along with the temperature. This difference is clearly displayed through the second exponential term which quantifies the generation of extra intrinsic charge careers together with the consequent enthalpy of vacancy formation (which in this case was considered to be 1 eV).

$$\sigma = \frac{c(z.F)^2.D_0}{R.T}e^{\left(\frac{-\Delta G_{act}}{R.T}\right)}$$

Equation V 8 - Extrinsic ionic conductivity for Activation Energy determination through linear regression, where "σ", "c", "z", "F", "D_0", "R", "T" and "ΔG_{act}" are the extrinsic conductivity, the carrier concentration, the valency state of the carrier, Faraday's constant, the diffusion constant, the ideal gas constant, the temperature and the activation energy (respectively in $S.m^{-1}$, $mol.m^{-3}$, dimensionless, $C.mol^{-1}$, $m^2.s^{-1}$, $J.K^{-1}.mol^{-1}$, K and $J.mol^{-1}$) [241]

$$\sigma = \frac{c_{sites}(z.F)^2.D_0}{R.T} e^{\left(\frac{-\Delta G_{act}}{R.T}\right)} e^{\left(\frac{-\Delta h_v}{2k_b.T}\right)}$$

Equation V 9 - Intrinsic ionic conductivity for Activation Energy determination through linear regression, where "σ", "c_{sites}", "z", "F", "D_0", "R", "T", "ΔG_{act}", "Δh_v" and "k_b" are the intrinsic ionic conductivity, latticesites concentration, the valency state of the carrier, Faraday's constant, the diffusion constant, the ideal gas constant, temperature, the activation energy, the enthalpy for vacancy formation and Boltzmann's constant (respectively in in $S.m^{-1}$, $mol.m^{-3}$, dimensionless units, $C.mol^{-1}$, $m^2.s^{-1}$, $J.K^{-1}.mol^{-1}$, K, $J.mol^{-1}$, J and $J.K^{-1}$) [241]

2. Experimental procedures

2.1 Bar synthesis

Using a hydraulic pressing machine, many bars were pressed from both powder compositions tested in the previous Chapter III (from sections 3.3 to 3.5). The LAemTMN ($La_{0.7}Aem_{0.3}Ti_{0.5}Mn_{0.4}Ni_{0.1}O_3$) specimen powders (where Aem= Ba, Ca) were shaped in a rectangular surface of 6.05 × 20.05 mm where 0.6 g of powder will result roughly in a 1.65 mm of bar thickness under a scale pressure of 2 MPa during 50 seconds. These bars were sintered at different temperature conditions starting from 1160 ^oC during 5 hours with a heating rate of 5 ^oC/min and natural cooldown until relative densities were at least above 80%.

2.2 Relative densities of the SDC pellets and bars

The sintering temperature will obviously affect sample proprieties such as porosities and densities. To attempt to choose the best conditions for these samples, these properties were measured before the assembly procedure of the samples occurs. Before measurements took place, the theoretical densities of the chemical compositions were determined using the XRD estimated "a" lattice parameters [242] so that the relative densities from the perovskite XRD refinements could be presented. The bulk densities were determined through the well-known Arquimedes procedure where the Thiensen, Sheel and Diesselhorst equation was used [243] - [244] along with 8 measurements of apparent mass along with the water temperature for accuracy purposes. The LBTMN bars achieved an average relative density of 81.551% calcined at 1160 ^oC during 5 hours, while the LCTMN samples revealed an average of 86.622% and required a calcination temperature of 1200 ^oC in order to firstly hold a water drop on its polished surface, displaying this way the first signs of

a considerable densification level. As for the SDC electrolyte pellets, a much higher average relative density value of 97.134% was displayed after being exposed to the respective higher sintering conditions of 1400 ^{o}C during 5 hours.

2.3 Considerations prior to sample assembly

Before the bars were assembled and tested, some considerations were made in order to decide if the obtained relative densities and the required sintering temperatures would provide meaningful information. Since the conductivity is suspected to be the performance inhibiting factor, it is important for the bar samples to remain within a set of conditions that are not too far from the ones the electrode material had during the performance test.

Three of the main reasons supporting the acceptance of these conditions (in the previous section 2.2) rely mainly on literature results. Since both tested electrodes share elemental similarities with the Lanthanum Strontium Manganese (LSM) state of the art material it becomes relevant to mention the influence of the relative density into the conductivity results. In this relationship, the highest difference of conductivity (obtained at 800 ^{o}C) revealed a loss of 5% with the respective relative densities going from 87.77% to 82.99% [245]. Since these materials are intended to be applied as electrodes for SOFCs, gas diffusion requires porosity so that triple phase boundary (TPB) regions can exist [246], therefore it is also relevant that the conductivity of these materials is measured in similar densities that of the electrodes. The Literature results of other Lanthanum oxides also state that the difference between the apparent and specific conductivities is usually small for relative densities superior than 70% [247].

The LBTMN perovskite purity estimation (of 98.524%) from the XRD analysis of the bar sample sintered at 1160 ^{o}C is consistent with the soft ascendant tendency displayed in Chapter IV section 3.4.2, supporting this way the relevance of the conductivity results. The phase purity calculations regarding calcination temperatures equal or larger than 1100 ^{o}C display small percentage differences, therefore, the conductivity results (with densification conditions obtained at 1160 ^{o}C) are indeed fair approximations. As for LCTMN perovskite, the fact that the densification conditions match the highest phase purity estimation (at a calcination temperature of 1200 ^{o}C as seen in section 2.4), enables the closest values of the main phase conductivity.

Another minor argument in favour of the acceptance of these relative density values is the slightly different thermal expansion coefficient (TEC) between both perovskites. Having the lowest relative density (of 81.551%), LBTMN bars also displayed smaller averages of cross-sectional area and length comparatively to the calcium ones (respectively 5.6837 mm^2 and 15.659 mm against 6.109 mm^2 and 16.079 mm). From the Equation V 6 it is easy to understand the proportionality between the samples dimensional attributes and the extracted conductivity output, in another words, this result is more accurate the larger the sample is. That being said, if higher calcination temperatures would be applied to the LBTMN samples (in attempt to obtain a closer value to the LCTMN specimens relative density), the further shrinkage would then increase the inaccuracy difference among both sample types.

2.4 Bar assembly

Once the sintered bars cooldown to room temperature, silver wires were attached, properly sealed with silver paste so that each sample can be submitted to the oven at 180 ^oC during 30 minutes to complete this sealing procedure. The final step of this phase simply consists in the assembling of the silver wired bars on the sample holder inside the furnace for data collection under both air and reducing conditions along with the temperature variation. The 4 probe method to measure the conductivity is then put into practice using the Keithley 2440 5A source meter to apply current and measure voltage. The data was collected at many temperatures (and at least 3 times at each temperature) so that the average in each point could overall provide a more accurate estimation.

3. Conductivity results

3.1 Under oxidizing atmosphere

3.1.1 BSCF conductivity and activation energy estimation

Analogously with the previous chapter, in order to verify the present methodology procedure, a bar sample of the pattern cathode BSCF was synthesized and tested in air (Figure V 4). Literature data was collected (Table V 1) so that a humble comparison regarding some similarity criteria could happen. The magnitude of the obtained values seems to be overall matching the collected literature results and the same is true regarding the graphic shapes found in these temperature

profiles. The 4 probe method is coexistent among the 11 literature references since it was the used technique. The obtained maximum conductivity value of 44.812 S/cm is very close to the average of these literature results (which is 41.068 $S.cm^{-1}$) only being higher by 9.116%. It must be acknowledged that the relevant standard deviation of this analysis corresponds to a conductivity increase of almost 50 % (where the measured value was reported as 60.45 $S.cm^{-1}$ [250]). The relevant reference fully highlights this aspect while providing a lower maximum value of 55.57 $S.cm^{-1}$ obtained at 409 ºC with a different powder specimen synthetized at pH 4.0, while stating the higher conductivity value is obtained with a respective powder synthesized at a ph of 6.0.

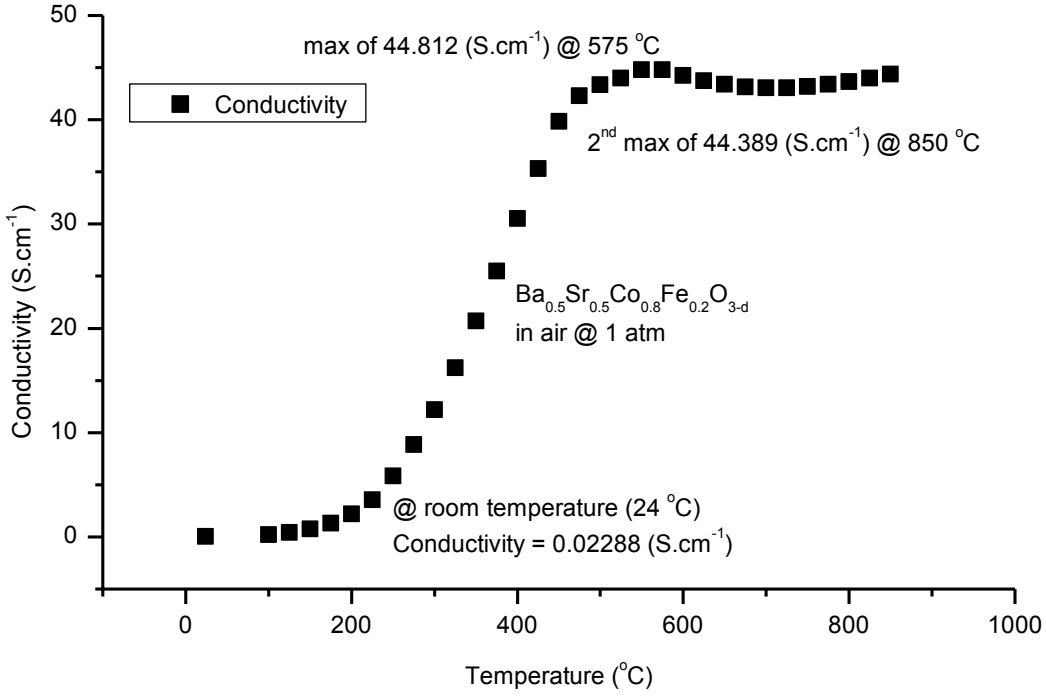

Figure V 4 - BSCF conductivity as funtion of temperature in air at atmospheric pressure

Within this modest comparison, the hardest variable to match is the temperature of the maximum conductivity value. Even though both conductivity values at 575 ºC and 850 ºC could be considered to match the literature results, only the first one represents the end of the ionization regime. Both values are close, however it must be acknowledged they belong to different zones, a fact that is easy to understand because the value of 44.812 S/cm represents a local maximum and

the one at the higher temperature does not. The reference of the fourth conductivity value presented in Table V 1 does not really display any decreasing conductivity behaviour, it rather exhibits a weaker increase of it, therefore it becomes harder to really identify if the end of the ionization zone would match the obtained result.

Table V 1 - Brief list of references with BSCF electrical conductivity values in air and relative temperatures

Reference	**Year**	**Temperature**	**σ**	**Diff**	**Average**
[#]		**(ºC)**	**(S.cm^{-1})**	**(%)**	**(S.cm^{-1})**
[248]	2015	451.85	38.5	-6.253	41.068
[249]	2007	550	29	-29.386	
[250]	2012	392	60.45	47.194	
[118]	2008	800	37.6	-8.445	
[251]	2012	550	40	-2.601	
[252]	2006	500	43	4.704	
[253]	2010	300	50.2	22.236	
[254]	2011	550	42	2.269	
[255]	2011	500	31.6 - 39	-14.045	
[157]	2007	600	40	-2.601	
[256]	2011	505	39	-5.036	
[257]	2010	350	32	-22.081	

BSCF is known for its high electrical p-type conductivity which has been confirmed by literature results through the increase of oxygen partial pressure (with measurements in air and in pure oxygen) that result in a respective conductivity increase [259 and [260]. As it was stated in the previous section 1, a positive value in the (Equation V 4) is also indicative of the BSCF p-type conduction predominance. The conductivity thermal behaviour in the ionization regime (roughly until 400-450 ºC) is evident, as well as the following effect of the mobility decreasing the conductivity in the freeze out region. The intrinsic behaviour is expected at much higher temperatures, however the ascending conductivity tendency is already observed from 750 to 850 ºC.

The activation energy (Ea) of the BSCF material in the lower temperatures (from 30 to 400 ºC) was firstly calculated through the Arrhenius expression (Equation V 10) to be compared with literature results in order to verify if this estimation was properly executed. The obtained linear fit result (Figure V 5) exhibited an activation energy of 0.3472 eV with a correlation coefficient of 0.9937. This result is also supported by literature as Table V 2 shows, where the differences and the average were calculated in kJ.mol^{-1}. The obtained value of 33.4549 kJ.mol^{-1} is slightly almost 3% below the average value of the literature results (34.454%) were the same method was applied. Since the obtained result seems to strongly match pervious works, this method is considered to be successfully executed. From this point on, this very same procedure can be further applied to data regarding more exotic materials that are not strongly reported in literature as BSCF is.

$$\sigma = \sigma_0 e^{-\frac{E_a}{RT}}$$

Equation V 10 - Arrhenius equation of conductivity where "σ", "σ_0", "E_a," ", "R" and "T" are the conductivity, pre-exponential factor, Activation energy, ideal gas constant and temperature (respectively in S.cm-1, S.cm^{-1}, kJ.mol^{-1}, kJ.mol^{-1}.K^{-1} and K)

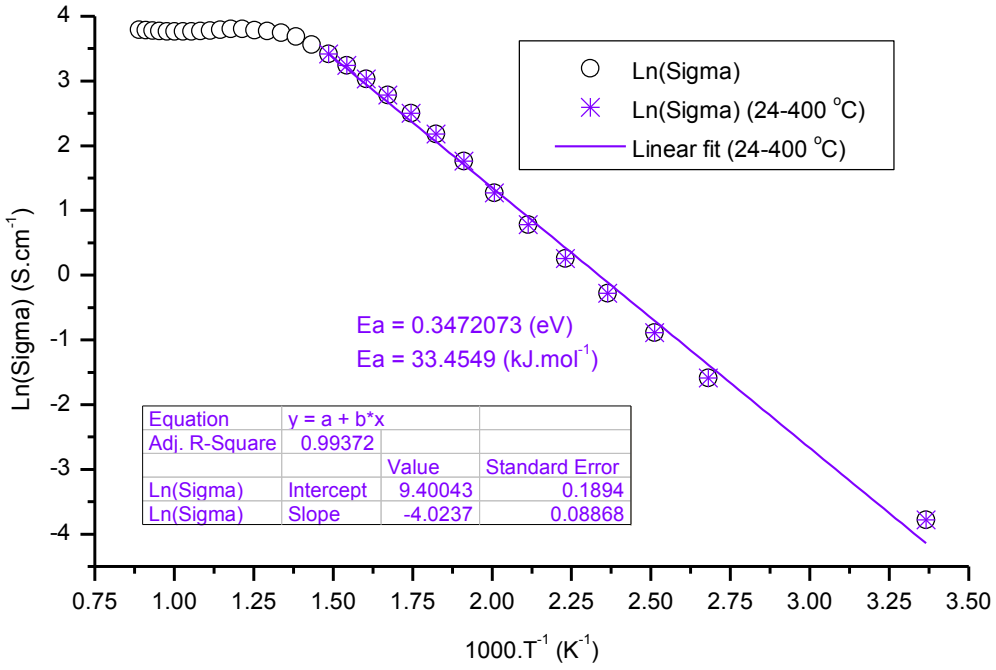

Figure V 5 - BSCF activation energy estimation considering the temperature range points from 24 to 400 ºC for the first thermal regime

Table V 2 - Brief list of references with BSCF estimated activation energy in air

Reference	Year	Ea		Diff	Average
[#]		(eV)	(kJ.mol^{-1})	(%)	(kJ.mol^{-1})
[249]	2007		35.23	2.254	34.454
[250]	2012		35.09	1.847	
[253]	2010		30.8	-10.604	
[258]	2016	0.38	36.610	6.259	
[259]	2015	0.358	34.491	0.109	
[261]	2010		34.5	0.135	

3.1.2 LBTMN and LCTMN conductivities and activation energy estimations

Both perovskite bar types were tested in air, where the conductivity profiles along with the temperature were obtained and verified with a second sample (Figure V 6). The difference in conductivity between both perovskites increases along with the temperature where the maximum values measured for both species revealed LCTMN as being 3.76 times more conductive than the LBTMN (at 800 ^{o}C). On the other hand, averaging the sample values, it is found that the proportion coefficients between each specimen overall decrease (ranging from 8.52 to 3.47 respectively from 450 to 850 ^{o}C. No signs of a tendency reversal (or even a decrease in the thermal coefficient) were observed which suggests that the end of the ionization regime is located above 850 ^{o}C.

Comparatively with Barium element, Calcium's higher conductivity (of roughly 10 times higher) as well as its reduced cation size constitute valid reasons to justify the resultant higher conductivity of LCTMN. Since the smaller cation radius is effectively decreasing the perovskite lattice parameter (as shown in Chapter IV), then the consequent bond length between the Oxygen atoms and the B site atom is also decreasing. Since decreasing this distance, has also been reported to increase mobility [262], then it is highly expected that the resulting conductivity will also be greater (Equation V 1).

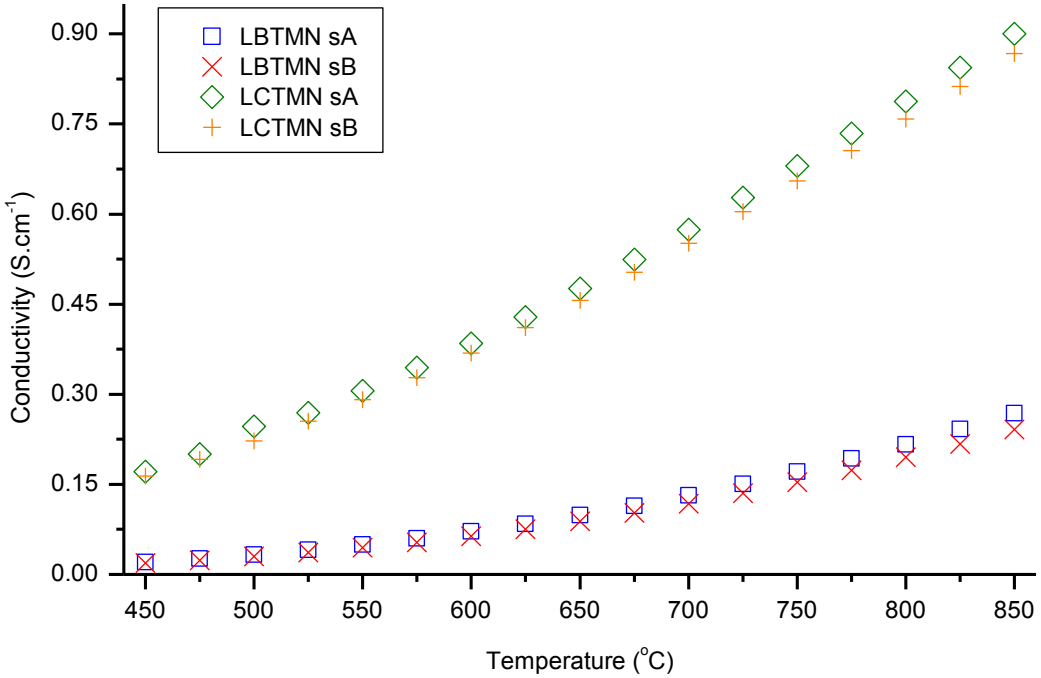

Figure V 6 - LBTMN and LCTMN perovskite conductivity profiles along with the temperature in air

The LCTMN XRD refinements (in chapter IV) also considered the presence of the P 3 2 1 and P 6_3/m m c space groups which can be displayed by the used reagent of La_2O_3. This oxide has been reported to have a thermal conductivity around 0.9 W.K.m^{-1} (at 1100 K) [263], which corresponds to about 300 S.cm^{-1} when converted with the Wiedemann-Franz law (Equation V 11). This oxide presence along with its semi-conductor nature [264], could constitute the third possible reason behind the superior LCTMN conductivity, however, most literature sources point out in the opposite direction [265] - [269] (and some further justify the conductivity decrease with the formation of oxygen vacancies as well as lattice strain fields caused by Lanthanum superior ionic radius [270]). It is also possible to find some results where there seems to be a maximum of conductivity for a certain dopant percentage [271] - [272], however, regardless of the reported behaviour, most of the literature results do not address the implications of this oxide in a perovskite structure specifically or when they do, the temperature conditions are too far [273] to allow any viable correlation. The total conductivity of La_2O_3 has also been reported to be 1x10^{-4} S.cm^{-1} [274], which is 3 orders of magnitude lower than the values observed in these perovskites in air. It is dangerous to extrapolate the implications of this oxide into the perovskite conductivity result without proceeding into a deeper relevant experimental

procedures, though, the presented literature sources suggest that its presence is very likely to not have a beneficial effect.

$$\begin{pmatrix} \frac{\sigma_{th}}{\sigma_e} = LT \\ where, L = \frac{\pi^2}{3}\left(\frac{k_B}{q}\right)^2 = 2.44 \times 10^{-8} \end{pmatrix}$$

Equation V 11 – Wiedemann-Franz law where "σ_{th}", "σ_e", "L", "T", "k_B" and "q" are the thermal conductivity, electrical conductivity, Lorenz constant number, temperature, Boltzmann constant and elementary charge constant (respectively in $W.m^{-1}.K^{-1}$, $S.m^{-1}$, $W.\Omega.K^{-2}$, K, J.K-1 and C)

Relating back to the similar cathode performance results (between these lanthanide oxides) obtained in Chapter III (in section 3.4), it seems that this conductivity difference (of 0.568 $S.cm^{-1}$) is not strong enough to output an evident discrepancy of peak power densities when these materials are assembled solely as cathodes. The conductivity differences between each sample are larger in the LCTMN samples and overall they also increase along with the temperature. The average of these differences in LCTMN (2.287%) is less than half of the one observed in the Barium perovskite samples (5.405%). It is understandable that a slightly stronger percentage difference can exist due to the fact that Barium conductivity differences are quantified within smaller values. Whenever similar deviations are observed while having higher measured values (as in the Calcium samples) the estimated resultant error will always be inferior because those standard deviations are divided by a larger conductivity value (and vice versa).

Once more using the Arrhenius equation, the activation energies of both samples in both species were determined (Figure V 7 and Figure V 8). The excellent correlation coefficients in both materials and regression considerations confirm that the activation energy remains constant through the whole temperature measurements under the oxidizing environment. In each specimen the linear regressions are extremely close to each other regardless of the applied napierian logarithm argument consideration as the slopes and intercept values show. As expected, the hopping consideration provides larger values of activation energy, however, the difference between each specimen presents a constant value (of 0.157906 eV or 15.2131 $kJ.mol^{-1}$) regardless of the chosen scenario.

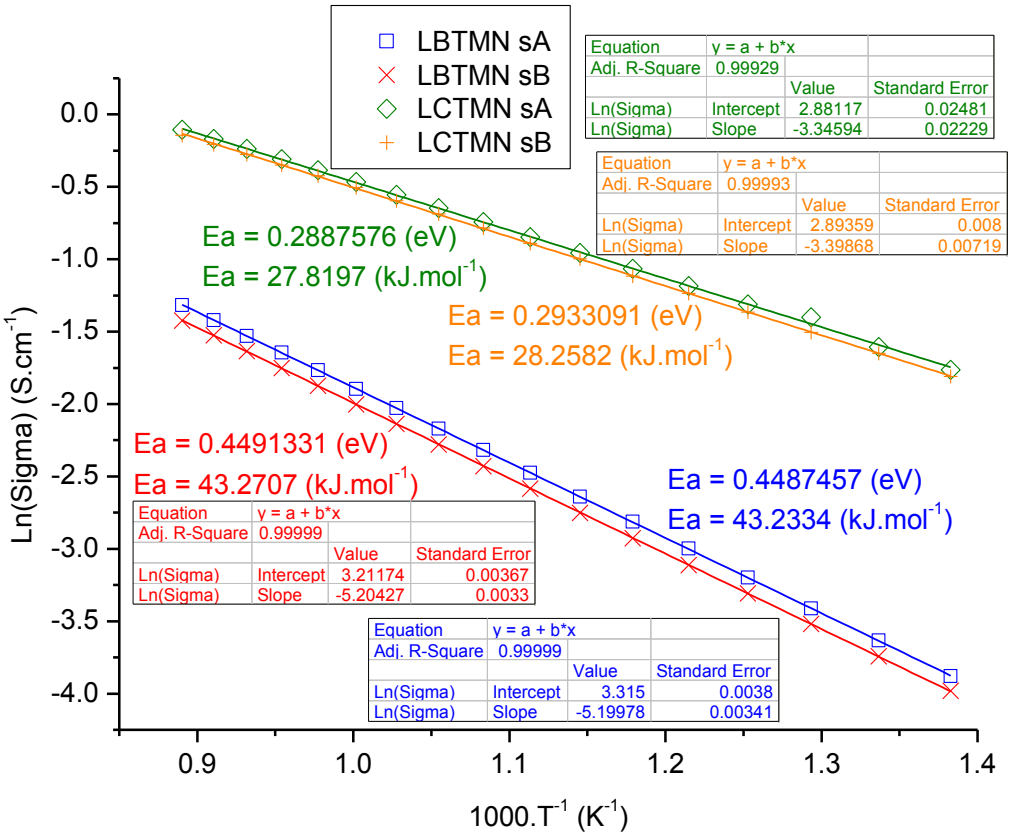

Figure V 7 - Linear fit of ln(σ) for both LBTMN and LCTMN specimens in air from 450 to 850 ºC for activation energy estimations

Comparatively to BSCF, these activation energies of the first temperature regime cannot really be correlated with lower performances as cathode. While having lower activation energy, the LCTMN perovskite still displayed lower performances than the benchmark material. This means that in order to fully compare the activation energy influence in the performance it is also necessary to have the materials in the same relevant temperature range. The performance of the cells tested in Chapter III was obtained in a temperature interval from 550 to 800 ºC, where BSCF energy would be extremely low from the fact that the Arrhenius slope is in fact close to zero (because the material is already ionized or activated). As it was stated before, these thermal conditions allow the BSCF material to be in the freeze out region, while the LAemTMN perovskites under the same conditions would have never even left the extrinsic/ionization regime (comparatively). To fully compare the implications of this variable with BSCF, the performances would have to be tested either at temperatures lower than 400 ºC where BSCF material would be in the same extrinsic zone as the

LBTMN and LCTMN perovskites seem to be, or at much higher temperatures than 850 ºC (also with conductivity data in the same range) so that both materials would be in the intrinsic region.

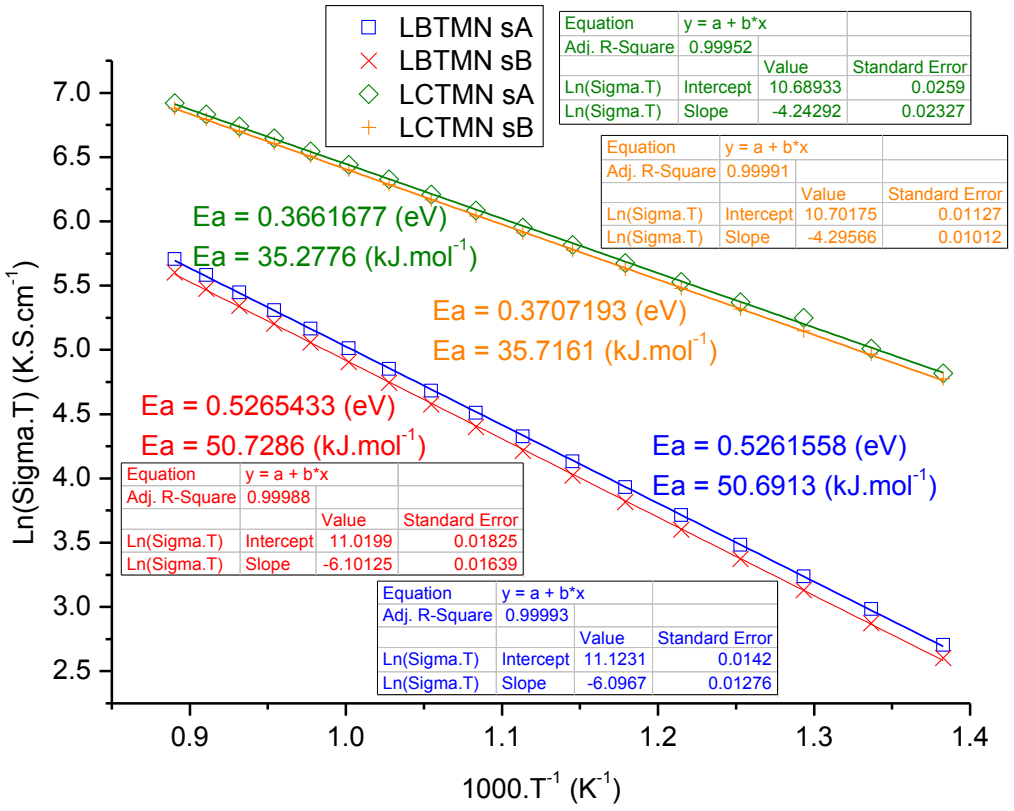

Figure V 8 - Linear fit of ln(σT) for both LBTMN and LCTMN specimens in air from 450 to 850 ºC for activation energy estimations

It is possible to compare both lanthanide perovskites from the fact that they seem to be in the same thermal regime. Under oxidizing conditions, not only LCTMN displayed higher conductivity values, but also lower activation energies. Though the conductivity differences can be taken as not strong enough to generate significant peak powder density (PPD) changes, the activation energy variations seem to have much less influence in the output performance result. The average activation energy difference (of 15.213 kJ.mol^{-1}) is also coherent with the average one estimated from the electrolyte supported cells (of Chapter III in section 3.4). Even though the difference estimated through the cells is slightly larger (19.728 kJ.mol^{-1}), it should be acknowledged that the method is much less precise and it is not only from the fact that the number of points in each linear regression method is not really similar. Even

though the same number of slurry layers are applied, the relative thickness variation will be much larger comparatively with the bar geometrical imperfections of less than 0.01 mm in a total average volume of more than 90 mm^3. As a result, the sample differences in the total activation energies estimated through the total polarization resistances will have larger variations (of 2.488 $kJ.mol^{-1}$ and 6.098 $kJ.mol^{-1}$) relatively to the values estimated through the conductivity (where values of 0.037 $kJ.mol^{-1}$ and 0.439 $kJ.mol^{-1}$ can be found).

Literature sources of perovskites with common chemical elements [22, [31], [75] tend to point out Manganese valency state alteration (between 3+ to 4+) as the dominant mechanism behind the charge transport, however in order to fully verify this hypothesis further analysis would have to take place. In short, the total activation energies between the lanthanide perovskites are very different regardless of the estimation method, which suggests that the conductivity difference is not the only reason behind the small respective performance difference. This idea might not be fully supported by the BSCF material, because though the pattern cells (in section 3.2) revealed total activation energies higher than most of the cathode cells, this pattern cathode is in a different thermal regime. These results under oxidizing conditions suggest that the conductivity thermal regime is the most relevant variable influencing the performance of these electrodes.

3.2 Under reducing atmosphere

The thermal profiles of the conductivity were also obtained under reducing conditions for both samples of each perovskite (Figure V 9). The LCTMN perovskite displayed higher conductivity values and once more this difference is increased by the temperature. Both samples in each specimen seem to provide relatively close values, though LCTMN exhibited a slightly lower agreement between its samples. Furthermore, under reducing conditions both perovskites do not fully display the same increasing conductivity gap along with the temperature in between samples, instead, the samples with the highest and lowest conductivity seem to permute positions in some temperature points (a phenomena that is far more frequent in the Calcium perovskite). Comparatively to the oxidizing conditions, the reducing atmosphere reveals an opposing ascending trend in the conductivity coefficients between specimens with values from 1.61 to 2.64 respectively from 450 to 850 ^oC.

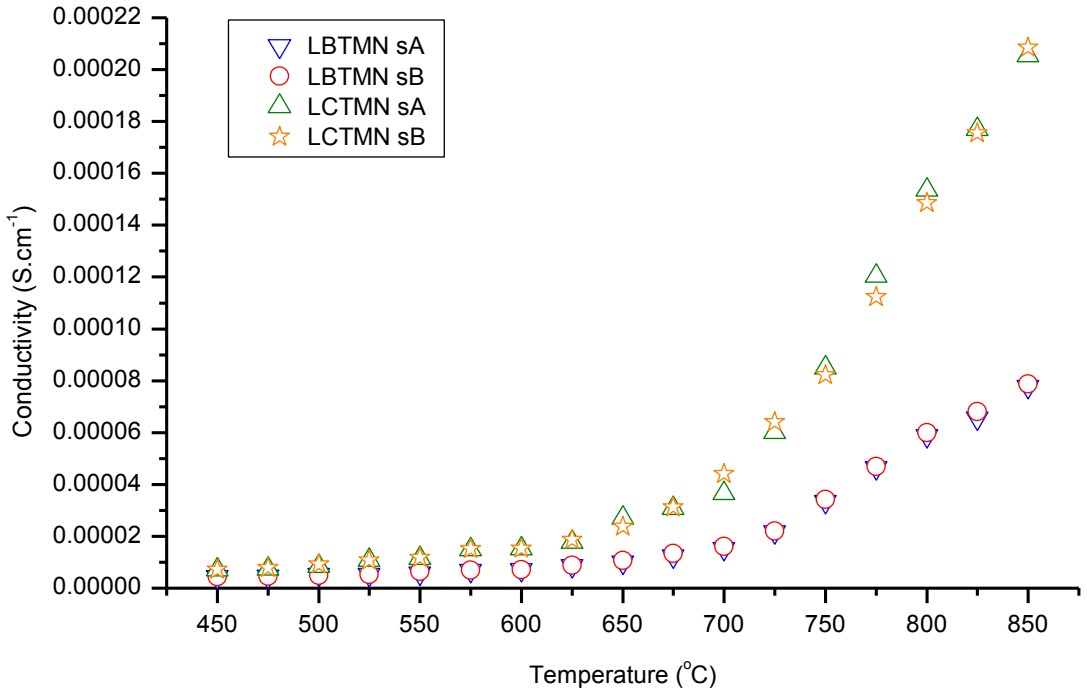

Figure V 9 - LBTMN and LCTMN perovskite conductivity profiles along with the temperature in hydrogen

The conductivity graphical shape under reducing conditions does not display an approximate constant increment through the whole data set (as seen before with the samples tested under oxidizing atmosphere). Instead, the conductivity seems to display 2 distinct thermal coefficients: a smaller one implemented in the lower temperatures (ruling the profile roughly until 650 – 700 ºC) and a larger one in the higher temperatures. This suggests that under reducing conditions, this temperature range is enough to ionize the materials and allow them to be in the intrinsic regime while operating as anodes. The results under oxidizing conditions lead to believe that the conductivity differences in the extrinsic regime seem to not be strong enough to generate higher power densities, however, an even smaller proportional conductivity multiplier (of 2.545 at 800 ºC) seems to boost the cell performances. If the smaller order of magnitude of these values is interpreted as mostly ionic conductivity, then it becomes relevant to also mention that this variable has been pointed out a reason behind an anode performance improvement [275]. These results can also suggest that the conductivity influence in the power densities is largely dictated by the relevant thermal regime of the material. The mechanism of intrinsic charge carrier's generation would have such a powerful influence in the output performance, that even displaying

lower conductivity relative differences, the measured PPD discrepancies are still much larger.

Many studies have used the oxygen partial pressure (PO_2) effect in the conductivity in order to classify the nature of the semiconductor electrical conductivity type [22], [275] - [284]. Since the measurements in hydrogen certainly provide much lower PO_2 conditions comparatively with the samples tested in air which resulted in lower conductivity values, the results suggest that both of the perovskite materials display P-type electrical conductivity. As it was previously stated, the conductivity increment along with the temperature does not really allow the consideration of a single linear regression through the whole temperature range, therefore two different temperature regimes had to be considered. The higher temperature regime contains the data ranging from 650 to 850 ^oC (Figure V 10 and Figure V 11) and the remaining points at lower temperatures (from 450 to 625 ^oC) were attributed to another region (Figure V 12 and Figure V 13). This data split was mainly guided by the solution that would provide overall the best correlation coefficients for the regressions. Overall, acceptable sample agreement in regards to the slopes, resultant estimated Ea and correlation coefficient values were obtained.

As it was mentioned in Chapter III (section 3.5.1), the NiO + SDC anode material performances cannot be fairly compared with the LAemTMN anode performances from the fact that adding electrolyte powder in the anode material will improve the effective anode-electrolyte surface area beyond the geometrical spray painted circumference area of 0.23758 cm^2. However both lanthanide perovskite activation energies can be correlated with chapter III performance results (specially the relevant intrinsic temperature regime). In the intrinsic regime of temperature (Figure V 10 and Figure V 11) both activation energies seem to not be too far from each other, a fact that matches the total Ea estimations obtained from the electrolyte supported cells (in Chapter III, section 3.5). This intrinsic thermal regime of conductivity is the most relevant variable to correlate with the performance results because most of the PPD measurements (from 800 600 ^oC) match this temperature interval. The only strong difference between both materials in this temperature range is in the values of the conductivity. This supports the idea of the conductivity influence in the performance being much stronger in the intrinsic thermal regime than in the extrinsic one.

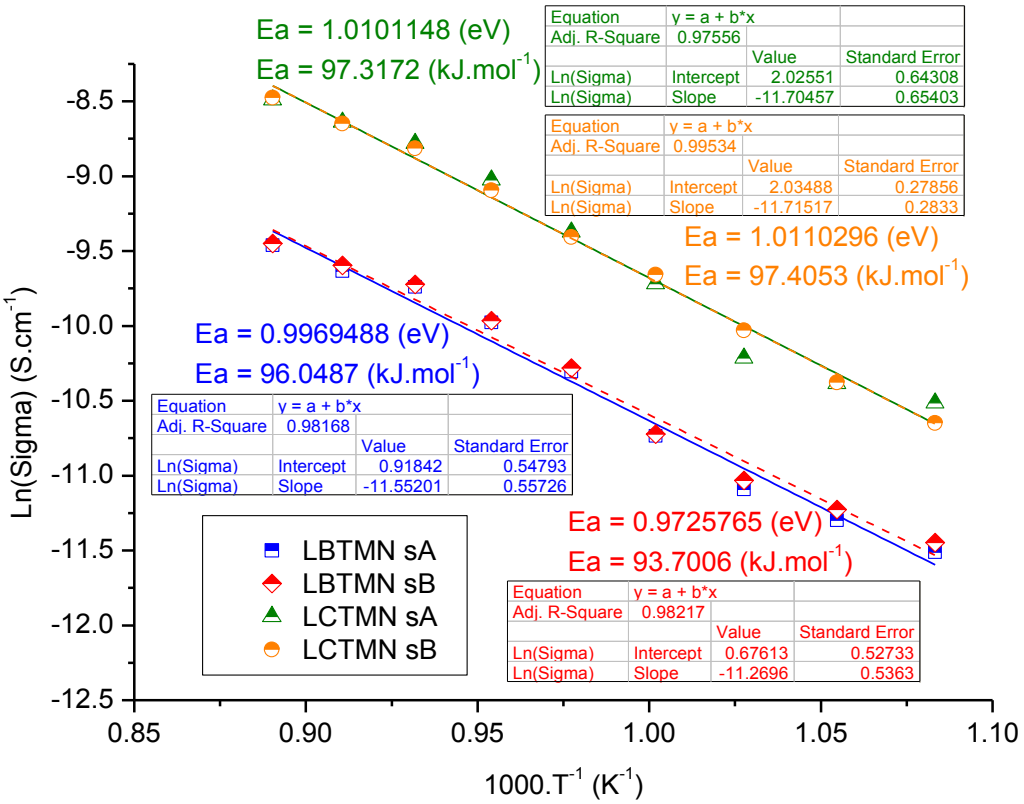

Figure V 10 - Linear fit of ln(σ) for both LBTMN and LCTMN conductivities in hydrogen from 650 to 850 ^{o}C for activation energy estimations

The previously explained equations for the Polaron model approach are now also alternatively applied to the measurements under reducing conditions. Comparatively with the spotted difference under oxidizing conditions (between ln(σ) and ln(σT) considerations), both of the implemented thermal regimes show lower differences in the activation energy. Just as before, the ln(σT) regression provides higher activation energy estimations, however, the differences between the averages of each specimen still present constant values (of 0.0258096 and 0.1005695 eV respectively at the higher and lower temperature intervals) regardless of the considered conduction mechanism.

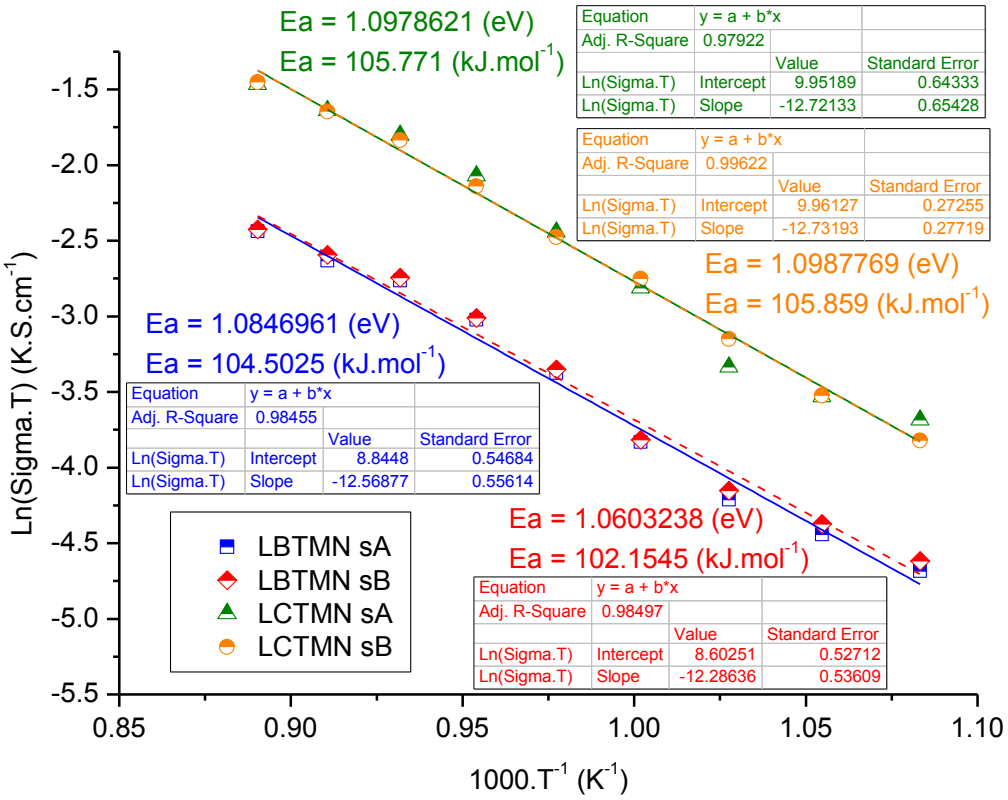

Equation	y = a + b*x		
Adj. R-Square	0.97922		
		Value	Standard Error
Ln(Sigma.T)	Intercept	9.95189	0.64333
Ln(Sigma.T)	Slope	-12.72133	0.65428

Equation	y = a + b*x		
Adj. R-Square	0.99622		
		Value	Standard Error
Ln(Sigma.T)	Intercept	9.96127	0.27255
Ln(Sigma.T)	Slope	-12.73193	0.27719

Equation	y = a + b*x		
Adj. R-Square	0.98455		
		Value	Standard Error
Ln(Sigma.T)	Intercept	8.8448	0.54684
Ln(Sigma.T)	Slope	-12.56877	0.55614

Equation	y = a + b*x		
Adj. R-Square	0.98497		
		Value	Standard Error
Ln(Sigma.T)	Intercept	8.60251	0.52712
Ln(Sigma.T)	Slope	-12.28636	0.53609

Figure V 11 - Linear fit of ln(σT) for both LBTMN and LCTMN specimens in hydrogen from 650 to 850 ºC for activation energy estimations

At lower temperatures the activation energies seem to be considerably lower (Figure V 12 and Figure V 13) comparatively to the previous intrinsic regime. Despite having a superior agreement among samples regarding the slopes and intercept parameters, the correlation coefficients are overall slightly worse, which is unexpected of lower temperatures where typically greater stability in the measurements generally leads to superior linear agreements. The activation energy (regardless of the atmosphere) seems to not have a strong influence in the performance. Even if the samples of LBTMN in the higher temperature range displayed a larger error, the precision of this method strongly suggests that the other variables (such as the conductivity and the temperature regime) have a greater impact on the performance.

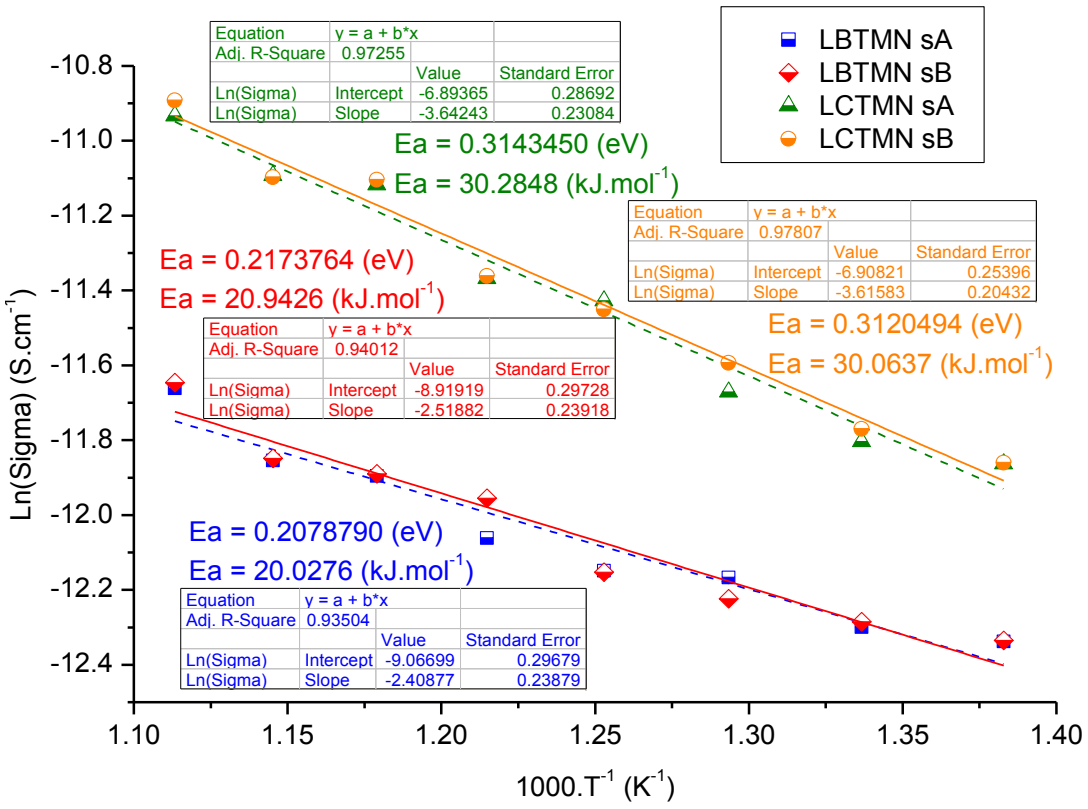

Figure V 12 - Linear fit of ln(σ) for both LBTMN and LCTMN specimens in hydrogen from 450 to 625 ºC for activation energy estimations

Under oxidizing conditions it was possible to estimate a higher Ea value for the LBTMN perovskite from the polarization resistances. A fact that remains true in the estimations obtained through the four probe method. It is likely that the same basic level of agreement was not achieved from the fact that the activation energy estimated in Chapter III (section 3.5) gathers polarization resistance data from 2 distinct thermal regimes. This leads to the underestimation of this variable from the fact that the lower temperature points (of 550 and 600 ºC) are decreasing the overall slopes.

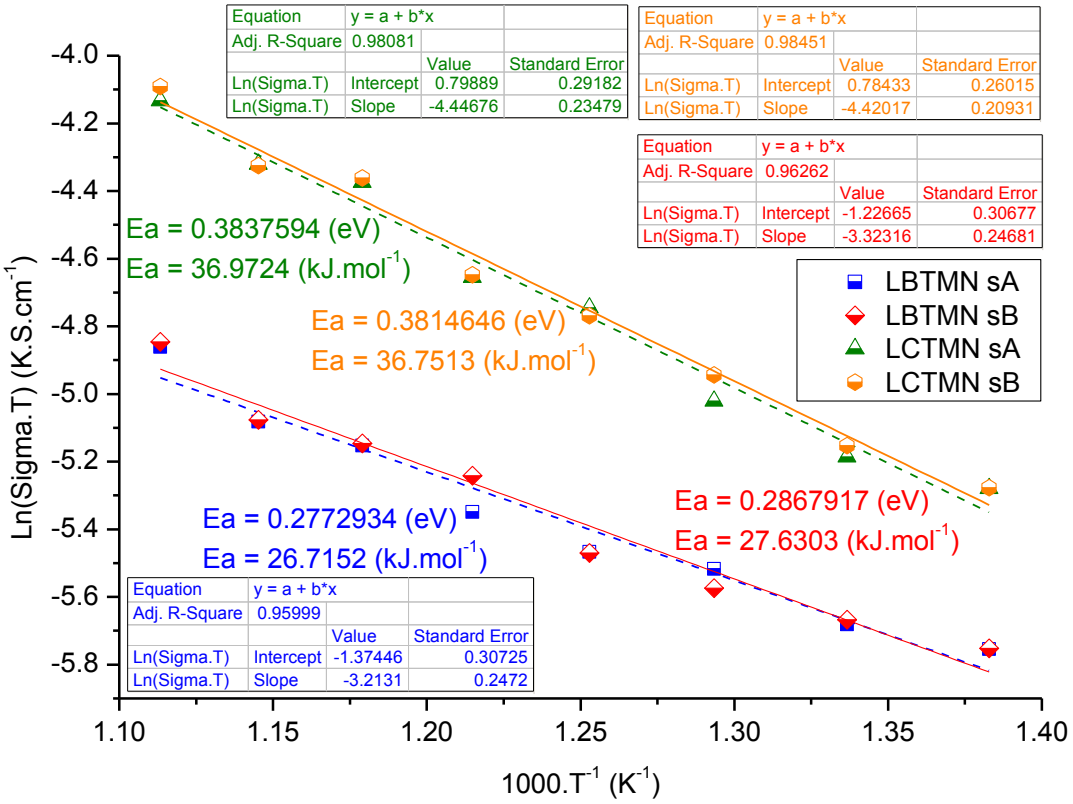

Figure V 13 - Linear fit of ln(σT) for both LBTMN and LCTMN specimens in hydrogen from 450 to 625 ºC for activation energy estimations)

4. Summary

In order to relate the performance results (obtained in chapter III) with the conductivity, it became mandatory to explain the importance of the temperature regime, therefore a brief introduction regarding the physical background theory regarding the conducting mechanisms has been provided (addressing the main variables of the concept such as charge carrier concentration, mobility and relaxation time). The band theory classifies materials as insulators, semiconductors and conductors based on the energy gap between the valency and conduction band. Conductivity describes the flow of charge carriers passing through an area over time in a given electric field. This transport process has two components, each named according with its relevant charge carrier type, such as ions/holes and electrons/vacancies (correspondingly for ionic and electronic conductivities). The electronic conductivity component is classified into N or P-type whether the main carrier are free electrons or electron holes respectively. The Seebeck coefficient and

the conductivity tendency along with PO_2 variation are some ways to find out which type of electrical charge carrier is dominant over the other, defining this way the type of electrical conductivity within a certain material. Semiconductors not only increase their conductivities as temperature increases, but also typically display different regimes (such as extrinsic and intrinsic) where these positive coefficients are very distinct.

The four probe method has been described as well as the experimental procedures required to its execution. To make sure the experiment and the data treatment method were both successfully implemented, the widely reported material of BSCF was firstly analysed. Since its results matched several literature references (in regards to conductivity and activation energy values), this technique was considered successfully applied and mastered to be carried out in the lanthanide perovskite chosen materials that are not yet reported in literature. Notwithstanding, literature sources of similar perovskite chemical compositions tend to attribute the current transport mechanism to the Manganese alteration of valency state from 3+ to 4+ [22], [31], [75].

The Appendix section also contains this chapter gathered results summarized in both Table IV A and Table V A2 together with the mentioned average differences that led to the formulation of its main hypothesis. Regardless of the considered atmosphere, the conductivities of the LCTMN samples are always higher than the ones observed in the LBTMN. This was somehow expected from the fact that the Calcium element is almost ten times more conductive than Barium (at room temperature conditions) and its smaller cationic size also decreases the perovskite unit cell (consequentially increasing the mobility), however the potential La_2O_3 impurity presence in the LCTMN perovskite cannot really be assigned as a conductivity improvement contributor. The results suggest the presence of P-type electrical conductivity in both perovskites from the fact that lower conductivities under reducing conditions are observed. The conductivity differences between samples and specimens increases along with the temperature under oxidizing atmosphere, however, this aspect is not clearly seen between samples in H_2.

The Ea results in air overall displayed better correlation coefficients, intercepts and slopes, leading to closer activation energies (in each specimen) and a superior agreement with the values estimated from polarization resistances (in Chapter III section 3.4) regardless of the applied linearization model (being $\ln(\sigma)$ or $\ln(\sigma T)$). The inferior agreement under reducing conditions is believed to come from the existence

of two thermal regimes in the conductivity. These results seem to be due to the existence of less collinear points in the lowest temperatures (of 550 and 600 ^{o}C) because these belong to the ionization regime, while the remaining ones are in the intrinsic region. A further clear difference of precision in the activation energy estimations from the two methods is spotted and it seems to be independent from the surrounding atmosphere. The precision superiority of the four probe method was believed to result from both its relative smaller sample dimension variations as well as its superior amount of data points from which the corresponding linear regressions are based on.

Under oxidizing conditions the conductivity difference seems to have little to no effect on the cells performance, whereas under reducing atmosphere the conductivity differences seem to actively increase the power densities. Given the fact that the two major differences between these two atmospheres were the much smaller order of magnitude in the measured values and the existence of different thermal regimes, two possible factors might be contributing to the power density differences. It is possible that under reducing conditions most of the conductivity is ionic (which improves the anode performance), but the (intrinsic) temperature zone is a factor whose potential influence in the performance should not be discarded. Another aspect to take into consideration is that the LAemTMN materials share compositional traces with the LSM cathode. This is further supported by the fact that both materials displayed similar reasonable cathodic performances (in Chapter III section 3.4), suggesting this way that the anodic performance holds a superior margin for improvement.

(Page intentionally left blank)

Chapter VI - B site element replacement

1. Introduction

The present chapter attempts to improve the results of the previously studied LCTMN ($La_{0.7}Ca_{0.3}Ti_{0.5}Mn_{0.4}Ni_{0.1}O_3$) perovskite (in Chapter III, Chapter IV and Chapter V) through replacing the Manganese element for another candidate. Literature data lead to establish the possibility of the Manganese presence to increase the reducing conditions to higher temperatures (of 1400 ^oC), being the reason why the exsolution phenomena could not be verified by XRD analysis (after submitting the electrode powder to reducing conditions under 800 ^oC). This hypothesis defined a 5 criteria strategy to select the replacing Iron cation which was followed by a purity estimation along with the calcination temperature of the resulting perovskites with two different ratios (of the Iron and Titanium elements), enabling this way a direct comparison with previous Manganese results as well as a humble understanding of this element's ratio implications against the Titanium cation. The purity estimations suggest the optimum calcination temperature to be 1300^oC and so the SDC electrolyte supported symmetrical cells were assembled so that the performance and total impedance results could be obtained.

The poor performance of both symmetrical cell species did not justify a deeper analysis of this chemical compositions, however cuboid shaped bars of both powders were still attempted. Despite applying the extreme temperature conditions of 1400^oC for 10 hours, the resulting samples were not dense enough to be used with the 4 probe method. This fact unfortunately leaves room for some conductivity positive influence speculation because Iron conductivity is about 4 times higher than Titanium, and the cells whose electrodes had a higher Iron ratio revealed both higher performance as well as much lower polarization resistances. The most valuable hypothesis formulated from these results states that if a tolerance factor closer to 1 results in better performance results, then the Titanium state of oxidation dominant species must be 3+ and not any of the other possible considered species (2+ or 4+), unfortunately, due to time constraints, no further analysis was carried in order to verify or disprove this theory.

2. Main reasons for replacing Manganese

In attempts to improve the previously observed performance (in Chapter III), new alternatives for the B site were taken into consideration to replace the Manganese position in the $La_{0.7}Ca_{0.3}Ti_{0.5}M_{0.4}Ni_{0.1}O_3$ perovskite. Comparing two relevant literature reports of successful exsolutions, one can easily deduct that the existence of the Manganese element in the perovskite (even if at a low ratio) seems to be increasing the temperature requirements for the phenomena to occur. Without Manganese, the Nickel peak (around 44 degrees in the 2θ axis) is visible for samples reduced at 1000 ^oC (Figure VI 1) [285], whether a similar perovskite under the same atmosphere of 5% H_2/Ar displays the same peak with a reducing temperature of 1400 ^oC (Figure VI 2 and Figure VI 3) [286].

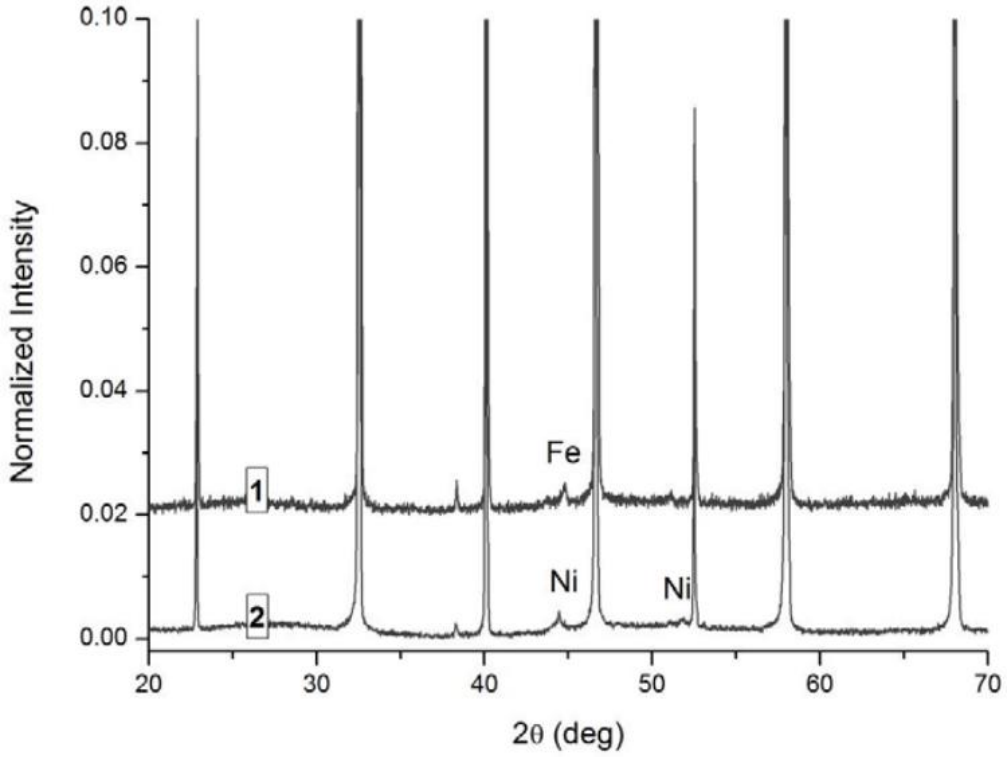

Figure VI 1 - Room temperature XRD pattern of (1) $La_{0.46}Sr_{0.34}Ti_{0.0.94}Fe_{0.06}O_3$ and (2) $La_{0.52}Sr_{0.28}Ti_{0.94}Ni_{0.06}O_3$ reduced at 1000 ^oC in 5%H2/Ar showing broad peaks of metalic Fe and Ni, respectively (from source's supplementary information Figure S 9) [285]

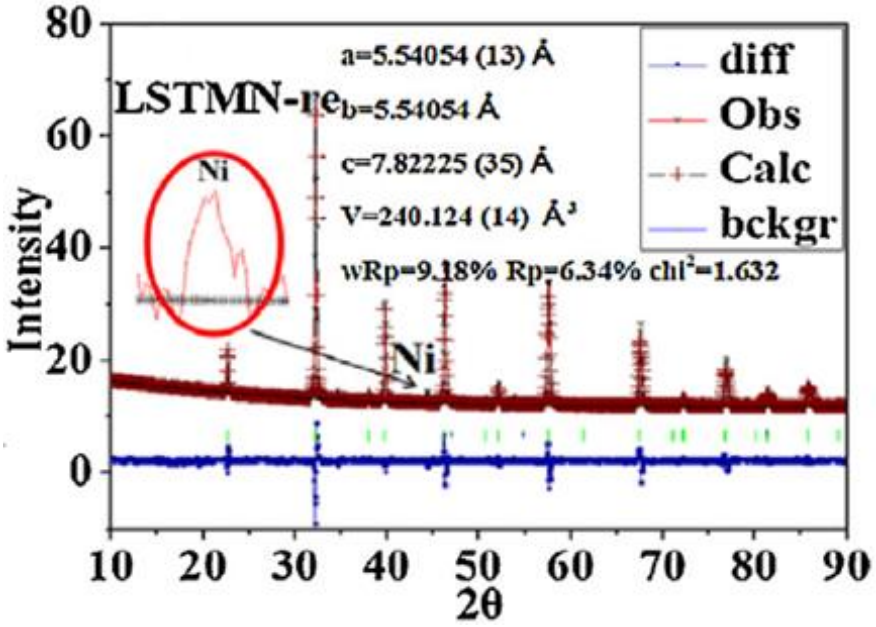

Figure VI 2 - Rietveld refinement pattern of $(La_{0.2}Sr_{0.8})_{0.9}(Ti_{0.9}Mn_{0.1})_{0.9}Ni_{0.1}O_{3-\delta}$ powder reduced in 5%H2/Ar at 1400 ºC [286]

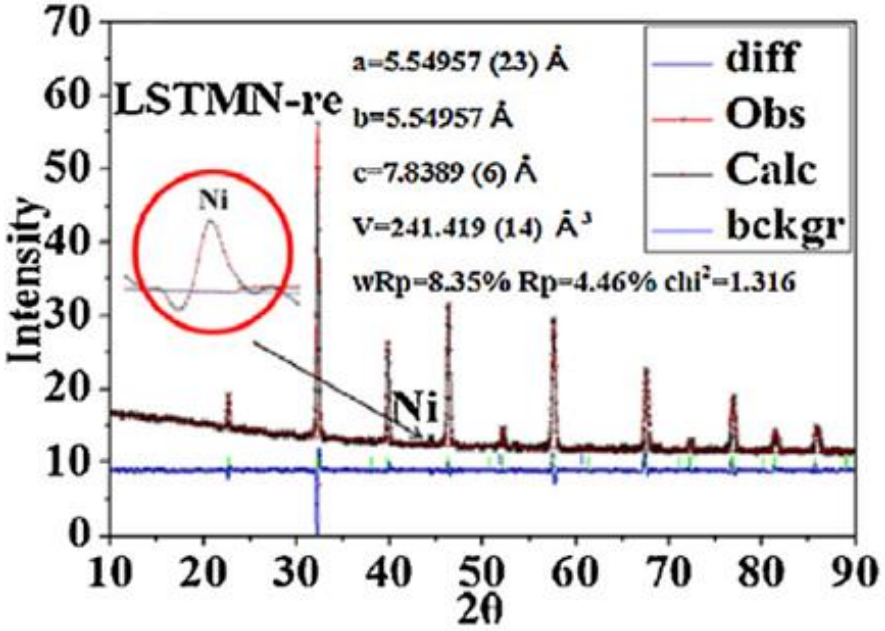

Figure VI 3 - Rietveld refinement pattern of $(La_{0.2}Sr_{0.8})_{0.9}(Ti_{0.9}Mn_{0.1})_{0.9}Ni_{0.1}O_{3-\delta}$ powder after 3 redox-reversible cycles at 1400 ºC reduced in 5%H2/Ar [286]

It is well-known that the A-site deficiency benefits the exsolution phenomena [285, [287] - [291], therefore, the chosen candidate to replace Manganese is intended

to also be further tested in a perovskite arrangement with this characteristic. This way, not only new perovskite materials are being tested, but also the differences between the stoichiometric and A-site deficient materials can also be experienced in each of the different selected elements. The resultant potential improvement in the different chosen materials can provide further understanding in regards to the cation deficiency influencing factors in the segregation event.

3. The strategy to select the replacement candidate

Given the reasons stated in the previous section, the selection procedure to find the optimum candidate to replace the Manganese element begins. The following strategy to select materials for the B site of this perovskite is an elimination process which briefly consists in establishing certain conditions, keeping all the possible elements which meet those particular requirements while discarding the remaining ones as they are no longer considered viable options at any certain step.

3.1 First criterion: cations with the coordination number VI

As it was already stated in Chapter I, the perovskite relevant coordination numbers of the A and B site are 12 and 6 respectively. Since the potential cations are meant to occupy the B site position, this selection starts merely with the selection of all cations species with coordination number 6. To select those, an online database [90] (which relies on relevant literature sources [292] - [294]) was used. This means that at this first state a total of 93 elements were gathered so that the next criteria could carry on the elimination process.

3.2 Second criterion: physical states, oxides volatility and radioactivity

At the first glance, all the 93 elements of the periodic table with the relevant coordination number can theoretically be assigned as possible candidates, but it is easily understandable that some of them are not suitable for the current application because they are gases at normal pressure and temperature conditions (like Nitrogen, Fluor and Chlorine). Many other elements (such as Sulphur, Phosphorus, Selenium, Arsenic, Bromine, Plutonium, Neptunium, Iodine and Tellurium) were also

discarded at this step because they become gases at the operation conditions due to having lower boiling points. Other elements such as Molybdenum, Osmium and Rhenium do not really have low melting points in their pure elemental state, however, either all their oxides are extremely volatile, or those which are not, they tend to volatile further states of oxidation. Carbon can also be included in this group from the fact that under oxidizing conditions it will form Carbon dioxide, obviously making it impossible to rely the perovskite structure on this element.

Still in this state, radioactivity is also implemented as a discarding characteristic, being the reason why Uranium and Technetium are not considered as replacing candidates. The three criteria presented in this section left a total of 16 elements left to be considered in the next step, also excluding B site elements that are already embodied in the perovskite such as Titanium, Nickel or the (Manganese) element that is being replaced.

3.3 Third criterion: Ellingham diagrams

The formation of nickel nanoparticles has been shown to be beneficial to the electro-catalytic activity and durability of the electrodes [291]. In order to provide the best conditions for this phenomena to occur, the next criteria applied intends to quantify the stability of the element bonding with oxygen along with the temperature, or how easily reducible that particular oxide is. The existence of Nickel in the host perovskite $La_{0.7}Ca_{0.3}Ti_{0.5}M_{0.4}Ni_{0.1}O_3$ serves the purpose of attempting its segregation into nanoparticles, therefore, the elements whose oxides have higher reducing tendency than nickel (at the operation temperature) are incompatible with this nickel exsolution objective.

This criteria can also potentially explain the temperature requirement increase for the Manganese perovskites intended to segregate Nickel. In the relevant coordination number, the highest Manganese state of oxidation +7 is mostly restricted to unstable compounds [295], however the Ellingham diagram relative to the oxide MnO_2 where its valency state is +4 might already be responsible for this temperature requirement increase (Figure VI 4). From this criteria the elements Gold, Silver, Copper, Iridium, Palladium, Platinum, Rhodium and Ruthenium, where eliminated from the fact that all of their oxide Gibbs energies are even less negative than Nickel's at the operation temperature. This means that under a reducing atmosphere these elements are more likely to be reduced instead of Nickel.

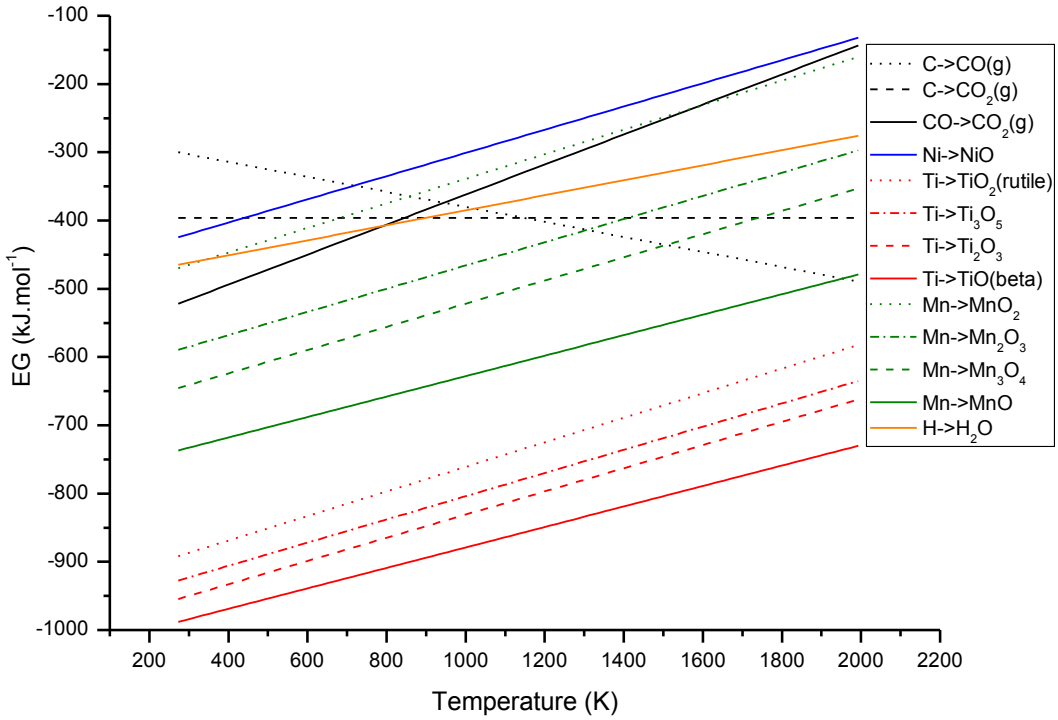

Figure VI 4 - Ellingham Diagrams of the B site element oxides (Titanium, Manganese and Nickel), Carbon and Hydrogen [202]

Cobalt was also discarded not only because the reduction of Co_3O_4 has higher Gibbs energy than Nickel, but also because there are several advantages in a cobalt free perovskite. This element is well known to provide low polarization losses and outstanding electrochemical performances. On the other hand, the consequent high thermal expansion coefficients, low intrinsic chemical stability and obviously the price, automatically stimulate the extensive research on cobalt-free materials [36], [296] - [301]. Out of the 16 elements submitted to this third criterion, 9 were discarded, allowing this way the remaining 7 candidates to be pondered in the next section where a brief literature search took place.

3.4 Fourth criterion: Element segregation in the 0.4 dopant ratio

At this step, 3 of the 7 remaining elements were discarded because they have been shown in previous works to originate segregation of secondary phases when doped above a certain ratio. The School of Chemistry from the University of

Birmingham in collaboration with the ISIS Facility in the Rutherford Appleton Laboratory in Harwell Oxford and the Rocasolano Chemistry Physics Institute in Madrid successfully doped Silicon [302] and Germanium [303] (respectively) in a Strontium Calcium Iron host perovskite in different ratios ($Sr_{(1-y)}Ca_yFe_{(1-x)}Si/Ge_xO_{3-\delta}$). The reports reveal that the single perovskite phase can only be achieved with a dopant ratio up to 0.15 of both elements. Molybdenum was also identified to have a maximum solid solution ratio of 0.1 within a Strontium Cobalt host perovskite through the presence of additional diffraction peaks observed in the XRD profiles [304]. Since the dopant ratio is intended to be studied with a maximum ratio of 0.4 for comparison purposes with previous chapters, these 3 elements were discarded at this step.

Regarding the remaining 4 elements (of Chromium, Vanadium, Tungsten and Iron), there are several reports of perovskites containing these elements in ratios superior than the minimum required to replace Manganese. For this reason, one last criterion had to be implemented in order to select the best candidate, theoretically.

3.5 Fifth criterion: Tolerance factor and price consideration

In order to implement the tolerance factor relationship, the ionic radius of the remaining elements (of Chromium, Vanadium, Tungsten, Iron and Manganese) in the relevant coordination number of 6 were considered. A Goldschmidt tolerance factor (Equation I 1) of 0.96 was applied among all of the 12 scenario host element states of oxidation combinations (Table VI 1) in order to distinguish the average cation sizes that would verify this condition from the ones that would fail it by less than 5% and fail it by more than that. It should be mentioned that the perovskite phase can be formed with theoretical tolerance factors below 0.96, however if a value such as 0.9 is considered among these remaining candidates, then all of them would verify this condition. From this, it is safe to assume that all of the remaining candidates can potentially form the desired perovskite structure so that the structural variable of this potential new component can still be compared with its Manganese predecessor ($La_{0.7}Ca_{0.3}Ti_{0.5}Mn_{0.4}Ni_{0.1}O_3$). The tolerance factor was therefore tightened to a value closer to the unity in order to obtain a humble scale to show which of the candidates in each scenario have the minimum amount of distortions, or are closer to the perfectly cubic structure (where t=1). It should also be mentioned that these calculations are not considering the formation of oxygen vacancies and are relying purely on the electrical neutrality condition.

Table VI 1 – Average cation size calculations of Chromium, Vanadium, Tungsten, Iron and Manganese in each of 12 scenario combinations of the host element states of oxidation where the numbers in green satisfy a tolerance factor of 0.96, the numbers in orange fail by less than 5% and the numbers in red fail by more than 5%.

Ti^+	2^+				3^+				4^+			
Ni^+	2	3_{ls}	3_{hs}	4_{ls}	2	3_{ls}	3_{hs}	4_{ls}	2	3_{ls}	3_{hs}	4_{ls}
M^+	5.25	5	5	4.75	4	3.75	3.75	3.5	2.75	2.5	2.5	2.25
Max size ($_{i=0.96}$) (Å)	0.3238	0.3563	0.3463	0.3763	0.5613	0.5938	0.5838	0.6138	0.6425	0.6750	0.6650	0.6950
M_t					$Mn_{0.5300}$	$Mn_{0.5425}$		$Mn_{0.5550}$	$Fe_{0.5650}$	$Fe_{0.5800}$		$Fe_{0.6188}$
					$Cr_{0.5500}$	$Cr_{0.5663}$		$Fe_{0.5675}$	$Mn_{0.6025}$	$Mn_{0.6250}$		$Mn_{0.6575}$
						$Fe_{0.5763}$		$Cr_{0.582}$		$Cr_{0.672}$		
								$V_{0.6100}$				
					$V_{0.5800}$	$V_{0.5950}$			$Cr_{0.6438}$		$Cr_{0.672}$	$Cr_{0.7013}$
					$Fe_{0.585}$							
	$Cr_{0.4775}$	$Cr_{0.4900}$		$Cr_{0.5050}$	$W_{0.660}$				$V_{0.6775}$	$V_{0.7150}$		$V_{0.7525}$
	$Mn_{0.5008}$	$Mn_{0.5067}$		$Mn_{0.5125}$								
	$W_{0.6150}$	$V_{0.5400}$		$V_{0.5500}$								
		$W_{0.6200}$		$W_{0.6300}$								

The first aspect to notice from these assumptions is the fact that considering the Titanium in a 2+ state of oxidation leads to a much harder size matching scenario. As Table VI 1 shows, the maximum sizes to pass the 0.96 factor criteria are much smaller than the ones observed in the remaining Titanium states of oxidation. This happens merely because (in this relevant coordination number) the cation size of Ti^{+2} (which is 0.86 Å) is much larger than the corresponding sizes of the remaining valency states (which are found to be 0.67 and 0.605Å). The second important detail about this analysis is the constant best or second best matching results of Manganese among the considered scenarios. If Titanium is considered in its larger size, Chromium takes the lead as the dopant (which best replaces Manganese) with the second best matching results, however in the smaller Titanium size scenarios Iron gets the spotlight (also verifying the tolerance factor of 0.96).

The best 3 matching results of Ti^{3+} scenarios highlight the same elements of Manganese, Chromium and Iron which were already seen in the remaining states of oxidation as well. Overall, these results suggest that among the remaining 4 candidates Chromium and Iron seem to provide the best chances of improving dopant size matching because they provide the best results among all of the scenarios. Chromium has the advantage of always providing an answer to the system regardless of the scenario, however, given the fact that there is no data regarding Iron 6+ size (within a coordination number of 6), the remaining options of 2+, 3+ and 4+ cannot possibly answer any of the demands to form a theoretical average state of oxidation from 4.75+ to 5.25+ which are required in the Ti^{2+} scenarios. This disadvantage was not strong enough to discard the Iron doping possibility without finally considering the price of both elements as well.

Both Iron and Chromium options do not seem to bring any extra future supply restriction since both elements are more abundant than Lanthanum or Nickel. Comparatively to each other, Iron presents an obvious advantage over Chromium because it is evidently much more abundant in the earth's crust. Regarding the prices of both elements, Iron once more presents an abysmal advantage over chromium, therefore, the following results of structural purity estimations, performance and impedance measurements are relative to this selected element. Using two distinct ratios of Titanium and Iron, the following results are an attempt to find the implications this dopant ratio in the structural stability, since previous chapters have shown the calcium doped perovskite to have much lower purity estimations. Testing both the same ratio as Manganese in the Chapter III (with $La_{0.7}Ca_{0.3}Ti_{0.5}Fe_{0.4}Ni_{0.1}O_3$) as well

as a comparatively higher ratio of Titanium (in $La_{0.7}Ca_{0.3}Ti_{0.7}Fe_{0.2}Ni_{0.1}O_3$), the present study attempts to understand if the performance results of the Manganese perovskite can be improved and if similar calcium perovskite purities improve through increasing the Titanium ratio.

4. Experimental procedures

After selecting the new B site dopant to replace Manganese, a strategy was defined in order to study the performance of the new dopant comparatively to the previous one (keeping the same 0.4 doping ratio). Two iron doped perovskites such as $La_{0.7}Ca_{0.3}Ti_{0.5}Fe_{0.4}Ni_{0.1}O_3$ (LCT0.5F0.4N) and $La_{0.7}Ca_{0.3}Ti_{0.7}Fe_{0.2}Ni_{0.1}O_3$ (LCT0.7F0.2N) were synthesised so that a dopant ratio closer to the mentioned successful exsolution report [285] can provide some information regarding the performance evolution along with the doping amount while keeping some novelty on the A site with the Calcium element instead of Strontium. Prior to obtaining the performance and electrochemical impedance spectra (EIS) results, a brief structural Xrd analysis took place in order to estimate the optimum calcination conditions in regards to the estimated desired phase structural purity.

4.1 SDC electrolyte pellet synthesis

The SDC electrolyte powder was firstly hand grinded in a mortar and then pressed in a hydraulic pressing machine at 2 MPa for 35 seconds in portions of 0.3 g. These pellets were then fired at 1400 ^oC for 5 hours and posteriorly polished in both sides for thickness minimization and surface smothering.

4.2 Electrode powders preparation

Two distinct ratios of Iron doping perovskites (LCTFN) such as $La_{0.7}Ca_{0.3}Ti_{0.5}Fe_{0.4}Ni_{0.1}O_3$ and $La_{0.7}Ca_{0.3}Ti_{0.7}Fe_{0.2}Ni_{0.1}O_3$ were synthesized through solid state reaction. Analogously with the Manganese doped perovskites tested in previous chapters, an ethanol solution of the oxides in the proper proportions was ball milled for 1 and a half hour at 400 rotations per minute (rpm). The grinded solutions were dried at 75 ^oC and then calcined at multiple temperatures starting at 1000 with an increment of 50 ^oC, before defining the calcination conditions.

4.3 Slurry synthesis and cell assembly

Both slurries are created by adding 1, 2 and 10 mL of glycerol, ethylene glycol and isopropyl alcohol (respectively) for each gram of calcined powder. The ball mill mixed each of the compositions for one and a half hour at 400 rpm, so that they could later be spray painted on the SDC electrolyte pellets. High temperature resistant tape pierced with an office hole puncher provided the circular painting area (of 0.23758 cm^2) concentric with the SDC pellets. The symmetrical cells were created by spray painting 7 layers on both sides of the pellets with the same slurry and then sintered at 1000 ^oC during 5 hours.

After sintering the electrodes, four layers of silver current collector were brush painted in both electrode areas. The silver current collector is a mixture of 0.2 grams of polyvinyl butyral (PVB) and 1 gram of silver paste diluted into 10mL of pure ethanol. Once the sample surfaces are dried, silver wires were attached on each of the cell sides with silver paste and later set to dry for half an hour at 180 ^oC. In order to be tested, each of the wired cells were sealed on alumina tubes that were assembled into a sample holder which was later introduced in the furnace that provides the thermal operating conditions.

5. Experimental results

5.1 XRD analysis

In attempts to choose the best calcination temperature, samples in both ratios were calcined at several temperatures starting from 1000 ^oC up to a maximum of 1400 ^oC with a constant gap of 50 ^oC. Each of the powders were then analysed through X-ray diffraction (XRD) on a Bruker D8 Advance diffractometer (Cu $K\alpha_1$ radiation) followed by their respective Rietveld refinements carried out in MAUD [144] (Materials Analysis Using Diffraction) software developed by Luca Lutterotti [145] - [149]. The chosen source of crystallographic information was the project Crystallography Open Database (C.O.D.) [150], which is an open-access collection of crystal structures [150] - [156]. In every refinement, the existence of both the main P m -3 m space group (number 221) and the trigonal P 3 2 1 (number 150) were considered.

Both of the ratios share an overall improvement in their P m3 m peak intensities as well as a reduction of non-perovskite aspects as the calcination temperature increases. The refinement parameters are also globally enhanced along with the temperature, however the calculated P m -3 m lattice displays an irregular trend in the compound with the lowest Iron ratio. The refinement calculations in the Iron ratio of 0.4 (Figure VI 5 and Figure VI 6) match the common sense first impressions of simply displaying minor unit cell differences directly related to the phase peak shifts from the fact that the displacement variables are generally lower in comparison to the other perovskite. According to the refinements, both the stronger displacement parameters as well as their smaller lattice lengths are providing the observed peak shifts in this 0.4 dopant ratio material calcined at 1250, 1350 and 1400 ^{o}C. Regarding the remaining calcination temperatures, the displacement, specific orientation and unit cell parameters do not reveal considerable alterations.

As for the perovskite with lower dopant ratio (Figure VI 7 and Figure VI 8), a naked eye observation could suggest these samples to be easily paired in two groups. The four highest temperatures display similar refinement results, so the remaining profiles would belong to the second group, however, this is not entirely the case. Though the samples calcined at 1150 and 1200 ^{o}C seem to display a similar profile that is only enhanced by peak definition, the refinements show that their apparent similarities are an equilibrium between higher displacement variables with a lower lattice parameter and respectively, the opposite behaviour. As for the three lower calcination temperatures the displacement values are strong, but there is no clear tendency observed in the perovskite unite cell, which has an enormous variation between 3.797 and 3.915 Å. Even though the peak widths are strongly quantified with higher microstrain values, it should also be noticed that these three refinements revealed substantially worse agreement parameters, where all weighted profile R-factors (R_{wp}) became higher than 10. The samples calcined at the two highest temperatures indeed display similar values of both displacement variables as well as estimated lattice parameters, but the slight peak shifts observed (at 1250 and 1300 ^{o}C) seem to result not only from an increase of the unit cell lattice parameter, but also from the the lowest displacement values.

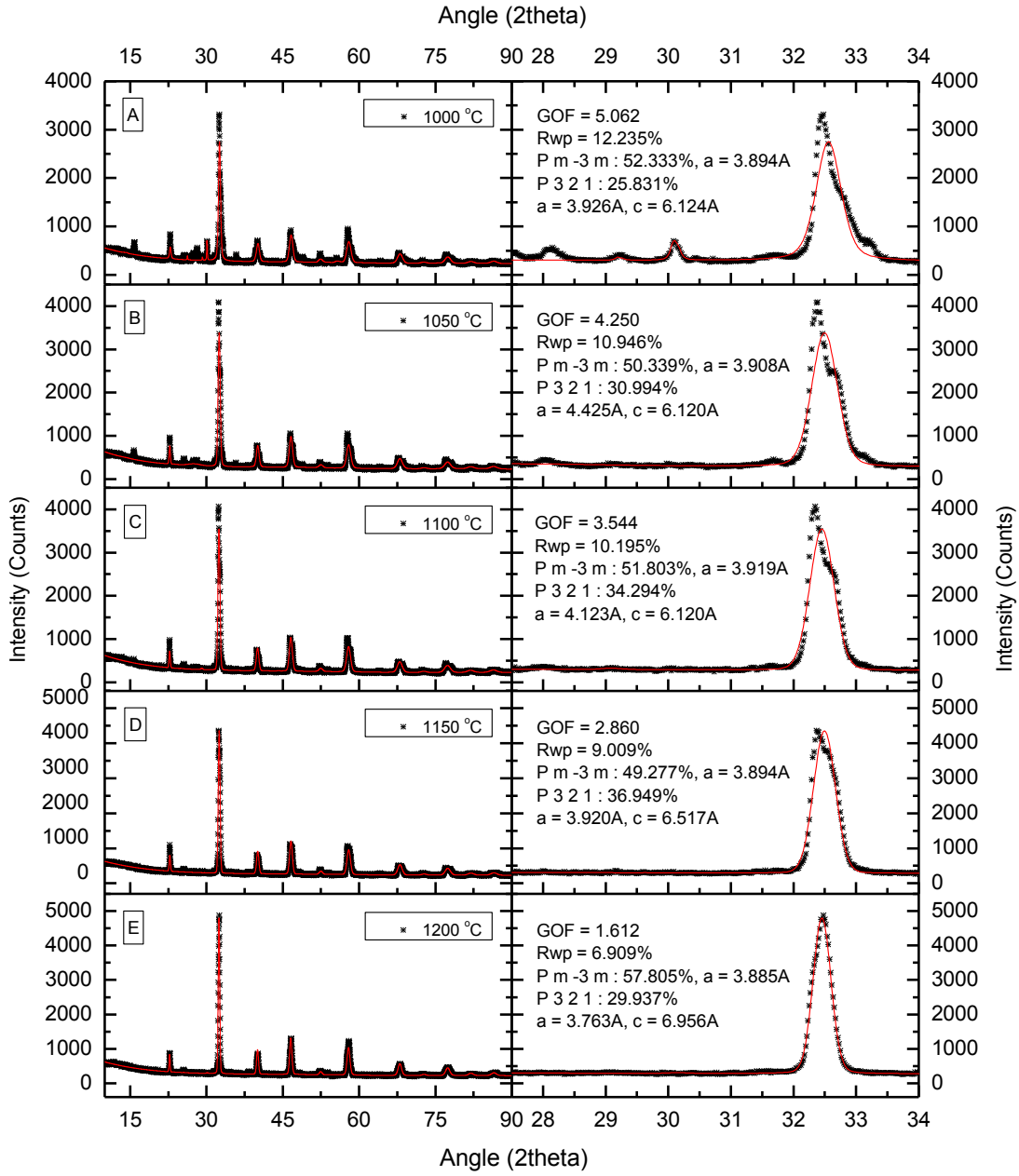

Figure VI 5 - Xrd refinements of the $La_{0.7}Ca_{0.3}Ti_{0.5}Fe_{0.4}Ni_{0.1}O_3$ perovskite calcined at several temperatures from 1000 ºC (top) to 1200 ºC (bottom) with zoomed view in the 2theta region from 27 to 34 at the right

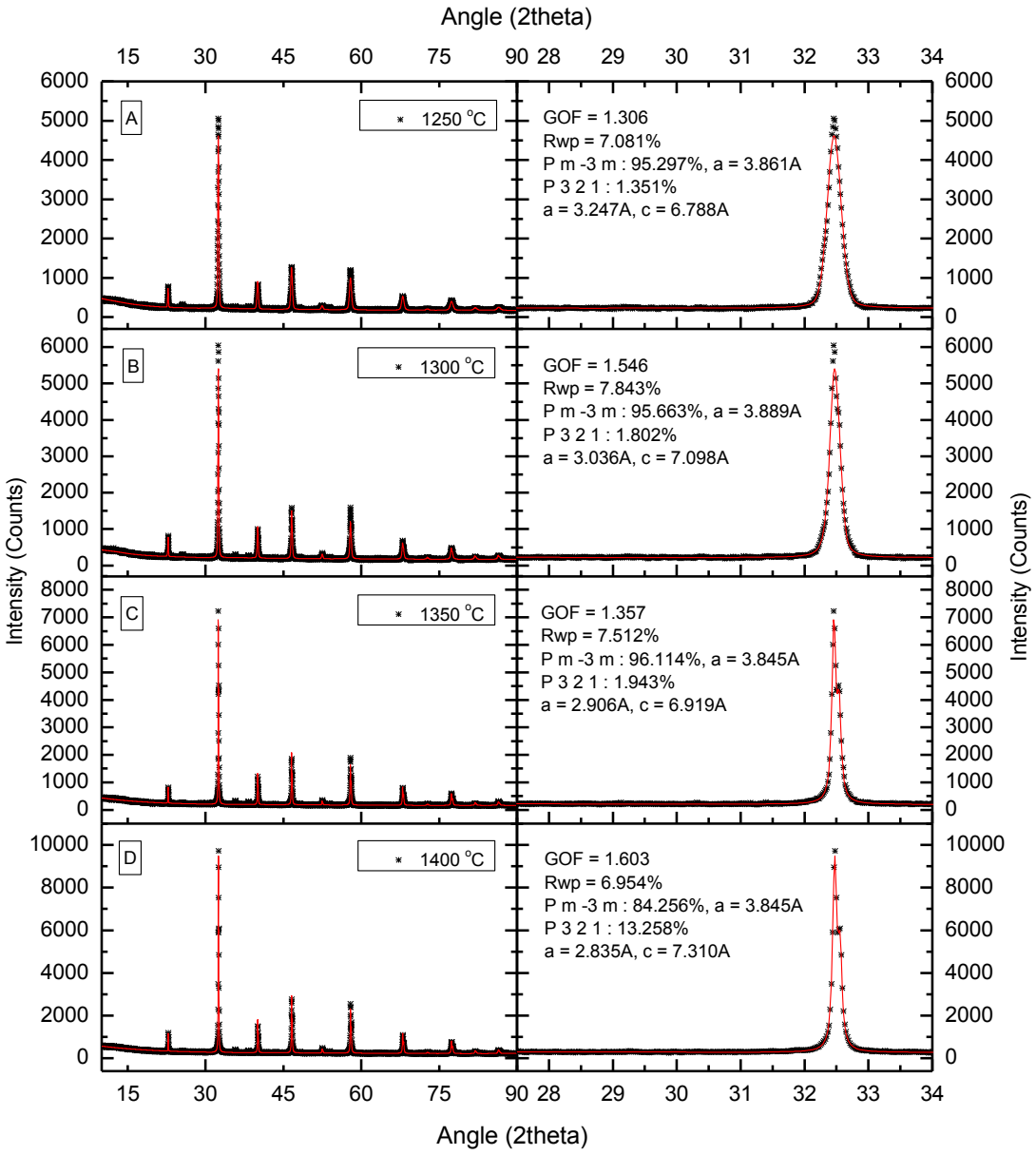

Figure VI 6 - Xrd refinements of the $La_{0.7}Ca_{0.3}Ti_{0.5}Fe_{0.4}Ni_{0.1}O_3$ perovskite calcined at several temperatures from 1250 °C (top) to 1400 °C (bottom) with zoomed view in the 2theta region from 27 to 34 at the right

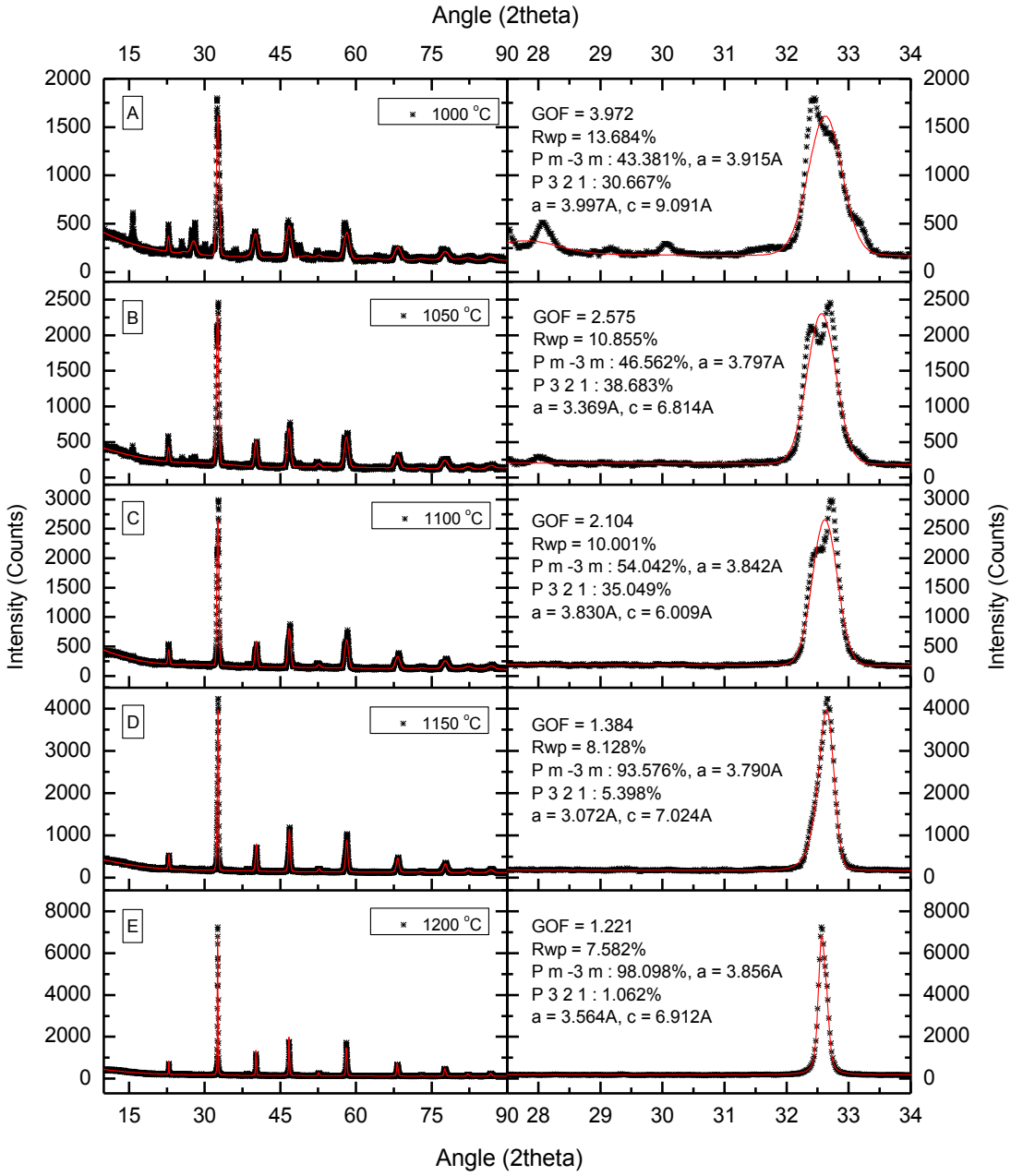

Figure VI 7 - Xrd refinements of the $La_{0.7}Ca_{0.3}Ti_{0.7}Fe_{0.2}Ni_{0.1}O_3$ perovskite calcined at several temperatures from 1000 ºC (top) to 1200 ºC (bottom) with zoomed view in the 2theta region from 27 to 34 at the right

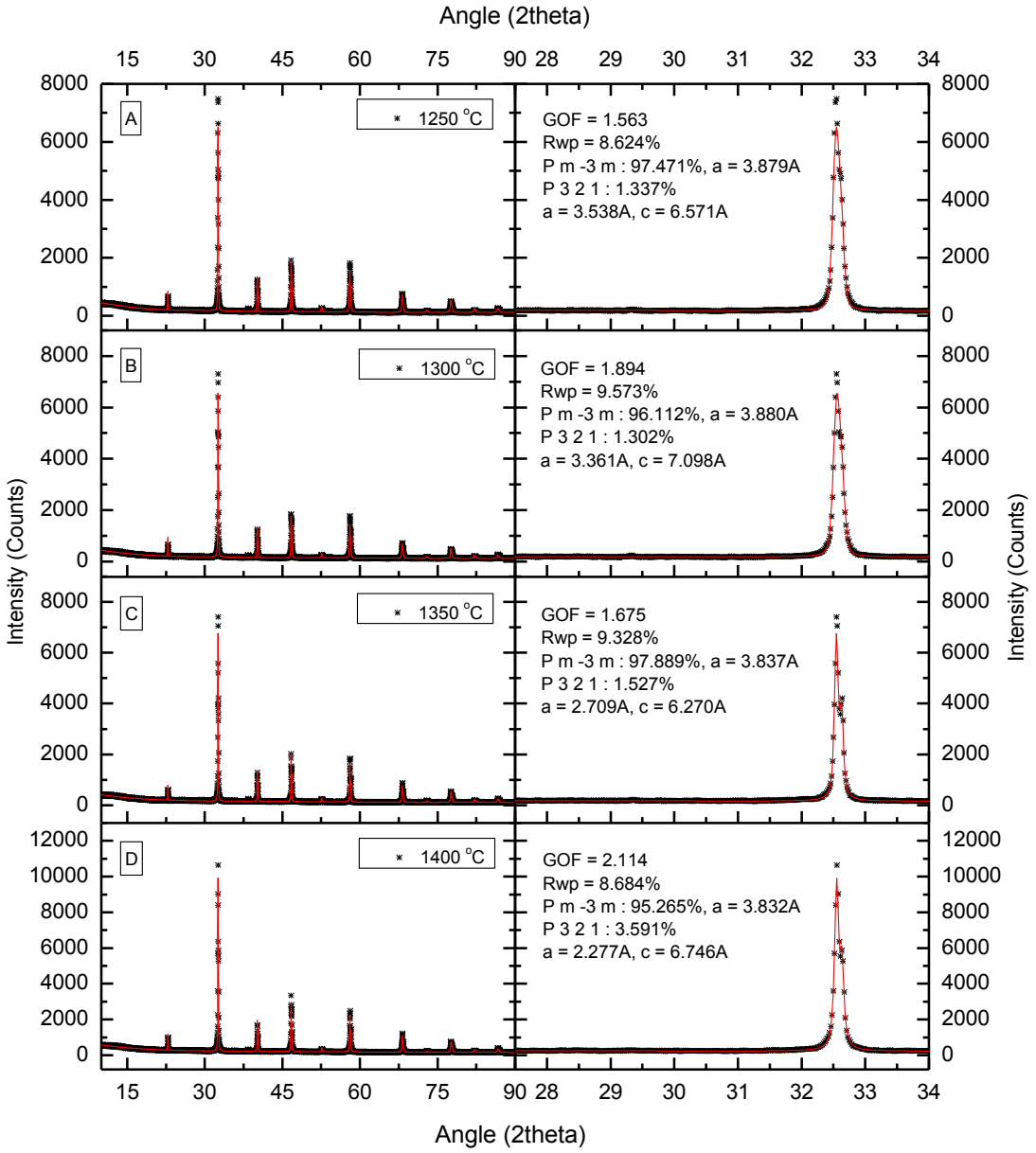

Figure VI 8 - Xrd refinements of the $La_{0.7}Ca_{0.3}Ti_{0.7}Fe_{0.2}Ni_{0.1}O_3$ perovskite calcined at several temperatures from 1250 ºC (top) to 1400 ºC (bottom) with zoomed view in the 2theta region from 27 to 34 at the right

5.1.1 Perovskite purity variation with calcination temperature

From the XRD experimental and computed data, the P m -3 m space group purities were once more estimated simply from the relation between each profile peak intensities (Equation IV 1). Just as in the prior Chapter IV, the peaks were defined assuming requirements of minimum and maximum tip widths (of 0.01 and 1 respectively) as well as a base width of 2 degrees in the 2theta scale so that the minimum second derivative method could be applied.

Since only one impurity phase was matched, several non-perovskite peaks can belong to the same second impurity phase or (in the extreme scenario) each peak can simply define a new phase. From this fact, two purity extreme concepts where created in order to establish the trust gap where the true purity value resides. If all the unknown peaks belong to the same impurity phase, then the purity calculation would only take into consideration the highest impurity peak, consequently resulting in an over estimated purity calculation which this work defines as Maximum Purity. In the same way, now it becomes easy to understand that the other extreme case scenario is simply the assumption that the main P m -3 m phase is the only one allowed to contain more than one peak. Obviously this results in the under estimation of the resultant calculated purity. Through this analysis this variable will simply be addressed as Minimum Purity. In both cases the purities were calculated from experimental and computed data to find out if significant differences between real data and the computed models could be spotted. Plotting the calculated purities from both sources in both materials easily displays the phase definition improvements. The differences between the Maximum and Minimum Purities decrease significantly as the temperature increases (Figure VI 9), which means that the temperature is not only providing higher values of purity but also greater assertiveness within these calculated values.

Comparing both perovskite trends, it seems the superior ratio of Iron is increasing the minimum temperature requirements to obtain the higher purity levels and also decreasing the temperature window at which those levels can be achieved roughly by half (from a gap of 200 to 100 ^{o}C). This means that the perovskite structure is thermally easier to be obtained from increasing the titanium ratio over the iron one. Both specimens seem to display the end of the higher purity gap before reaching the highest calcination temperature (where the sample with the highest amount of Iron shows a much sharper purity decrease). As for the lattice parameter, the variation gap seems to be larger where less Iron was doped.

This material is aimed to be used as an electrode of a Solid Oxide Fuel Cell, where ionic conductivity plays an important role in its performance. The lattice expansion phenomena have been consistently justified with the formation of oxygen vacancies. Some oxides may display the opposite effect of a lattice shrinkage [305] - [306] or even no lattice size change at all [307]. However, regarding perovskite materials, the unite cell lattice consistently expands in the presence of oxygen vacancies [308] - [314]. This does not entirely mean that a larger lattice parameter

directly implies a superior oxygen vacancy concentration, however it is still a possibility strongly supported by the average Iron valency state decrease [312], [315]. Another possible indicator of the presence of oxygen vacancies is the shift of the perovskite peak (0 0 2) located around 47º to lower angles [315] which in both cases also corresponds to the larger unit cell within the high purity window of each of the specimens. In short, the chosen calcination temperature to be used in both iron weighting ratios performance comparison is 1300 ºC from the fact that it is believed to be the optimal choice that balances high purity with decent lattice length.

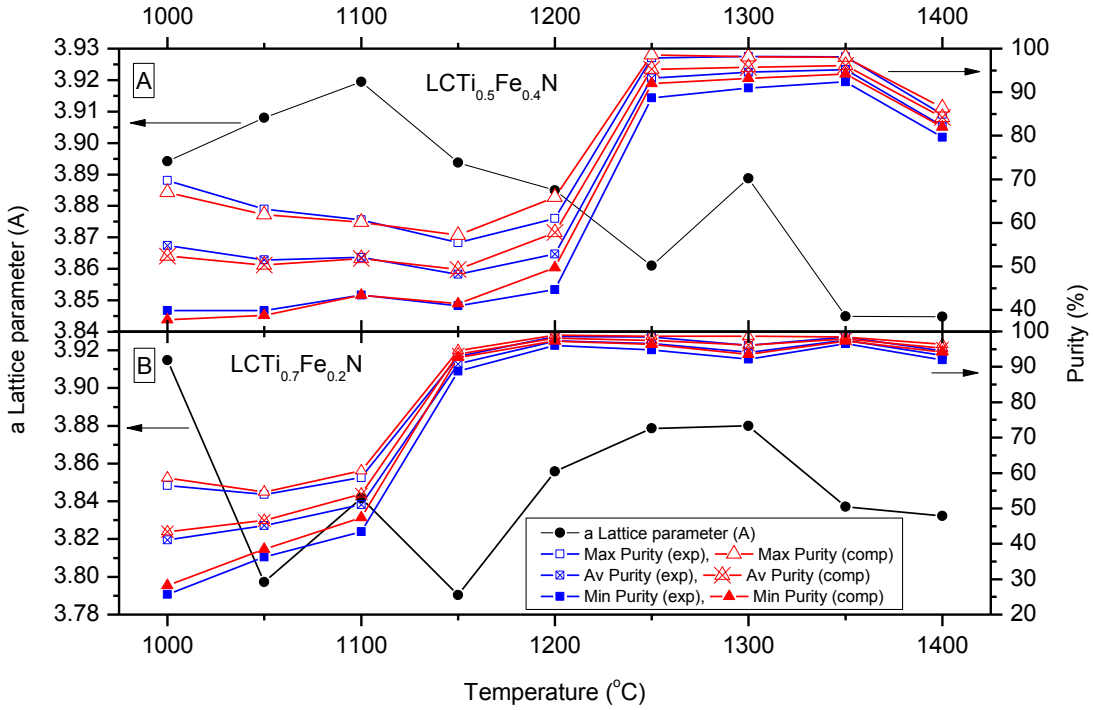

Figure VI 9 - Perovskite purities and the calculated P m -3 m lattice parameter of $La_{0.7}Ca_{0.3}Ti_{0.5}Fe_{0.4}Ni_{0.1}O_3$ (A) and $La_{0.7}Ca_{0.3}Ti_{0.7}Fe_{0.2}Ni_{0.1}O_3$ (B) powders along with the calcination temperature

5.2 Performance and impedance of symmetrical cells

Performance and impedance results of symmetrical cells with the iron ratios of 0.4 and 0.2 were successfully obtained (Figure VI 10), however, the results are not promising. As expected, the higher power densities are observed in the cells with the electrode which revealed the lower polarization resistance values. These differences in the polarization resistances of each electrode increased severely as the

temperature decreases, however the fact that the open circuit voltages (OCV) are much lower in the higher performance sample is unexpected. Since such low peak power densities (PPD) were obtained, no time was invested in further parameter estimations from these results such as the activation energy. From this very same reason, also no further XRD analysis (such as after submitting the electrode powders under reducing conditions) took place in order to see if the Nickel peak could support the occurrence of the ex-solution phenomena.

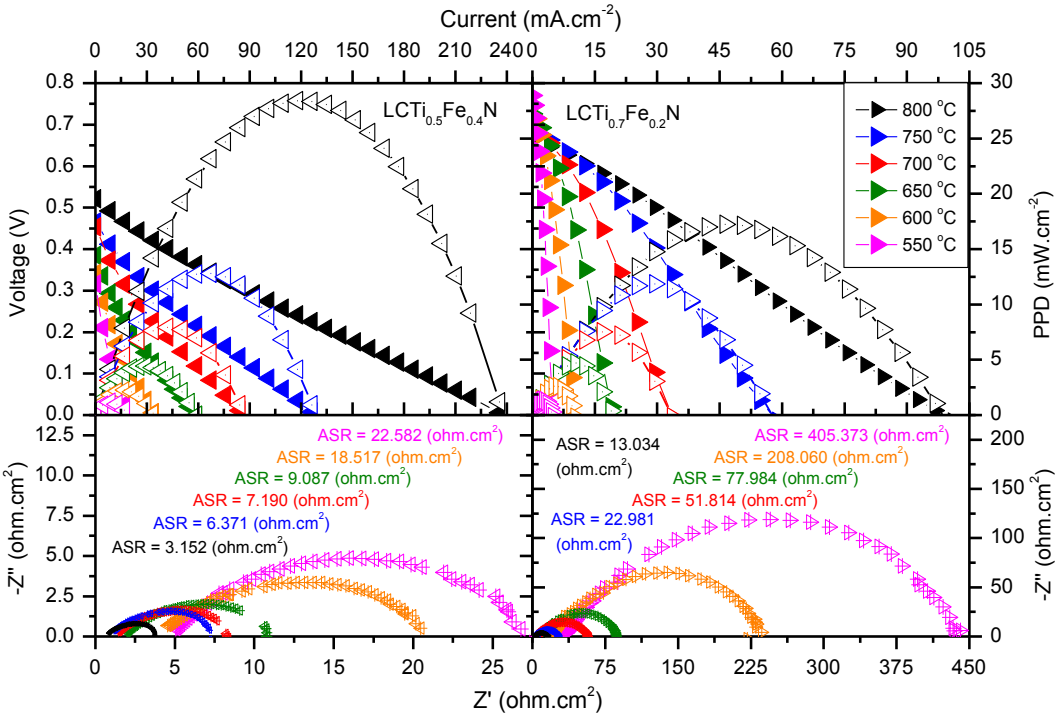

Figure VI 10 – I-P I-V (top) and respective total impedances (bottom) at temperatures from 550 ºC to 800 ºC of $La_{0.7}Ca_{0.3}Ti_{0.5}Fe_{0.4}Ni_{0.1}O_3$ (left) and $La_{0.7}Ca_{0.3}Ti_{0.7}Fe_{0.2}Ni_{0.1}O_3$ (right)

The conductivity property was attempted to be studied, however it was impossible to fully densify the LCTFN samples into bars. Even raising the temperature profile to 1400 ºC during 10 hours, none of the samples were able to hold a drop of water on the surface, which means they fail first densification test. Despite not having conductivity measurements of these compounds, it is well known that Iron is roughly 4 times more conductive than Titanium, therefore it is possible that this aspect might play a role in the electrode performance. The fact that lower polarization resistances

were observed in the sample with a superior Iron ratio also supports this hypothesis in which the conductivity influences in the performance.

There is still a valid possibility to be pointed out from these results which comes from the direct comparison with Chapter III results where Manganese takes the place of Iron. The relevant considered scenarios in which Manganese cation can possibly be a better match than Iron belong exclusively to the four scenarios where the titanium valency state is considered to be 4+ (Table VI 1).Since the Iron doped perovskite was not found to be an improvement over LCTMN, then it is valid to conclude that if a tolerance factor closer to the unity (which theoretically is a better match) really increases the performance results, then the Ti^{+3} species must be dominant over the remaining oxidation states of Ti^{2+} and Ti^{4+}.

6. Summary

After expressing the reasons behind the Manganese cation replacement within the perovskite structure of LCTMN, the present work defines a strategy to attempt to find the best possible cation through establishing criteria to gradually eliminate unsuitable candidates in a methodical process of selection (Table VI 2). Choosing Iron led to much worse performance results and the attempts to manufacture samples to measure the conductivity of both electrodes failed due to insufficient calcination temperature conditions, leaving room to a mere humble hypothesis based on the fact that Iron conductivity is approximately 4 times higher than Titanium. This could indeed explain the higher performance obtained in the samples with higher iron ratios, however, not only there is no concrete proof of the conductivity influence in these results as Manganese conductivity is also much lower than Iron's thought the performance results of LCTMN were much higher. Even though the polarization resistances agree with the power density curves, unexpectedly the OCV values were higher in the samples with lower performance results.

Table VI 2 - Elimination proccess to selection the Iron candidate where in each of the 5 criteria the elements in green pass the criteria and the elements in red are eliminated in that particular criterion preventing them from being reconsidered in the following step

Criterion	CN = 6	State & others	Ellingham diag.	Lit. info.	t & value
Elements	Fe ->	Fe ->	Fe ->	Fe ->	Fe ->
	Cr ->	Cr ->	Cr ->	Cr ->	Cr
	W ->	W ->	W ->	W ->	W
	V ->	V ->	V ->	V ->	V
	Si ->	Si ->	Si ->	Si	
	Ge ->	Ge ->	Ge ->	Ge	
	Mo ->	Mo ->	Mo ->	Mo	
	Au ->	Au ->	Au		
	Ag ->	Ag ->	Ag		
	Co ->	Co ->	Co		
	Cu ->	Cu ->	Cu		
	Ir ->	Ir ->	Ir		
	Pd ->	Pd ->	Pd		
	Pt ->	Pt ->	Pt		
	Rh ->	Rh ->	Rh		
	Ru ->	Ru ->	Ru		
	N->	N			
	F->	F			
	Cl->	Cl			
	S->	S			
	P->	P			
	Se->	Se			
	As->	As			
	Br->	Br			
	Pu->	Pu			
	Np->	Np			
	I->	I			
	Te->	Te			
	C->	C			
	Tc->	Tc			
	U->	U			
	Os->	Os			
	Re->	Re			
	Ru->	Ru			
	+ 59 others	+ 59 others			

The most valuable resultant hypothesis from this analysis hints that Manganese might actually already be the best element if a tolerance factor value closer to 1 really improves the performance. This would mean that, the 3+ state of oxidation of Titanium would have to be dominant over the remaining possibilities. It is possible to find further support or complete disproval of this hypothesis through an X-ray photoelectron spectroscopy (XPS), however, time restrictions prevent further analysis on this possibility. Improving the dopant-host match in the perovskite B site might not have such an evident effect in the performance results as previously pondered, though if it has, further evidence is required.

Chapter VII - Conclusions

1. Introduction

Relating the most important aspects from the previous chapters, the following analysis concludes the comparison between the studied perovskites of the LAemTMN form. The dopant implications in the aspects of performance, impedance, structure stability, segregation tendency and conductivity are addressed accordingly. A deeper analysis solely focused into understanding the conductivity intrinsic regime implications in the performance of the materials as anodes gave birth to a simple mathematical approach which attempts to describe the bridge between both variables within defined temperature restrictions. The model suggests that it is possible to quantify the intrinsic conductivity implications into the performance accounting for a silver infiltration phenomena with errors of about 6% between calculated and experimental data. A future direction to study the composition of LCTMN + 40%SDC as an anode material is identified as the optimal direction output from this extensive comparison between both LAemTMN perovskites. This analysis is believed to bring a much closer comparison between the suggested compound and the current state of the art anode SOFC high performance materials.

2. Proposed theory to explain the results

The humble concept of segregation tendency (Equation IV 3) attempts to explain the results obtained in the HAADF-STEM analysis where the LCTMN's higher segregation tendency as well as its inferior homogeneity is also well observed. The fact that Calcium reduction (according to its Ellingham diagram) would require even more energy comparatively to any of the other elements (Figure VII 1), leads to believe that the phase purity decrease under reducing conditions is likely to be a consequence of the Nickel segregation, instead of being the cause of it. The Strontium's location in the Ellingham diagram could also support its popularity together with Lanthanum due to simply being the balanced solution between the following aspects of having its size to be providing an intermediate structure stabilization (in the presence of a segregation event) also together with an intermediate conductivity contribution. The later observed superior conductivity of

LCTMN is supported by both its superior segregation tendency as well as by its smaller B site octahedron volume [262], a hypothesis that led to a deeper analysis of the conductivity under both oxidizing and reducing conditions.

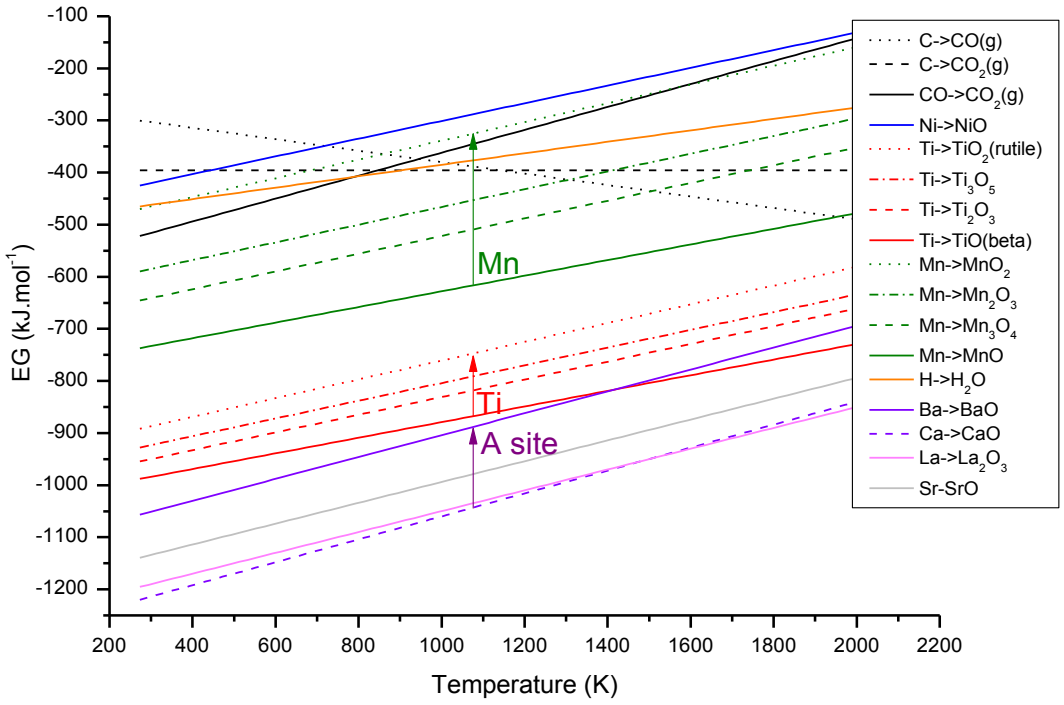

Figure VII 1 - Ellingham Diagrams of the element oxides on the B site (Titanium, Manganese and Nickel), on the A site (Lanthanum, Barium and Calcium) as well as the oxides of Strontium, Carbon and Hydrogen [202]

The superior performance of LCTMN as a symmetrical material is believed to come from a significant anodic behaviour improvement (as Chapter III shows). This idea seems to be a consequence of a conductivity improvement especially at higher temperatures under reducing conditions where the relative differences in both variables seem to be highly related (Figure VII 2). The differences in PPD (from chapter III section 4.5) between the averages of each specimen were plotted together with the respective conductivity differences to attempt to eliminate the common factors between each material while focusing the observations on the resultant difference from the cation substitution. Since under reducing conditions, the conductivity thermal behaviour could only be described through the consideration of at least 2 regimes, the same considerations were applied to the performance results,

considering once more both thermal regimes. Even superior correlation coefficients were found in the linear regressions of the PPD differences, a fact that suggests that there seems to be a strong relationship between both variable differences in regards to their thermal regime adaptation. Moreover, the fact that these PPD differences seem to also display the presence of both thermal regime influences can also mean that the influence of the intrinsic regime in the cell's output performance is stronger than simply the influence of the conductivity values.

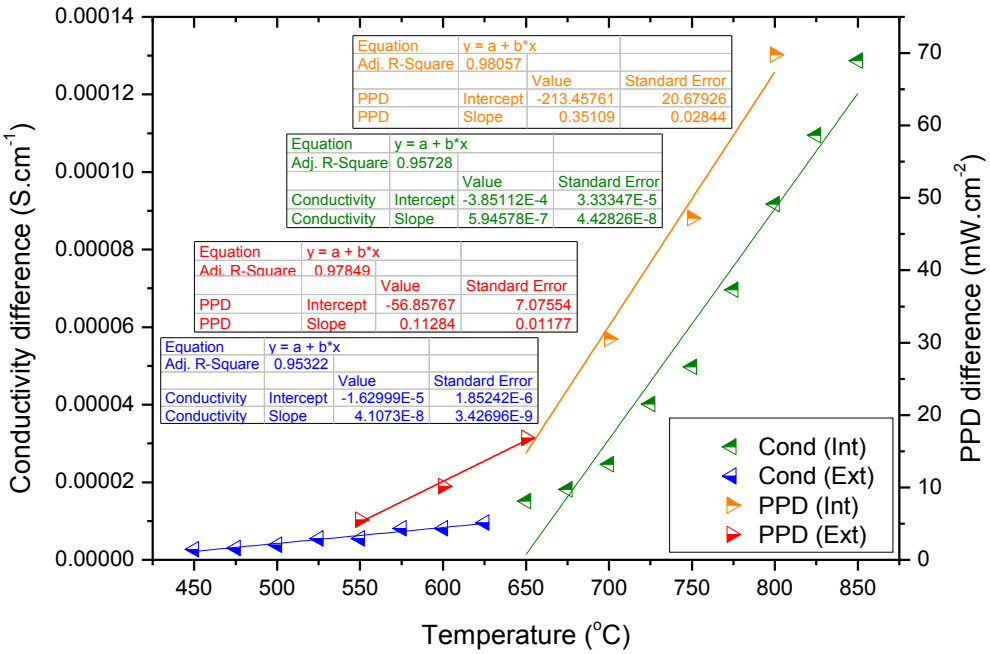

Figure VII 2 - Single cell peak power density differences (from section 3.5 of Chapter III) and the conductivity differences in hydrogen between the LCTMN and LBTMN perovskites separated by Extrinsic and Intrinsic regime assumptions

If the same differences are calculated using the conductivities measured in air, not only a single thermal regime is enough to describe the whole range of conductivity points, as the PPD respective differences (now obtained from the cells in Chapter III section 3.4) do not fully follow the same ascendant tendency. Observing smaller conductivity differences under the intrinsic regime together with larger PPD differences as well as larger conductivity differences (in air) paired with smaller differences of performance, one could conclude that the influence of conductivity is

stronger under reducing conditions. Since the LAemTMN materials share some compositional similarities with the well-known LSM ($La_xSr_{(1-x)}MnO_3$) cathode [98], [102] - [103], it is also reasonable to accept that the limiting factor where improvements could potentially emerge would be in the anodic performance, and as results have shown, both lanthanide cathodic performances are extremely close to each other.

Some aspects can further improve this analysis and it is still important to understand some of its limitations. It should be acknowledged that reducing the PPD temperature step from 50 to 25 ^oC as well as acquiring more PPD measurements at lower temperatures could strengthen this upcoming section 2.1 hypothesis. Furthermore, according to previous assumptions, the PPD difference point located at 650 ^oC would belong solely to the intrinsic regime, however, the lack of I-V data at lower temperatures (and the fact that its difference from the highest extrinsic temperature point considered is 25 ^oC) made it reasonable to consider this data point to belong to both regimes.

2.1 Anodic performance as an intrinsic conductivity consequence hypothesis

Pushing the narrative of the Anodic performance as a consequence of the respective conductivity under (reducing conditions), efforts were made to attempt to create an expression to describe one variable in function of the other. The presented model simply assumes the potential difference as a linear function of the current density (Equation VII 1), in which the resistive factor pushing this voltage down is taken to be the Area of Specific Resistance (ASR). From this modest assumption, two main approximations arise as direct consequences. Firstly the Power Density curve is taken to be approximately symmetric, a reasoning that is also now reflected in the respective current density (Equations VII 2).

$$V(j) = -ASR.j + V_{OCV}$$

Equation VII 1 - Linear assumption of the Voltage in function of the current density "V(j)", where "ASR", "j" and "V_{OCV}" are respectively the Area of Specific Resistannce, the current density and the Open Circuit Voltage (respectively in $\Omega.cm^2$, $A.cm^{-2}$ and V)

From the fundamental definition of Power (P=V.I) and the Pouillet's law (previously summoned in the deduction of Equation V 6) it is possible to write an expression to describe the Peak Power Densities of the electrodes assembled as anodes in function of the intrinsic conductivity in hydrogen "PPD(σ_{int})". After using this expression (Equation VII 3) to calculate the "Anodic Peak Power Densities" (PPD_{anodic}), a simple comparison with the respective real performance values (measured in section 3.5.1 of Chapter III) took place.

$$\begin{pmatrix} V_{PPD} \cong \frac{1}{2} V_{OCV} \\ j_{PPD} \cong \frac{1}{2}\left(\frac{V_{OCV}}{ASR}\right) \end{pmatrix}$$

Equations VII 2 - Consequences of the linear assumption where V_{PPD}, V_{OCV}, j_{PPD} and ASR are the Peak Power Density voltage, the Open Circuit Voltage, the Peak Power Density's Current density and the Area of Specific Resistance (respectively in V, V, A.cm^{-2} and Ω.cm^2)

$$PPD_{anodic} = \frac{1}{4} V_{OCV}^2 \frac{\sigma_{(in\ H_2)}}{l}$$

Equation VII 3 - Peak Power Density in function of the Conductivity in H_2, where the PPD_{anodic}, V_{OCV}, σ and l are the expected Peak Power Density, the Open Circuit Voltage, the conductivity in hydrogen, and the electrode thickness (respectively in mW.cm^{-2}, V^2, S.cm^{-1}, cm)

The applied model provides surprisingly close results, however, as expected, the power density only provides reasonable predictions within the intrinsic temperature gap (where t>600ºC). In these conditions, the average errors of 6 and 7% can be found in the Barium and Calcium perovskites respectively. The importance of staying within this thermal regime is evident at 550ºC where the error of both predictions displays errors larger than 50%. This is understandable from the fact that not only at lower temperatures the values of performance will be smaller (making it so that in the presence of a similar standard deviation the relative error becomes much larger), but also once outside of the intrinsic temperature regime, the linear variation of the conductivity will provide a different increment (or slope) in the conductivity values.

It is mandatory to notice that this simple SOFC model is outputting these close performance estimations under the assumption of an optimum anode thickness "l" of

1.756 µm, which SEM pictures (Figure III 17 C and D) have already shown this to be an underestimation, revealing values of 4-5 µm. However, these pictures have also revealed a phenomena of silver infiltration in both anode sides. Since silver is the most conductive metal there is, then it is plausible to assume that the anode conductivity is underestimated by the 4 probe measurements under reducing conditions, where the bars have an "l" distance of 15 mm. This length between the voltage probes effectively turns any silver infiltration phenomena much less significant, providing this way an accurate value of the perovskite conductivity under reducing conditions, however it does not accurately describe the reality displayed in the anodes of that very same material during cell operation conditions as well as the SEM cross sections do.

Establishing that the conductivity of silver infiltrated anode is indeed larger than the perovskite conductivity, the new goal of quantifying this gain naturally emerged based on the ratio "$\frac{\sigma_{(in\ H_2)}}{l}$" adjustment. The simple model (Equation VII 3) to estimate the performance based on the conductivity can be seen as containing only 2 independent variables simply because the OCV values are obtained from real PPD measurements. Focusing on the relevant quotient, it is easy to understand that the same ratio can be introduced in the model through 2 different ways, which means that a conductive material that is also thick can output the same result comparatively to a thinner but more resistive material.

As it was stated, the optimum performance estimation results which yelled errors of 6 and 7% were obtained adjusting an electrode thickness of 1.756 µm ($PPD\left[\sigma_{(in\ H_2)}, l = 1.756\mu m\right]$). Since SEM pictures suggest this thickness to be around 4-5 µm, then if the real thickness is 4.5 µm, then this means the real anode conductivity values are about 2.56 times larger than pervious considerations with the bars of the 4 probe method results (such as $\frac{l_{from\ SEM}=4.5\mu m}{l_{optimized}=1.756\mu m} = 2.56 = \frac{\sigma_{silver\ infiltrated\ anode}}{\sigma_{bars\ of\ 4\ probe\ method}}$). Obviously the average expected error between both materials for a multiplier of 2.56 is 6.509%, which is exactly between the previous 6 and 7%. Still, taking into consideration the SEM electrode thickness information, the lowest errors between the model and real data (Figure VII 3) were obtained for conductivity factors of 2.57 and 2.46 with respective errors of 6.03 and 5.30% (for LBTMN and LCTMN correspondingly).

Minimizing the errors of both materials individually allows the exclusion of the idea of LCTMN to have a greater benefit from the anodic silver infiltration aspect

comparatively to LBTMN. Not only are both factors roughly similar (2.57≈2.46) but also even if this difference is taken into consideration, then the Barium doped perovskite seems to benefit more from the silver infiltration phenomena. Regardless, the model results seem to provide a fair and extremely practical anodic performance estimation under intrinsic regimes of temperature. Both multiplier values (of 2.57 and 2.46) suggest that perhaps a general function to quantify the anode silver infiltration phenomena into the conductivity of LAemTMN materials could be done by adjusting the constant of $^1/_4$ to $^5/_8$ (as seen in Equation VII 4).

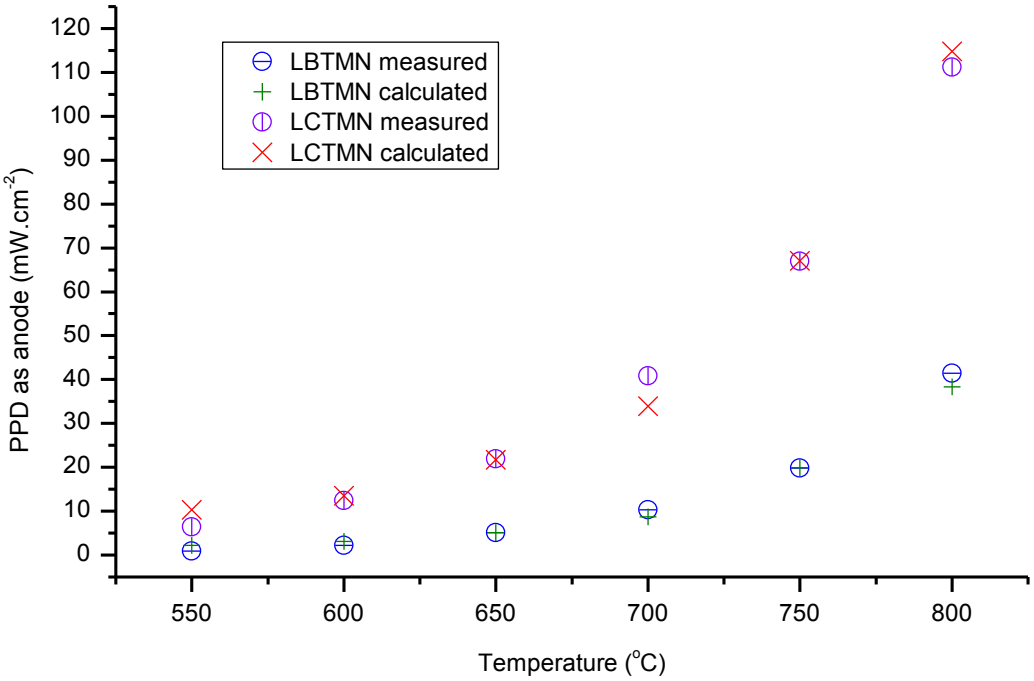

Figure VII 3 - Comparation between the calculated and measured average PPDs of LBTMN and LCTMN

$$PPD = \frac{5}{8} V_{OCV}^2 \frac{\sigma_{(in\ H_2)}}{l}$$

Equation VII 4 - Peak Power Density in function of the Conductivity in H_2, where the PPD, V_{OCV}, σ and l are the expected Peak Power Density, the Open Circuit Voltage, the conductivity in hydrogen, and the electrode thickness (respectively in $mW.cm^{-2}$, V^2, $S.cm^{-1}$, cm)

3. Future work

In order to really understand how far the studied material really is in terms of performance comparatively with the used bench mark anode material, two suggestions are believed to work together towards a deeper understanding of the relevant phenomena influencing the performance of the studied perovskite. The LCTMN electrode composition can still be altered through the addiction of 40%wt of SDC, similarly to what was done in the synthesis of NiO+SDC (described in the section 2.1 of Chapter III). Just like the impregnation technique, this SDC inclusion would increase the number of triple phase boundaries (TPBs). On the other hand, given the fact that the presented results revealed the conductivity as a major inhibiting factor in the performance, the compound LCTMN+40%wt of NiO could also be tested so that a further performance effect can be seen through the comparing both suggestions with the basic perovskite material. Starting from electrolyte supported cells and following the analysis with corresponding anode supported cells, the chemical compositions of 60%LCTMN+40%SDC/40%NiO seem to be the optimal starting direction output of this research (also given the fact that literature review already revels this ratio as the most commonly used).

The SDC electrolyte material is also known to have some electrical conductivity, being the reason behind the typical lower OCV values comparatively with other electrolyte materials such as Yttria based or LSGM. With this in mind, the best performance results from the previously suggested materials assembled as anodes could be further tested with a buffer layer to reduce the conductivity of the electrode, improving the OCV, consequentially improving the cell's resultant performance. This further optimization can take place after the best anode candidate is found so that the competitiveness aspect of the resultant material can also be understood, potentially providing knowledge of how well the extensively studied perovskite material would perform in a scenario much closer to the current SOFC anode state of the art materials.

As explained in the precious section, since it was observed that the silver infiltration in the anode sides of the LAemTMN perovskites seems to boost their conductivities by a factor of 2.56, then the real anode conductivities could still be measured through the Van Der Pauw method [316] - [317]. This procedure can potentially bring further agreement or disproval to the previous quantification of the silver conductivity boost in the anode.

References

[1] – Mekhilef, S., Saidur, R., & Safari, A. (2012). Comparative study of different fuel cell technologies. *Renewable and Sustainable Energy Reviews*, *16*(1), 981–989. https://doi.org/10.1016/j.rser.2011.09.020

[2] – Derek, F., Varga, Á., Mounsey, S., & Tan, C. T. (2006, May 3). Types of fuel Cells. Retrieved October 21, 2019, from https://www.doitpoms.ac.uk/tlplib/fuel-cells/printall.php

[3] - Wang, J. (2015). Barriers of scaling-up fuel cells: Cost, durability and reliability. *Energy*, *80*, 509–521. https://doi.org/10.1016/j.energy.2014.12.007

[4] – Tsai, T.-I. (2015). Carbon Formation in Solid Oxide Fuel Cells During internal Reforming and Anode Off-Gas Recirculation, (May).

[5] – Li, M., Hua, B., Pu, J., Chi, B., & Jian, L. (2015). Electrochemical performance and carbon deposition resistance of M-$BaZr_{0.1}Ce_{0.7}Y_{0.1}Yb_{0.1}O_{3-\delta}$(M = Pd, Cu, Ni or NiCu) anodes for solid oxide fuel cells. *Scientific Reports*, *5*, 2–8. https://doi.org/10.1038/srep07667

[6] – Hagen, A., Winiwarter, A., Langnickel, H., & Johnson, G. (2017). SOFC Operation with Real Biogas. *Fuel Cells*, *17*(6), 854–861. https://doi.org/10.1002/fuce.201700031

[7] – Nobrega, S. D., Gelin, P., Georges, S., Steil, M. C., Augusto, B. L., Noronha, F. B., & Fonseca, F. C. (2014). A Fuel-Flexible Solid Oxide Fuel Cell Operating in Gradual Internal Reforming. *Journal of the Electrochemical Society*, *161*(3), F354–F359. https://doi.org/10.1149/2.107403jes

[8] - Gorte, R. J., & Vohs, J. M. (2003). Novel SOFC anodes for the direct electrochemical oxidation of hydrocarbons. *Journal of Catalysis*, *216*(1–2), 477–486. http://doi.org/10.1016/S0021-9517(02)00121-5

[9] – Ruiz-Morales, J. C., Marrero-López, D., Canales-Vázquez, J., & Irvine, J. T. S. (2011). Symmetric and reversible solid oxide fuel cells. *RSC Advances*, *1*(8), 1403–1414. https://doi.org/10.1039/c1ra00284h

[10] – Su, C., Wang, W., Liu, M., Tadé, M. O., & Shao, Z. (2015). Progress and Prospects in Symmetrical Solid Oxide Fuel Cells with Two Identical Electrodes. *Advanced Energy Materials*, *5*(14), 1–19. https://doi.org/10.1002/aenm.201500188

[11] – Savaniu, C., & Irvine, J. T. S. (2007). Materials for Symmetrical Solid Oxide Fuel Cells. *ECS Transactions*, *7*(1), 905–912. https://doi.org/10.1149/1.2729183

[12] – Yang, G., Su, C., Ran, R., Tade, M. O., & Shao, Z. (2014). Advanced symmetric solid oxide fuel cell with an infiltrated K 2NiF4-Type La2NiO4 electrode. *Energy and Fuels*, *28*(1), 356–362. https://doi.org/10.1021/ef401473w

[13] – Yang, Z., Chen, Y., Jin, C., Xiao, G., Han, M., & Chen, F. (2015). $La_{0.7}Sr_{0.3}Fe_{0.7}Ga_{0.3}O_{3-\delta}$ as electrode material for a symmetrical solid oxide fuel cell. *RSC Advances*, *5*(4), 2702–2705. https://doi.org/10.1039/c4ra11358f

[14] - Richter, J., Holtappels, P., Graule, T., Nakamura, T., & Gauckler, L. J. (2009). Materials design for perovskite SOFC cathodes. *Monatshefte Für Chemie - Chemical Monthly*, *140*(9), 985–999. http://doi.org/10.1007/s00706-009-0153-3

[15] - Inoue, I. H. (2005). Electrostatic carrier doping to perovskite transition-metal oxides. *Semiconductor Science and Technology*, *20*(4), S112–S120. http://doi.org/10.1088/0268-1242/20/4/013

[16] - Capuano, L., & U.S. Energy Information Administration. (2018). *International Energy Outlook 2018 (IEO2018)* (Vol. 2018).

[17] - BP Energy. (2018). *2018 BP Energy Outlook 2018 BP Energy Outlook*. *2018 BP Energy Outlook*. https://doi.org/10.1088/1757-899X/342/1/012091

[18] - Exxon Mobil Corporation. (2018). *2018 Outlook for Energy: A View to 2040*. Irving, Texas, USA. https://doi.org/10.1080/01998595.2012.10491656

[19] - Organization of the Petroleum Exporting Countries. (2017). *World Oil Outlook 2040*. (J. Griffin & A.-M. Fantini, Eds.). https://doi.org/10.1190/1.1439163

[20] – Jiang, S. P., Zhang, L., & Zhang, Y. (2007). Lanthanum strontium manganese chromite cathode and anode synthesized by gel-casting for solid oxide fuel cells. *Journal of Materials Chemistry*, *17*(25), 2627. https://doi.org/10.1039/b701339f

[21] – Zhou, Y., Liu, X., Li, J., Nie, H., Ye, X., Wang, S., & Zhan, Z. (2014). Novel metal-supported solid oxide fuel cells with impregnated symmetric $La_{0.6}Sr_{0.4}Fe_{0.9}Sc_{0.1}O_{3-\delta}$ electrodes. *Journal of Power Sources*, *252*, 164–168. https://doi.org/10.1016/j.jpowsour.2013.12.020

[22] – Luo, X., Yang, Y., Yang, Y., Tian, D., Lu, X., Chen, Y., Huang Q., & Lin, B. (2018). Reduced-temperature redox-stable LSM as a novel symmetrical electrode material for SOFCs. *Electrochimica Acta*, *260*, 121–128. https://doi.org/10.1016/j.electacta.2017.11.071

[23] – Xu, N., Zhu, T., Yang, Z., & Han, M. (2018). Co-synthesis of LSCFN-GDC electrode for symmetric solid oxide fuel cell running on propane. *Electrochimica Acta*, *265*, 259–264. https://doi.org/10.1016/j.electacta.2017.12.096

[24] – Fan, W., Sun, Z., Wang, J., Zhou, J., Wu, K., & Cheng, Y. (2016). A new family of Ce-doped $SmFeO_3$ perovskite for application in symmetrical solid oxide fuel cells. *Journal of Power Sources*, *312*, 223–233. https://doi.org/10.1016/j.jpowsour.2016.02.069

[25] – Xu, N., Zhu, T., Yang, Z., & Han, M. (2017). Fabrication and optimization of $La_{0.4}Sr_{0.6}Co_{0.2}Fe_{0.7}Nb_{0.1}O_{3-\delta}$ electrode for symmetric solid oxide fuel cell with zirconia based electrolyte. *Journal of Materials Science and Technology*, *33*(11), 1329–1333. https://doi.org/10.1016/j.jmst.2017.03.012

[26] – Cao, Z., Zhang, Y., Miao, J., Wang, Z., Lü, Z., Sui, Y., Huang, X. & Jiang, W. (2015). Titanium-substituted lanthanum strontium ferrite as a novel electrode material for symmetrical solid oxide fuel cell. *International Journal of Hydrogen Energy*, *40*(46), 16572–16577. https://doi.org/10.1016/j.ijhydene.2015.10.010

[27] – Song, Y., Zhong, Q., & Tan, W. (2014). Synthesis and electrochemical behaviour of ceria-substitution LSCM as a possible symmetric solid oxide fuel cell electrode material exposed to H_2 fuel containing H2S. *International Journal of Hydrogen Energy*, *39*(25), 13694–13700. https://doi.org/10.1016/j.ijhydene.2014.03.179

[28] – Tian, D., Lin, B., Yang, Y., Chen, Y., Lu, X., Wang, Z, Liu W., & Traversa, E. (2016). Enhanced performance of symmetrical solid oxide fuel cells using a doped ceria buffer layer. *Electrochimica Acta*, *208*, 318–324. https://doi.org/10.1016/j.electacta.2016.04.189

[29] – Xu, R., Wu, Y., Wang, X., Zhang, J., Yang, X., & Zhu, B. (2017). Enhanced ionic conductivity of yttria-stabilized ZrO_2 with natural CuFe-oxide mineral heterogeneous composite for low temperature solid oxide fuel cells. *International Journal of Hydrogen Energy*, *42*(27), 17495–17503. https://doi.org/10.1016/j.ijhydene.2017.05.218

[30] – Zheng, Y., Guo, L., Zhang, Y., Gu, Y., Ge, L., & Chen, H. (2018). YSZ electrolyte support with novel symmetric structure by phase inversion process for solid oxide fuel cells. *Energy Conversion and Management*, *177*(June), 11–18. https://doi.org/10.1016/j.enconman.2018.09.051

[31] – Zheng, Y., Zhang, C., Ran, R., Cai, R., Shao, Z., & Farrusseng, D. (2009). A new symmetric solid-oxide fuel cell with $La_{0.8}Sr_{0.2}Sc_{0.2}Mn_{0.8}O_{3-\delta}$ perovskite oxide as both the anode and cathode. *Acta Materialia*, *57*(4), 1165–1175. https://doi.org/10.1016/j.actamat.2008.10.047

[32] – Liu, L., Sun, K., Li, X., Zhang, M., Liu, Y., Zhang, N., & Zhou, X. (2012). A novel doped CeO_2-$LaFeO_3$ composite oxide as both anode and cathode for solid oxide fuel cells. *International Journal of Hydrogen Energy*, *37*(17), 12574–12579. https://doi.org/10.1016/j.ijhydene.2012.06.064

[33] – Lu, J., Yin, Y. M., Li, J., Xu, L., & Ma, Z. F. (2015). A cobalt-free electrode material $La_{0.5}Sr_{0.5}Fe_{0.8}Cu_{0.2}O_{3-\delta}$ for symmetrical solid oxide fuel cells. *Electrochemistry Communications*, *61*, 18–22. https://doi.org/10.1016/j.elecom.2015.09.020

[34] – Kong, X., Wu, X., Zuo, W., Tian, Y., Zhou, X., & Zhang, J. (2016). Niobium doped lanthanum calcium ferrite perovskite as a novel electrode material for symmetrical solid oxide fuel cells. *Journal of Power Sources*, *326*, 35–42. https://doi.org/10.1016/j.jpowsour.2016.06.111

[35] Ruiz-Morales, J. C., Canales-Vázquez, J., Ballesteros-Pérez, B., Peña-Martínez, J., Marrero-López, D., Irvine, J. T. S., & Núñez, P. (2007). LSCM-(YSZ-CGO) composites as improved symmetrical electrodes for solid oxide fuel cells. *Journal of the European Ceramic Society*, *27*(13–15), 4223–4227. https://doi.org/10.1016/j.jeurceramsoc.2007.02.117

[36] Yang, G., Shen, J., Chen, Y., Tadé, M. O., & Shao, Z. (2015). Cobalt-free $Ba_{0.5}Sr_{0.5}Fe_{0.8}Cu_{0.1}Ti_{0.1}O_{3-\delta}$ as a bi-functional electrode material for solid oxide fuel cells. *Journal of Power Sources*, *298*, 184–192. https://doi.org/10.1016/j.jpowsour.2015.08.064

[37] Chen, G., Sun, W., Luo, Y., Liu, H., Geng, S., Yu, K., & Liu, G. (2017). Investigation of layered $Ni_{0.8}Co_{0.15}Al_{0.05}LiO_2$ in electrode for low-temperature solid oxide fuel cells. *International Journal of Hydrogen Energy*, *43*(1), 417–425. https://doi.org/10.1016/j.ijhydene.2017.11.056

[38] – Yang, G., Su, C., Chen, Y., Tadé, M. O., & Shao, Z. (2014). Nano $La_{0.6}Ca_{0.4}Fe_{0.8}Ni_{0.2}O_{3-\delta}$ decorated porous doped ceria as a novel cobalt-free electrode for “symmetrical” solid oxide fuel cells. *J. Mater. Chem. A*, *2*(45), 19526–19535. https://doi.org/10.1039/C4TA03485F

[39] – Shen, J., Chen, Y., Yang, G., Zhou, W., Tadé, M. O., & Shao, Z. (2015). Impregnated $LaCo_{0.3}Fe_{0.67}Pd_{0.03}O_{3-\delta}$ as a promising electrocatalyst for “symmetrical” intermediate-temperature solid oxide fuel cells. *Journal of Power Sources*, *306*, 92–99. https://doi.org/10.1016/j.jpowsour.2015.12.021

[40] – Fan, L., Zhang, H., Chen, M., Wang, C., Wang, H., Singh, M., & Zhu, B. (2013). Electrochemical study of lithiated transition metal oxide composite as symmetrical electrode for low temperature ceramic fuel cells. *International Journal of Hydrogen Energy*, *38*(26), 11398–11405. https://doi.org/10.1016/j.ijhydene.2013.06.050

[41] – Fan, W., Sun, Z., Zhou, J., Wu, K., & Cheng, Y. (2017). Characterization of Sr/Ru co-doped ferrite based perovskite as a symmetrical electrode material for solid oxide fuel cells. *Journal of Power Sources*, *348*, 94–106. https://doi.org/10.1016/j.jpowsour.2017.02.090

[42] – Ding, X., Liu, H., Gao, Z., Hua, G., Wang, L., Ding, L., & Yuan, G. (2017). $La_{0.6}Ca_{0.4}Fe_{0.8}Ni_{0.2}O_{3-\delta}$ – $Sm_{0.2}Ce_{0.8}O_{1.9}$ composites as symmetrical bi-electrodes for solid oxide fuel cells through infiltration and in-situ exsolution. *International Journal of Hydrogen Energy*, *42*(39), 24968–24977. https://doi.org/10.1016/j.ijhydene.2017.08.089

[43] – Lin, Y., Su, C., Huang, C., Kim, J. S., Kwak, C., & Shao, Z. (2012). A new symmetric solid oxide fuel cell with a samaria-doped ceria framework and a silver-infiltrated electrocatalyst. *Journal of Power Sources*, *197*, 57–64. https://doi.org/10.1016/j.jpowsour.2011.09.040

[44] – Raza, R., Liu, Q., Nisar, J., Wang, X., Ma, Y., & Zhu, B. (2011). ZnO/NiO nanocomposite electrodes for low-temperature solid oxide fuel cells. *Electrochemistry Communications*, *13*(9), 917–920. https://doi.org/10.1016/j.elecom.2011.05.032

[45] – Mi, Y., Xia, C., Zhu, B., Raza, R., Afzal, M., & Riess, I. (2018). Experimental and physical approaches on a novel semiconducting-ionic membrane fuel cell. *International Journal of Hydrogen Energy*, *43*(28), 12756–12764. https://doi.org/10.1016/j.ijhydene.2018.03.204

[46] – Gao, Z., Ding, X., Ding, D., Ding, L., Zhang, S., & Yuan, G. (2018). Infiltrated Pr_2NiO_4 as promising bi-electrode for symmetrical solid oxide fuel cells. *International Journal of Hydrogen Energy*, *43*(18), 8953–8961. https://doi.org/10.1016/j.ijhydene.2018.03.164

[47] – Shen, J., Yang, G., Zhang, Z., Tadé, M. O., Zhou, W., & Shao, Z. (2017). Improved performance of a symmetrical solid oxide fuel cell by swapping the roles of doped ceria and $La_{0.6}Sr_{1.4}MnO_{4+\delta}$ in the electrode. *Journal of Power Sources*, *342*, 644–651. https://doi.org/10.1016/j.jpowsour.2016.12.109

[48] – Shen, J., Yang, G., Zhang, Z., Zhou, W., Wang, W., & Shao, Z. (2016). Tuning layer-structured $La_{0.6}Sr_{1.4}MnO_{4+\delta}$ into a promising electrode for intermediate-temperature symmetrical solid oxide fuel cells through surface modification. *Journal of Materials Chemistry A*, *4*(27), 10641–10649. https://doi.org/10.1039/c6ta02986h

[49] – Wei, T., Zhang, Q., Huang, Y.-H., & Goodenough, J. B. (2012). Cobalt-based double-perovskite symmetrical electrodes with low thermal expansion for solid oxide fuel cells. *Journal of Materials Chemistry*, *22*(1), 225. https://doi.org/10.1039/c1jm14756k

[50] – Yang, Z., Xu, N., Han, M., & Chen, F. (2014). Performance evaluation of $La_{0.4}Sr_{0.6}Co_{0.2}Fe_{0.7}Nb_{0.1}O_{3-\delta}$ as both anode and cathode material in solid oxide fuel cells. *International Journal of Hydrogen Energy*, *39*(14), 7402–7406. https://doi.org/10.1016/j.ijhydene.2014.01.009

[51] – Liu, X., Han, D., Zhou, Y., Meng, X., Wu, H., Li, J., Zeng F., & Zhan, Z. (2014). Sc-substituted $La_{0.6}Sr_{0.4}FeO_{3-\delta}$ mixed conducting oxides as promising electrodes for symmetrical solid oxide fuel cells. *Journal of Power Sources*, *246*, 457–463. https://doi.org/10.1016/j.jpowsour.2013.07.111

[52] – Zhang, Y., Zhou, Q., & He, T. (2011). $La_{0.7}Ca_{0.3}CrO_3$-$Ce_{0.8}Gd_{0.2}O_{1.9}$ composites as symmetrical electrodes for solid-oxide fuel cells. *Journal of Power Sources*, *196*(1), 76–83. https://doi.org/10.1016/j.jpowsour.2010.07.035

[53] – Zhang, Y., Shen, Y., Du, X., Li, J., Cao, X., & He, T. (2011). Nanostructured GDC-impregnated $La_{0.7}Ca_{0.3}CrO_{3-\delta}$ symmetrical electrodes for solid oxide fuel cells operating on hydrogen and city gas. *International Journal of Hydrogen Energy*, *36*(5), 3673–3680. https://doi.org/10.1016/j.ijhydene.2010.12.104

[54] – Liu, Q., Dong, X., Xiao, G., Zhao, F., & Chen, F. (2010). A novel electrode material for symmetrical SOFCs. *Advanced Materials*, *22*(48), 5478–5482. https://doi.org/10.1002/adma.201001044

[55] – Yang, C., Yang, Z., Jin, C., Xiao, G., Chen, F., & Han, M. (2012). Sulfur-tolerant redox-reversible anode material for direct hydrocarbon solid oxide fuel cells. *Advanced Materials*, *24*(11), 1439–1443. https://doi.org/10.1002/adma.201104852

[56] – Meng, X., Liu, X., Han, D., Wu, H., Li, J., & Zhan, Z. (2014). Symmetrical solid oxide fuel cells with impregnated $SrFe_{0.75}Mo_{0.25}O_{3-\delta}$ electrodes. *Journal of Power Sources*, *252*, 58–63. https://doi.org/10.1016/j.jpowsour.2013.11.049

[57] – Rath, M. K., & Lee, K. T. (2016). Superior electrochemical performance of non-precious Co-Ni-Mo alloy catalyst-impregnated $Sr_2FeMoO_{6-\delta}$ as an electrode material for symmetric solid oxide fuel cells. *Electrochimica Acta*, *212*, 678–685. https://doi.org/10.1016/j.electacta.2016.07.037

[58] – Zhang, P., Guan, G., Khaerudini, D. S., Hao, X., Han, M., Kasai, Y., Sasagawa K., & Abudula, A. (2014). Properties of A-site nonstoichiometry $(Pr_{0.4})_xSr_{0.6}Co_{0.2}Fe_{0.7}Nb_{0.1}O_{3-\sigma}$ ($0.9 \leq x \leq 1.1$) as symmetrical electrode material for solid oxide fuel cells. *Journal of Power Sources*, *248*, 163–171. https://doi.org/10.1016/j.jpowsour.2013.09.077

[59] – Bian, L., Duan, C., Wang, L., Zhu, L., O'Hayre, R., & Chou, K. C. (2018). Electrochemical performance and stability of $La_{0.5}Sr_{0.5}Fe_{0.9}Nb_{0.1}O_{3-\delta}$ symmetric electrode for solid oxide fuel cells. *Journal of Power Sources*, *399*(August), 398–405. https://doi.org/10.1016/j.jpowsour.2018.07.119

[60] – Niu, B., Jin, F., Zhang, L., Shen, P., & He, T. (2018). Performance of double perovskite symmetrical electrode materials $Sr_2TiFe_{1-x}Mo_xO_{6-\delta}$ (x = 0.1, 0.2) for solid oxide fuel cells. *Electrochimica Acta*, *263*, 217–227. https://doi.org/10.1016/j.electacta.2018.01.062

[61] – Zhou, J., Chen, Y., Chen, G., Wu, K., & Cheng, Y. (2015). Evaluation of $La_xSr_{2-x}FeO_4$ layered perovskite as potential electrode materials for symmetrical solid oxide fuel cells. *Journal of Alloys and Compounds*, *647*, 778–783. https://doi.org/10.1016/j.jallcom.2015.05.261

[62] – Zurlo, F., Natali Sora, I., Felice, V., Luisetto, I., D'Ottavi, C., Licoccia, S., & Di Bartolomeo, E. (2016). Copper-doped lanthanum ferrites for symmetric SOFCs. *Acta Materialia*, *112*, 77–83. https://doi.org/10.1016/j.actamat.2016.04.015

[63] – Zhang, P., Guan, G., Khaerudini, D. S., Hao, X., Xue, C., Han, M., Kasai, Y., & Abudula, A. (2015). B-site Mo-doped perovskite $Pr_{0.4}Sr_{0.6}$ $(Co_{0.2}Fe_{0.8})_{1-x}Mo_xO_{3-\sigma}$ (x = 0, 0.05, 0.1 and 0.2) as electrode for symmetrical solid oxide fuel cell. *Journal of Power Sources*, *276*, 347–356. https://doi.org/10.1016/j.jpowsour.2014.11.141

[64] – Niu, B., Jin, F., Feng, T., Zhang, L., Zhang, Y., & He, T. (2018). A-site deficient $(La_{0.6}Sr_{0.4})_{1-x}Co_{0.2}Fe_{0.6}Nb_{0.2}O_{3-\delta}$ symmetrical electrode materials for solid oxide fuel cells. *Electrochimica Acta*, *270*, 174–182. https://doi.org/10.1016/j.electacta.2018.03.085

[65] – Lu, X., Yang, Y., Ding, Y., Chen, Y., Gu, Q., Tian, D., Yu, W., & Lin, B. (2017). Mo-doped $Pr_{0.6}Sr_{0.4}Fe_{0.8}Ni_{0.2}O_{3-\delta}$ as potential electrodes for intermediate-temperature symmetrical solid oxide fuel cells. *Electrochimica Acta*, *227*, 33–40. https://doi.org/10.1016/j.electacta.2016.12.170

[66] – Liu, J., Lei, Y., Li, Y., Gao, J., Han, D., Zhan, W., Huang, F, & Wang, S. (2017). Infiltrated $Sr_2Fe_{1.5}Mo_{0.5}O_6/La_{0.9}Sr_{0.1}Ga_{0.8}Mg_{0.2}O_3$ electrodes towards high performance symmetrical solid oxide fuel cells fabricated by an ultra-fast and time-saving procedure. *Electrochemistry Communications*, *78*, 6–10. https://doi.org/10.1016/j.elecom.2017.02.019

[67] – Zhou, Q., Yuan, C., Han, D., Luo, T., Li, J., & Zhan, Z. (2014). Evaluation of $LaSr_2Fe_2CrO_{9-\delta}$ as a potential electrode for symmetrical solid oxide fuel cells. *Electrochimica Acta*, *133*, 453–458. https://doi.org/10.1016/j.electacta.2014.04.104

[68] – Rath, M. K., & Lee, K. T. (2015). Investigation of aliovalent transition metal doped $La_{0.7}Ca_{0.3}Cr_{0.8}X_{0.2}O_{3-\delta}$ (X=Ti, Mn, Fe, Co, and Ni) as electrode materials for symmetric solid oxide fuel cells. *Ceramics International*, *41*(9), 10878–10890. https://doi.org/10.1016/j.ceramint.2015.05.029

[69] – Gao, J., Meng, X., Luo, T., Wu, H., & Zhan, Z. (2017). Symmetrical solid oxide fuel cells fabricated by phase inversion tape casting with impregnated $SrFe_{0.75}Mo_{0.25}O_{3-\delta}$ (SFMO) electrodes. *International Journal of Hydrogen Energy*, *42*(29), 18499–18503. https://doi.org/10.1016/j.ijhydene.2017.03.205

[70] – Dos Santos-Gómez, L., Compana, J. M., Bruque, S., Losilla, E. R., & Marrero-López, D. (2015). Symmetric electrodes for solid oxide fuel cells based on Zr-doped $SrFeO_{3-\delta}$. *Journal of Power Sources*, *279*, 419–427. https://doi.org/10.1016/j.jpowsour.2015.01.043

[71] – Zhang, P., Guan, G., Khaerudini, D. S., Hao, X., Xue, C., Han, M., Kasai, Y., & Abudula, A. (2014). Evaluation of performances of solid oxide fuel cells with symmetrical electrode material. *Journal of Power Sources*, *266*, 241–249. https://doi.org/10.1016/j.jpowsour.2014.05.013

[72] – Ding, H., Fang, S., Yang, Y., Yang, Y., Wu, W., & Tao, Z. (2018). High-performing and stable electricity generation by ceramic fuel cells operating in dry methane over 1000 hours. *Journal of Power Sources*, *401*(August), 322–328. https://doi.org/10.1016/j.jpowsour.2018.08.084

[73] – Zhou, J., Chen, G., Wu, K., & Cheng, Y. (2014). The performance of $La_{0.6}Sr_{1.4}MnO_4$ layered perovskite electrode material for intermediate temperature symmetrical solid oxide fuel cells. *Journal of Power Sources*, *270*, 418–425. https://doi.org/10.1016/j.jpowsour.2014.06.163

[74] – He, W., Wu, X., Dong, F., & Ni, M. (2017). A novel layered perovskite electrode for symmetrical solid oxide fuel cells: $PrBa(Fe_{0.8}Sc_{0.2})_2O_{5+\delta}$. *Journal of Power Sources*, *363*, 16–19. https://doi.org/10.1016/j.jpowsour.2017.07.059

[75] – Zhao, L., Chen, K., Liu, Y., & He, B. (2017). A novel layered perovskite as symmetric electrode for direct hydrocarbon solid oxide fuel cells. *Journal of Power Sources*, *342*, 313–319. https://doi.org/10.1016/j.jpowsour.2016.12.066

[76] – Choi, S., Sengodan, S., Park, S., Ju, Y. W., Kim, J., Hyodo, J., Jeong, H. Y., Ishihara, T., Shin, J., & Kim, G. (2016). A robust symmetrical electrode with layered perovskite structure for direct hydrocarbon solid oxide fuel cells: $PrBa_{0.8}Ca_{0.2}Mn_2O_{5+\delta}$. *Journal of Materials Chemistry A, 4(5), 1747–1753*. https://doi.org/10.1039/c5ta08878j

[77] – Xia, C., Wang, B., Ma, Y., Cai, Y., Afzal, M., Liu, Y., He, Y., Zhang, W., Dong, W., Li, J., & Zhu, B. (2016). Industrial-grade rare-earth and perovskite oxide for high-performance electrolyte layer-free fuel cell. *Journal of Power Sources*, *307*, 270–279. https://doi.org/10.1016/j.jpowsour.2015.12.086

[78] – Xia, C., Cai, Y., Wang, B., Afzal, M., Zhang, W., Soltaninazarlou, A., & Zhu, B. (2017). Strategy towards cost-effective low-temperature solid oxide fuel cells: A mixed-conductive membrane comprised of natural minerals and perovskite oxide. *Journal of Power Sources*, *342*, 779–786. https://doi.org/10.1016/j.jpowsour.2016.12.120

[79] – Qiao, Z., Xia, C., Cai, Y., Afzal, M., Wang, H., Qiao, J., & Zhu, B. (2018). Electrochemical and electrical properties of doped CeO_2-ZnO composite for low-temperature solid oxide fuel cell applications. *Journal of Power Sources*, *392*(February), 33–40. https://doi.org/10.1016/j.jpowsour.2018.04.096

[80] – Liu, Y., Wu, Y., Zhang, W., Zhang, J., Wang, B., Xia, C., Afzal, M., Li, J., Singh, M., & Zhu, B. (2017). Natural $CuFe_2O_4$ mineral for solid oxide fuel cells. *International Journal of Hydrogen Energy*, *42*(27), 17514–17521. https://doi.org/10.1016/j.ijhydene.2017.01.039

[81] – Zhang, W., Cai, Y., Wang, B., Xia, C., Dong, W., Li, J., & Zhu, B. (2016). Mixed ionic-electronic conductor membrane based fuel cells by incorporating semiconductor $Ni_{0.8}Co_{0.15}Al_{0.05}LiO_{2-\delta}$ into the $Ce_{0.8}Sm_{0.2}O_{2-\delta}$-$Na_2CO_3$ electrolyte. *International Journal of Hydrogen Energy*, *41*(34), 15346–15353. https://doi.org/10.1016/j.ijhydene.2016.07.032

[82] – Fergus, J. W. (2006). Electrolytes for solid oxide fuel cells. *Journal of Power Sources*, *162*(1), 30–40. https://doi.org/10.1016/j.jpowsour.2006.06.062

[83] – Novik, N. N., Konakov, V. G., & Archakov, I. Y. (2015). Zirconia and ceria based ceramics and nanoceramics - A review on electrochemical and mechanical properties. *Reviews on Advanced Materials Science*, *40*(2), 188–207.

[84] – Liu, T., Zhang, X., Wang, X., Yu, J., & Li, L. (2016). A review of zirconia-based solid electrolytes. *Ionics*, *22*(12), 2249–2262. https://doi.org/10.1007/s11581-016-1880-1

[85] – Muhammed Ali, S. A., Muchtar, A., Muhamad, N., & Sulong, A. B. (2011). A review on preparation of SDC-carbonate as composite electrolyte material for intermediate temperature Solid Oxide Fuel Cells (IT-SOFC). *2011 IEEE 1st Conference on Clean Energy and Technology, CET 2011*, 394–399. https://doi.org/10.1109/CET.2011.6041504

[86] – Liu, Y. H., Yin, C. Q., Wang, L. H., Li, D. B., Lian, J. S., Hu, J. D., & Guo, Z. X. (2008). Properties of a ceria-based (C6S2G2) solid oxide electrolyte sintered with Al2O3 additive. *Science of Sintering*, *40*(1), 13–20. https://doi.org/10.2298/SOS0801013L

[87] – Spiridigliozzi, L. (2018). Doped-Ceria Electrolytes: Synthesis, Sintering and Characterization. Springer.

[88] – Rajesh, S., Macedo, D. A., & Nascimento, R. M. (2013). Composite Electrolytes and electrodes for Intermediate Temperature Hybrid Fuel Cells. Materials and Process for Energy, 485–494.

[89] – Garche, J., Dyer, C. K., Moseley, P. T., Ogumi, Z., Rand, D. A., & Scrosati, B. (Eds.). (2013). *Encyclopedia of electrochemical power sources*. Newnes.

[90] – Atomistic Simulation Group in the Materials Department of Imperial College. (n.d.). Database of Ionic Radii. Retrieved January 1, 2017, from http://abulafia.mt.ic.ac.uk/shannon/radius.php

[91] – Shimura, K., Nishino, H., Kakinuma, K., Brito, M. E., & Uchida, H. (2017). Effect of samaria-doped ceria (SDC) interlayer on the performance of $La_{0.6}Sr_{0.4}Co_{0.2}Fe_{0.8}O_{3-\delta}$/SDC composite oxygen electrode for reversible solid oxide fuel cells. *Electrochimica Acta*, *225*, 114–120. https://doi.org/10.1016/j.electacta.2016.12.100

[92] – Mosiałek, M., Michna, A., Dziubaniuk, M., Bielańska, E., Kežionis, A., Šalkus, T., Kazakevičius, E., Bożek, B., Krawczyk, A., Wyrwa, J., & Orliukas, A. F. (2018). Composite cathode material LSCF-Ag for solid oxide fuel cells obtained in one step sintering procedure. *Electrochimica Acta*, *282*, 427–436. https://doi.org/10.1016/j.electacta.2018.06.063

[93] – Ni, Q., Chen, H., Ge, L., Yu, S., & Guo, L. (2017). Investigation of $La_{1-x}Sm_{x-y}Sr_yCoO_{3-\delta}$ cathode for intermediate temperature solid oxide fuel cells. *Journal of Power Sources*, *349*, 130–137. https://doi.org/10.1016/j.jpowsour.2017.03.037

[94] – Yoon, B. Y., Kim, J. H., & Bae, J. (2013). Effects of infiltrated Sr and Mn doped $LaCrO_3$ on porous $La_{0.8}Sr_{0.2}Ga_{0.8}Mg_{0.2}O_{3-\delta}$ scaffolds used as anodes in solid oxide fuel cells. *Solid State Ionics*, *249–250*, 26–33. https://doi.org/10.1016/j.ssi.2013.07.007

[95] – Zhou, Q., Xu, L., Guo, Y., Jia, D., Li, Y., & Wei, W. C. J. (2012). $La_{0.6}Sr_{0.4}Fe_{0.8}Cu_{0.2}O_{3-\delta}$ perovskite oxide as cathode for IT-SOFC. *International Journal of Hydrogen Energy*, *37*(16), 11963–11968. https://doi.org/10.1016/j.ijhydene.2012.05.114

[96] – Han, D., Liu, Y., Wang, S., & Zhan, Z. (2014). Enhanced performance of solid oxide fuel cell fabricated by a replica technique combined with infiltrating process. *International Journal of Hydrogen Energy*, *39*(25), 13217–13223. https://doi.org/10.1016/j.ijhydene.2014.06.123

[97] – Peña-Martínez, J., Marrero-López, D., Ruiz-Morales, J. C., Buergler, B. E., Núñez, P., & Gauckler, L. J. (2006). Fuel cell studies of perovskite-type materials for IT-SOFC. *Journal of Power Sources*, *159*(2), 914–921. https://doi.org/10.1016/j.jpowsour.2005.11.036

[98] – Tian, R., Fan, J., Liu, Y., & Xia, C. (2008). Low-temperature solid oxide fuel cells with $La_{1-x}Sr_xMnO_3$ as the cathodes. *Journal of Power Sources*, *185*(2), 1247–1251. https://doi.org/10.1016/j.jpowsour.2008.09.058

[99] – Zhou, Y., Chen, T., Li, J., Yuan, C., Xin, X., Chen, G., Miao, G., Zhan, W., Zhan, Z., & Wang, S. (2015). Long-term stability of metal-supported solid oxide fuel cells employing infiltrated electrodes. *Journal of Power Sources*, *295*, 67–73. https://doi.org/10.1016/j.jpowsour.2015.06.114

[100] – Nicolae, A., Preda, O., & Nogales, F. F. (2011). Endometrial metaplasias and reactive changes: A spectrum of altered differentiation. *Journal of Clinical Pathology*, *64*(2), 97–106. https://doi.org/10.1016/j.jpowsour.2017.10.066

[101] – Chang, H., Chen, H., Yang, G., Zhou, W., Bai, J., Li, S., & Shao, Z. (2019). Enhanced coking resistance of a Ni cermet anode by a chromates protective layer. *Journal of Energy Chemistry*, *37*, 117–125. https://doi.org/10.1016/j.jechem.2018.12.007

[102] – Masciandaro, S., Torrell, M., Leone, P., & Tarancón, A. (2019). Three-dimensional printed yttria-stabilized zirconia self-supported electrolytes for solid oxide fuel cell applications. *Journal of the European Ceramic Society*, *39*(1), 9–16. https://doi.org/10.1016/j.jeurceramsoc.2017.11.033

[103] - Moriche, R., Marrero-López, D., Gotor, F. J., & Sayagués, M. J. (2014). Chemical and electrical properties of LSM cathodes prepared by mechanosynthesis. *Journal of Power Sources*, *252*, 43–50. https://doi.org/10.1016/j.jpowsour.2013.11.093

[104] - Prices of elements and their compounds. (2013). Retrieved February 10, 2017, from https://en.wikipedia.org/wiki/Prices_of_elements_and_their_compounds

[105] - Chemicool. (n.d.). Retrieved February 10, 2017, from http://www.chemicool.com/

[106] - Liu, C., Massé, R., Nan, X., & Cao, G. (2016). A promising cathode for Li-ion batteries: $Li_3V_2(PO_4)_3$. *Energy Storage Materials*, *4*, 15–58. https://doi.org/10.1016/j.ensm.2016.02.002

[107] – Patra, H., Rout, S. K., Pratihar, S. K., & Bhattacharya, S. (2011). Effect of process parameters on combined EDTA-citrate synthesis of $Ba_{0.5}Sr_{0.5}Co_{0.8}Fe_{0.2}O_{3-\delta}$ perovskite. *Powder Technology*, *209*(1–3), 98–104. https://doi.org/10.1016/j.powtec.2011.02.015

[108] – Chen, Y., Wang, F., Chen, D., Dong, F., Park, H. J., Kwak, C., & Shao, Z. (2012). Role of silver current collector on the operational stability of selected cobalt-containing oxide electrodes for oxygen reduction reaction. *Journal of Power Sources*, *210*, 146–153. https://doi.org/10.1016/j.jpowsour.2012.03.019

[109] - Bian, L. Z., Chen, Z. Y., Wang, L. J., Li, F. S., & Chou, K. C. (2017). Electrochemical performance and carbon deposition of anode-supported solid oxide fuel cell exposed to H_2-CO fuels. *International Journal of Hydrogen Energy*, *42*(20), 14246–14252. https://doi.org/10.1016/j.ijhydene.2016.08.214

[110] - Zhao, B., Song, J., Ran, R., & Shao, Z. (2012). Catalytic decomposition of hydrous hydrazine to hydrogen over oxide catalysts at ambient conditions for PEMFCs. *International Journal of Hydrogen Energy*, *37*(1), 1133–1139. https://doi.org/10.1016/j.ijhydene.2011.02.076

[111] - Guo, Y., Ran, R., & Shao, Z. (2011). A novel way to improve performance of proton-conducting solid-oxide fuel cells through enhanced chemical interaction of anode components. *International Journal of Hydrogen Energy*, *36*(2), 1683–1691. https://doi.org/10.1016/j.ijhydene.2010.10.081

[112] - Guo, Y., Ran, R., & Shao, Z. (2010). Fabrication and performance of a carbon dioxide-tolerant proton-conducting solid oxide fuel cells with a dual-layer electrolyte. *International Journal of Hydrogen Energy*, *35*(19), 10513–10521. https://doi.org/10.1016/j.ijhydene.2010.07.179

[113] - Liu, Y., Guo, Y., Ran, R., & Shao, Z. (2012). A new neodymium-doped $BaZr_{0.8}Y_{0.2}O_{3-\delta}$ as potential electrolyte for proton-conducting solid oxide fuel cells. *Journal of Membrane Science*, *415–416*, 391–398. https://doi.org/10.1016/j.memsci.2012.05.062

[114] - Liu, Y., Guo, Y., Ran, R., & Shao, Z. (2013). A novel approach for substantially improving the sinterability of $BaZr_{0.4}Ce_{0.4}Y_{0.2}O_{3-\delta}$ electrolyte for fuel cells by impregnating the green membrane with zinc nitrate as a sintering aid. *Journal of Membrane Science*, *437*, 189–195. https://doi.org/10.1016/j.memsci.2013.03.002

[115] - Guo, Y., Lin, Y., Ran, R., & Shao, Z. (2009). Zirconium doping effect on the performance of proton-conducting $BaZr_yCe_{0.8-y}Y_{0.2}O_{3-\delta}$ ($0.0 \leq y \leq 0.8$) for fuel cell applications. *Journal of Power Sources*, *193*(2), 400–407. https://doi.org/10.1016/j.jpowsour.2009.03.044

[116] - Gao, J., Song, X., Zhou, F., An, S., & Tian, Y. (2012). Substituent effects of Ba^{2+} for Sm^{3+} on the structure and electrochemical performances of $Sm_{0.5}Sr_{0.5}Co_{0.8}Fe_{0.2}O_{3-\delta}$ cathode for intermediate temperature solid oxide fuel cells. *Journal of Power Sources*, *218*, 383–392. https://doi.org/10.1016/j.jpowsour.2012.05.070

[117] – Wang, Z., Li, Y., & Schwank, J. W. (2014). Evaluation of Ni/SDC as anode material for dry CH_4 fueled Solid Oxide Fuel Cells. *Journal of Power Sources*, *248*, 239-245. https://doi.org/10.1016/j.jpowsour.2013.09.043

[118] – Zhang, Y., Liu, J., Huang, X., Lu, Z., & Su, W. (2008). Low temperature solid oxide fuel cell with $Ba_{0.5}Sr_{0.5}Co_{0.8}Fe_{0.2}O_3$ cathode prepared by screen printing. *Solid State Ionics*, *179*(7-8), 250-255. https://doi.org/10.1016/j.ssi.2008.02.008

[119] – Zhang, Y., Huang, X., Lu, Z., Liu, Z., Ge, X., Xu, J., Xin, X., Sha, X., & Su, W. (2006). A screen-printed $Ce_{0.8}Sm_{0.2}O_{1.9}$ film solid oxide fuel cell with a $Ba_{0.5}Sr_{0.5}Co_{0.8}Fe_{0.2}O_{3-\delta}$ cathode. *Journal of Power Sources*, *160*(2), 1217-1220. https://doi.org/10.1016/j.jpowsour.2006.02.048

[120] – Zhao, L., Huang, X., Zhu, R., Lu, Z., Sun, W., Zhang, Y., Ge, Z., Liu, Z., & Su, W. (2008). Optimization on technical parameters for fabrication of SDC film by screen-printing used as electrolyte in IT-SOFC. *Journal of Physics and Chemistry of Solids*, *69*(8), 2019-2024. https://doi.org/10.1016/j.jpcs.2008.02.011

[121] – Zhao, J., Xu, X., Zhou, W., & Zhu, Z. (2017). MnO-Co composite modified Ni-SDC anode for intermediate temperature solid oxide fuel cells. *Fuel Processing Technology*, *161*, 241-247. https://doi.org/10.1016/j.fuproc.2016.08.024

[122] – Guo, Y., Liu, Y., Cai, R., Chen, D., Ran, R., & Shao, Z. (2012). Electrochemical contribution of silver current collector to oxygen reduction reaction over $Ba_{0.5}Sr_{0.5}Co_{0.8}Fe_{0.2}O_{3-\delta}$ electrode on oxygen-ionic conducting electrolyte. *International Journal of Hydrogen Energy*, *37*(19), 14492-14500. https://doi.org/10.1016/j.ijhydene.2012.07.031

[123] – Ai, N., Lü, Z., Chen, K., Huang, X., Wei, B., Zhang, Y., Li, S., Xin, X., Sha, X, & Su, W. (2006). Low temperature solid oxide fuel cells based on $Sm_{0.2}Ce_{0.8}O_{1.9}$ films

fabricated by slurry spin coating. *Journal of Power Pources*, *159*(1), 637-640. https://doi.org/10.1016/j.jpowsour.2005.11.057

[124] – Qu, J., Wang, W., Chen, Y., Deng, X., & Shao, Z. (2016). Stable direct-methane solid oxide fuel cells with calcium-oxide-modified nickel-based anodes operating at reduced temperatures. *Applied Energy*, *164*, 563-571. https://doi.org/10.1016/j.apenergy.2015.12.014

[125] – Su, C., Wu, Y., Wang, W., Zheng, Y., Ran, R., & Shao, Z. (2010). Assessment of nickel cermets and $La_{0.8}Sr_{0.2}Sc_{0.2}Mn_{0.8}O_3$ as solid-oxide fuel cell anodes operating on carbon monoxide fuel. *Journal of Power Sources*, *195*(5), 1333-1343. https://doi.org/10.1016/j.jpowsour.2009.09.015

[126] – Zhou, W., Ran, R., Shao, Z. P., Gu, H. X., Jin, W. Q., & Xu, N. P. (2007). Significant impact of nitric acid treatment on the cathode performance of $Ba_{0.5}Sr_{0.5}Co_{0.8}Fe_{0.2}O_{3-\delta}$ perovskite oxide via combined EDTA–citric complexing process. *Journal of Power Sources*, *174*(1), 237-245. https://doi.org/10.1016/j.jpowsour.2007.08.087

[127] – Song, J., Ran, R., & Shao, Z. (2010). Hydrazine as efficient fuel for low-temperature SOFC through ex-situ catalytic decomposition with high selectivity toward hydrogen. *International journal of hydrogen energy*, *35*(15), 7919-7924. https://doi.org/10.1016/j.ijhydene.2010.05.094

[128] – Chen, D., Huang, C., Ran, R., Park, H. J., Kwak, C., & Shao, Z. (2011). New $Ba_{0.5}Sr_{0.5}Co_{0.8}Fe_{0.2}O_{3-\delta}$ + Co_3O_4 composite electrode for IT-SOFCs with improved electrical conductivity and catalytic activity. *Electrochemistry Communications*, *13*(2), 197-199. https://doi.org/10.1016/j.elecom.2010.12.012

[129] – Ai, N., Chen, K., Liu, S., Lü, Z., Su, W., & Jiang, S. P. (2012). Effect of characteristics of (Sm, Ce) O_2 powder on the fabrication and performance of anode-supported solid oxide fuel cells. *Materials Research Bulletin*, *47*(1), 121-129. https://doi.org/10.1016/j.materresbull.2011.09.017

[130] – Yan, A., Yang, M., Hou, Z., Dong, Y., & Cheng, M. (2008). Investigation of $Ba_{1-x}Sr_xCo_{0.8}Fe_{0.2}O_{3-\delta}$ as cathodes for low-temperature solid oxide fuel cells both in the absence and presence of CO_2. *Journal of Power Sources*, *185*(1), 76-84. https://doi.org/10.1016/j.jpowsour.2008.06.088

[131] – Shi, H., Zhou, W., Ran, R., & Shao, Z. (2010). Comparative study of doped ceria thin-film electrolytes prepared by wet powder spraying with powder synthesized

via two techniques. *Journal of Power Sources*, *195*(2), 393-401. https://doi.org/10.1016/j.jpowsour.2009.07.056

[132] – Ai, N., Lü, Z., Chen, K., Huang, X., Du, X., & Su, W. (2007). Effects of anode surface modification on the performance of low temperature SOFCs. *Journal of power sources*, *171*(2), 489-494. https://doi.org/10.1016/j.jpowsour.2007.06.055

[133] – Ai, N., Lü, Z., Tang, J., Chen, K., Huang, X., & Su, W. (2008). Improvement of output performance of solid oxide fuel cell by optimizing Ni/samaria-doped ceria anode functional layer. *Journal of Power Sources*, *185*(1), 153-158. https://doi.org/10.1016/j.jpowsour.2008.06.030

[134] – Zhou, W., Ran, R., Shao, Z., Zhuang, W., Jia, J., Gu, H., Jin, W., & Xu, N. (2008). Barium-and strontium-enriched $(Ba_{0.5}Sr_{0.5})_{1+x}Co_{0.8}Fe_{0.2}O_{3-\delta}$ oxides as high-performance cathodes for intermediate-temperature solid-oxide fuel cells. *Acta Materialia*, *56*(12), 2687-2698. https://doi.org/10.1016/j.actamat.2008.02.002

[135] - Wang, K., Ran, R., Hao, Y., Shao, Z., Jin, W., & Xu, N. (2008). A high-performance no-chamber fuel cell operated on ethanol flame. *Journal of Power Sources*, *177*(1), 33-39. https://doi.org/10.1016/j.jpowsour.2007.11.004

[136] - Pivac, I., Šimić, B., & Barbir, F. (2017). Experimental diagnostics and modeling of inductive phenomena at low frequencies in impedance spectra of proton exchange membrane fuel cells. *Journal of Power Sources*, *365*, 240–248. https://doi.org/10.1016/j.jpowsour.2017.08.087

[137] – Techniques for Measuring Fuel Cell Resistance. (2017). Retrieved December 19, 2017, from http://www.fuelcellstore.com/blog-section/techniques-for-measuring-fuel-cell-resistance

[138] – Yonglai, F., & Ong, C. K. (2000). The magnetoresistance effect of La-Ca-Sr-Mn-O perovskites under a very low magnetic field. *Journal of Magnetism and Magnetic Materials*, *208*, 69–73. https://doi.org/10.1016/S0304-8853(99)00557-0

[139] - Speakman, S. A., & Ph, D. (2017). Basics of X-Ray Powder Diffraction.

[140] - Lutterotti, L. (2014). Introduction to Rietveld refinements.

[141] – Vittayakorn, N., Rujijanagul, G., Tunkasiri, T., Tan, X., & Cann, D. P. (2003). Perovskite phase formation and ferroelectric properties of the lead nickel niobate-lead zinc niobate-lead zirconate titanate ternary system. *Journal of Materials Research*, *18*(12), 2882–2889. https://doi.org/10.1557/JMR.2003.0402

[142] – Thongtha, A., Angsukased, K., & Bongkarn, T. (2010). Influences of firing temperatures on phase and morphology evolution of $(Ba_{0.25}Sr_{0.75})(Zr_{0.75}Ti_{0.25})O_3$ ceramics synthesized via solid-state reaction method. *Key Engineering Materials*, *421–422*(December 2015), 247–250. https://doi.org/10.4028/www.scientific.net/KEM.421-422.247

[143] – Sriphan, S., Kiravittaya, S., & Bongkarn, T. (2017). Effects of calcination temperature on the synthesis of $[KNbO_3]_{0.9} – [BaNi_{0.5}Nb_{0.5}O_3]_{0.1}$ perovskite powders. *Integrated Ferroelectrics*, *177*(1), 112–120. https://doi.org/10.1080/10584587.2017.1285660

[144] – Lutterotti, L. (n.d.). MAUD (Materials Analysis Using Diffraction). Retrieved from http://maud.radiographema.eu/

[145] - Lutterotti, L. (2010). Total pattern fitting for the combined size-strain-stress-texture determination in thin film diffraction. *Nuclear Instruments and Methods in Physics Research, Section B: Beam Interactions with Materials and Atoms*, *268*(3–4), 334–340. https://doi.org/10.1016/j.nimb.2009.09.053

[146] - Lutterotti, L., Bortolotti, M., Ischia, G., Lonardelli, I., & Wenk, H. R. (2007). Rietveld texture analysis from diffraction images. *Zeitschrift Fur Kristallographie, Supplement*, *1*(26), 125–130. https://doi.org/10.1524/zksu.2007.2007.suppl_26.125

[147] - Lutterotti, L., Chateigner, D., Ferrari, S., & Ricote, J. (2004). Texture, residual stress and structural analysis of thin films using a combined X-ray analysis. *Thin Solid Films*, *450*(1), 34–41. https://doi.org/10.1016/j.tsf.2003.10.150

[148] - Lutterotti, L., Matthies, S., Wenk, H. R., Schultz, A. S., & Richardson, J. W. (1997). Combined texture and structure analysis of deformed limestone from time-of-flight neutron diffraction spectra. *Journal of Applied Physics*, *81*(2), 594–600. https://doi.org/10.1063/1.364220

[149] - Lutterotti, L., Voltolini, M., Wenk, H. R., Bandyopadhyay, K., & Vanorio, T. (2010). Texture analysis of a turbostratically disordered Ca-montmorillonite. *American Mineralogist*, *95*(1), 98–103. https://doi.org/10.2138/am.2010.3238

[150] – Crystallography Open Database. (2013). Retrieved July 25, 2017, from http://crystallography.net/cod/index.php

[151] – Merkys, A., Vaitkus, A., Butkus, J., Okulič-Kazarinas, M., Kairys, V., & Gražulis, S. (2016). COD::CIF::Parser: An error-correcting CIF parser for the Perl

language. *Journal of Applied Crystallography*, *49*, 292–301. https://doi.org/10.1107/S1600576715022396

[152] – Gražulis, S., Merkys, A., Vaitkus, A., & Okulič-Kazarinas, M. (2015). Computing stoichiometric molecular composition from crystal structures. *Journal of Applied Crystallography*, *48*(1), 85–91. https://doi.org/10.1107/S1600576714025904

[153] – Gražulis, S., Daškevič, A., Merkys, A., Chateigner, D., Lutterotti, L., Quirós, M., Serebryanaya, N. R., Moeck, P., Downs, R. T., & Le Bail, A. (2012). Crystallography Open Database (COD): An open-access collection of crystal structures and platform for world-wide collaboration. *Nucleic Acids Research*, *40*(D1), 420–427. https://doi.org/10.1093/nar/gkr900

[154] – Gražulis, S., Chateigner, D., Downs, R. T., Yokochi, A. F. T., Quirós, M., Lutterotti, L., Manakova, E., Butkus, J., Moeck, P., & Le Bail, A. (2009). Crystallography Open Database - An open-access collection of crystal structures. *Journal of Applied Crystallography*, *42*(4), 726–729. https://doi.org/10.1107/S0021889809016690

[155] – Downs, R. T., & Hall-Wallace, M. (2003). The American Mineralogist crystal structure database. *American Mineralogist*, *88*, 247–250. Retrieved from http://www.geo.arizona.edu/xtal//group/pdf/am88_247.pdf

[156] – Le Bail, A. (2005). Inorganic structure prediction with GRINSP. *Journal of Applied Crystallography*, *38*(2), 389–393. https://doi.org/10.1107/S0021889805002384

[157] – Zhou, W., Shao, Z., Ran, R., Zeng, P., Gu, H., Jin, W., & Xu, N. (2007). $Ba_{0.5}Sr_{0.5}Co_{0.8}Fe_{0.2}O_{3-\delta}$ + $LaCoO_3$ composite cathode for $Sm_{0.2}Ce_{0.8}O_{1.9}$-electrolyte based intermediate-temperature solid-oxide fuel cells. *Journal of Power Sources*, *168*(2), 330–337. https://doi.org/10.1016/j.jpowsour.2007.03.041

[158] – Wang, H., Tablet, C., Yang, W., & Caro, J. (2005). In situ high temperature X-ray diffraction studies of mixed ionic and electronic conducting perovskite-type membranes. *Materials Letters*, *59*(28), 3750–3755. https://doi.org/10.1016/j.matlet.2005.06.067

[159] – Niedrig, C., Taufall, S., Burriel, M., Menesklou, W., Wagner, S. F., Baumann, S., & Ivers-Tiffée, E. (2011). Thermal stability of the cubic phase in $Ba_{0.5}Sr_{0.5}Co_{0.8}Fe_{0.2}O_{3-\delta}$ (BSCF)1. *Solid State Ionics*, *197*(1), 25–31. https://doi.org/10.1016/j.ssi.2011.06.010

[160] – Ovenstone, J., Jung, J. Il, White, J. S., Edwards, D. D., & Misture, S. T. (2008). Phase stability of BSCF in low oxygen partial pressures. *Journal of Solid State Chemistry*, *181*(3), 576–586. https://doi.org/10.1016/j.jssc.2008.01.010

[161] – Patra, H., Rout, S. K., Pratihar, S. K., & Bhattacharya, S. (2011). Thermal, electrical and electrochemical characteristics of $Ba_{1-x}Sr_xCo_{0.8}Fe_{0.2}O_{3-\delta}$ cathode material for intermediate temperature solid oxide fuel cells. *International Journal of Hydrogen Energy*, *36*(18), 11904–11913. https://doi.org/10.1016/j.ijhydene.2011.06.021

[162] – Wang, H., Tablet, C., Feldhoff, A., & Caro, J. (2005). Investigation of phase structure, sintering, and permeability of perovskite-type $Ba_{0.5}Sr_{0.5}Co_{0.8}Fe_{0.2}O_{3-\delta}$ membranes. *Journal of Membrane Science*, *262*(1–2), 20–26. https://doi.org/10.1016/j.memsci.2005.03.046

[163] – Li, S., Lü, Z., Wei, B., Huang, X., Miao, J., Cao, G., Zhu, R., & Su, W. (2006). A study of $(Ba_{0.5}Sr_{0.5})_{1-x}Sm_xCo_{0.8}Fe_{0.2}O_{3-\delta}$ as a cathode material for IT-SOFCs. *Journal of Alloys and Compounds*, *426*(1–2), 408–414. https://doi.org/10.1016/j.jallcom.2006.02.040

[164] – Haworth, P., Smart, S., Glasscock, J., & Diniz Da Costa, J. C. (2012). High performance yttrium-doped BSCF hollow fibre membranes. *Separation and Purification Technology*, *94*, 16–22. https://doi.org/10.1016/j.seppur.2012.04.005

[165] – Hashimoto, D., Han, D., & Uda, T. (2014). Dependence of lattice constant of Ba, Co-contained perovskite oxides on atmosphere, and measurements of water content. *Solid State Ionics*, *262*, 687–690. https://doi.org/10.1016/j.ssi.2013.12.029

[166] – Su, C., Xu, X., Chen, Y., Liu, Y., Tadé, M. O., & Shao, Z. (2015). A top-down strategy for the synthesis of mesoporous $Ba_{0.5}Sr_{0.5}Co_{0.8}Fe_{0.2}O_{3-\delta}$ as a cathode precursor for buffer layer-free deposition on stabilized zirconia electrolyte with a superior electrochemical performance. *Journal of Power Sources*, *274*, 1024–1033. https://doi.org/10.1016/j.jpowsour.2014.10.177

[167] – Athayde, D. D., Souza, D. F., Silva, A. M. A., Vasconcelos, D., Nunes, E. H. M., Motuzas, J., Diniz da Costa, J. C., & Vasconcelos, W. L. (2017). Carbonation passivation layer of scandium loaded BSCF perovskite. *Ceramics International*, *43*(17), 15179–15184. https://doi.org/10.1016/j.ceramint.2017.08.049

[168] – Wei, H., Zeng, Y., Wang, L., Cai, T., & Sun, X. (2010). Preparation of $Sm_xCe_{1-x}O_2$(SDC) electrolyte film with gradient structure via a gas-phase controlling

convection-diffusion approach on porous substrate. *Advances in Colloid and Interface Science*, *161*(1–2), 181–194. https://doi.org/10.1016/j.cis.2010.06.004

[169] – Anwar, M., Muhammed, M. A., Baharuddin, N. A., Raduwan, N. F., Muchtar, A., & Somalu, M. R. (2018). Structural, optical and electrical properties of $Ce_{0.8}Sm_{0.2-x}Er_xO_{2-\delta}$ (x = 0–0.2) Co-doped ceria electrolytes. *Ceramics International*, *44*(12), 13639–13648. https://doi.org/10.1016/j.ceramint.2018.04.200

[170] – Zhu, C., Hou, L., Li, S., Gan, L., & Xie, K. (2017). Efficient carbon dioxide electrolysis with metal nanoparticles loaded $La_{0.75}Sr_{0.25}Cr_{0.5}Mn_{0.5}O_{3-\delta}$ cathodes. *Journal of Power Sources*, *363*, 177–184. https://doi.org/10.1016/j.jpowsour.2017.07.070

[171] – Khakpour, Z., Yuzbashi, A., Maghsodipour, A., & Ahmadi, K. (2012). Electrical conductivity of Sm-doped CeO_2 electrolyte produced by two-step sintering. *Solid State Ionics*, *227*, 80–85. https://doi.org/10.1016/j.ssi.2012.09.009

[172] – Acharya, S. A., Gaikwad, V. M., D'Souza, S. W., & Barman, S. R. (2014). Gd/Sm dopant-modified oxidation state and defect generation in nano-ceria. *Solid State Ionics*, *260*, 21–29. https://doi.org/10.1016/j.ssi.2014.03.008

[173] – Gupta, M., Shirbhate, S., Ojha, P., & Acharya, S. (2018). Processing and conductivity behavior of La, Sm, Fe singly and doubly doped ceria: As electrolytes for IT-SOFCs. *Solid State Ionics*, *320*(March), 199–209. https://doi.org/10.1016/j.ssi.2018.03.005

[174] – Kahlaoui, M., Inoubli, A., Chefi, S., Kouki, A., Madani, A., & Chefi, C. (2013). Electrochemical and structural study of $Ce_{0.8}Sm_{0.2-x}La_xO_{1.9}$ electrolyte materials for SOFC. *Ceramics International*, *39*(6), 6175–6182. https://doi.org/10.1016/j.ceramint.2013.01.036

[175] – Melde, K., Jackson, S., Bartlett, K., Sherratt, H. S. A., & Ghisla, S. (1991). Metabolic consequences of methylenecyclopropylglycine poisoning in rats. *Biochemical Journal*, *274*(2), 395–400. https://doi.org/10.1016/j.ceramint.2018.03.060

[176] – Martínez-Amesti, A., Larrañaga, A., Rodríguez-Martínez, L. M., Nó, M. L., Pizarro, J. L., Laresgoiti, A., & Arriortua, M. I. (2009). Chemical compatibility between YSZ and SDC sintered at different atmospheres for SOFC applications. *Journal of Power Sources*, *192*(1), 151–157. https://doi.org/10.1016/j.jpowsour.2009.02.011

[177] – Akbari-Fakhrabadi, A., Meruane, V., Jamshidijam, M., Gracia-Pinilla, M. A., & Mangalaraja, R. V. (2016). Effect of rare earth dopants on structural and mechanical properties of nanoceria synthesized by combustion method. *Materials Science and Engineering A*, *649*, 168–173. https://doi.org/10.1016/j.msea.2015.09.125

[178] – Chiu, F. (2014). A Review on Conduction Mechanisms in Dielectric Films. *Advances in Materials Science and Engineering*, *2014*. https://doi.org/10.1155/2014/578168

[179] – Australian Standard. (2014). Refractories and refractory materials — Physical test methods Method 5 : Determination of bulk density, apparent porosity and true porosity. Sydney: Standards Australia Limited. Retrieved from https://www.standards.org.au/standards-catalogue/sa-snz/mining/mn-007/as--1774-dot-5-colon-2014

[180] – Levy, M. R. (2005). Crystal structure and defect property predictions in ceramic materials, (January). Imperial College of Science, Technology and Medicine. Retrieved from https://spiral.imperial.ac.uk/bitstream/10044/1/11804/2/Levy-MR-2005-PhD-Thesis.pdf

[181] – Ionic radius. (2017). Retrieved April 12, 2018, from https://en.wikipedia.org/wiki/Ionic_radius

[182] –Zachariasen, W. H. (1926). Die Kristallstruktur der A-Modifikation von den Sesquioxyden der seltenen Erdmetalle. (La_2O_3, Ce_2O_3, Pr_2O_3, Nd_2O_3). *Zeitschrift Fuer Physikalische Chemie (Leipzig)*, *123*, 134–150 http://doi:10.1515/zpch-1926-12309. Retrieved from http://crystallography.net/cod/1010278.html

[183] – Mehl, M. J., Hicks, D., Gossett, E., Toher, C., Levy, O., Hanson, R. M., Hart, G. L. W., & Curtarolo, S. (2019). Library of Crystallographic Prototypes. Retrieved from http://aflowlib.org/CrystalDatabase/A2B3_hP5_164_d_ad.html

[184] – Mehl, M. J., Hicks, D., Toher, C., Levy, O., Hanson, R. M., Hart, G., & Curtarolo, S. (2017). The AFLOW Library of Crystallographic Prototypes: Part 1. *Computational Materials Science*, 136, S1-S828. https://doi.org/10.1016/j.commatsci.2017.01.017

[185] – Hicks, D., Mehl, M. J., Gossett, E., Toher, C., Levy, O., Hanson, R. M., Hart, G., & Curtarolo, S. (2019). The AFLOW Library of Crystallographic Prototypes: Part 2. *Computational Materials Science*, 161, S1-S1011. https://doi.org/10.1016/j.commatsci.2018.10.043

[186] – Bommer, H. (1939). Die Gitterkonstanten der C-Formen der Oxyde der seltenen Erdmetalle. *Zeitschrift Fuer Anorganische Und Allgemeine Chemie*, *241*, 273–273. Retrieved from http://crystallography.net/cod/1537842.html

[187] – Wang, C., Tan, M., Feng, C., Ma, Z., Jiang, S., Xu, Z., Cao, G., Matsubayashi, K., & Uwatoko, Y. (2010). $La_2Co_2Se_2O_3$: A Quasi-Two-Dimensional Mott Insulator with Unusual Cobalt Spin State and Possible Orbital Ordering. *Journal of the American Chemical Society*, *132*, 7069–7073. Retrieved from http://crystallography.net/cod/4102405.html

[188] – Titanium dioxide. (2018). Retrieved July 22, 2018, from https://en.wikipedia.org/wiki/Titanium_dioxide#cite_note-Greenwood-11

[189] – Fontaine, M. L., Laberty-Robert, C., Barnabé, A., Ansart, F., & Tailhades, P. (2004). Synthesis of $La_{2-x}NiO_{4+\delta}$ oxides by polymeric route: Non-stoichoimetry control. *Ceramics International*, *30*(8), 2087–2098. https://doi.org/10.1016/j.ceramint.2003.11.013

[190] – Gao, L., Guo, H., Gong, S., & Xu, H. (2014). Plasma-sprayed $La_2Ce_2O_7$ thermal barrier coatings against calcium-magnesium-alumina-silicate penetration. *Journal of the European Ceramic Society*, *34*(10), 2553–2561. https://doi.org/10.1016/j.jeurceramsoc.2014.02.031

[191] – Herrera, G., Jiménez-Mier, J., & Chavira, E. (2014). Layered-structural monoclinic-orthorhombic perovskite $La_2Ti_2O_7$ to orthorhombic $LaTiO_3$ phase transition and their microstructure characterization. *Materials Characterization*, *89*, 13–22. https://doi.org/10.1016/j.matchar.2013.12.013

[192] – Valderrama, G., Urbina De Navarro, C., & Goldwasser, M. R. (2013). CO_2 reforming of CH_4 over Co-La-based perovskite-type catalyst precursors. *Journal of Power Sources*, *234*, 31–37. https://doi.org/10.1016/j.jpowsour.2013.01.142

[193] – Watanabe, R., Hondo, Y., Mukawa, K., Fukuhara, C., Kikuchi, E., & Sekine, Y. (2013). Stable and selective perovskite catalyst for dehydrogenation of propane working with redox mechanism. *Journal of Molecular Catalysis A: Chemical*, *377*, 74–84. https://doi.org/10.1016/j.molcata.2013.04.033

[194] – Hu, Y., Liu, W., Chen, H., Zhou, Z., Wang, W., Sun, J., Yang, X., Li X., & Xu, M. (2016). Screening of inert solid supports for CaO-based sorbents for high temperature CO_2 capture. *Fuel*, *181*, 199–206. https://doi.org/10.1016/j.fuel.2016.04.138

[195] – Franca, R. V., Thursfield, A., & Metcalfe, I. S. (2012). $La_{0.6}Sr_{0.4}Co_{0.2}Fe_{0.8}O_{3-\delta}$ microtubular membranes for hydrogen production from water splitting. *Journal of Membrane Science*, *389*, 173–181. https://doi.org/10.1016/j.memsci.2011.10.027

[196] – Ortiz, C., Eriksson, O., & Klintenberg, M. (2009). Data mining and accelerated electronic structure theory as a tool in the search for new functional materials. *Computational Materials Science*, *44*(4), 1042–1049. https://doi.org/10.1016/j.commatsci.2008.07.016

[197] – Arrivé, C., Delahaye, T., Joubert, O., & Gauthier, G. (2013). Exsolution of nickel nanoparticles at the surface of a conducting titanate as potential hydrogen electrode material for solid oxide electrochemical cells. *Journal of Power Sources*, *223*, 341–348. https://doi.org/10.1016/j.jpowsour.2012.09.062

[198] – Shaula, A. L., Kharton, V. V., & Marques, F. M. B. (2006). Ionic and electronic conductivities, stability and thermal expansion of $La_{10-x}(Si,Al)_6O_{26\pm\delta}$ solid electrolytes. *Solid State Ionics*, *177*(19–25 SPEC. ISS.), 1725–1728. https://doi.org/10.1016/j.ssi.2005.11.023

[199] – Shiratani, K., Hirata, Y., Sameshima, S., Matsunaga, N., & Nakahara, S. (2011). Synthesis and electrical conductivity of La-Sr-X-Mg-O (X = Ti, Zr, Al) perovskite solid solution. *Ceramics International*, *37*(5), 1525–1531. https://doi.org/10.1016/j.ceramint.2011.01.027

[200] –Setevich, C., Toscani, L., Larrondo, S., Prado, F., & Caneiro, A. (2017). Effect of Nb^{5+} content on the high temperature properties of the mixed conductors system $La_{1-x}Ba_xCo_{1-y}Nb_yO_{3-\delta}$ with $0.6 \leq x \leq 1.0$ and $0 \leq y \leq 0.4$. *Solid State Ionics*, *300*, 140–148. https://doi.org/10.1016/j.ssi.2016.12.016

[201] –Earnshaw, N. N. G. A. (1997). *Chemistry of the elements*. *Butterworth-Heinemann* (2nd ed.). Butterworth-Heinemann. https://doi.org/10.1016/S0277-5387(00)84180-7

[202] – University of Cambridge: The interactive Ellingham diagram. (2007, February 9). Retrieved January 7, 2018 from https://www.doitpoms.ac.uk/tlplib/ellingham_diagrams/interactive.php

[203] – Toby, B. H. (2006). R factors in Rietveld analysis: How good is good enough? *Powder Diffraction*, *21*(01), 67–70. https://doi.org/10.1154/1.2179804

[204] – Mahıa, J., Vieiro, A., Mira, J., Rivas, J., López-Quintela, M. A., & Oseroff, S.B. (1996). Influence of Calcination Temperature on Lattice Parameters and Particle Size of R_2CuO_4 Compounds (R = Gd, Nd) Prepared by a Sol – Gel Method. *Journal of Solid State Chemistry*, *30*(122), 25–30. https://doi.org/10.1006/jssc.1996.0076

[205] – Zhang, W., Li, C., Ma, Z., Yang, L., & He, H. (2016). Photocatalyst Prepared using Sol-gel Method. *Journal of Advanced Oxidation Technologies*, *19*(1), 119–124.

[206] – Murugan, R., Thangadurai, V., & Weppner, W. (2008). Lattice Parameter and Sintering Temperature Dependence of Bulk and Grain-Boundary Conduction of Garnet-like Solid Li-Electrolytes. *Journal of The Electrochemical Society*, *155*(1), A90. https://doi.org/10.1149/1.2800764

[207] – El-Shabiny, A. M., El-Shobaky, I. F., Hewaidy, I. F., & Ramadan, A. A. (1988). Microstrain and Lattice Parameter of Pure and Li_2O-doped Nickel Oxide Solid. *Crystal Research and Technology*, *23*(7), 911–917. https://doi.org/10.1002/crat.2170230714

[208] – Tüysüz, H., Weidenthaler, C., Grewe, T., Salabaş, E. L., Benitez Romero, M. J., & Schüth, F. (2012). A Crystal Structure Analysis and Magnetic Investigation on Highly Ordered Mesoporous Cr_2O_3. *Inorganic Chemistry*, *51*(21), 11745–11752. https://doi.org/10.1021/ic301671a

[209] – Kurian, M., & Kunjachan, C. (2014). Investigation of size dependency on lattice strain of nanoceria particles synthesised by wet chemical methods. *International Nano Letters*, *4*(4), 73–80. https://doi.org/10.1007/s40089-014-0122-7

[210] – Pandu, R., Yadav, K. L., Kumar, A., Reddy, P. R., & Gupta, A. V. S. S. K. S. (2010). Effect of sintering temperature on structural and electrical properties of $BiFeO_3$ multiferroics. *Indian Journal of Engineering & Materials Sciences*, *17*, 481–485. https://doi.org/10.4028/www.scientific.net/AMM.378.202

[211] – Agustinawati, D., Isnaini, N. L., & Suasmoro, S. (2017). Analysis of the crystal structure and electrical properties of Li-doped (K, Na)NbO_3 prepared by solid state reaction. In *International Conference on Engineering, Science and Nanotechnology 2016 (ICESNANO 2016)* (Vol. 30129, pp. 1–7). AIP Publishing. https://doi.org/10.1063/1.4968382

[212] – DAI, X., YU, C., LI, R., WU, Q., SHI, K., & HAO, Z. (2008). Effect of calcination temperature and reaction conditions on methane partial oxidation using lanthanum-based perovskite as oxygen donor. *Journal of Rare Earths*, *26*(3), 341–346. https://doi.org/10.1016/S1002-0721(08)60092-7

[213] – Sittiketkorn, P., & Bongkarn, T. (2011). The preparation of lead strontium titanate ceramics by the combustion method. *Ferroelectrics*, *414*(1), 170–179. https://doi.org/10.1080/00150193.2011.577335

[214] – Sittiketkorn P., Thountom, S., & Bongkarn, T. (2008). Effect of Calcination Temperatures on Phase Formation and Microstructure of Lead Titanate Powders Synthesized via Combustion Technique. *N U Science Journal*, *5*(2), 143–150.

[215] – Zeng, P., Wang, K., Falkenstein-Smith, R. L., & Ahn, J. (2015). Effects of Sintering Temperature on the Performance of $SrSc_{0.1}Co_{0.9}O_{3-\delta}$ Oxygen Semipermeable Membrane. *Brazilian Journal of Chemical Engineering*, *32*(3), 757–765. https://doi.org/10.1590/0104-6632.20150323s00003269

[216] – Bongkarn, T., & Wattanawikkam, C. (2009). The Influence of Calcination Temperature on Phase and Morphology of $Ba(Sn_{0.05}Ti_{0.95})O_3$ Powders Synthesized via Solid State Reaction Method and Combustion Technique. *Ferroelectrics*, *382*(October 2014), 42–48. https://doi.org/10.1080/00150190902881512

[217] – Triamnak, N., Brennecka, G., Brown-Shaklee, J., Rodriguez, M., & Cann, D. (2014). Phase formation of $BaTiO_3$–$Bi(Zn_{1/2}Ti_{1/2})O_3$ perovskite ceramics. *Journal of the Ceramic Society of Japan*, *122*, 260. https://doi.org/10.2109/jcersj2.122.260

[218] – Lee, W., Han, J. W., Chen, Y., Cai, Z., & Yildiz, B. (2013). Cation size mismatch and charge interactions drive dopant segregation at the surfaces of manganite perovskites. *Journal of the American Chemical Society*, *135*(21), 7909–7925. https://doi.org/10.1021/ja3125349

[219] – Bartel, C. J., Sutton, C., Goldsmith, B. R., Ouyang, R., Musgrave, C. B., Ghiringhelli, L. M., & Scheffler, M. (2019). New tolerance factor to predict the stability of perovskite oxides and halides. *Science Advances*, *5*(2), 1–10. https://doi.org/10.1126/sciadv.aav0693

[220] – Arrivé, C., Delahaye, T., Joubert, O., & Gauthier, G. H. (2019). Study of $(La,Sr)(Ti,Ni)O_{3-\delta}$ materials for symmetrical Solid Oxide Cell electrode - Part A: Synthesis and structure analysis in air. *Ceramics International*, (June), 1–9. https://doi.org/10.1016/j.ceramint.2019.06.015

[221] – Thalinger, R., Gocyla, M., Heggen, M., Dunin-Borkowski, R., Grünbacher, M., Stöger-Pollach, M., Schmidmair, D., Klötzer, B., & Penner, S. (2016). Ni-perovskite interaction and its structural and catalytic consequences in methane

steam reforming and methanation reactions. *Journal of Catalysis*, *337*, 26–35. https://doi.org/10.1016/j.jcat.2016.01.020

[222] – Agüero, F. N., Beltrán, A. M., Fernández, M. A., & Cadús, L. E. (2019). Surface nickel particles generated by exsolution from a perovskite structure. *Journal of Solid State Chemistry*, *273* (December 2018), 75–80. https://doi.org/10.1016/j.jssc.2019.02.036

[223] – Ben Mya, O., dos Santos-Gómez, L., Porras-Vázquez, J. M., Omari, M., Ramos-Barrado, J. R., & Marrero-López, D. (2017). $La_{1-x}Sr_xFe_{0.7}Ni_{0.3}O_{3-\delta}$ as both cathode and anode materials for Solid Oxide Fuel Cells. *International Journal of Hydrogen Energy*, *42*(36), 23160–23169. https://doi.org/10.1016/j.ijhydene.2017.07.150

[224] – Baikie, T., Fang, Y., Kadro, J. M., Schreyer, M., Wei, F., Mhaisalkar, S., Graetzel, M., & White, T. J. (2013). Synthesis and crystal chemistry of the hybrid perovskite $(CH_3NH_3)PbI_3$ for solid-state sensitised solar cell applications. *Journal of Materials Chemistry A*, *1*(18), 5628–5641. Retrieved from http://hdl.handle.net/10220/18178

[225] – Gai, C., Zhu, N., Hoekman, S. K., Liu, Z., Jiao, W., & Peng, N. (2019). Highly dispersed nickel nanoparticles supported on hydrochar for hydrogen-rich syngas production from catalytic reforming of biomass. *Energy Conversion and Management*, *183*(January), 474–484. https://doi.org/10.1016/j.enconman.2018.12.121

[226] – Fiévet, F., Germi, P., de Bergevin, F., & Figlarz, M. (1979). Lattice parameter, microstrains and non-stoichiometry in NiO. Comparison between mosaic microcrystals and quasi-perfect single microcrystals. *Journal of Applied Crystallography*, *12*(4), 387–394. https://doi.org/10.1107/s0021889879012747

[227] – Chen, Y., Sakata, O., Yamauchi, R., Yang, A., Kumara, L. S. R., Song, C., Palina N., Taguchi M., Ina T., Katsuya Y., Daimon H., Matsuda A., & Yoshimoto, M. (2017). Lattice distortion and electronic structure of magnesium-doped nickel oxide epitaxial thin films. *Physical Review B*, *95*(24), 1–10. https://doi.org/10.1103/PhysRevB.95.245301

[228] – Flege, J. I., Meyer, A., Falta, J., & Krasovskii, E. E. (2011). Self-limited oxide formation in Ni(111) oxidation. *Physical Review B*, *84*(11), 1–11. https://doi.org/10.1103/PhysRevB.84.115441

[229] – He, Y., Li, T., Zhong, X., Zhou, M., Dong, G., & Diao, X. (2019). Lattice and electronic structure variations in critical lithium doped nickel oxide thin film for superior anode electrochromism. *Electrochimica Acta*, *316*, 143–151. https://doi.org/10.1016/j.electacta.2019.05.112

[230] – Su, D., Ford, M., & Wang, G. (2012). Mesoporous NiO crystals with dominantly exposed {110} reactive facets for ultrafast lithium storage. *Scientific Reports*, *2*, 1–7. https://doi.org/10.1038/srep00924

[231] – Iida, Y. (1960). The Lattice Parameter of Nickel Oxide as a Function of Lithium Oxide Dissolved. *Journal of the American Ceramic Society*, *43*(4), 225–225. https://doi.org/10.1201/b11031-14

[232] – Colinge, J.-P., & Colinge, C. A. (2005). *Physics of semiconductor devices*. *Kluwer Academic Publishers* (Vol. 39). New York: Springer-Verlag New York Inc. Retrieved from http://phylab.fudan.edu.cn/lib/exe/fetch.php?media=course:j.p._colinge.physics_of_semiconductor_devices.springer.2005.pdf

[233] – Leadley, D. (n.d.). Department of Physics of University of Warwick. Retrieved November 21, 2018, from https://warwick.ac.uk/fac/sci/physics/current/postgraduate/regs/mpagswarwick/ex5/techniques/electronic/hall-effect/temperature/

[234] – Staras, S. (2008). Elektronikos pagrindai: Conductivity of solids. Vilnius, Lithuania: Vilnius Gediminas Technical University. Retrieved from http://www2.el.vgtu.lt/skaidres/Fundamentals/Conductivity of solids.pdf

[235] – Menoufia University. (2018). 1.9. Temperature Dependence of Semiconductor Conductivity Such. Al Minufya, Egypt: Menoufia University. Retrieved from http://mu.menofia.edu.eg/PrtlFiles/Staff/89/Portal/Files/Presentation5.pdf

[236] – Green, E. D. H. (2017). Temperature Dependence of Semiconductor Conductivity. Silicon Valley, California, USA: San Jose State University. Retrieved from http://www.iiserkol.ac.in/~ph324/StudyMaterials/ResistivityTdep.pdf

[237] – Parasuraman, S. (2014). Lecture 8: Extrinsic semiconductors - mobility. *Electronic Materials, Devices, and Fabrication*. National Programme on Technology Enhanced Learning. Retrieved from https://nptel.ac.in/courses/113106062/Lec8.pdf

[238] – RWTH Aachen University, D. of P. (n.d.). 9 Electrical conductivity of metals, semiconductors, and superconductors. Aachen, North Rhine-Westphalia, Germany: RWTH Aachen University. Retrieved from https://institut2a.physik.rwth-aachen.de/de/teaching/praktikum/Anleitungen/FK09-Leitfaehigkeit-englisch.PDF

[239] – Kuphaldt, T. R. (2018). All about circuits. Retrieved November 27, 2018, from https://www.allaboutcircuits.com/textbook/semiconductors/chpt-2/electrons-and-holes/

[240] – Hummel, R. E. (2011). *Electronic Properties of Materials* (3rd ed.). New York: Springer-Verlag Berlin Heidelberg. https://doi.org/10.1007/978-3-642-86538-1

[241] – O'Hayre, R. S. C. G. C. F. B. P. (2016). *Fuel Cell Fundamentals*. (J. W. & Sons, Ed.) (3rd ed.). New Jersey. Retrieved from http://books.google.com/books/about/Fuel_Cell_Fundamentals.html?id=_EyJQwAACAAJ&pgis=1

[242] – Rosten, R., Koski, M., & Koppana, E. (2006). A Guide to the Calculation of Theoretical Densities of Crystal Structures for Solid Oxide Fuel Cells. *Journal of Undergraduate Materials Research*, 38–41. Retrieved from https://jumr.org/articles/10.21061/jumr.v2i0.0605/

[243] – Tilton, L. W., & Taylor, J. K. (1937). Accurate representation of the refractivity and density of distilled water as a function of temperature. *Journal of Research of the National Bureau of Standards*, *18*(2), 205–214. https://doi.org/10.6028/jres.018.008

[244] – TutorVista.com: Water Density Calculator. (n.d.). Retrieved August 8, 2018 from https://calculator.tutorvista.com/water-density-calculator.html

[245] – Marinšek, M. (2009). Electrical Conductivity of Sintered LSM Ceramics. *Materiali In Tehnologije*, 43(2), 79–84.

[246] – Cowin, P. I., Lan, R., Petit, C. T. G., Du, D., Xie, K., Wang, H., & Tao, S. (2017). Conductivity and redox stability of new perovskite oxides $SrFe_{0.7}TM_{0.2}Ti_{0.1}O_{3-\delta}$ (TM = Mn, Fe, Co, Ni, Cu). *Solid State Ionics*, 301, 99–105. https://doi.org/10.1016/j.ssi.2017.01.017

[247] – Panteix, P. J., Julien, I., Abélard, P., & Bernache-Assollant, D. (2008). Influence of porosity on the electrical properties of $La_{9.33}(SiO_4)_6O_2$ oxyapatite. *Ceramics International*, 34(7), 1579–1586. https://doi.org/10.1016/j.ceramint.2007.05.004

[248] – Pang, S., Jiang, X., & Li, X. (2015). Defect Chemical Models for Temperature Dependence of Oxygen Stoichiometry and Electrical Conductivities of $Ba_{0.5}Sr_{0.5}Co_{0.8}Fe_{0.2}O_{3-\delta}$ *Ferroelectrics*, *478*(1), 26–39. https://doi.org/10.1080/00150193.2015.1011024

[249] – Li, S., Lü, Z., Huang, X., & Su, W. (2008). Thermal, electrical, and electrochemical properties of Nd-doped $Ba_{0.5}Sr_{0.5}Co_{0.8}Fe_{0.2}O_{3-\delta}$ as a cathode material for SOFC. *Solid State Ionics*, *178*(35–36), 1853–1858. https://doi.org/10.1016/j.ssi.2007.11.016

[250] – Bonturim, E., Vargas, R. A., Andreoli, M., & Seo, E. S. M. (2012). Crystal structure and electrical conductivity evaluation of $Ba_{0.50}Sr_{0.50}Co_{0.80}Fe_{0.20}O_{3-d}$ obtained by complexing method. In *20º CBECIMAT - Congresso Brasileiro de Engenharia e Ciência dos Materiais 04 a 08 de Novembro de 2012, Joinville, SC, Brasil* (pp. 1427–1436).

[251] – Park, H. J., Kwak, C., Kim, J. S., & Ahn, S. J. (2012). Electrochemical properties of pure $Ba_{0.5}Sr_{0.5}Co_{0.8}Fe_{0.2}O_3$ and $Ba_{0.5}Sr_{0.5}Co_{0.8}Fe_{0.2}O_3$-based composite cathodes for an intermediate temperature solid oxide fuel cell with Sc-doped zirconia solid electrolyte. *Journal of Power Sources*, *213*, 31–39. https://doi.org/10.1016/j.jpowsour.2012.03.093

[252] – Wang, Y., Wang, S., Wang, Z., Wen, T., & Wen, Z. (2007). Performance of $Ba_{0.5}Sr_{0.5}Co_{0.8}Fe_{0.2}O_{3-\delta}$-CGO-Ag cathode for IT-SOFCs. *Journal of Alloys and Compounds*, *428*(1–2), 286–289. https://doi.org/10.1016/j.jallcom.2006.02.071

[253] – Hung, I. M., Liang, C. Y., Ciou, C. J., & Lee, Y. C. (2010). Conductivity and electrochemical performance of $(Ba_{0.5}Sr_{0.5})_{0.8}La_{0.2}CoO_{3-\delta}$ cathode for intermediate-temperature solid oxide fuel cell. *Ceramics International*, *36*(6), 1937–1943. https://doi.org/10.1016/j.ceramint.2010.03.014

[254] – Ran, R., Guo, Y., Gao, D., Liu, S., & Shao, Z. (2011). Effect of foreign oxides on the phase structure, sintering and transport properties of $Ba_{0.5}Sr_{0.5}Co_{0.8}Fe_{0.2}O_{3-\delta}$ as ceramic membranes for oxygen separation. *Separation and Purification Technology*, *81*(3), 384–391. https://doi.org/10.1016/j.seppur.2011.08.005

[255] – Guo, Y., Zhou, Y., Chen, D., Shi, H., Ran, R., & Shao, Z. (2011). Significant impact of the current collection material and method on the performance of $Ba_{0.5}Sr_{0.5}Co_{0.8}Fe_{0.2}O_{3-\delta}$ electrodes in solid oxide fuel cells. *Journal of Power Sources*, *196*(13), 5511–5519. https://doi.org/10.1016/j.jpowsour.2011.02.056

[256] – Yáng, Z., Harvey, A. S., Infortuna, A., Schoonman, J., & Gauckler, L. J. (2011). Electrical conductivity and defect chemistry of $Ba_xSr_{1-x}Co_yFe_{1-y}O_{3-\delta}$ perovskites. *Journal of Solid State Electrochemistry*, 15(2), 277–284. https://doi.org/10.1007/s10008-010-1208-4

[257] – Jung, J. Il, Misture, S. T., & Edwards, D. D. (2010). Oxygen stoichiometry, electrical conductivity, and thermopower measurements of BSCF ($Ba_{0.5}Sr_{0.5}Co_xFe_{1-x}O_{3-\delta}$, $0 \leq x \leq 0.8$) in air. *Solid State Ionics*, 181(27–28), 1287–1293. https://doi.org/10.1016/j.ssi.2010.06.033

[258] – Shen, F. (2016). Study of Perovskite Structure Cathode Materials and Protective Coatings on Interconnect for Solid Oxide Fuel Cells. (Doctoral dissertation, Faculty of the Virginia Polytechnic Institute and State University).

[259] – Niedrig, C. (2015). Electrochemical Performance and Stability of $Ba_{0.5}Sr_{0.5}Co_{0.8}Fe_{0.2}O_{3-\delta}$ for Oxygen Transport Membranes (Doctoral dissertation, Dissertation, KIT Scientific Publishing). https://doi.org/10.5445/KSP/1000049670

[260] – Jung, J. Il, Misture, S. T., & Edwards, D. D. (2012). Seebeck coefficient and electrical conductivity of BSCF ($Ba_{0.5}Sr_{0.5}Co_xFe_{1-x}O_{3-\delta}$, $0 \leq x \leq 0.8$) as a function of temperature and partial oxygen pressure. *Solid State Ionics*, *206*, 50–56. https://doi.org/10.1016/j.ssi.2011.09.023

[261] – Burriel, M., Niedrig, C., Menesklou, W., Wagner, S. F., Santiso, J., & Ivers-Tiffée, E. (2010). BSCF epitaxial thin films: Electrical transport and oxygen surface exchange. Solid State Ionics, 181(13–14), 602–608. https://doi.org/10.1016/j.ssi.2010.03.005

[262] – Kozuka, H., Ohbayashi, K., & Koumoto, K. (2015). Electronic conduction in La-based perovskite-type oxides. *Science and technology of advanced materials*, *16*(2), 026001. https://doi.org/10.1088/1468-6996/16/2/026001

[263] – Fornarini, L., Conde, J. C., Alvani, C., Olevano, D., & Chiussi, S. (2008). Experimental determination of La_2O_3 thermal conductivity and its application to the thermal analysis of a-Ge/La_2O_3/c-Si laser annealing. *Thin Solid Films*, *516*(21), 7400–7405. https://doi.org/10.1016/j.tsf.2008.02.032

[264] – Kale, S. S., Jadhav, K. R., Patil, P. S., Gujar, T. P., & Lokhande, C. D. (2005). Characterizations of spray-deposited lanthanum oxide (La_2O_3) thin films. *Materials Letters*, *59*(24-25), 3007-3009. https://doi.org/10.1016/j.matlet.2005.02.091

[265] – Matsumoto, M., Yamaguchi, N., & Matsubara, H. (2004). Low thermal conductivity and high temperature stability of ZrO_2-Y_2O_3-La_2O_3 coatings produced by electron beam PVD. *Scripta Materialia*, *50*(6), 867–871. https://doi.org/10.1016/j.scriptamat.2003.12.008

[266] – Chaogui, Z., Shuangyan, W., Fuhui, L., Shujian, T., & Guobao, L. (1999). Phase equilibria, and electrical properties of compounds in the system MgO–La_2O_3-TiO_2 at 1200 ^oC. *Journal of Alloys and Compounds*, *289*, 257–259. https://doi.org/10.1016/S0925-8388(99)00143-7

[267] – Matsumoto, M., Kato, T., Yamaguchi, N., Yokoe, D., & Matsubara, H. (2009). Thermal conductivity and thermal cycle life of La_2O_3 and HfO_2 doped ZrO_2-Y_2O_3 coatings produced by EB-PVD. *Surface and Coatings Technology*, *203*(19), 2835–2840. https://doi.org/10.1016/j.surfcoat.2009.01.033

[268] – Qian, K., Liang, S., Xiao, P., & Wang, X. (2012). In situ synthesis and electrical properties of CuW-La_2O_3 composites. *International Journal of Refractory Metals and Hard Materials*, *31*, 147–151. https://doi.org/10.1016/j.ijrmhm.2011.10.005

[269] – Matsumoto, M., Aoyama, K., Matsubara, H., Takayama, K., Banno, T., Kagiya, Y., & Sugita, Y. (2005). Thermal conductivity and phase stability of plasma sprayed ZrO_2-Y_2O_3-La_2O_3 coatings. *Surface and Coatings Technology*, *194*(1), 31–35. https://doi.org/10.1016/j.surfcoat.2004.04.078

[270] – Matsumoto, M., Takayama, H., Yokoe, D., Mukai, K., Matsubara, H., Kagiya, Y., & Sugita, Y. (2006). Thermal cycle behavior of plasma sprayed La_2O_3, Y_2O_3 stabilized ZrO_2 coatings. *Scripta Materialia*, *54*(12), 2035–2039. https://doi.org/10.1016/j.scriptamat.2006.03.015

[271] – Dong, X., Gan, Y., Wang, Y., Peng, S., & Dong, L. (2013). Effect of La_2O_3 on high-temperature thermoelectric properties of WO_3. *Journal of Alloys and Compounds*, *581*, 52–55. https://doi.org/10.1016/j.jallcom.2013.07.052

[272] – Thangadurai, P., Sabarinathan, V., Bose, A. C., & Ramasamy, S. (2004). Conductivity behaviour of a cubic/tetragonal phase stabilized nanocrystalline La_2O_3-ZrO_2. *Journal of Physics and Chemistry of Solids*, *65*(11), 1905–1912. https://doi.org/10.1016/j.jpcs.2004.06.017

[273] – Zhang, B., Zhao, Q., Chang, A., Huang, X., Hou, J., Zhao, P., & Ji, G. (2013). La_2O_3-doped $0.6Y_2O_3$-$0.4YCr_{0.5}Mn_{0.5}O_3$ composite NTC ceramics for wide range of

temperature sensing. *Journal of Alloys and Compounds*, *581*, 573–578. https://doi.org/10.1016/j.jallcom.2013.07.060

[274] – Borchert, H., & Baerns, M. (1997). The effect of oxygen-anion conductivity of metal-oxide doped lanthanum oxide catalysts on hydrocarbon selectivity in the oxidative coupling of methane. *Journal of Catalysis*, *168*(2), 315–320. https://doi.org/10.1006/jcat.1997.1662

[275] – Singh, K., Nowotny, J., & Thangadurai, V. (2013). Amphoteric oxide semiconductors for energy conversion devices: A tutorial review. *Chemical Society Reviews*, *42*(5), 1961–1972. https://doi.org/10.1039/c2cs35393h

[276] – Rodríguez-López, S., Haanappel, V. A. C., Durán, A., Muñoz, F., Mather, G. C., Pascual, M. J., & Gross-Barsnick, S. M. (2016). Glass–ceramic seals in the system MgO-BaO-B_2O3-SiO_2 operating under simulated SOFC conditions. *International Journal of Hydrogen Energy*, *41*(34), 15335–15345. https://doi.org/10.1016/j.ijhydene.2016.07.051

[277] – Zhang, L., Shan, J., & Wang, Q. (2019). $BaCo_{0.4}Fe_{0.4}Zr_{0.2}O_{3-\delta}$: Evaluation as a cathode for ceria-based electrolyte IT-SOFCs. *Journal of Alloys and Compounds*, *771*, 221–227. https://doi.org/10.1016/j.jallcom.2018.08.232

[278] – Jeong, J., Azad, A. K., Schlegl, H., Kim, B., Baek, S. W., Kim, K., Kang H., & Kim, J. H. (2015). Structural, thermal and electrical conductivity characteristics of $Ln_{0.5}Sr_{0.5}Ti_{0.5}Mn_{0.5}O_{3\pm d}$ (Ln: La, Nd and Sm) complex perovskites as anode materials for solid oxide fuel cell. *Journal of Solid State Chemistry*, *226*, 154–163. https://doi.org/10.1016/j.jssc.2015.02.001

[279] – Magrasó, A. (2013). Transport number measurements and fuel cell testing of undoped and Mo-substituted lanthanum tungstate. *Journal of Power Sources*, *240*, 583–588. https://doi.org/10.1016/j.jpowsour.2013.04.087

[280] – Magrasó, A., Ballesteros, B., Rodríguez-Lamas, R., Sunding, M. F., & Santiso, J. (2018). Optimisation of growth parameters to obtain epitaxial Y-doped $BaZrO_3$ proton conducting thin films. *Solid State Ionics*, *314*(November 2017), 9–16. https://doi.org/10.1016/j.ssi.2017.11.002

[281] – Sarno, C., Luisetto, I., Zurlo, F., Licoccia, S., & Di Bartolomeo, E. (2018). Lanthanum chromite based composite anodes for dry reforming of methane. *International Journal of Hydrogen Energy*, *43*(31), 14742–14750. https://doi.org/10.1016/j.ijhydene.2018.06.021

[282] – Christie, G. M., Middleton, P. H., & Steele, B. C. H. (1994). Liquid phase sintering, electrical conductivity, and chemical stability of lanthanum chromite doped with calcium and nickel. *Journal of the European Ceramic Society*, *14*(2), 163–175. https://doi.org/10.1016/0955-2219(94)90104-X

[283] – Marques, R. M. C., Marques, F. M. B., & Frade, J. R. (1994). Characterization of mixed conductors by dc techniques. Part I: Theoretical solutions. *Solid State Ionics*, *73*(1–2), 15–25. https://doi.org/10.1016/0167-2738(94)90259-3

[284] – Steiner, H. J., Middleton, P. H., & Steele, B. C. H. (1993). Ternary titanates as anode materials for solid oxide fuel cells. *Journal of Alloys and Compounds*, *190*(2), 279–285. https://doi.org/10.1016/0925-8388(93)90412-G

[285] – Neagu, D., Tsekouras, G., Miller, D. N., Ménard, H., & Irvine, J. T. S. (2013). In situ growth of nanoparticles through control of non-stoichiometry. *Nature Chemistry*, *5*(11), 916–923. https://doi.org/10.1038/nchem.1773

[286] – Li, Y., Xie, K., Chen, S., Li, H., Zhang, Y., & Wu, Y. (2015). Efficient carbon dioxide electrolysis based on perovskite cathode enhanced with nickel nanocatalyst. *Electrochimica Acta*, *153*, 325–333. https://doi.org/10.1016/j.electacta.2014.11.151

[287] – Gao, Y., Chen, D., Saccoccio, M., Lu, Z., & Ciucci, F. (2016). From material design to mechanism study: Nanoscale Ni exsolution on a highly active A-site deficient anode material for solid oxide fuel cells. *Nano Energy*, *27*, 499–508. https://doi.org/10.1016/j.nanoen.2016.07.013

[288] – Hua, B., Li, M., Sun, Y. F., Li, J. H., & Luo, J. L. (2017). Enhancing Perovskite Electrocatalysis of Solid Oxide Cells Through Controlled Exsolution of Nanoparticles. *ChemSusChem*, *10*(17), 3333–3341. https://doi.org/10.1002/cssc.201700936

[289] – Cassidy, M. (2017). Trends in the processing and manufacture of solid oxide fuel cells. *Wiley Interdisciplinary Reviews: Energy and Environment*, *6*(5). https://doi.org/10.1002/wene.248

[290] – Ishihara, T. (2016). Nanomaterials for advanced electrode of low temperature solid oxide fuel cells (SOFCs). *Journal of the Korean Ceramic Society*, *53*(5), 469–477. https://doi.org/10.4191/kcers.2016.53.5.469

[291] – Li, Y., Zhang, W., Zheng, Y., Chen, J., Yu, B., Yan, C., & Liu, M. (2017). Controlling cation segregation in perovskite- based electrodes for high electro-

catalytic activity and durability †. *Chemical Society Reviews*, (46), 6345–6378. https://doi.org/10.1039/C7CS00120G

[292] – Shannon, R. D. (1976). Revised Effective Ionic Radii and Systematic Studies of Interatomic Distances in Halides and Chalcogenides. *Acta crystallographica section A: crystal physics, diffraction, theoretical and general crystallography*, 32(5), 751–767. https://doi.org/10.1107/S0567739476001551

[293] – Ahrens, L. H. (1952). The use of ionization potentials Part 1. Ionic radii of the elements. *Geochimica et cosmochimica Acta*, *2(3)*, 155–169. https://doi.org/10.1016/0016-7037(52)90004-5

[294] – Pauling, L. (1960). The Nature of the Chemical Bond and the Structure of Molecules and Crystals: An Introduction to Modern Structural Chemistry. (No. 04; RMD, QD469 P3.) (1960 Cornell University Press, Ed.).

[295] – Wikipedia, the free encyclopedia: Manganese. (n.d.). Retrieved January 7, 2018 from https://en.wikipedia.org/wiki/Manganese

[296] – Niu, Y., Zhou, W., Sunarso, J., Ge, L., Zhu, Z., & Shao, Z. (2010). High performance cobalt-free perovskite cathode for intermediate temperature solid oxide fuel cells. *Journal of Materials Chemistry*, *20*(43), 9619. https://doi.org/10.1039/c0jm02816a

[297] – Zhu, L., Ran, R., Tadé, M., Wang, W., & Shao, Z. (2016). Perovskite materials in energy storage and conversion. *Asia-Pacific Journal of Chemical Engineering*, *11*(May), 338–369. https://doi.org/10.1002/apj.2000

[298] – Dong, F., Chen, D., Chen, Y., Zhao, Q., & Shao, Z. (2012). La-doped $BaFeO_{3-\delta}$ perovskite as a cobalt-free oxygen reduction electrode for solid oxide fuel cells with oxygen-ion conducting electrolyte. *Journal of Materials Chemistry*, *22*(30), 15071. https://doi.org/10.1039/c2jm31711g

[299] – Chen, D., Wang, F., Shi, H., Ran, R., & Shao, Z. (2012). Systematic evaluation of Co-free $LnBaFe_2O_{5+\delta}$ (Ln = Lanthanides or Y) oxides towards the application as cathodes for intermediate-temperature solid oxide fuel cells. *Electrochimica Acta*, *78*, 466–474. https://doi.org/10.1016/j.electacta.2012.06.073

[300] – Jiang, S., Sunarso, J., Zhou, W., Shen, J., Ran, R., & Shao, Z. (2015). Cobalt-free $SrNb_xFe_{1-x}O_{3-\delta}$ (x = 0.05, 0.1 and 0.2) perovskite cathodes for intermediate temperature solid oxide fuel cells. *Journal of Power Sources*, *298*, 209–216. https://doi.org/10.1016/j.jpowsour.2015.08.063

[301] – Dong, F., Chen, Y., Chen, D., & Shao, Z. (2014). Surprisingly high activity for oxygen reduction reaction of selected oxides lacking long oxygen-ion diffusion paths at intermediate temperatures: A case study of cobalt-free $BaFeO_{3-\delta}$. *ACS Applied Materials and Interfaces*, *6*(14), 11180–11189. https://doi.org/10.1021/am502240m

[302] – Porras-Vazquez, J. M., Marco, J. F., Berry, F. J., & Slater, P. R. (2015). Synthesis and characterization of novel Ge doped $Sr_{1-y}Ca_yFeO_{3-\delta}$ SOFC cathode materials. *Materials Research Bulletin*, *67*, 63–69. https://doi.org/10.1016/j.materresbull.2015.02.014

[303] – Porras-Vazquez, J. M., Smith, R. I., & Slater, P. R. (2014). Investigation into the effect of Si doping on the cell symmetry and performance of $Sr_{1-y}Ca_yFeO_{3-\delta}$ SOFC cathode materials. *Journal of Solid State Chemistry*, *213*, 132–137. https://doi.org/10.1016/j.jssc.2014.02.027

[304] – Wang, R., Jin, F., Ta, L., & He, T. (2016). $SrCo_{1-x}Mo_xO_{3-\delta}$ perovskites as cathode materials for $LaGaO_3$-based intermediate-temperature solid oxide fuel cells. *Solid State Ionics*, *288*, 32–35. https://doi.org/10.1016/j.ssi.2015.11.030

[305] – Hong, S. J., & Virkar, A. V. (1995). Lattice Parameters and Densities of Rare-Earth Oxide Doped Ceria Electrolytes. *Journal of the American Ceramic Society*, *78*(2), 433–439. https://doi.org/10.1111/j.1151-2916.1995.tb08820.x

[306] – Li, X., Wang, Y., Liu, W., Jiang, G., & Zhu, C. (2012). Study of oxygen vacancies′ influence on the lattice parameter in ZnO thin film. *Materials Letters*, *85*, 25–28. https://doi.org/10.1016/j.matlet.2012.06.107

[307] – Lee, S. A., Jeong, H., Woo, S., Hwang, J. Y., Choi, S. Y., Kim, S. D., Choi, M., Roh, S., Yu, H., Hwang, J., Kim, S. D., & Choi, W. S. (2016). Phase transitions via selective elemental vacancy engineering in complex oxide thin films. *Scientific Reports*, *6*, 1–28. https://doi.org/10.1038/srep23649

[308] – Gazquez, J., Bose, S., Sharma, M., Torija, M. A., Pennycook, S. J., Leighton, C., & Varela, M. (2013). Lattice mismatch accommodation via oxygen vacancy ordering in epitaxial $La_{0.5}Sr_{0.5}CoO_{3-\delta}$ thin films. *APL Materials*, *1*(1), 0–7. https://doi.org/10.1063/1.4809547

[309] – Zamani, S. M. M., & Behdinan, K. (2017). The effect of oxygen vacancy and temperature on the lattice parameters of mullite using a novel bridging cell multiscale method. *Ceramics International*, *43*(15), 12239–12248. https://doi.org/10.1016/j.ceramint.2017.06.085

[310] – Nord, M., Vullum, P. E., Moreau, M., Boschker, J. E., Selbach, S. M., Holmestad, R., & Tybell, T. (2015). Structural phases driven by oxygen vacancies at the $La_{0.7}Sr_{0.3}MnO_3/SrTiO_3$ hetero-interface. *Applied Physics Letters*, *106*(4), 0–4. https://doi.org/10.1063/1.4906920

[311] – Wang, C., Cheng, B. L., Wang, S. Y., Lu, H. B., Zhou, Y. L., Chen, Z. H., & Yang, G. Z. (2005). Effects of oxygen pressure on lattice parameter, orientation, surface morphology and deposition rate of $(Ba_{0.02}Sr_{0.98})TiO_3$ thin films grown on MgO substrate by pulsed laser deposition. *Thin Solid Films*, *485*(1–2), 82–89. https://doi.org/10.1016/j.tsf.2005.03.055

[312] – Ederer, C., & Spaldin, N. A. (2005). Influence of strain and oxygen vacancies on the magnetoelectric properties of multiferroic bismuth ferrite. *Physical Review B*, *71*(22), 224103 https://doi.org/10.1103/PhysRevB.71.224103

[313] – Cazorla, C. (2017). Lattice Effects on the Formation of Oxygen Vacancies in Perovskite Thin Films. *Physical Review Applied*, *7*(4), 1–8. https://doi.org/10.1103/PhysRevApplied.7.044025

[314] – Chang, Y. J., Kim, J. I., & Jung, C. U. (2008). Electrical Properties of $SrRuO_3$ Thin Films with Varying c-axis Lattice Constant. *Journal of Magnetics*, *13*(2), 61–64.

[315] – Kawashima, K., Logvenov, G., Christiani, G., & Habermeier, H. U. (2015). Interrelation of epitaxial strain and oxygen deficiency in $La_{0.7}Ca_{0.3}MnO_{3-\delta}$ thin films. *Journal of Magnetism and Magnetic Materials*, *378*, 539–545. https://doi.org/10.1016/j.jmmm.2014.11.055

[316] – Pauw, L. (1958). A method of measuring the resistivity and Hall coefficient on lamellae of arbitrary shape. *Philips technical review*, *20*(8), 220-224.

[317] – Ngo, N., Niu, H., Bharadwaj, P., Bhatti, H., & Adhikari, S. (2017). *Van der Pauw Resisitivity Measurement*, Technical Report. https://doi.org/10.13140/RG.2.2.23468.67208

Appendix

Table II A1 – Several symmetrical cell results of OCV and PPD with Zirconia based electrolytes

		Cell components				Performance				
Source		Electrolyte			Electrodes	Result		Conditions		Fig/Tab
Ref	Year	name	Chemical composition	Thickness	Chemical composition	OCV	PPD	Temp.	Fuel	-
#	-	-	-	(mm)	-	(V)	($mW.cm^{-2}$)	(^oC)	-	-
[20]	2007	YSZ	mol8%Y_2O_3 + mol92%ZrO_2	1.2	(wt50%$La_{0.75}Sr_{0.25}Cr_{0.5}Mn_{0.5}O_3$ + wt50%YSZ)+imp($Ce_{0.8}Gd_{0.2}$)	1.01	275	850	97%H_2 3%H_2O	14b
[21]	2014		mol8%Y_2O_3 + mol92%ZrO_2	0.025	($La_{0.6}Sr_{0.4}Fe_{0.9}Sc_{0.1}O_{3-\delta}$) - (mol8%$Y_2$ O_3+mol92%ZrO_2)	1.06	650	800	H_2	3a
[22]	2018		mol8%Y_2O_3 + mol92%ZrO_2	0.4	70wt%($La_{0.8}Sr_{0.2}MnO_{3-\delta}$) + 30wt%(and $Gd_{0.2}Ce_{0.8}O_{2-\delta}$)	1.06	150.8	800	97%H_2 3%H_2O	7b
				0.4	$La_{0.8}Sr_{0.2}MnO_{3-\delta}$	1.08	67.45	800	97%H_2 3%H_2O	7a
[23]	2018		mol8%Y_2O_3 + mol92%ZrO_2 + (Barrier layer of GDC)	0.21	$La_{0.4}Sr_{0.6}Co_{0.2}Fe_{0.7}Nb_{0.1}O_{3-\delta}$ -- $Gd_{0.1}Ce_{0.9}O_{2-\delta}$	1.03	348	850	H_2	4a
				0.21		1.05	251	800	H_2	4a
[24]	2016		mol8%Y_2O_3 + mol92%ZrO_2	0.7	$Sm_{0.95}Ce_{0.05}FeO_{3-\delta}$	1.02	130	800	H_2	8a
				0.7	70wt%($Sm_{0.95}Ce_{0.05}FeO_{3-\delta}$) + 30wt%(mol8%$Y_2O_3$+mol92%$ZrO_2$)	1.02	193	800	H_2	8b
[25]	2017		mol8%Y_2O_3 + mol92%ZrO_2 + (Barrier layer of GDC)	0.2	50wt%($La_{0.4}Sr_{0.6}Co_{0.2}Fe_{0.7}Nb_{0.1}O_{3-\delta}$) + 50wt%(and $Gd_{0.2}Ce_{0.8}O_{2-\delta}$)	1.1	395	850	H_2	6a
				0.2		1.09	230	800	H_2	6a
[26]	2015		mol8%Y_2O_3 + mol92%ZrO_2 + (Barrier layer of SDC)	0.4	$La_{0.3}Sr_{0.7}Ti_{0.3}Fe_{0.7}O_{3-\delta}$	1.1	374	900	H_2	3b
				0.4		1.1	215	800	H_2	3b
[27]	2014		mol8%Y_2O_3 + mol92%ZrO_2	1	$La_{0.75}Sr_{0.25}Cr_{0.5}Mn_{0.5}O_{3-d}$	?	175	900	wet H_2	-
				1	$La_{0.75}Sr_{0.125}Ce_{0.125}Cr_{0.5}Mn_{0.5}O_{3-\delta}$	1.03	52.12	900	dry H_2	4e
				1		0.95	18	800	dry H_2	4e
				1		1.03	76.5	900	wet H_2	4f
				1		0.95	45	800	wet H_2	4f
[28]	2016		mol8%Y_2O_3 + mol92%ZrO_2	0.4	$La_{0.8}Sr_{0.2}FeO_{3-\delta}$	1.01	316	800	97%H_2 3%H_2O	5a
			mol8%Y_2O_3 + mol92%ZrO_2 + (Barrier layer of $Gd_{0.2}Ce_{0.8}O_{2-\delta}$)	0.404		1	387	800	97%H_2 3%H_2O	5b
[29]	2017		7(CuFe-oxide mineral) + 3(YSZ)	0.562	$Ni_{0.8}Co_{0.15}Al_{0.05}LiO_{2-\delta}$ + (Ni foam pasted)	1.1	360	550	H_2	5a
			6(CuFe-oxide mineral) + 4(YSZ)	0.562		1.1	450	550	H_2	5a
			5(CuFe-oxide mineral) + 5(YSZ)	0.562		1.2	562	550	H_2	5a
			4(CuFe-oxide mineral) + 6(YSZ)	0.562		1.16	325	550	H_2	5a
[30]	2018		mol8%Y_2O_3 + mol92%ZrO_2 + (Barrier layer of $Gd_{0.2}Ce_{0.8}O_{2-\delta}$)	0.45	$PrBaMn_2O_{5+\delta}$	1.07	253	800	H_2	9a

			mol8%Y_2O_3 + mol92%ZrO_2	0.4		1.04	125	800	H_2	9a
[31]	2009	SSZ	$(Sc_2O_3)_{0.1}(ZrO_2)_{0.9}$	0.3	$La_{0.8}Sr_{0.2}Sc_{0.2}Mn_{0.8}O_3$	1	310	900	H_2	9
				0.3		1.02	220	850	H_2	9
[32]	2012		$Sc_{0.1}Zr_{0.9}O_{1.95}$	0.18	wt87.5%$La_{0.6}Sr_{0.4}Fe_{0.9}Sc_{0.1}O_{3-\delta}$ + wt12.5%$Ce_{0.6}Fe_{0.1}Mn_{0.3}O_2$	1.1	335	800	H_2	2a
[33]	2015		10Sc1CeSZ (Sc-doped ZrO_2 + $Sm_{0.2}Ce_{0.8}O_{1.9}$ buffer layer)	0.23	$La_{0.5}Sr_{0.5}Fe_{0.8}Cu_{0.2}O_{3-\delta}$ - $Ce_{0.8}Sm_{0.2}O_{1.9}$	1.1	1054	900	humid H_2	3a
				0.23		1.1	795	850	humid H_2	3a
				0.23		1.07	577	800	humid H_2	3a
[34]	2016		$Sc_{0.2}Zr_{0.8}O_{2-\delta}$	0.06	$La_{0.9}Ca_{0.1}Fe_{0.9}Nb_{0.1}O_{3-\delta}$	1.07	392	850	H_2	5a
				0.06		1.09	322	800	H_2	5a
				0.06	40%($La_{0.9}Ca_{0.1}Fe_{0.9}Nb_{0.1}O_{3-d}$) + 25%($Ce_{0.8}Sm_{0.2}O_{2-\delta}$)	1.08	528	850	H_2	5b
				0.06		1.1	446.1	800	H_2	5b

Table II A2 – Several symmetrical cell results of impedance with Zirconia based electrolytes

		Cell components				Impedance					
Source		Electrolyte			Electrodes	Different atmospheres		Same atmosphere		Condition	Fig/Tab
Ref	Year	name	Chemical composition	Thickness	Chemical composition	Electrolyte	Electrodes	air	H_2	Temp.	
#	-	-	-	(mm)	-	(Ω.cm²)				(ºC)	-
[20]	2007	YSZ	mol8%Y_2O_3 + mol92%ZrO_2	1.2	(wt50%.$La_{0.75}Sr_{0.25}Cr_{0.5}Mn_{0.5}O_3$ + wt50%.YSZ)+imp($Ce_{0.8}Gd_{0.2}$)	0.6	0.46	-	-	850	14a
[21]	2014		mol8%Y_2O_3 + mol92%ZrO_2	0.025	($La_{0.6}Sr_{0.4}Fe_{0.9}Sc_{0.1}O_{3-\delta}$) - (mol8%$Y_2$ O_3+mol92%ZrO_2)	0.1	0.2	0.21	0.04	800	3b, 4a, 4b
[22]	2018		mol8%Y_2O_3 + mol92%ZrO_2	0.4	70wt%($La_{0.8}Sr_{0.2}MnO_{3-\delta}$) + 30wt%(and $Gd_{0.2}Ce_{0.8}O_{2-\delta}$)	0.1	1.63	1.44	5.19	800	6a, 8b
				0.4	$La_{0.8}Sr_{0.2}MnO_{3-\delta}$	0.09	3.23	3.03	10.49	800	6a, 8a
[23]	2018		mol8%Y_2O_3+mol92%ZrO_2 + (Barrier layer of GDC)	0.21	$La_{0.4}Sr_{0.6}Co_{0.2}Fe_{0.7}Nb_{0.1}O_{3-\delta}$ + $Gd_{0.1}Ce_{0.9}O_{2-\delta}$	0.022	0.051	-	-	850	3a, 3b
				0.21		0.034	0.167	-	-	800	3a, 3b
[24]	2016		mol8%Y_2O_3 + mol92%ZrO_2	0.7	$Sm_{0.95}Ce_{0.05}FeO_{3-\delta}$	-	0.23	0.15	0.08	800	6a, 6b
				0.7	70wt%($Sm_{0.9}5Ce_{0.05}FeO_{3-\delta}$) + 30wt%(mol8%$Y_2O_3$+mol92%$ZrO_2$)	-	0.13	0.08	0.05	800	6c, 6d
[25]	2017		mol8%Y_2O_3+mol92%ZrO_2 + (Barrier layer of GDC)	0.2	50wt%($La_{0.4}Sr_{0.6}Co_{0.2}Fe_{0.7}Nb_{0.1}O_{3-\delta}$) + 50wt%($Gd_{0.2}Ce_{0.8}O_{2-\delta}$)	-	0.05	-	-	850	5b
				0.2		-	0.16	-	-	800	5b
[26]	2015		mol8%Y_2O_3+mol92%ZrO_2 + (Barrier layer of SDC)	0.4	$La_{0.3}Sr_{0.7}Ti_{0.3}Fe_{0.7}O_{3-\delta}$	0.55	0.23	0.04	0.18	900	3c, T1
				0.4		1.05	0.4	0.11	0.25	800	3c, T1
[28]	2016		mol8%Y_2O_3 + mol92%ZrO_2	0.4	$La_{0.8}Sr_{0.2}FeO_{3-\delta}$	0.58	0.197	0.48	0.92	800	6a, 6c, T1
			mol8%Y_2O_3 + mol92%ZrO_2 + (Barrier layer of $Gd_{0.2}Ce_{0.8}O_{2-\delta}$)	0.404		0.64	0.118	0.31	0.58	800	6b, 6c, T1
[29]	2017		5(CuFe - oxide mineral) + 5(YSZ)	0.562	$Ni_{0.8}Co_{0.1}5Al_{0.05}LiO_{2-\delta}$ + (Ni foam pasted)	0.147	3.078	-	-	550	T3
[30]	2018		mol8%Y_2O_3 + mol92%ZrO_2 + (Barrier layer of $Gd_{0.2}Ce_{0.8}O_{2-\delta}$)	0.45	$PrBaMn_2O_{5+\delta}$	1.12	0.32	0.12	0.26	800	7b, 8a, 8b, 9c
			mol8%Y_2O_3 + mol92%ZrO_2	0.4		1.16	0.75	0.19	0.49	800	7b, 8a, 8b, 9c
[31]	2009	SSZ	$(Sc_2O_3)_{0.1}(ZrO_2)_{0.9}$	0.3	$La_{0.8}Sr_{0.2}Sc_{0.2}Mn_{0.8}O_3$	-	-	6.5	-	850	5a
[32	2012		$Sc_{0.1}Zr_{0.9}O_{1.95}$	0.18	wt87.5%$La_{0.6}Sr_{0.4}Fe_{0.9}Sc_{0.1}O_{3-\delta}$ + wt12.5%$Ce_{0.6}Fe_{0.1}Mn_{0.3}O_2$	0.075	2.5	0.103	1.877	800	2c, 2e, 2f, 3c
[33]	2015		10Sc1CeSZ (Sc-doped ZrO_2+ $Sm_{0.2}Ce_{0.8}O_{1.9}$ buffer layer)	0.23	$La_{0.5}Sr_{0.5}Fe_{0.8}Cu_{0.2}O_{3-\delta}$-$Ce_{0.8}Sm_{0.2}O_{1.9}$	0.1875	0.15	-	-	900	3c
				0.23		0.25	0.1625	-	-	850	3c
				0.23		0.35	0.2	-	-	800	3c
[34]	2016		$Sc_{0.2}Zr_{0.8}O_{2-\delta}$	0.06	$La_{0.9}Ca_{0.1}Fe_{0.9}Nb_{0.1}O_{3-\delta}$	-	0.78	0.66	0.12	850	T1, T2
				0.06		-	1.67	1.46	0.21	800	T1, T2
				0.06	40%($La_{0.9}Ca_{0.1}Fe_{0.9}Nb_{0.1}O_{3-\delta}$) + 25%($Ce_{0.8}Sm_{0.2}O_{2-\delta}$)	-	0.184	0.12	0.064	850	T1, T2
				0.06		-	0.326	0.24	0.086	800	T1, T2

Table II A3 – Several symmetrical cell results of OCV and PPD with Ceria based electrolytes

		Cell components				Performance				
Source		Electrolyte			Electrodes	Result		Conditions		Fig/Tab
Ref	Year	name	Chemical composition	Thickness	Chemical composition	OCV	PPD	Temp.	Fuel	-
#	-	-	-	(mm)	-	(V)	($mW.cm^{-2}$)	(^oC)	-	-
[35]	2007	GDC	$50\%Ce_{0.8}Gd_{0.2}O_{2-\delta} + 50\%(mol8\%Y_2O_3 + mol92\%ZrO_2)$	0.18	$La_{0.75}Sr_{0.25}Cr_{0.5}Mn_{0.5}O_3$	1.1	400	950	Wet H_2	4b
[36]	2015		$Ce_{0.8}Gd_{0.2}O_{1.9}$	0.3	$Ba_{0.5}Sr_{0.5}Fe_{0.8}Co_{0.1}Ti_{0.1}O_{3-\delta}$	0.79	480	800	H_2	8b
				0.3	$Ba_{0.5}Sr_{0.5}Fe_{0.9}Cu_{0.1}O_{3-\delta}$	0.79	400	800	H_2	8a
[37]	2018		$Ce_{0.9}Gd_{0.1}O_{2-\delta}$	0.5	$Ni_{0.8}Co_{0.15}Al_{0.05}LiO_2$ - (Ni foam)	1.038	159.7	550	H_2	2b
[38]	2014	SDC	$Ce_{0.8}Sm_{0.2}O_{1.9}$	0.3	$wt30\%La_{0.6}Ca_{0.4}Fe0_{.8}Ni_{0.2}O_{3-\delta}$ + wt70%inf($Ce_{0.8}Sm_{0.2}O_{1.9}$)	0.79	507	800	H_2	8
[39]	2016		$Ce_{0.8}Sm_{0.2}O_{1.9}$	0.3	$LaCo_{0.3}Fe_{0.67}Pd_{0.03}O_{3-\delta}$ + 20wt%inf(SDC)	0.8	535	750	H_2	7a
				0.3	$LaCo_{0.3}Fe_{0.7}O_{3-\delta}$ + 20wt%inf(SDC)	0.82	291	750	H_2	7b
[40]	2013		$wt80\%Ce_{0.8}Sm_{0.2}O_{2-\delta}$ + $wt20\%(Li,Na)_2CO_3$	0.25	$wt60\%Li_{0.5}NiCu_{0.5}ZnO_{3-\delta}$ + wt40%(Electrolyte)	0.99	680	600	H_2	7
[41]	2017		$Sm_{0.2}Ce_{0.8}O_{1.9}$	0.6	$Sm_{0.9}Sr_{0.1}Fe_{0.9}Ru_{0.1}O_{3-\delta}$	0.83	119.69	800	H_2	7a
[42]	2017		$Sm_{0.2}Ce_{0.8}O_{1.9}$	0.28	$La_{0.6}Ca_{0.4}Fe_{0.8}Ni_{0.2}O_{3-\delta}$ + inf(30%SDC)	0.73	303	800	H_2	5a
				0.28	$La_{0.6}Ca_{0.4}Fe_{0.8}Ni_{0.2}O_{3-\delta}$ + physical mix(30%SDC)	0.76	140	800	H_2	5b
[12]	2013		$Ce_{0.8}Sm_{0.2}O_{1.9}$	0.3	La_2NiO_4 + inf($Ce_{0.8}Sm_{0.2}O_{1.9}$)	0.8	550	800	H_2	4b, T1
				0.3	La_2NiO_4	0.8	248	800	H_2	4c
[43]	2012		$Ce_{0.8}Sm_{0.2}O_{1.9}$	0.4	45wt%(Ag) + SDC	0.78	200	750	H_2	10
[44]	2011		$80wt\%SDC + 20wt\%Na_2CO_3$	0.4	$50vol\%(Zn_{0.969}Ni_{0.031}O) + 50vol\%(80wt\%SDC + 20wt\%Na_2CO_3)$	1.01	1257	520	H_2	3a
[45]	2018		$mass\%4(LiCo_{0.8}Fe_{0.2}O_2) + mass\%6$(Sm-doped CeO_2)	0.417	$Ni_{0.8}Co_{0.15}Al_{0.05}LiO_{2-\delta}$ + (Ni foam pasted)	1.1	1150	550	H_2	3a, 3b, 3c
			Sm-doped CeO_2	0.417	$Ni_{0.8}Co_{0.15}Al_{0.05}LiO_{2-\delta}$ + (Ni foam pasted)	1	400	550	H_2	3b
[46]	2018		$Sm_{0.2}Ce_{0.8}O_{1.9}$	0.21	Pr_2NiO_4 + 40wt%inf($Sm_{0.2}Ce_{0.8}O_{1.9}$)	0.72	375	800	H_2	5
[47]	2017		$Sm_{0.2}Ce_{0.8}O_{1.9}$	0.3	NiO + SDC + imp($La_{0.6}Sr_{1.4}MnO_{4+\delta}$)	0.8178	714	800	H_2	5a. 6b, T2
[48]	2016			0.3	NiO + $La_{0.6}Sr_{1.4}MnO_{4+\delta}$ + imp(SDC)	0.8357	614	800	H_2	7

Table II A4 – Several symmetrical cell results of impedance with Ceria based electrolytes

		Cell components				Impedance					
Source		Electrolyte			Electrodes	Different atmospheres		Same atmosphere		Condition	Fig/Tab
Ref	Year	name	Chemical composition	Thickness	Chemical composition	Electrolyte	Electrodes	air	H_2	Temp.	
#	-	-	-	(mm)	-	(Ω.cm²)				(ºC)	-
[35]	2007	GDC	$50\%Ce_{0.8}Gd_{0.2}O_{2-\delta} + 50\%(mol8\%Y_2O_3 + mol92\%ZrO_2)$	0.18	$La_{0.75}Sr_{0.25}Cr_{0.5}Mn_{0.5}O_3$	1.02	0.53	0.2675	0.2625	950	4a
[36]	2015		$Ce_{0.8}Gd_{0.2}O_{1.9}$	0.3	$Ba_{0.5}Sr_{0.5}Fe_{0.8}Co_{0.1}Ti_{0.1}O_{3-\delta}$	-	0.013	-	-	750	5b
				0.3	$Ba_{0.5}Sr_{0.5}Fe_{0.9}Cu_{0.1}O_{3-\delta}$	-	0.009	-	-	750	5b
[37]	2018		$Ce_{0.9}Gd_{0.1}O_{2-\delta}$	0.5	$Ni_{0.8}Co_{0.15}Al_{0.05}LiO_2$-(Ni foam)	1.25	0.625	0.393	0.31	550	3a
[38]	2014	SDC	$Ce_{0.8}Sm_{0.2}O_{1.9}$	0.3	$wt30\%La_{0.6}Ca_{0.4}Fe0_{.8}Ni_{0.2}O_{3-\delta} + wt70\%inf(Ce_{0.8}Sm_{0.2}O_{1.9})$	0.266	0.013	-	-	800	9, T2
[39]	2016		$Ce_{0.8}Sm_{0.2}O_{1.9}$	0.3	$LaCo_{0.3}Fe_{0.67}Pd_{0.03}O_{3-\delta}$ + 20wt%inf(SDC)	-	0.0116	-	-	800	6a
				0.3		-	0.0176	-	-	750	6b
				0.3	$LaCo_{0.3}Fe_{0.7}O_{3-\delta}$ + 20wt%inf(SDC)	-	0.02	-	-	800	6a
				0.3		-	0.065	-	-	750	6b
[40]	2013		$wt80\%Ce_{0.8}Sm_{0.2}O_{2-\delta} + wt20\%(Li/Na)_2CO_3$	0.25	$wt60\%Li_{0.5}NiCu_{0.5}ZnO_{3-\delta} + wt40\%$(Electrolyte)	0.546	0.1	-	-	600	2, T1
[41]	2017		$Sm_{0.2}Ce_{0.8}O_{1.9}$	0.6	$Sm_{0.9}Sr_{0.1}Fe_{0.9}Ru_{0.1}O_{3-\delta}$	0.5993		0.1615	0.1956	800	5a, 5b, T3
[42]	2017		$Sm_{0.2}Ce_{0.8}O_{1.9}$	0.28	$La_{0.6}Ca_{0.4}Fe_{0.8}Ni_{0.2}O_{3-\delta}$ + inf(30%SDC)	-	0.12	-	-	800	4a
				0.28	$La_{0.6}Ca_{0.4}Fe_{0.8}Ni_{0.2}O_{3-\delta}$ + physical mix(30%SDC)	-	0.15	-	-	800	4a
[12]	2013		$Ce_{0.8}Sm_{0.2}O_{1.9}$	0.3	$La_2NiO_4 + inf(Ce_{0.8}Sm_{0.2}O_{1.9})$	0.2458	0.0142	-	-	800	5b
				0.3	La_2NiO_4	0.6897	0.0353	-	-	800	5c
[43]	2012		$Ce_{0.8}Sm_{0.2}O_{1.9}$	0.4	45wt%(Ag) + SDC	0.422	3.126	1.07	2.056	750	T1
[44]	2011		$80wt\%SDC + 20wt\%Na_2CO_3$	0.4	$50vol\%(Zn_{0.969}Ni_{0.031}O) + 50vol\%(80wt\%SDC + 20wt\%Na_2CO_3)$	0.3514		-	0.0269	500	2a
[45]	2018		$mass\%4(LiCo_{0.8}Fe_{0.2}O_2) + mass\%6$(Sm-doped CeO_2)	0.417	$Ni_{0.8}Co_{0.15}Al_{0.05}LiO_{2-\delta}$ + (Ni foam pasted)	0.0541	0.2795	0.0829	0.1966	550	4, T1
			Sm-doped CeO_2	0.417	$Ni_{0.8}Co_{0.15}Al_{0.05}LiO_{2-\delta}$ + (Ni foam pasted)	0.4019	13.8509	4.0781	9.7728	550	4, T1
[46]	2018		$Sm_{0.2}Ce_{0.8}O_{1.9}$	0.21	$Pr_2NiO_4 + 40wt\%inf(Sm_{0.2}Ce_{0.8}O_{1.9})$	-		0.067	-	800	4a, T1
[47]	2017		$Sm_{0.2}Ce_{0.8}O_{1.9}$	0.3	$NiO + SDC + imp(La_{0.6}Sr_{1.4}MnO_{4+\delta})$	0.3407	0.0093	0.0099	-	800	4a, T3, 5b
[48]	2016			0.3	$NiO + La_{0.6}Sr_{1.4}MnO_{4+\delta}$ + imp(SDC)	-		0.02	-	800	6a

Table II A5 – Several symmetrical cell results of OCV and PPD with LSGM electrolytes

		Cell components				Performance				
Source		Electrolyte			Electrodes	Result		Conditions		Fig/Tab
Ref	Year	name	Chemical composition	Thickness	Chemical composition	OCV	PPD	Temp.	Fuel	-
#	-	-	-	(mm)	-	(V)	(mW.cm^{-2})	(^{o}C)	-	-
[49]	2012	LSGM	$La_{0.8}Sr_{0.2}Ga_{0.83}Mg_{0.17}O_3$	0.3	$Sr_2Co_{1.15}Mo_{0.85}O_{6-\delta}$	1.16	460	800	H_2	6c
				0.3	$Sr_2Co_{1.2}Mo_{0.8}O_{6-\delta}$	1.16	450	800	H_2	6c
				0.3	$Sr_2Co_{1.1}Mo_{0.9}O_{6-\delta}$	1.16	390	800	H_2	6c
[50]	2014		$La_{0.8}Sr_{0.2}Ga_{0.83}Mg_{0.17}O_3$	0.3	$La_{0.4}Sr_{0.6}Co_{0.2}Fe_{0.7}Nb_{0.1}O_{3-\delta}$	1.025	500	850	H_2	4a
				0.3		1.025	375	800	H_2	4a
[51]	2014		$La_{0.9}Sr_{0.1}Ga_{0.8}Mg_{0.2}O_{3-\delta}$	0.018	$La_{0.6}Sr_{0.4}Fe_{0.9}Sc_{0.1}O_{3-\delta}$ + imp($La_{0.9}Sr_{0.1}Ga_{0.8}Mg_{0.2}O_{3-\delta}$)	1.088	560	800	97%H_2 3%H_2O	7a
				0.2		1.047	536.36	800	97%H_2 3%H_2O	6c
[52]	2011		$La_{0.9}Sr_{0.1}Ga_{0.8}Mg_{0.2}O_{3-\delta}$	0.3	wt80%$La_{0.7}Ca_{0.3}CrO_3$ + wt20%$Ce_{0.8}Gd_{0.2}O_{1.9}$	1.05	573	900	H_2	6a, T2
				0.3		0.96	220	800	H_2	6a
				0.3	Wt60%$La_{0.7}Ca_{0.3}CrO_3$ + wt40%$Ce_{0.8}Gd_{0.2}O_{1.9}$	1.1	476	900	H_2	6c, T2
				0.3		1.04	205	800	H_2	6c
[53]	2011		$La_{0.9}Sr_{0.1}Ga_{0.8}Mg_{0.2}O_{3-\delta}$	0.3	$La_{0.7}Ca_{0.3}CrO_{3-\delta}$ + imp($Ce_{0.9}Gd_{0.1}O_{1.95}$)	1.05	638	900	H_2	4c
				0.3		1.07	400	800	H_2	4c
[54]	2010		$La_{0.9}Sr_{0.1}Ga_{0.8}Mg_{0.2}O_3$	0.265	$Sr_2Fe_{1.5}Ga_{0.5}O_{6-\delta}$	1.04	835	900	H_2	4a
				0.265		1.055	650	850	H_2	4a
				0.265		1.07	500	800	H_2	4a
[55]	2012		$La_{0.8}Sr_{0.2}Ga_{0.83}Mg_{0.17}O_3$	0.3	$Pr_{0.4}Sr_{0.6}Co_{0.2}Fe_{0.7}Nb_{0.1}O_{3-\delta}$	1.084	960	850	H_2	1a
				0.3		-	-	800	H_2	-
[56]	2014		$La_{0.9}Sr_{0.1}Ga_{0.8}Mg_{0.2}O_{3-\delta}$	0.015	$La_{0.9}Sr_{0.1}Ga_{0.8}Mg_{0.2}O_{3-\delta}$ + imp($Sr_1Fe_{0.75}Mo_{0.25}O_{3-\delta}$)	1.04	970	800	H_2	2a
				0.015		1.05	850	750	H_2	2a
[57]	2016		$La_{0.8}Sr_{0.2}Ga_{0.8}Mg_{0.2}O_{3-\delta}$	0.3	$Sr_2FeMoO_{6-\delta}$ + imp(Co:Ni:Mo; 1:5:1mol%)	0.975	1066	800	H_2	8b
				0.3	$Sr_2FeMoO_{6-\delta}$	1.025	247	800	H_2	8a
[58]	2014		$La_{0.8}Sr_{0.2}Ga_{0.8}Mg_{0.2}O_{3-\delta}$	0.265	$(Pr_{0.4})_{1.05}Sr_{0.6}Co_{0.2}Fe_{0.7}Nb_{0.1}O_{3-s}$	1.11	1130	900	Wet H_2	11a
				0.265		1.13	766	800	Wet H_2	11a
[59]	2018		$La_{0.8}Sr_{0.2}Ga_{0.83}Mg_{0.17}O_{3-\delta}$	0.3	$La_{0.5}Sr_{0.5}Fe_{0.9}Nb_{0.1}O_{3-\delta}$	1.06	1000	850	97%H_2 3%H_2O	7a
				0.3		1.07	820	800	97%H_2 3%H_2O	7a
[60]	2018		$La_{0.9}Sr_{0.1}Ga_{0.8}Mg_{0.2}O_{3-\delta}$ + (SDC buffer layer)	0.2	$Sr_2TiFe_{0.9}Mo_{0.1}O_{6-\delta}$	1.06	573	850	H_2	9a
				0.2		1.07	444	800	H_2	9a
			$La_{0.9}Sr_{0.1}Ga_{0.8}Mg_{0.2}O_{3-\delta}$ + (SDC buffer layer)	0.2	$Sr_2TiFe_{0.8}Mo_{0.2}O_{6-\delta}$	1.15	383	850	H_2	9c
				0.2		1.175	313	800	H_2	9c
[61]	2015		$La_{0.9}Sr_{0.1}Ga_{0.8}Mg_{0.2}O_{3-\delta}$	1.1	70wt%($\underline{La_{0.8}Sr_{1.2}FeO_4}$) + 30wt%($La_{0.9}Sr_{0.1}Ga_{0.8}Mg_{0.2}O_{3-\delta}$)	0.94	73	800	H_2	9
[62]	2016		$La_{0.8}Sr_{0.2}Ga_{0.8}Mg_{0.2}O_{3-\delta}$	0.3	$La_{0.8}Sr_{0.2}Fe_{0.8}Cu_{0.2}O_3$	1.05	103	800	H_2	8a
				0.3	$La_{0.6}Sr_{0.4}Fe_{0.8}Cu_{0.2}O_3$	1.05	162	800	H_2	8a
				0.3	30wt%($Ce_{0.9}Gd_{0.1}O_2$) + 70%($La_{0.8}Sr_{0.2}Fe_{0.8}Cu_{0.2}O_3$)	1.04	203	800	H_2	8a

				0.3	30wt%($Ce_{0.9}Gd_{0.1}O_2$) + 70%($La_{0.6}Sr_{0.4}Fe_{0.8}Cu_{0.2}O_3$)	1.05	294	800	H_2	8a
[63]	2015		$La_{0.8}Sr_{0.2}Ga_{0.8}Mg_{0.2}O_{3-\sigma}$	0.293	$Pr_{0.4}Sr_{0.6}(Co_{0.2}Fe_{0.8})_{0.95}$ $Mo_{0.05}O_{3-\sigma}$	1.08	493	850	H_2	13a
[64]	2018		$La_{0.9}Sr_{0.1}Ga_{0.8}Mg_{0.2}O_{3-\delta}$ + (SDC buffer layer)	0.2	$(La_{0.6}Sr_{0.4})Co_{0.2}Fe_{0.6}Nb_{0.2}O_{3-\delta}$	1.1	651	850	H_2	6a
				0.2		1.11	539	800	H_2	6a
[65]	2017		$La_{0.9}Sr_{0.1}Ga_{0.8}Mg_{0.2}O_{3-\delta}$ + (GDC buffer layer)	0.38	$Pr_{0.6}Sr_{0.4}Fe_{0.8}Ni_{0.2}O_{3-\delta}$	1.04	500	800	H_2	7a
				0.38	$Pr_{0.6}Sr_{0.4}Fe_{0.7}Ni_{0.2}Mo_{0.1}O_{3-\delta}$	1	435	800	H_2	7b
[66]	2017		$La_{0.9}Sr_{0.1}Ga_{0.8}Mg_{0.2}O_3$	0.018	$Sr_2Fe_{1.5}Mo_{0.5}O_6$ + inf($La_{0.9}Sr_{0.1}Ga_{0.8}Mg_{0.2}O_3$)	1.1	880	700	H_2	3a
[67]	2014		$La_{0.9}Sr_{0.1}Ga_{0.8}Mg_{0.2}O_{3-\delta}$	0.5	50%wt($LaSr_2Fe_2CrO_{9-\delta}$) + 50%($Gd_{0.2}Ce_{0.8}O_{2-\delta}$)	1.07	264	800	H_2	6b
				0.5	$LaSr_2Fe_2CrO_{9-\delta}$	1.05	224	800	H_2	6a
[68]	2015		$La_{0.8}Sr_{0.2}Ga_{0.8}Mg_{0.2}O_{3-\delta}$	0.4	$La_{0.7}Ca_{0.3}Cr_{0.8}Mn_{0.2}O_{3-\delta}$	1.02	220	800	H_2	12a
				]0.4	$La_{0.7}Ca_{0.3}Cr_{0.8}Ni_{0.2}O_{3-\delta}$	1.05	254	800	H_2	12b
[69]	2017		$La_{0.9}Sr_{0.1}Ga_{0.8}Mg_{0.2}O_3$ + wt35%($SrFe_{0.75}Mo_{0.25}O_{3-\delta}$)	0.05	$SrFe_{0.75}Mo_{0.25}O_{3-\delta}$	1.02	703	800	H_2	2a
[70]	2015		$La_{0.8}Sr_{0.2}Ga_{0.8}Mg_{0.2}O_{3-\delta}$	0.4	**$SrFe_{0.75}Zr_{0.25}O_{3-\delta}$** + 50wt%($Ce_{0.8}Gd_{0.2}O_{1.9}$)	1.13	425	800	H_2	11
				0.4		1.12	294	750	H_2	11
[71]	2014		$La_{0.8}Sr_{0.2}Ga_{0.8}Mg_{0.2}O_{3-\delta}$	0.265	$Pr_{0.38}Sr_{0.6}Co_{0.2}Fe_{0.7}Nb_{0.1}O_{3-\delta}$	1.1	653	900	Wet H_2	1a
				0.265		1.12	575	800	Wet H_2	1a
				0.265	$Pr_{0.40}Sr_{0.6}Co_{0.2}Fe_{0.7}Nb_{0.1}O_{3-\delta}$	1.1	859	900	Wet H_2	1b
				0.265		1.12	650	800	Wet H_2	1b
				0.265	$Pr_{0.42}Sr_{0.6}Co_{0.2}Fe_{0.7}Nb_{0.1}O_{3-\delta}$	1.12	1133	900	Wet H_2	1c
				0.265		1.13	762	800	Wet H_2	1c
				0.265	$Pr_{0.44}Sr_{0.6}Co_{0.2}Fe_{0.7}Nb_{0.1}O_{3-\delta}$	1.11	972	900	Wet H_2	1d
				0.265		1.125	645	800	Wet H_2	1d
[13]	2014		$La_{0.8}Sr_{0.2}Ga_{0.83}Mg_{0.17}O_{3-\delta}$	0.32	$La_{0.7}Sr_{0.3}Fe_{0.7}Ga_{0.3}O_{3-\delta}$	1.04	489	800	H_2 (3%vol H_2O)	5
[12]	2013		$La_{0.9}Sr_{0.1}Ga_{0.8}Mg_{0.2}O_{3-\delta}$	0.6	La_2NiO_4 + inf($La_{0.9}Sr_{0.1}Ga_{0.8}Mg_{0.2}O_{3-\delta}$)	1.1	520	800	H_2	4a, T1
[72]	2018		$La_{0.9}Sr_{0.1}Ga_{0.8}Mg_{0.2}O_{3-\delta}$	0.2	$(PrBa)_{0.95}(Fe_{0.9}Mo_{0.1})_2O_{5+\delta}$	0.97	760	800	H_2	2a
				0.2	$(PrBa)_{0.95}(Fe_{0.9}Mo_{0.1})_2O_{5+\delta}$ + inf(PBFM)	1.01	1050	800	H_2	3b
[73]	2014		$La_{0.9}Sr_{0.1}Ga_{0.8}Mg_{0.2}O_{3-\delta}$	1.1	$La_{0.6}Sr_{1.4}MnO_4$	1.01	59	800	H_2	10
[74]	2017		$La_{0.9}Sr_{0.1}Ga_{0.8}Mg_{0.2}O_{3-\delta}$	0.275	$PrBa(Fe_{0.8}Sc_{0.2})_2O_{5+\delta}$	1.07	921	850	H_2	3
[75]	2017		$La_{0.8}Sr_{0.2}Ga_{0.8}Mg_{0.2}O_{3-\delta}$	0.52	$PrBaMn_{1.5}Fe_{0.5}O_{5+\delta}$	1	540	800	H_2 (3%vol H_2O)	7a
[76]	2016		$La_{0.9}Sr_{0.1}Ga_{0.8}Mg_{0.2}O_{3-\delta}$ + ($La_{0.4}Ce_{0.6}O_2$ buffer layer)	0.25	$Pr_{0.5}Ba_{0.4}Ca_{0.1}MnO_3$	1.08	1101	800	97%H_2 3%H_2O	8a

Table II A6 – Several symmetrical cell results of impedance with LSGM electrolytes

		Cell components				Impedance					
Source		Electrolyte			Electrodes	Different atmosphere		Different atmospheres		Condition	Fig/Tab
Ref	Year	name	Specific Chemical composition	Thickness	Chemical composition	Electrolyte	Electrodes	air	H_2	Temp.	
#	-	-	-	(mm)	-	(Ω.cm²)				(ºC)	-
[49]	2012	LSGM	$La_{0.8}Sr_{0.2}Ga_{0.83}Mg_{0.17}O_3$	0.3	$Sr_2Co_{1.15}Mo_{0.85}O_{6-\delta}$	-	0.49	0.15	0.34	800	9a, 9b
				0.3	$Sr_2Co_{1.2}Mo_{0.8}O_{6-\delta}$	-	0.4872	0.1372	0.35	800	9a, 9b
				0.3	$Sr_2Co_{1.1}Mo_{0.9}O_{6-\delta}$	-	0.8244	0.1744	0.65	800	9a, 9b
[50]	2014		$La_{0.8}Sr_{0.2}Ga_{0.83}Mg_{0.17}O_3$	0.3	$La_{0.4}Sr_{0.6}Co_{0.2}Fe_{0.7}Nb_{0.1}O_{3-\delta}$	0.37	0.22	0.075	0.145	850	2, 4b
				0.3		0.445	0.305	0.1	0.205	800	2, 4b
[51]	2014		$La_{0.9}Sr_{0.1}Ga_{0.8}Mg_{0.2}O_{3-\delta}$	0.018	$La_{0.6}Sr_{0.4}Fe_{0.9}Sc_{0.1}O_{3-\delta}$ + imp($La_{0.9}Sr_{0.1}Ga_{0.8}Mg_{0.2}O_{3-\delta}$)	0.2	0.55	-	-	800	7b
				0.2		0.25	0.325	-	-	800	6d
[54]	2010		$La_{0.9}Sr_{0.1}Ga_{0.8}Mg_{0.2}O_3$	0.265	$Sr_2Fe_{1.5}Ga_{0.5}O_{6-\delta}$	0.175	0.35	-	-	900	4b, 4c
				0.265		0.22	0.4	0.1	0.21	850	3a, 3b
				0.265		0.28	0.475	0.24	0.27	800	3a, 3b
[55]	2012		$La_{0.8}Sr_{0.2}Ga_{0.83}Mg_{0.17}O_3$	0.3	$Pr_{0.4}Sr_{0.6}Co_{0.2}Fe_{0.7}Nb_{0.1}O_{3-\delta}$	-	-	-	0.31	850	850
				0.3		-	-	-	0.44	800	800
[56]	2014		$La_{0.9}Sr_{0.1}Ga_{0.8}Mg_{0.2}O_{3-\delta}$	0.015	$La_{0.9}Sr_{0.1}Ga_{0.8}Mg_{0.2}O_{3-\delta}$ + imp($Sr_1Fe_{0.75}Mo_{0.25}O_{3-\delta}$)	0.12	0.18	-	-	800	2b
				0.015		0.13	0.35	0.048	0.26	750	2b, 3a, 3b
[57]	2016		$La_{0.8}Sr_{0.2}Ga_{0.8}Mg_{0.2}O_{3-\delta}$	0.3	$Sr_2FeMoO_{6-\delta}$ + imp(Co:Ni:Mo; 1:5:1mol%)	-	-	-	0.062	800	7a
				0.3	$Sr_2FeMoO_{6-\delta}$	-	-	-	0.167	800	7a
[58]	2014		$La_{0.8}Sr_{0.2}Ga_{0.8}Mg_{0.2}O_{3-\delta}$	0.265	$(Pr_{0.4})_{1.05}$ $Sr_{0.6}Co_{0.2}Fe_{0.7}Nb_{0.1}O_{3-s}$	0.19	0.21	0.007	0.13	900	8, 10, 12
				0.265		0.23	0.38	0.025	0.2	800	8, 10, 12
[59]	2018		$La_{0.8}Sr_{0.2}Ga_{0.83}Mg_{0.17}O_{3-\delta}$	0.3	$La_{0.5}Sr_{0.5}Fe_{0.9}Nb_{0.1}O_{3-\delta}$	0.16	0.14	0.02	0.105	850	7b, T1
				0.3		0.19	0.185	0.03	0.12	800	7b, T1
[60]	2018		$La_{0.9}Sr_{0.1}Ga_{0.8}Mg_{0.2}O_{3-\delta}$ + (SDC buffer layer)	0.2	$Sr_2TiFe_{0.9}Mo_{0.1}O_{6-\delta}$	-	0.278	0.041	0.237	850	T1, 8a, 8b
				0.2		-	0.327	0.056	0.271	800	T1, 8a, 8b
			$La_{0.9}Sr_{0.1}Ga_{0.8}Mg_{0.2}O_{3-\delta}$ + (SDC buffer layer)	0.2	$Sr_2TiFe_{0.8}Mo_{0.2}O_{6-\delta}$	-	0.554	0.059	0.495	850	T2, 8c, 8d
				0.2		-	0.642	0.095	0.547	800	T2, 8c, 8d
[61]	2015		$La_{0.9}Sr_{0.1}Ga_{0.8}Mg_{0.2}O_{3-\delta}$	1.1	70wt%($\underline{La_{0.8}Sr_{1.2}FeO_4}$) + 30wt%($La_{0.9}Sr_{0.1}Ga_{0.8}Mg_{0.2}O_{3-\delta}$)	-	9.9	2	7.9	800	8a, 8b
[62]	2016		$La_{0.8}Sr_{0.2}Ga_{0.8}Mg_{0.2}O_{3-\delta}$	0.3	$La_{0.8}Sr_{0.2}Fe_{0.8}Cu_{0.2}O_3$	1.13	1.3	-	-	800	8b
				0.3	$La_{0.6}Sr_{0.4}Fe_{0.8}Cu_{0.2}O_3$	0.73	0.7	-	-	800	8b
				0.3	30wt%($Ce_{0.9}Gd_{0.1}O_2$) + 70%($La_{0.8}Sr_{0.2}Fe_{0.8}Cu_{0.2}O_3$)	0.73	0.55	-	-	800	8b
				0.3	30wt%($Ce_{0.9}Gd_{0.1}O_2$) + 70%($La_{0.6}Sr_{0.4}Fe_{0.8}Cu_{0.2}O_3$)	0.59	0.3	-	-	800	8b
[63]	2015		$La_{0.8}Sr_{0.2}Ga_{0.8}Mg_{0.2}O_{3-\sigma}$	0.293	$Pr_{0.4}Sr_{0.6}(Co_{0.2}Fe_{0.8})_{0.95}$ $Mo_{0.05}O_{3-\sigma}$	0.1	0.65	-	-	800	12b
[64]	2018		$La_{0.9}Sr_{0.1}Ga_{0.8}Mg_{0.2}O_{3-\delta}$ + (SDC buffer layer)	0.2	$(La_{0.6}Sr_{0.4})Co_{0.2}Fe_{0.6}Nb_{0.2}O_{3-\delta}$	-	0.679	0.192	0.487	850	5a,T2
				0.2		-	0.947	0.355	0.592	800	5a, T2
[65]	2017		$La_{0.9}Sr_{0.1}Ga_{0.8}Mg_{0.2}O_{3-\delta}$ + (GDC buffer layer)	0.38	$Pr_{0.6}Sr_{0.4}Fe_{0.8}Ni_{0.2}O_{3-\delta}$	0.48	0.07	0.3	0.35	800	8a, 5a, 5c

				0.38	$Pr_{0.6}Sr_{0.4}Fe_{0.7}Ni_{0.2}Mo_{0.1}O_{3-\delta}$	0.48	0.102	0.5	0.25	800	8b 5b, 5d
[66]	2017		$La_{0.9}Sr_{0.1}Ga_{0.8}Mg_{0.2}O_3$	0.018	$Sr_2Fe_{1.5}Mo_{0.5}O_6$ + inf($La_{0.9}Sr_{0.1}Ga_{0.8}Mg_{0.2}O_3$)	1.65	0.2825	0.12	0.1625	700	2c, 2d
[67]	2014		$La_{0.9}Sr_{0.1}Ga_{0.8}Mg_{0.2}O_{3-\delta}$	0.5	50%wt($LaSr_2Fe_2CrO_{9-\delta}$) + 50%($Gd_{0.2}Ce_{0.8}O_{2-\delta}$)	0.67	0.455	0.2377	0.3685	800	T3, 5a, 5b
				0.5	$LaSr_2Fe_2CrO_{9-\delta}$	0.7	0.52	0.293	0.5617	800	T3, 5a, 5b
[68]	2015		$La_{0.8}Sr_{0.2}Ga_{0.8}Mg_{0.2}O_{3-\delta}$	0.4	$La_{0.7}Ca_{0.3}Cr_{0.8}Mn_{0.2}O_{3-\delta}$	-		-	0.227	800	10
				0.4	$La_{0.7}Ca_{0.3}Cr_{0.8}Ni_{0.2}O_{3-\delta}$	-		-	0.743	800	10
[69]	2017		$La_{0.9}Sr_{0.1}Ga_{0.8}Mg_{0.2}O_3$ + wt35%($SrFe_{0.75}Mo_{0.25}O_{3-\delta}$)	0.05	$SrFe_{0.75}Mo_{0.25}O_{3-\delta}$	0.145	0.17	0.05	0.09	800	2b, 3a, 3b
[70]	2015		$La_{0.8}Sr_{0.2}Ga_{0.8}Mg_{0.2}O_{3-\delta}$	0.4	**$SrFe_{0.75}Zr_{0.25}O_{3-\delta}$** + 50 wt.%($Ce_{0.8}Gd_{0.2}O_{1.9}$)	-	0.1595	0.097	0.0625	750	6a, 6b
[71]	2014		$La_{0.8}Sr_{0.2}Ga_{0.8}Mg_{0.2}O_{3-\delta}$	0.265	$Pr_{0.38}Sr_{0.6}Co_{0.2}Fe_{0.7}Nb_{0.1}O_{3-\delta}$	0.35	0.16	-	-	900	2a
				0.265		0.4125	0.2425	-	-	800	2a
				0.265	$Pr_{0.40}Sr_{0.6}Co_{0.2}Fe_{0.7}Nb_{0.1}O_{3-\delta}$	0.27	0.2	-	-	900	2b
				0.265		0.33	0.2325	-	-	800	2b
				0.265	$Pr_{0.42}Sr_{0.6}Co_{0.2}Fe_{0.7}Nb_{0.1}O_{3-\delta}$	0.2	0.17	-	-	900	2c
				0.265		0.24	0.36	-	-	800	2c
				0.265	$Pr_{0.44}Sr_{0.6}Co_{0.2}Fe_{0.7}Nb_{0.1}O_{3-\delta}$	0.23	0.2	-	-	900	2d
				0.265		0.3	0.45	-	-	800	2d
[13]	2014		$La_{0.8}Sr_{0.2}Ga_{0.83}Mg_{0.17}O_{3-\delta}$	0.32	$La_{0.7}Sr_{0.3}Fe_{0.7}Ga_{0.3}O_{3-\delta}$	0.16	0.44	-	-	800	6
[12]	2013		$La_{0.9}Sr_{0.1}Ga_{0.8}Mg_{0.2}O_{3-\delta}$	0.6	La_2NiO_4 + inf($La_{0.9}Sr_{0.1}Ga_{0.8}Mg_{0.2}O_{3-\delta}$)	0.45	0.29	-	-	800	5a
[72]	2018		$La_{0.9}Sr_{0.1}Ga_{0.8}Mg_{0.2}O_{3-\delta}$	0.2	$(PrBa)_{0.95}(Fe_{0.9}Mo_{0.1})_2O_{5+\delta}$	0.125	0.175	-	-	800	-
				0.2	$(PrBa)_{0.95}(Fe_{0.9}Mo_{0.1})_2O_{5+\delta}$ + inf(PBFM)	0.48	0.09	0.027	0.074	800	6b
[73]	2014		$La_{0.9}Sr_{0.1}Ga_{0.8}Mg_{0.2}O_{3-\delta}$	1.1	$La_{0.6}Sr_{1.4}MnO_4$	-	2.94	0.87	2.07	800	9a,9b
[74]	2017		$La_{0.9}Sr_{0.1}Ga_{0.8}Mg_{0.2}O_{3-\delta}$	0.275	$PrBa(Fe_{0.8}Sc_{0.2})_2O_{5+\delta}$	-	0.23	0.05	0.18	800	2
[75]	2017		$La_{0.8}Sr_{0.2}Ga_{0.8}Mg_{0.2}O_{3-\delta}$	0.52	$PrBaMn_{1.5}Fe_{0.5}O_{5+\delta}$	1	0.9	0.22	0.68	800	5a, 5b, 5c

Table II A7 – Some symmetrical cell results of OCV, PPD and impedance with NCAL electrodes

Source		Cell components			Performance					Impedance			
		Electrolyte		Electrodes	Result		Conditions		Fig/Tab	Different atmospheres		Condition	Fig/Tab
Ref	Year	Chemical composition	Thickness	Chemical composition	OCV	PPD	Temp.	Fuel		Electrolyte	Electrodes	Temp.	
#	-	-	(mm)		(V)	($mW.cm^{-2}$)	(ºC)	-	-	($\Omega.cm^2$)		(ºC)	-
[77]	2016	80 wt%(LaCePr-oxide) + 20wt%($La_{0.6}Sr_{0.4}Co_{0.2}Fe_{0.8}O_{3-\delta}$	0.4	$Ni_{0.8}Co_{0.15}Al_{0.05}Li$ + (Ni foam pasted)	0.86	350	575	H_2	5a	-		-	-
		70 wt%(LaCePr-oxide) + 30wt%($La_{0.6}Sr_{0.4}Co_{0.2}Fe_{0.8}O_{3-\delta}$	0.4		0.95	325	575	H_2	5a	-		-	-
		60 wt%(LaCePr-oxide) + 40wt%($La_{0.6}Sr_{0.4}Co_{0.2}Fe_{0.8}O_{3-\delta}$	0.4		-	-	-	-	-	1.195	0.93	550	8a, 8b
					1.04	745	575	H_2	5a	1.11	0.89625	575	Calculated
					-	-	-	-	-	1.025	0.8625	600	8a, 8b
		50 wt%(LaCePr-oxide) + 50wt%($La_{0.6}Sr_{0.4}Co_{0.2}Fe_{0.8}O_{3-\delta}$	0.4		0.97	532	575	H_2	5a	-		-	-
[78]	2017	60 wt%(hematite/LaCePrOx) + 40wt%($La_{0.6}Sr_{0.4}Co_{0.2}Fe_{0.8}O_{3-\delta}$)	0.4	$Ni_{0.8}Co_{0.15}Al_{0.05}Li$ $O_{2-\delta}$ + (Ni foam pasted)	1	448	600	H_2	5a	0.55	3.2	600	6
		70 wt%(hematite/LaCePrOx) + 30wt%($La_{0.6}Sr_{0.4}Co_{0.2}Fe_{0.8}O_{3-\delta}$)	0.4		1.04	662	600	H_2	5a	0.55	2.2	600	6
		80 wt%(hematite/LaCePrOx) + 20wt%($La_{0.6}Sr_{0.4}Co_{0.2}Fe_{0.8}O_{3-\delta}$)	0.4		1	533	600	H_2	5a	0.55	2.4	600	6
		90 wt%(hematite/LaCePrOx) + 10wt%($La_{0.6}Sr_{0.4}Co_{0.2}Fe_{0.8}O_{3-\delta}$)	0.4		0.91	389	600	H_2	5a	0.55	3.6	600	6
[79]	2018	(8(La/Pr co-doped CeO_2) + 2(ZnO)) + ($BaZr_{0.1}Ce_{0.7}Y_{0.2}O_{3-\delta}$ layer)	0.709	$Ni_{0.8}Co_{0.15}Al_{0.05}Li$ $O_{2-\delta}$ + (Ni foam pasted)	1.05	880	550	H_2	3a	0.0471	0.23549	550	4a, T1
		(7(La/Pr co-doped CeO_2) + 3(ZnO)) + ($BaZr_{0.1}Ce_{0.7}Y_{0.2}O_{3-\delta}$ layer)	0.709		1.04	1055	550	H_2	3a	0.04962	0.14495	550	4b, T1
		(6(La/Pr co-doped CeO_2) + 4(ZnO)) + ($BaZr_{0.1}Ce_{0.7}Y_{0.2}O_{3-\delta}$ layer)	0.709		1.04	1010	550	H_2	3a	0.0502	0.1131	550	4c, T1
		(5(La/Pr co-doped CeO_2) + 5(ZnO)) + ($BaZr_{0.1}Ce_{0.7}Y_{0.2}O_{3-\delta}$ layer)	0.709		1.07	905	550	H_2	3a	-		-	-
		(4(La/Pr co-doped CeO_2) + 6(ZnO)) + ($BaZr_{0.1}Ce_{0.7}Y_{0.2}O_{3-\delta}$ layer)	0.709		1.07	780	550	H_2	3a	-		-	-
[45]	2018	$LiCo_{0.8}Fe_{0.2}O_2$	0.417	$Ni_{0.8}Co_{0.15}Al_{0.05}Li$ $O_{2-\delta}$ + (Ni foam pasted)	1	430	550	H_2	3c	-		-	-
[80]	2017	Li_2O-$ZnOSm_{0.2}Ce_{0.8}O_2$ + (50%vol(LZSDC) + 50%vol($CuFe_2O_4$)) layer)	1	$LiNi_{0.8}Co_{0.15}Al_{0.05}$ O_2 + (Ni foam pasted)	0.94	587	550	H_2	7a	0.7		550	T2, 8b
		50vol%(Li_2O-$ZnOSm_{0.2}Ce_{0.8}O_2$ + $CuFe_2O_4$) + 50vol%($LiNi_{0.8}Co_{0.15}Al_{0.05}O_2$)	1		0.988	354	550	H_2	7a	0.656	3.579	550	T2, 8c
[81]	2016	($Ce_{0.8}Sm_{0.2}O_{2-\delta}$ + Na_2CO_3)	1	$Ni_{0.8}Co_{0.15}Al_{0.05}Li$ $O_{2-\delta}$ + (Ni foam)	1	400	550	H_2	3b	0.4019	9.7728	550	T1, 4a
		8(Na_2CO_3 + $Ce_{0.8}Sm_{0.2}O_{2-\delta}$) + 2($Ni_{0.8}Co_{0.15}Al_{0.05}LiO_{2-\delta}$)	1		1.0125	733	550	H_2	3b	-		-	-
		6(Na_2CO_3 + $Ce_{0.8}Sm_{0.2}O_{2-\delta}$) + 4($Ni_{0.8}Co_{0.15}Al_{0.05}LiO_{2-\delta}$)	1		0.96875	1072	550	H_2	3b	0.1019	0.4608	550	T1, 4a
		4(Na_2CO_3 + $Ce_{0.8}Sm_{0.2}O_{2-\delta}$) + 6($Ni_{0.8}Co_{0.15}Al_{0.05}LiO_{2-\delta}$)	1		0.825	440	550	H_2	3b	-		-	-
[29]	2017	CuFe	0.562	$Ni_{0.8}Co_{0.15}Al_{0.05}Li$ $O_{2-\delta}$ + (Ni foam pasted)	0.97	281.25	550	H_2	5a	0.17	0.472	550	7a,T2
		50%wt(CuFe) + 50%wt(YSZ)	0.562		1.2	562.5	550	H_2	5a, 5b	0.147	0.106	550	7b,T2
		CuFe + (BZY layer)	1		0.88	187.5	550	H_2	8b	-		-	-
		CuFe + (SDC layer)	1		0.93	180	550	H_2	8d	-		-	-

Table II A8 – Activation energy estimations from symmetrical cells

Source		Cell components				Activation energy		
		Electrolyte			Electrodes	Atmosphere		Fig/Tab
Ref	Year	name	Specific Chemical composition	Thickness	Chemical composition	air	H_2	-
#	-	-	-	(mm)	-	(eV)		-
[20]	2017	YSZ	mol8%Y_2O_3 + mol92%ZrO_2	1.2	[wt50%.$La_{0.75}Sr_{0.25}Cr_{0.5}Mn_{0.5}O_3$ + wt50%.YSZ]+imp($Ce_{0.8}Gd_{0.2}$)	-	0.726573055	10
[21]	2014		mol8%Y_2O_3 + mol92%ZrO_2	0.025	($La_{0.6}Sr_{0.4}Fe_{0.9}Sc_{0.1}O_{3-\delta}$) - (mol8%$Y_2$ O_3+mol92%ZrO_2)	1.06	-	5
[22]	2018		mol8%Y_2O_3 + mol92%ZrO_2	0.4	70wt%(La0.8Sr0.2MnO3-δ) + 30wt%(Gd0.2Ce0.8O2-δ)	1.02	1.24	6b, 8d
				0.4	La0.8Sr0.2$MnO_{3-\delta}$	1.68	1.35	6b, 8d
[24]	2016		mol8%Y_2O_3 + mol92%ZrO_2	0.7	Sm0.95Ce0.05$FeO_{3-\delta}$	0.52	0.48	7a
				0.7	70wt%($Sm_{0.95}Ce_{0.05}FeO_{3-\delta}$) + 30wt%(mol8%$Y_2O_3$+mol92%$ZrO_2$)	0.47	0.45	7a
[27]	2014		mol8%Y_2O_3 + mol92%ZrO_2	1	$La_{0.75}Sr_{0.25}Cr_{0.5}Mn_{0.5}O_{3-\delta}$	0.39	0.53	3
				1	$La_{0.75}Sr_{0.125}Ce_{0.125}Cr_{0.5}Mn_{0.5}O_{3-\delta}$	0.56	0.55	3
[28]	2016		mol8%Y_2O_3 + mol92%ZrO_2	0.4	$La_{0.8}Sr_{0.2}FeO_{3-\delta}$	0.19	0.96	3a, 3b
			mol8%Y_2O_3 + mol92%ZrO_2 + (Barrier layer of Gd0.2Ce0.8O2-δ)	0.404		0.19	0.96	3a, 3b
[34]	2016	SSZ	$Sc_{0.2}Zr_{0.8}O_{2-\delta}$	0.06	$La_{0.9}Ca_{0.1}Fe_{0.9}Nb_{0.1}O_{3-\delta}$	1.1296	0.9864	4
				0.06	40%($La_{0.9}Ca_{0.1}Fe_{0.9}Nb_{0.1}O_{3-\delta}$) + 25%($Ce_{0.8}Sm_{0.2}O_{2-\delta}$)	1.3039	0.6058	4
[40]	2013	SDC	wt80%$Ce_{0.8}Sm_{0.2}O_{2-\delta}$ + wt20%(LiNa)$_2CO_3$	0.25	wt60%$Li_{0.5}NiCu_{0.5}ZnO_{3-\delta}$ + wt40%(Electrolyte)	0.4359	0.5813	5
[41]	2017		$Sm_{0.2}Ce_{0.8}O_{1.9}$	0.6	$Sm_{0.9}Sr_{0.1}Fe_{0.9}Ru_{0.1}O_{3-\delta}$	0.39	0.42	6a
[43]	2012		$Ce_{0.8}Sm_{0.2}O_{1.9}$	0.4	45wt%(Ag) + SDC	81	-	6
[46]	2018		$Sm_{0.2}Ce_{0.8}O_{1.9}$	0.21	Pr_2NiO_4+40wt%inf($Sm_{0.2}Ce_{0.8}O_{1.9}$)	0.8	-	4b
[51]	2014	LSGM	$La_{0.9}Sr_{0.1}Ga_{0.8}Mg_{0.2}O_{3-\delta}$	0.218	$La_{0.6}Sr_{0.4}Fe_{0.9}Sc_{0.1}O_{3-\delta}$ + imp($La_{0.9}Sr_{0.1}Ga_{0.8}Mg_{0.2}O_{3-\delta}$)	0.027	0.96	2a, 2b
[52]	2011		$La_{0.9}Sr_{0.1}Ga_{0.8}Mg_{0.2}O_{3-\delta}$	0.3	wt80%$La_{0.7}Ca_{0.3}CrO_3$ + wt20%$Ce_{0.8}Gd_{0.2}O_{1.9}$	0.1505	0.3259	3, 4
				0.3	wt80%$La_{0.7}Ca_{0.3}CrO_3$ + wt40%$Ce_{0.8}Gd_{0.2}O_{1.9}$	0.1318	0.4152	3, 4
[56]	2014		$La_{0.9}Sr_{0.1}Ga_{0.8}Mg_{0.2}O_{3-\delta}$	0.015	$La_{0.9}Sr_{0.1}Ga_{0.8}Mg_{0.2}O_{3-\delta}$ + imp($Sr_1Fe_{0.75}Mo_{0.25}O_{3-\delta}$)	0.77	0.6	3c
[57]	2016		$La_{0.8}Sr_{0.2}Ga_{0.8}Mg_{0.2}O_{3-\delta}$	0.3	$Sr_2FeMoO_{6-\delta}$ + imp(Co:Ni:Mo; 1:5:1mol%)	-	1.03	7d
				0.3	$Sr_2FeMoO_{6-\delta}$	-	1.38	7d
[59]	2018		$La_{0.8}Sr_{0.2}Ga_{0.83}Mg_{0.17}O_{3-\delta}$	0.3	$La_{0.5}Sr_{0.5}Fe_{0.9}Nb_{0.1}O_{3-\delta}$	0.35	0.32	5b, 5d
[60]	2018		$La_{0.9}Sr_{0.1}Ga_{0.8}Mg_{0.2}O_{3-\delta}$ + (SDC buffer layer)	0.2	$Sr_2TiFe_{0.9}Mo_{0.1}O_{6-\delta}$	0.8410	0.7499	8a, 8b T1
				0.2	$Sr_2TiFe_{0.8}Mo_{0.2}O_{6-\delta}$	0.9489	0.5349	8c, 8d, T2
[61]	2015		$La_{0.9}Sr_{0.1}Ga_{0.8}Mg_{0.2}O_{3-\delta}$	1.1	70wt%(**$La_{0.8}Sr_{1.2}FeO_4$**) + 30wt%($La_{0.9}Sr_{0.1}Ga_{0.8}Mg_{0.2}O_{3-\delta}$)	0.08	0.972	6a,6b
[62]	2016		$La_{0.8}Sr_{0.2}Ga_{0.8}Mg_{0.2}O_{3-\delta}$	0.3	$La_{0.8}Sr_{0.2}Fe_{0.8}Cu_{0.2}O_3$	1.52	-	7
				0.3	$La_{0.6}Sr_{0.4}Fe_{0.8}Cu_{0.2}O_3$	1.48	-	7
				0.3	30wt%($Ce_{0.9}Gd_{0.1}O_2$) + 70%($La_{0.8}Sr_{0.2}Fe_{0.8}Cu_{0.2}O_3$)	1.63	-	7
				0.3	30wt%($Ce_{0.9}Gd_{0.1}O_2$) + 70%($La_{0.6}Sr_{0.4}Fe_{0.8}Cu_{0.2}O_3$)	1.45	-	7
[63]	2015		$La_{0.8}Sr_{0.2}Ga_{0.8}Mg_{0.2}O_{3-\sigma}$	0.293	$Pr_{0.4}Sr_{0.6}(Co_{0.2}Fe_{0.8})_{0.95}$ $Mo_{0.05}O_{3-\sigma}$	0.093	-	7b
[65]	2017		$La_{0.9}Sr_{0.1}Ga_{0.8}Mg_{0.2}O_{3-\delta}$ + (GDC buffer layer)	0.38	$Pr_{0.6}Sr_{0.4}Fe_{0.8}Ni_{0.2}O_{3-\delta}$	0.086	-	3b
				0.38	$Pr_{0.6}Sr_{0.4}Fe_{0.7}Ni_{0.2}Mo_{0.1}O_{3-\delta}$	0.14	-	3b

[67]	2014		$La_{0.9}Sr_{0.1}Ga_{0.8}Mg_{0.2}O_{3-\delta}$	0.5	$50\%wt(LaSr_2Fe_2CrO_{9-\delta}) + 50\%(Gd_{0.2}Ce_{0.8}O_{2-\delta})$	1.38	0.93	5d
				0.5	$LaSr_2Fe_2CrO_{9-\delta}$	1.47	1	5d
[68]	2015		$La_{0.8}Sr_{0.2}Ga_{0.8}Mg_{0.2}O_{3-\delta}$	0.4	$La_{0.7}Ca_{0.3}Cr_{0.8}Mn_{0.2}O_{3-\delta}$	-	0.39	T1
				0.4	$La_{0.7}Ca_{0.3}Cr_{0.8}Ni_{0.2}O_{3-\delta}$	-	0.44	T1
[70]	2015		$La_{0.8}Sr_{0.2}Ga_{0.8}Mg_{0.2}O_{3-\delta}$	0.4	$\underline{\mathbf{SrFe_{0.75}Zr_{0.25}O_{3-\delta}}}$ + 50wt%$(Ce_{0.8}Gd_{0.2}O_{1.9})$	1.22	0.75	T2
[72]	2018		$La_{0.9}Sr_{0.1}Ga_{0.8}Mg_{0.2}O_{3-\delta}$	0.2	$(PrBa)_{0.95}(Fe_{0.9}Mo_{0.1})_2O_{5+\delta}$ + inf(PBFM)	1.41	1.02	1d
[73]	2014		$La_{0.9}Sr_{0.1}Ga_{0.8}Mg_{0.2}O_{3-\delta}$	1.1	$La_{0.6}Sr_{1.4}MnO_4$	0.11	1.395	7
[74]	2017		$La_{0.9}Sr_{0.1}Ga_{0.8}Mg_{0.2}O_{3-\delta}$	0.275	$PrBa(Fe_{0.8}Sc_{0.2})_2O_{5+\delta}$	1.1729	1.0899	given
[75]	2017		$La_{0.8}Sr_{0.2}Ga_{0.8}Mg_{0.2}O_{3-\delta}$	0.52	$PrBaMn_{1.5}Fe_{0.5}O_{5+\delta}$	1.42	1.5	5a
[77]	2016		60wt%(LaCePr-oxide) + 40wt%$(La_{0.6}Sr_{0.4}Co_{0.2}Fe_{0.8}O_{3-\delta})$	0.4	$Ni_{0.8}Co_{0.15}Al_{0.05}Li$ + (Ni foam pasted)	0.18	0.29	8d

Table II A9 – Electrodes of symmetrical cells also tested for conductivity

Source		Cell components				Conductivity			
		Electrolyte			Electrodes	Atmosphere		Condition	Figure
Ref	Year	name	Chemical composition	Thickness	Chemical composition	air	H_2	Temp.	-
#	-	-	-	(mm)	-	(S.cm^{-1})		(ºC)	-
[22]	2018	YSZ	mol8%Y_2O_3 + mol92%ZrO_2	0.4	$La_{0.8}Sr_{0.2}MnO_{3-\delta}$	0.1567	0.0261	800	4
[24]	2016		mol8%Y_2O_3 + mol92%ZrO_2	0.7	$Sm_{0.95}Ce_{0.05}FeO_{3-\delta}$	25.0193	14.6091	800	7b
[25]	2017		mol8%Y_2O_3 + mol92%ZrO_2 + (Barrier layer of GDC)	0.2	50wt%($La_{0.4}Sr_{0.6}Co_{0.2}Fe_{0.7}Nb_{0.1}O_{3-\delta}$) + 50wt%($Gd_{0.2}Ce_{0.8}O_{2-\delta}$)	0.0648	-	850	4
				0.2		37	-	800	4
[27]	2014		mol8%Y_2O_3 + mol92%ZrO_2	1	$La_{0.75}Sr_{0.25}Cr_{0.5}Mn_{0.5}O_{3-\delta}$	10.0498	0.93478	900	3
				1	$La_{0.75}Sr_{0.125}Ce_{0.125}Cr_{0.5}Mn_{0.5}O_{3-\delta}$	20.7501	1.5412	900	3
				1		12.4491	1.0219	800	3
[28]	2016		(mol8%Y_2O_3 + mol92%ZrO_2) / YSZ + (Barrier layer of $Gd_{0.2}Ce_{0.8}O_{2-\delta}$)	0.4/0.404	$La_{0.8}Sr_{0.2}FeO_{3-\delta}$	141.1	0.138	800	3a, 3b
[31]	2009	SSZ	$(Sc_2O_3)_{0.1}(ZrO_2)_{0.9}$	0.3	$La_{0.8}Sr_{0.2}Sc_{0.2}Mn_{0.8}O_3$	0.0909	0.0362	900	4
				0.3		0.0931	0.0360	850	4
[36]	2015	GDC	$Ce_{0.8}Gd_{0.2}O_{1.9}$	0.3	$Ba_{0.5}Sr_{0.5}Fe_{0.8}Co_{0.1}Ti_{0.1}O_{3-\delta}$	6.5625	-	800	4a
				0.3	$Ba_{0.5}Sr_{0.5}Fe_{0.9}Cu_{0.1}O_{3-\delta}$	8.75	-	800	4a
[41]	2017	SDC	$Sm_{0.2}Ce_{0.8}O_{1.9}$	0.6	$Sm_{0.9}Sr_{0.1}Fe_{0.9}Ru_{0.1}O_{3-\delta}$	82.6890	22.7668	800	6a
[44]	2011		80wt%SDC + 20wt%Na_2CO_3	0.4	50vol%($Zn_{0.969}Ni_{0.031}O$) + 50vol%(80wt%SDC + 20wt%Na_2CO_3)	2	4.5	500	2c
[46]	2018		$Sm_{0.2}Ce_{0.8}O_{1.9}$	0.21	Pr2NiO4+40wt%inf(Sm0.2Ce0.8O1.9)	70	35	800	3c
[49]	2012	LSGM	$La_{0.8}Sr_{0.2}Ga_{0.83}Mg_{0.17}O_3$	0.3	$Sr_2Co_{1.15}Mo_{0.85}O_{6-\delta}$	3.75	8.25	800	3a, 3b
				0.3	$Sr_2Co_{1.2}Mo_{0.8}O_{6-\delta}$	4.5	7.5	800	3a, 3b
				0.3	$Sr_2Co_{1.1}Mo_{0.9}O_{6-\delta}$	1.125	3.75	800	3a, 3b
[51]	2014		$La_{0.9}Sr_{0.1}Ga_{0.8}Mg_{0.2}O_{3-\delta}$	0.218	$La_{0.6}Sr_{0.4}Fe_{0.9}Sc_{0.1}O_{3-\delta}$ + imp($La_{0.9}Sr_{0.1}Ga_{0.8}Mg_{0.2}O_{3-\delta}$)	99.5	0.69	800	2a, 2b
[52]	2011		$La_{0.9}Sr_{0.1}Ga_{0.8}Mg_{0.2}O_{3-\delta}$	0.3	wt80%$La_{0.7}Ca_{0.3}CrO_3$ + wt20%$Ce_{0.8}Gd_{0.2}O_{1.9}$	18.6	1.86	850	3, 4
				0.3		18.1820	1.625	800	3, 4
				0.3	Wt60%$La_{0.7}Ca_{0.3}CrO_3$ + wt40%$Ce_{0.8}Gd_{0.2}O_{1.9}$	3.8811	1.032	850	3, 4
				0.3		3.8638	0.97	800	3, 4
[54]	2010		$La_{0.9}Sr_{0.1}Ga_{0.8}Mg_{0.2}O_3$	0.265	$Sr_2Fe_{1.5}Ga_{0.5}O_{6-\delta}$	541.9740	303.4504	775	2
[57]	2016		$La_{0.8}Sr_{0.2}Ga_{0.8}Mg_{0.2}O_{3-\delta}$	0.3	$Sr_2FeMoO_{6-\delta}$	100	25	800	6
[58]	2014		$La_{0.8}Sr_{0.2}Ga_{0.8}Mg_{0.2}O_{3-\delta}$	0.265	$(Pr_{0.4})_{1.05}Sr_{0.6}Co_{0.2}Fe_{0.7}Nb_{0.1}O_{3-s}$	100	25	900/850	3, 4
				0.265		126	22	800	3, 4
[59]	2018		$La_{0.8}Sr_{0.2}Ga_{0.83}Mg_{0.17}O_{3-\delta}$	0.3	$La_{0.5}Sr_{0.5}Fe_{0.9}Nb_{0.1}O_{3-\delta}$	72.5	0.767	850	2
				0.3		82	0.47	800	2
[60]	2018		$La_{0.9}Sr_{0.1}Ga_{0.8}Mg_{0.2}O_{3-\delta}$ + (SDC buffer layer)	0.2	$Sr_2TiFe_{0.9}Mo_{0.1}O_{6-\delta}$	0.825	0.34	850	7a, 7b
				0.2		0.9	0.25	800	7a, 7b
			$La_{0.9}Sr_{0.1}Ga_{0.8}Mg_{0.2}O_{3-\delta}$ + (SDC buffer layer)	0.2	$Sr_2TiFe_{0.8}Mo_{0.2}O_{6-\delta}$	0.9	2.02	850	7a, 7b
				0.2		0.75	1.75	800	7a, 7b

[61]	2015		$La_{0.9}Sr_{0.1}Ga_{0.8}Mg_{0.2}O_{3-\delta}$	1.1	70wt%($\underline{La_{0.8}Sr_{1.2}FeO_4}$) + 30wt%($La_{0.9}Sr_{0.1}Ga_{0.8}Mg_{0.2}O_{3-\delta}$)	22.35	0.0204	800	5a, 5b
[62]	2016		$La_{0.8}Sr_{0.2}Ga_{0.8}Mg_{0.2}O_{3-\delta}$	0.3	$La_{0.8}Sr_{0.2}Fe_{0.8}Cu_{0.2}O_3$	150	-	750	5
				0.3	$La_{0.6}Sr_{0.4}Fe_{0.8}Cu_{0.2}O_3$	148	-	750	5
[63]	2015		$La_{0.8}Sr_{0.2}Ga_{0.8}Mg_{0.2}O_{3-\sigma}$	0.293	$Pr_{0.4}Sr_{0.6}(Co_{0.2}Fe_{0.8})_{0.95}Mo_{0.05}O_{3-\sigma}$	150	-	800	7a
[64]	2018		$La_{0.9}Sr_{0.1}Ga_{0.8}Mg_{0.2}O_{3-\delta}$ + (SDC buffer layer)	0.2	$(La_{0.6}Sr_{0.4})Co_{0.2}Fe_{0.6}Nb_{0.2}O_{3-\delta}$	5.67	0.49	850	4a, 4b
				0.2		5	0.375	800	4a, 4b
[65]	2017		$La_{0.9}Sr_{0.1}Ga_{0.8}Mg_{0.2}O_{3-\delta}$ + (GDC buffer layer)	0.38	$Pr_{0.6}Sr_{0.4}Fe_{0.8}Ni_{0.2}O_{3-\delta}$	280	-	800	3a
				0.38	$Pr_{0.6}Sr_{0.4}Fe_{0.7}Ni_{0.2}Mo_{0.1}O_{3-\delta}$	66.67	-	800	3a
[67]	2014		$La_{0.9}Sr_{0.1}Ga_{0.8}Mg_{0.2}O_{3-\delta}$	0.5	$LaSr_2Fe_2CrO_{9-\delta}$	72.5	0.16	800	3a, 3b
[68]	2015		$La_{0.8}Sr_{0.2}Ga_{0.8}Mg_{0.2}O_{3-\delta}$	0.4	$La_{0.7}Ca_{0.3}Cr_{0.8}Mn_{0.2}O_{3-\delta}$	10.9863	-	800	13
				0.4	$LaSr_2Fe_2CrO_{9-\delta}$	33.8401	-	800	13
[70]	2015		$La_{0.8}Sr_{0.2}Ga_{0.8}Mg_{0.2}O_{3-\delta}$	0.4	$\underline{SrFe_{0.75}Zr_{0.25}O_{3-\delta}}$ + 50wt.%($Ce_{0.8}Gd_{0.2}O_{1.9}$)	-	0.95	800	5a, 5b
				0.4		-	0.77	750	5a, 5b
[13]	2014		$La_{0.8}Sr_{0.2}Ga_{0.83}Mg_{0.17}O_{3-\delta}$	0.32	$La_{0.7}Sr_{0.3}Fe_{0.7}Ga_{0.3}O_{3-\delta}$	47.45	0.422	800	2
[73]	2014		$La_{0.9}Sr_{0.1}Ga_{0.8}Mg_{0.2}O_{3-\delta}$	1.1	$La_{0.6}Sr_{1.4}MnO_4$	5.0119	0.0056	837.96	7
[74]	2017		$La_{0.9}Sr_{0.1}Ga_{0.8}Mg_{0.2}O_{3-\delta}$	0.275	$PrBa(Fe_{0.8}Sc_{0.2})_2O_{5+\delta}$	5.75	1	800	s3
[75]	2017		$La_{0.8}Sr_{0.2}Ga_{0.8}Mg_{0.2}O_{3-\delta}$	0.52	$PrBaMn_{1.5}Fe_{0.5}O_{5+\delta}$	112.5	7.4	800	4
[76]	2016		$La_{0.9}Sr_{0.1}Ga_{0.8}Mg_{0.2}O_{3-\delta}$ + ($La_{0.4}Ce_{0.6}O_2$ buffer layer)	0.25	$Pr_{0.5}Ba_{0.4}Ca_{0.1}MnO_3$	13.4	5.48	800	4
[77]	2016	Other	60wt%(LaCePr-oxide) + 40wt%($La_{0.6}Sr_{0.4}Co_{0.2}Fe_{0.8}O_{3-\delta}$)	0.4	$Ni_{0.8}Co_{0.15}Al_{0.05}Li$ + (Ni foam pasted)	0.4415	0.6809	575	8d

Table III A1 - Summary of the electrolyte supported pattern cells results displayed in section 3.2

Pattern cells			Sample	Temp.	OCV	I (PPD)	V (PPD)	PPD	Ro	Rp	Freq (max -Z'')	Time (max -Z'')	Z' (max -Z'')	max -Z''	ASR	Ea
cathode	Electrolyte	Anode		(°C)	(V)	(mA)	(V)	($mW.cm^{-2}$)	(ohm)	(ohm)	(Hz)	(s)	(ohm)	(ohm)	($ohm.cm^2$)	($kJ.mol^{-1}$)
BSCF	SDC	NiO + SDC	A	800	0.8118	190	0.46553	372.29548	1.3453	0.173222	15.84893	41.33	1.431	0.05833	0.041154053	120.753814
				750	0.85148	131	0.47701	263.0225	1.797469	0.279238	7.94328	45.96	1.9631	0.08997	0.066341347	
				700	0.88762	86	0.49286	178.40569	2.757990	0.645428	5.01187	47.87	3.0682	0.17188	0.15334074	
				650	0.91962	53	0.50363	112.35081	4.026910	1.224164	2.51189	49.75	4.6435	0.3056	0.290836829	
				600	0.951	29	0.57477	70.15937	6.823471	3.112885	1.25893	53.73	8.1949	0.70419	0.739559236	
				550	0.97663	17	0.55986	40.06053	9.709596	10.81639	0.39811	65.54	16.189	1.8973	2.569758437	
			B	800	0.80269	164	0.44973	310.44873	1.708289	0.178569	15.84893	41.67	1.8028	0.05312	0.042424368	110.554726
				750	0.83972	118	0.45786	227.40777	2.269614	0.351151	10	45.42	2.4259	0.08739	0.083426499	
				700	0.87338	82	0.47722	164.70945	3.116150	0.649966	5.01187	47.28	3.4138	0.15783	0.154418957	
				650	0.90585	53	0.49536	110.50533	4.625617	1.274831	2.51189	49.62	5.1815	0.30992	0.302874463	
				600	0.93695	33	0.5008	69.56166	7.311824	3.037340	0.79433	56.86	8.8254	0.78487	0.721611144	
				550	0.96239	18	0.53318	40.39618	12.30318	8.113033	0.50119	62.74	16.406	1.5182	1.927494379	

Table III A2 - Summary of the electrolyte supported LBTMN and LCTMN symmetrical cells results displayed in section 3.3

Symmetrical cells			Sample	Temp.	OCV	I (PPD)	V (PPD)	PPD	Ro	Rp	Freq (max -Z'')	Time (max -Z'')	Z' (max -Z'')	max -Z''	ASR	Ea
cathode	Electrolyte	Anode		(°C)	(V)	(mA)	(V)	(mW.cm^{-2})	(ohm)	(ohm)	(Hz)	(s)	(ohm)	(ohm)	(ohm.cm^2)	(kJ.mol^{-1})
LBTMN	SDC	LBTMN	A	800	0.61548	14	0.34915	20.57434	3.398974	10.71165	199.5262	32.42	7.0969	2.9665	2.544874953	116.052721
				750	0.62325	7	0.35822	10.55459	4.667771	23.54393	79.43282	35.56	13.124	4.5635	5.593567502	
				700	0.61182	3	0.36318	4.58601	6.768169	56.53495	39.81072	38.25	24.549	10.017	13.4315739	
				650	0.59	1	0.4355	1.83308	10.57651	140.4585	12.58925	44.34	60.215	27.094	33.37012401	
				600	0.58712	1	0.19128	0.8051	15.53607	187.9364	0.12589	97.25	148.3	39.943	44.64993085	
				550	-	-	-	-	-	-	-	-	-	-	-	
			B	800	0.6547	18	0.36907	27.96202	4.002074	9.027252	199.5262	32.42	6.927	1.6555	2.144694441	119.326425
				750	0.6717	10	0.38923	16.38305	5.452787	17.78750	100	35	10.279	2.1591	4.225953695	
				700	0.67148	5	0.39711	8.35731	7.762843	36.91632	0.0631	153.54	34.707	6.7775	8.770578121	
				650	0.66648	3	0.34063	4.30129	11.42215	91.62803	0.0631	138.79	79.837	17.705	21.76898822	
				600	0.64024	1	0.46196	1.94443	17.92519	183.6111	0.0631	137.96	140.43	39.171	43.62232518	
				550	0.59894	1	0.08717	0.36692	-	-	-	-	-	-	-	
LCTMN		LCTMN	A	800	0.65489	69	0.33535	97.39583	2.119367	4.945638	199.5262	35.58	4.9095	1.9149	1.174984777	91.5153451
				750	0.66401	40	0.33576	56.53057	2.914490	12.71732	79.43282	39.66	9.9587	4.9222	3.021379793	
				700	0.67038	24	0.32532	32.86365	4.224281	30.32990	31.62278	38.96	21.471	11.617	7.205777696	
				650	0.772	16	0.33547	22.59239	6.355439	39.93932	25.11886	39.89	27.869	13.223	9.488783351	
				600	0.68887	13	0.2918	15.96711	10.14585	75.81947	12.58925	44.45	49.747	20.424	18.01319011	
				550	0.85484	8	0.27542	9.27413	17.15444	132.0652	15.84893	43.28	51.923	14.86	31.37605948	
			B	800	0.65986	52	0.34445	75.39052	1.993162	5.966280	316.2278	30.78	5.2533	2.4043	1.417468822	97.3381539
				750	0.68785	30	0.35749	45.14194	2.618210	14.83638	100	38.83	11.727	6.4309	3.52482717	
				700	0.7171	18	0.3409	25.82803	3.675081	37.22248	50.11872	37.19	25.873	15.166	8.84331722	
				650	0.76427	11	0.33697	15.60171	5.547235	45.86505	31.62278	38.84	32.554	18.672	10.89661893	
				600	0.79876	6	0.34308	8.66439	8.063282	137.7152	25.11886	41.98	82.821	53.126	32.7183792	
				550	0.82486	3	0.34185	4.31671	13.79693	164.0453	10	44.91	118.39	60.871	38.97387737	

Table III A3 - Summary of the electrolyte supported LBTMN and LCTMN cathode cells results displayed in section 3.4

Cathode cells			Sample	Temp.	OCV	I (PPD)	V (PPD)	PPD	Ro	Rp	Freq (max -Z'')	Time (max -Z'')	Z' (max -Z'')	max -Z''	ASR	Ea
cathode	Electrolyte	Anode		(°C)	(V)	(mA)	(V)	(mW.cm^{-2})	(ohm)	(ohm)	(Hz)	(s)	(ohm)	(ohm)	(ohm.cm^2)	(kJ.mol^{-1})
LBTMN	SDC	NiO + SDC	A	800	0.57258	72	0.27235	82.53764	2.094729	5.973569	398.1072	31.7	5.2404	2.177	1.419200625	107.856963
				750	0.5443	44	0.23668	43.83395	2.649170	10.95213	251.1886	35.32	8.9428	4.0621	2.602006578	
				700	0.50267	26	0.20533	22.47029	3.724944	22.57726	158.4893	33.38	17.208	8.4551	5.363905447	
				650	0.43464	14	0.16967	9.99831	5.599047	49.65914	125.8925	33.92	33.202	20.092	11.79801884	
				600	0.40346	8	0.14973	5.04185	9.633618	105.9594	50.11872	39.03	73.665	53.365	25.17382683	
				550	0.57516	4	0.19396	3.26557	16.229	223.6432	25.11886	41.31	160.44	116.79	53.13315432	
			B	800	0.63813	89	0.31349	117.43625	1.971947	5.889193	25.11886	41.3	5.478	1.9162	1.399154418	110.345081
				750	0.61953	54	0.27403	62.28522	2.545310	12.07340	39.81072	41.84	9.8823	3.9622	2.868398882	
				700	0.59717	29	0.25299	30.8815	3.360635	16.82575	15.84893	45.31	13.549	4.8795	3.997461711	
				650	0.63279	16	0.23763	16.00356	4.915597	44.61603	63.09573	36.74	28.969	16.146	10.59987754	
				600	0.66988	9	0.21282	8.06217	7.789412	100.4545	50.11872	39.08	64.379	41.447	23.86598867	
				550	0.7494	5	0.19723	4.15076	14.58690	253.9611	25.11886	41.79	162.29	113.65	60.33608908	
LCTMN			A	800	0.60005	83	0.28711	100.30402	1.585026	6.821462	199.5262	34.09	5.5149	2.6492	1.620642988	86.324186
				750	0.55415	50	0.24736	52.05874	2.244446	11.89310	100	41.64	9.2118	4.4811	2.825562614	
				700	0.50077	31	0.22225	29.00003	3.344596	12.78763	100	38.59	10.848	4.2418	3.038085327	
				650	0.47303	19	0.21485	17.18233	4.915597	29.99200	31.62278	38.65	21.488	9.9148	7.125499829	
				600	0.55049	11	0.21292	9.85827	7.938727	59.08762	19.95262	42.35	42.121	16.716	14.03803636	
				550	0.62382	6	0.19744	4.9862	11.29834	129.2871	50.11872	39.86	85.351	46.267	30.71601799	
			B	800	0.63076	96	0.32488	131.27606	1.834482	5.716138	199.5262	34.47	5.1469	2.1982	1.358040024	92.421872
				750	0.557	64	0.246	66.26791	2.027490	7.901686	79.43282	37.3	6.5464	2.7747	1.877282457	
				700	0.49572	41	0.22036	38.02799	3.352818	12.81552	125.8925	37.54	10.243	4.0117	3.044711467	
				650	0.52734	25	0.21766	22.90394	3.710546	26.46192	158.4893	33.13	18.41	10.048	6.286823214	
				600	0.48548	15	0.20718	13.08053	4.915597	44.61603	63.09573	36.74	28.969	16.146	10.59987754	
				550	0.61421	8	0.23945	8.06293	10.61342	136.5313	25.11886	41.9	89.721	54.403	32.43710435	

Table III A4 - Summary of the electrolyte supported LBTMN and LCTMN anode cells results displayed in section 3.5

Anode cells			Sample	Temp.	OCV	I (PPD)	V (PPD)	PPD	Ro	Rp	Freq (max -Z'')	Time (max -Z'')	Z' (max -Z'')	max -Z''	ASR	Ea
cathode	Electrolyte	Anode		(ºC)	(V)	(mA)	(V)	(mW.cm^{-2})	(ohm)	(ohm)	(Hz)	(s)	(ohm)	(ohm)	(ohm.cm^2)	(kJ.mol^{-1})
BSCF	SDC	LBTMN	A	800	0.63733	30	0.33233	41.9644	2.607954	4.872906	0.1	112.45	6.0669	1.7879	1.157704923	128.433129
				750	0.6211	16	0.32368	21.79814	3.750525	11.66603	0.12589	96.01	10.977	3.7756	2.77161551	
				700	0.59981	8	0.31416	10.57861	5.642715	29.62937	0.12589	100.82	24.193	8.3533	7.039345562	
				650	0.56423	4	0.29876	5.03001	8.858175	76.45204	0.31623	72.42	50.994	17.643	18.16347516	
				600	0.5062	2	0.22729	1.91338	14.85040	156.5822	1	56.73	95.664	40.069	37.20079937	
				550	0.46538	1	0.17188	0.72346	21.16548	395.7230	1.99526	54.04	198.68	97.125	94.01587764	
			B	800	0.70669	21	0.46274	40.90245	2.658704	5.403529	0.1	112.94	6.1103	1.7543	1.283770365	138.371075
				750	0.6624	12	0.35246	17.8026	4.184186	9.670745	0.0631	136.94	12.86	4.4498	2.297575486	
				700	0.64418	7	0.33887	9.98448	6.144483	35.24564	0.07943	131.3	29.574	10.466	8.373658062	
				650	0.61479	4	0.30944	5.20981	9.317245	75.78517	0.05012	166.03	66.325	21.528	18.00504145	
				600	0.59102	2	0.30697	2.58415	15.138	242.1182	0.39811	67.87	114.98	45.591	57.52244181	
				550	0.53423	1	0.25515	1.07395	26.039	498.9447	1.25893	56.64	241.21	119.07	118.5392789	
		LCTMN	A	800	0.74982	58	0.43675	106.62403	2.203364	1.945225	0.05012	171.11	3.4662	0.61089	0.462146614	116.025914
				750	0.78721	32	0.4948	66.64592	3.097801	3.724083	0.05012	190.41	5.1712	1.1085	0.884767682	
				700	0.80769	18	0.54104	40.99154	5.242509	7.237787	0.15849	86.39	9.7521	1.7464	1.719553441	
				650	0.81316	10	0.5435	22.87643	7.322944	25.47484	0.03162	219.1	22.82	7.4163	6.052313602	
				600	0.84733	6	0.56783	14.34027	11.37567	30.58011	0.02512	282.94	28.384	8.1666	7.265221551	
				550	0.85808	3	0.60368	7.62289	20.29268	107.5488	0.02512	275.69	79.511	25.459	25.55144554	
			B	800	0.74118	65	0.42331	115.81401	3.077714	1.447381	0.07943	136.09	4.0763	0.38156	0.343868792	122.323320
				750	0.74528	38	0.42098	67.33453	4.431068	3.115456	0.07943	120.54	6.4094	0.81152	0.740169943	
				700	0.76153	22	0.43871	40.62458	5.955097	6.525199	0.0631	136.67	10.486	1.7443	1.550256896	
				650	0.7664	10	0.49925	21.01386	9.438010	17.18030	0.05012	166.18	21.457	4.4831	4.081695867	
				600	0.76463	5	0.49827	10.48633	14.76806	39.98076	0.0631	151.09	41.497	10.31	9.498629301	
				550	0.75405	3	0.41639	5.25783	24.698	88.44552	0.12589	99.42	76.633	21.187	21.01288707	

Table IV A1 - Summary of the XRD refinements for chemical stability

Sample Type	Treatment conditions	Sample composition	Agreement parameters		Considered space group	Lattice parameters (Å)		Estimated purities (%)			Rietveld Weight %
			GOF	R_{wp}							
			(dimensionless)	(%)	(name)	a	average	average	min	max	(%)
Single powder	As calcined	BSCF	1.081532401	3.3700778	P m -3 m	3.983442	-	99.54114414	-	-	100
		SDC	1.477616746	9.134209	F m -3 m	5.430008	-	99.50412945	-	-	100
		LBTMN	1.364240586	7.503115	P m -3 m	3.9114068	-	97.02101511	95.456	98.58603	100
		LCTMN	2.729160499	10.394065	P m -3 m	3.8888793	-	74.79087017	64.69072	84.89102	100
			2.159613647	8.826794	P m -3 m	3.8860257	-	74.5950789	71.86562	77.32453	39.444378
					P 3 2 1	3.8088562	5.965911	13.27649407	12.7907	13.76228	42.163994
					P 63/m m c	16.876997	6.92956	5.596226817	5.391459	5.800994	18.391626
	2h at 800C in H2	LBTMN	1.203179738	6.8785205	P m -3 m	3.972394	-	98.14063497	97.34214	98.93913	100
		LCTMN	4.473584557	13.084688	P m -3 m	3.9128366	-	52.01387856	31.38386	72.6439	100
			2.012069623	8.758454	P m -3 m	3.9175258	-	42.91982159	36.87755	48.9621	15.01787
					P 3 2 1	3.8930683	6.307757	13.36401397	11.48262	15.24541	14.488299
					smaller P 3 2 1	3.773689	6.118245	11.98946295	10.30158	13.67735	21.142874
					P 63/m m c	10.027976	7.480073	3.223315624	2.769536	3.677096	49.350956
Mixture	5h at 1000C in air	LBTMN + SDC	1.075845036	6.47859	P m -3 m	3.918684	-	40.6542321	40.53336	40.7751	47.626305
					F m -3 m	5.4091454	-	50.25595611	50.10654	50.40538	52.373695
		LCTMN + SDC	1.309671959	6.9464035	P m -3 m	3.86875	-	36.54581419	35.78118	37.31045	45.586002
					F m -3 m	5.4210863	-	58.50321501	57.27917	59.72726	54.413998
			1.114193825	6.402471	P m -3 m	3.895808	-	36.3110374	35.9427	36.67938	16.13072
					F m -3 m	5.459103	-	58.12737999	57.53773	58.71703	42.024235
					P 3 2 1	3.8217585	5.974296	2.882941352	2.853697	2.912186	16.767324
					P 63/m m c	14.938253	7.007152	0.895570378	0.886486	0.904655	25.077719
	2h at 800C in H2	LBTMN + SDC	2.525810601	6.0684204	P m -3 m	3.967134	-	43.91625249	42.29131	45.54119	47.071125
					F m -3 m	5.429458	-	44.8012674	43.14358	46.45895	52.928875
		LCTMN + SDC	3.678015141	7.1233726	P m -3 m	3.9277582	-	12.27943694	11.53493	13.02394	44.767017
					F m -3 m	5.443814	-	77.18654308	72.5067	81.86639	55.232983
			2.044420406	5.306519	P m -3 m	3.9280486	-	12.2580107	11.99409	12.52193	13.007646
					F m -3 m	5.446912	-	77.05186121	75.39288	78.71084	34.934517
					P 3 2 1	3.9280486	6.140524	4.80916869	4.705624	4.912713	12.751467
					smaller P 3 2 1	3.8028257	5.996466	2.372984364	2.321892	2.424076	18.52929
					P 63/m m c	15.66523	6.350577	0.171169312	0.167484	0.174855	20.77708

Table IV A2 – summary of the XRD refinements for Calcination temperature analysis

Sample Type	Sample composition	Calcination temperature	Agreement parameters		Considered space group	Lattice parameters (Å)		Estimated purities (%)			Rietveld Weight %
			GOF	R_{wp}							
		(ºC)	(dimensionless)	(%)	(name)	a	(%)	average	min	max	(%)
Single powder	LBTMN	1000	1.705678576	8.77613	P m -3 m	3.9365058	-	76.44294121	68.76899	84.1169	100
		1100	1.364240586	7.503115	P m -3 m	3.9114068	-	97.02101511	95.45600	98.58603	100
		1250	1.405310196	8.400506	P m -3 m	3.9426916	-	99.14777256	98.99558	99.29996	100
	LCTMN	1000	-	-	P m -3 m	-	-	61.71310056	47.65814	75.76806	-
			2.152531177	8.692589	P m -3 m	3.8757582	-	66.70289172	64.69114	68.71465	59.235058
					P 3 2 1	3.932226	6.12726	21.3327434	20.68935	21.97614	28.90014
					P 63/m m c	17.292128	6.125252	7.335768201	7.114522	7.557014	11.864802
		1100	2.729160499	10.394065	P m -3 m	3.8888793	-	74.79087017	64.69072	84.89102	100
			2.159613647	8.826794	P m -3 m	3.8860257	-	74.5950789	71.86562	77.32453	39.444378
					P 3 2 1	3.8088562	5.965911	13.27649407	12.7907	13.76228	42.163994
					P 63/m m c	16.876997	6.92956	5.596226817	5.391459	5.800994	18.391626
		1150	-	-	P m -3 m	-	-	82.23441375	71.19694	93.27189	-
			2.929133326	10.380421	P m -3 m	3.868998	-	81.3706467	74.92083	87.82046	59.02341
					P 3 2 1	3.7837646	5.977915	5.869619577	5.404366	6.334873	19.242315
					P 63/m m c	15.586502	5.935878	2.15409652	1.983353	2.32484	21.734274
		1200	-	-	P m -3 m	-	-	83.50496331	73.80833	93.2016	-
			2.606224076	9.724022	P m -3 m	3.8674345	-	83.81279703	77.9702	89.6554	65.892044
					P 3 2 1	3.7733567	6.052841	6.113554439	5.687378	6.539731	21.449514
					P 63/m m c	16.203459	7.423283	1.498953741	1.394461	1.603446	12.658442
		1250	-	-	P m -3 m	-	-	77.96110422	65.09546	90.82675	-
			2.70916062	10.515643	P m -3 m	3.8870335	-	83.10305338	82.29798	83.90813	30.115593
					P 3 2 1	3.7962139	6.063545	8.393175091	8.311865	8.474485	33.25725
					P 63/m m c	16.716776	7.146739	4.342761	4.30069	4.384832	36.627155

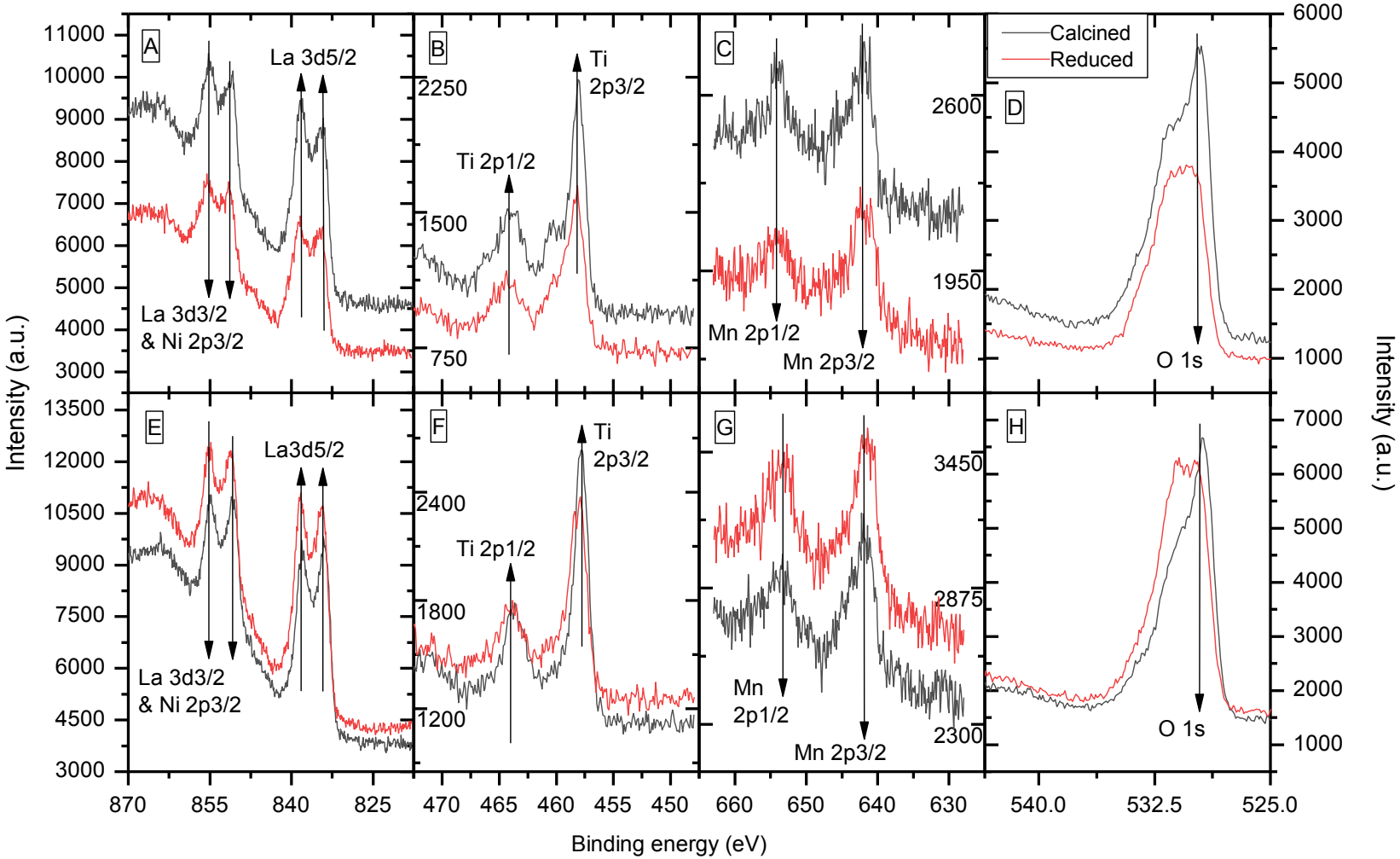

Figure IV A1 - Calcined and reduced LBTMN (top) and LCTMN (bottom) XPS analysis typical binding energy intensities of the elements in common (from left to right: Lanthanum, Titanium, Manganese and Oxygen)

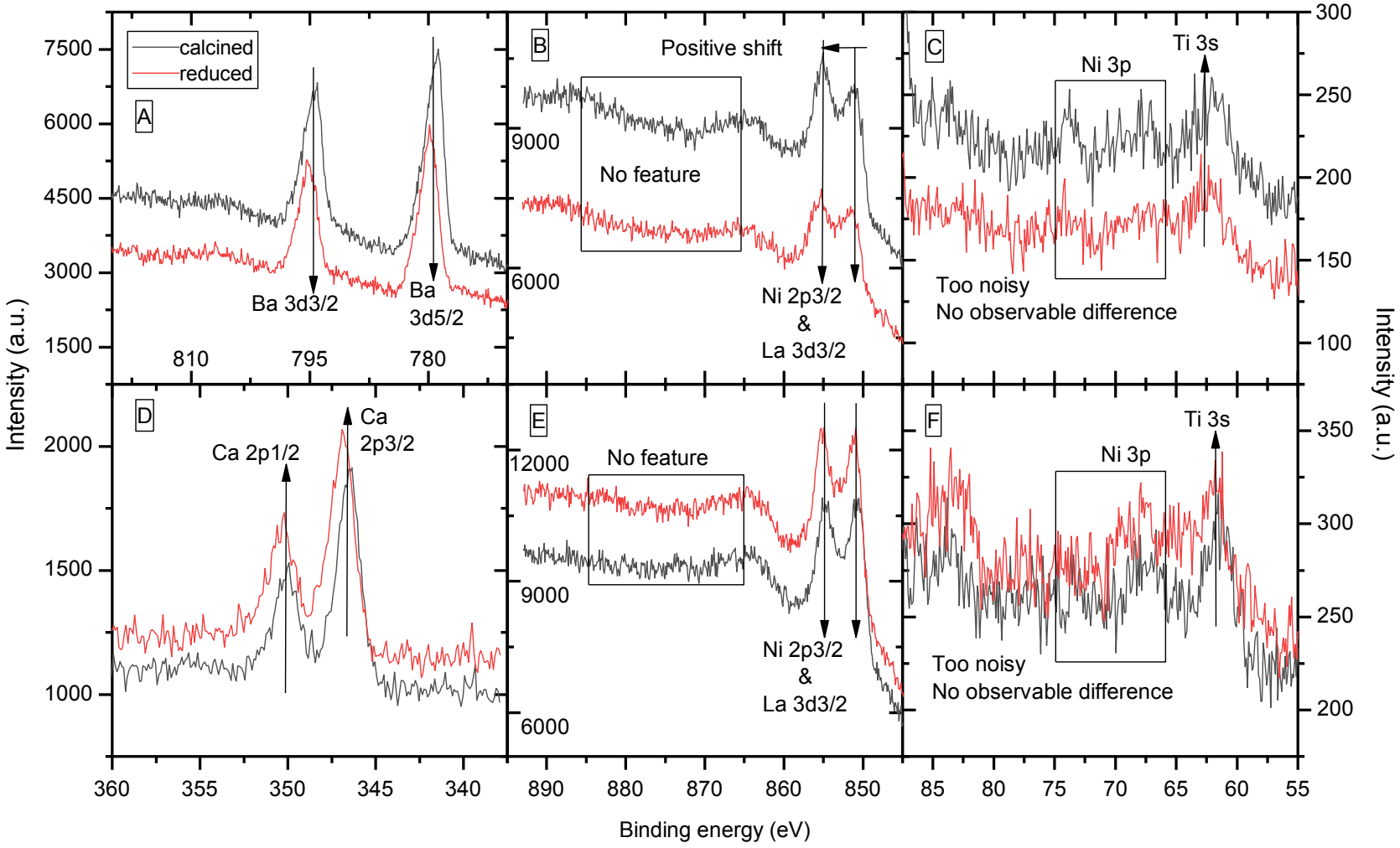

Figure IV A2 - Calcined and reduced LBTMN (top) and LCTMN (bottom) XPS analysis typical binding energy intensities of Barium (A), Calcium (C) and Nickel $2p_{3/2}$ (B and E) and 3p (C and F)

Table V A1 – PPD of the cathode cells from Chapter III (section 3.4), conductivities and estimated activation energies of LBTMN and LCTMN measured in air and relative average differences

Temperature		LBTMN						LCTMN						Diferences	
		σ			Chapter III Cathode cells PPD			σ			Chapter III Cathode cells PPD			σ	PPD
(ºC)		(S.cm^{-1})			(mW.cm^{-2})			(S.cm^{-1})			(mW.cm^{-2})			(S.cm^{-1})	(mW.cm^{-2})
		Sample		Average	Sample		Average	Sample		Average	Sample		Average	-	-
		A	B	(A+B)/2	A	B	(A+B)/2	A	B	(A+B)/2	A	B	(A+B)/2	-	-
850		0.26804	0.24098	0.25451	-	-	-	0.90059	0.8671	0.883845	-	-	-	0.629335	-
825		0.24176	0.21735	0.229555	-	-	-	0.84377	0.8128	0.828285	-	-	-	0.59873	-
800		0.21637	0.1949	0.205635	82.53764	117.43625	99.986945	0.78798	0.7586	0.77329	100.30402	131.27606	115.79004	0.567655	15.803095
775		0.19303	0.17356	0.183295	-	-	-	0.73412	0.70604	0.72008	-	-	-	0.536785	-
750		0.17093	0.15373	0.16233	43.83395	62.28522	53.059585	0.67979	0.65534	0.667565	52.05874	66.26791	59.163325	0.505235	6.10374
725		0.15035	0.13515	0.14275	-	-	-	0.62718	0.6039	0.61554	-	-	-	0.47279	-
700		0.13144	0.11809	0.124765	22.47029	30.8815	26.675895	0.57429	0.55166	0.562975	29.00003	38.02799	33.51401	0.43821	6.838115
675		0.11405	0.10236	0.108205	-	-	-	0.52407	0.5031	0.513585	-	-	-	0.40538	-
650		0.09846	0.08819	0.093325	9.99831	16.00356	13.000935	0.47585	0.45636	0.466105	17.18233	22.90394	20.043135	0.37278	7.0422
625		0.08422	0.07537	0.079795	-	-	-	0.42874	0.4109	0.41982	-	-	-	0.340025	-
600		0.07138	0.06386	0.06762	5.04185	8.06217	6.55201	0.38454	0.36866	0.3766	9.85827	13.08053	11.4694	0.30898	4.91739
575		0.06011	0.0536	0.056855	-	-	-	0.34413	0.32788	0.336005	-	-	-	0.27915	-
550		0.04985	0.04449	0.04717	3.26557	4.15076	3.708165	0.30595	0.291	0.298475	4.9862	8.06293	6.524565	0.251305	2.8164
525		0.04082	0.03658	0.0387	-	-	-	0.26943	0.2551	0.262265	-	-	-	0.223565	-
500		0.03297	0.02964	0.031305	-	-	-	0.24631	0.22229	0.2343	-	-	-	0.202995	-
475		0.02641	0.02368	0.025045	-	-	-	0.20038	0.19193	0.196155	-	-	-	0.17111	-
450		0.02065	0.01865	0.01965	-	-	-	0.17125	0.16376	0.167505	-	-	-	0.147855	-
-		-	-	-	-	-	-	-	-	-	-	-	-	-	-
Ea	(eV)	0.4487457	0.4491331	0.4489394	-	-	-	0.2887576	0.2933091	0.29103335	-	-	-	0.15790605	-
[Ln(σ)]	(k.J.mol^{-1})	43.2334	43.2707	43.25205	-	-	-	27.8197	28.2582	28.03895	-	-	-	15.2131	-
Ea	(eV)	0.5261558	0.5265433	0.5263496	-	-	-	0.3661677	0.3707193	0.36844354	-	-	-	0.15790604	-
[Ln(σT)]	(k.J.mol^{-1})	50.6913	50.7286	50.70993	-	-	-	35.2776	35.7161	35.49684	-	-	-	15.2131	-

Table V A2 – PPDs of the anode cells from Chapter III (section 3.5), conductivities and estimated activation energies of LBTMN and LCTMN measured in hydrogen and relative average differences

Temperature			LBTMN						LCTMN						Differences	
			σ			Chapter III Anode cells PPD			σ			Chapter III Anode cells PPD			σ	PPD
(ºC)			(S.cm^{-1})			(mW.cm^{-2})			(S.cm^{-1})			(mW.cm^{-2})			(S.cm^{-1})	(mW.cm^{-2})
			Sample		Average	Sample		Average	Sample		Average	Sample		Average	-	-
			A	B	(A+B)/2	A	B	(A+B)/2	A	B	(A+B)/2	A	B	(A+B)/2	-	-
850			7.77892E-05	7.87226E-05	7.82559E-05	-	-	-	0.000205452	0.000208425	0.000206939	-	-	-	0.000128683	-
825			6.54875E-05	6.80516E-05	6.67696E-05	-	-	-	0.000176991	0.000175464	0.000176228	-	-	-	0.000109458	-
800			5.88465E-05	5.99081E-05	5.93773E-05	41.9644	40.90245	41.433425	0.000153641	0.000148605	0.000151123	106.62403	115.81401	111.21902	9.17457E-05	69.785595
775			4.64346E-05	4.69871E-05	4.67109E-05	-	-	-	0.000120386	0.000112347	0.000116367	-	-	-	6.96557E-05	-
750			3.34311E-05	0.000034225	3.38281E-05	21.79814	17.8026	19.80037	8.49506E-05	8.22063E-05	8.35785E-05	66.64592	67.33453	66.990225	4.97504E-05	47.189855
725			2.17488E-05	2.20515E-05	2.19002E-05	-	-	-	6.01654E-05	0.000063988	6.20767E-05	-	-	-	4.01766E-05	-
700			0.000015217	1.61582E-05	1.56876E-05	10.57861	9.98448	10.281545	3.66042E-05	4.40938E-05	0.000040349	40.99154	40.62458	40.80806	2.46614E-05	30.526515
675			1.24047E-05	1.33118E-05	1.28583E-05	-	-	-	3.08865E-05	3.11265E-05	3.10065E-05	-	-	-	1.81483E-05	-
650			1.00139E-05	1.06927E-05	1.03533E-05	5.03001	5.20981	5.11991	2.71824E-05	2.37444E-05	2.54634E-05	22.87643	21.01386	21.945145	1.51101E-05	16.825235
625			8.61636E-06	8.75247E-06	8.68442E-06	-	-	-	1.78557E-05	0.000018609	1.82324E-05	-	-	-	9.54794E-06	-
600			0.000007111	7.15143E-06	7.13122E-06	1.91338	2.58415	2.248765	1.52297E-05	1.51583E-05	0.000015194	14.34027	10.48633	12.4133	8.06279E-06	10.164535
575			6.81888E-06	6.86059E-06	6.83974E-06	-	-	-	1.48458E-05	1.50516E-05	1.49487E-05	-	-	-	8.10897E-06	-
550			5.77506E-06	6.4269E-06	6.10098E-06	0.72346	1.07395	0.898705	1.15607E-05	1.16408E-05	1.16008E-05	7.62289	5.25783	6.44036	5.49977E-06	5.541655
525			5.29442E-06	5.27391E-06	5.28417E-06	-	-	-	1.08916E-05	1.06424E-05	0.000010767	-	-	-	5.48284E-06	-
500			5.19811E-06	4.91033E-06	5.05422E-06	-	-	-	8.53846E-06	9.2249E-06	8.88168E-06	-	-	-	3.82746E-06	-
475			4.55608E-06	4.62111E-06	4.5886E-06	-	-	-	7.47972E-06	7.73184E-06	7.60578E-06	-	-	-	3.01719E-06	-
450			4.38071E-06	4.39458E-06	4.38765E-06	-	-	-	7.0455E-06	7.06458E-06	7.05504E-06	-	-	-	2.6674E-06	-
-			-	-	-	-	-	-	-	-	-	-	-	-	-	-
Ea [Ln(σ)]	(high T)	(eV)	0.9969488	0.9725765	0.98476265	-	-	-	1.0101148	1.0110296	1.0105722	-	-	-	0.02580955	-
		(k.J.mol^{-1})	96.0487	93.7006	94.87465	-	-	-	97.3172	97.4053	97.36125	-	-	-	2.4866	-
	(low T)	(eV)	0.207879	0.2173764	0.2126277	-	-	-	0.314345	0.3120494	0.3131972	-	-	-	0.1005695	-
		(k.J.mol^{-1})	20.0276	20.9426	20.4851	-	-	-	30.2848	30.0637	30.17425	-	-	-	9.68915	-
Ea [Ln(σT)]	(high T)	(eV)	1.084696066	1.060323831	1.07250995	-	-	-	1.09786213	1.098776919	1.098319525	-	-	-	0.025809576	-
		(k.J.mol^{-1})	104.5025329	102.1544463	103.32849	-	-	-	105.7709869	105.8591202	105.8150535	-	-	-	2.48656392	-
	(low T)	(eV)	0.277293397	0.286791673	0.28204254	-	-	-	0.383759356	0.381464615	0.382611985	-	-	-	0.10056945	-
		(k.J.mol^{-1})	26.71519078	27.63028023	27.1727355	-	-	-	36.97240726	36.75132577	36.86186652	-	-	-	9.689131011	-